Modelling and optimization

of a permanent magnet machine

in a flywheel

Modelling and optimization

of a permanent magnet machine

in a flywheel

PROEFSCHRIFT

ter verkrijging van de graad van doctor
aan de Technische Universiteit Delft,
op gezag van de Rector Magnificus prof.dr.ir. J.T. Fokkema,
voorzitter van het College voor Promoties,
in het openbaar te verdedigen op donderdag 20 november 2003 om 10:30 uur
door

Stanley Robert HOLM

Magister Ingeneriae, Randse Afrikaanse Universiteit
geboren te Johannesburg, Zuid-Afrika

Dit proefschrift is goedgekeurd door de promotor: Prof.dr. J.A. Ferreira

Toegevoegd promotor: Dr.ir. H. Polinder

Samenstelling promotiecommissie:

Rector Magnificus, voorzitter
Prof.dr. J.A. Ferreira, Technische Universiteit Delft, promotor
Dr.ir. H. Polinder, Technische Universiteit Delft, toegevoegd promotor
Prof.dr.ir. J.C. Compter, Technische Universiteit Eindhoven
Prof.Dr.-Ing. W.-R. Canders, Technische Universiteit Braunschweig
Prof.dr.ir. H. Blok, Technische Universiteit Delft
Prof.dr. J.J. Smit, Technische Universiteit Delft
Dr.ir. H. Huisman, CCM, Nuenen
Prof.ir. L. van der Sluis, Technische Universiteit Delft, reservelid

To my wife Renate

FOREWORD

A thesis like this one is the result of the efforts of not only one person, but many. Some contribute directly to the thesis by giving guidance, constructive comments, etc. Other people do not contribute to the thesis directly, but provide friendship and support. I am very grateful to both these groups of people for having played such an important part of my life over the past four years, and some even longer.

Firstly, the people who directly contributed to this work include:

Prof. Braham Ferreira, my promotor. I would like to thank him for his insightful guidance and for freely using his ability to quickly see those things which are really important, and those which are not, to my advantage.

Henk Polinder, my co-promotor. With no one did I have more hours of fruitful talks about the thesis content (and other important things in life), and for these hours I am very grateful. Without the able leadership of both my promotors this thesis would never have seen the light in four years' time.

Martin Hoeijmakers, who gave me a "kick start" in analytical field calculations, and for the many discussions we had on this very interesting and too often neglected research field.

Some of the people of TNO PML formed part of the research project initially. I am grateful for the participation of TNO PML in general in these initial stages. In particular, I would like to thank Remco Dill for the flywheel literature survey and the application survey that we worked on together, and also for other constructive comments. To Timo Huijser, who did the FLUX2D calculations to verify the analytical results, a big thank you. I would also like to thank Peter van Gelder, whose wisdom shined through every time we had our weekly meetings.

Our industrial partner in this project, CCM, for the collaboration and the opportunity to work on part of a very interesting system. I would like to especially thank Henk Huisman for his help with the measurements on location in Nuenen and for sharing his knowledge and skills, also in his capacity as member of the PhD

commission.

Prof. Blok shared with me a great deal of insight in electromagnetic field theory. I would like to thank him in particular for his comments and suggestions regarding Appendix B.

With gratitude I received comments and suggestions from the other members of the PhD commission. These are: Prof. Compter, Prof. Canders, Prof. Smit and Prof. van der Sluis.

A sincere thank you also to Mirjam Nieman, who did the English editing of the manuscript.

To Andreas Kellert and Delano Richardson of DAWFX who did the cover design: thank you, guys, it looks great.

The second group of persons (those that did not directly contribute to the thesis but provided friendship and support) include:

The many friends I made at the research group. I would like to mention Maxime Dubois in particular, who started with me in September, 1999 – we shared much of our walk towards a PhD.

My friends at the Christelijke Gemeente Levend Water in Delft, too many to mention by name, who have become like family.

My family and family in law for their unwavering love, support and encouragement.

My wife Renate, whose steady support and love made me stand strong through the rough times. I also thank her for her patience and understanding when I had to work many long hours to finish this thesis. The thesis is dedicated to her; she truly fits the description of the virtuous wife of Proverbs 31:10–31.

Finally, and above all, my gratitude towards God, who is faithful beyond human comprehension, cannot be expressed by words.

CONTENTS

LIST OF SYMBOLS

Latin letters

A	Magnetic vector potential	$[\text{T.m}]=[\text{Vs/m}]$
B	Magnetic flux density	$[\text{T}]=[\text{Vs/m}^2]$
D	Electric flux density	$[\text{C/m}^2]$
E	Electric field intensity	$[\text{V/m}]$
f	Lorentz force density	$[\text{N/m}^3]$
H	Magnetic field intensity	$[\text{A/m}]$
J	Current density	$[\text{A/m}^2]$
K	Surface current density	$[\text{A/m}]$
M	Magnetization	$[\text{A/m}]$
P	Polarization	$[\text{C/m}^2]$
S	Poynting vector	$[\text{W/m}^2]$
T	Electric vector potential	$[\text{A/m}]$
T$_e$	Electromagnetic torque	$[\text{N.m}]$
v	Speed	$[\text{m/s}]$
n̂	Unit normal vector	$[\text{m}]$
A	Effective plate area of a capacitor (Chapter 2)	$[\text{m}^2]$
C	Capacitance	$[\text{F}]$

E	Stored energy (Chapter 2)	[J]
h	Height	[m]
I	Current	[A]
I	Mass moment of inertia (Chapter 2)	[kg.m^2]
K	Flywheel shape factor (Chapter 2)	
k	Space harmonic	
L	Inductance	[H]
l	Length	[m]
m	Mass (Chapter 2)	[kg]
m	Number of phases	
N	Number of turns	
n	Number of electrons (Chapter 2)	
n	Time harmonic	
n_s	Winding distribution	[rad^{-1}]
P	Power	[W]
p	Number of pole pairs	
q	Number of slots per pole per phase	
r	Radial coordinate	[m]
s	Number of slots	
T	Temperature	[K]
t	Time	[s]
V	Voltage	[V]
V_m	Magnetic scalar potential	[A]
X	Reactance	[Ω]
E_p	RMS value of the no-load voltage	[V]
I_s	RMS value of the stator current	[A]
U_s	RMS value of the machine terminal voltage	[V]

$\ddot{k}$ Double-sided index: $\ddot{k} \in \mathbb{Z}$; related to the space harmonic by: $k = 6\ddot{k} + 1$

$\ddot{n}$ Double-sided index: $\ddot{n} \in \mathbb{Z}$; related to the time harmonic by: $n = 6\ddot{n} + 1$

$\dot{k}$ Single-sided index: $\dot{k} \in \mathbb{Z}^+$; related to the space harmonic by: $k = 6\dot{k} + 3$

$\dot{n}$ Single-sided index: $\dot{n} \in \mathbb{Z}^+$; related to the time harmonic by: $n = 6\dot{n} + 3$

Greek letters

δ	Power angle (angle between $\underline{E}_p$ and $\underline{U}_s$)	[rad]
δ	Skin depth	[m]
ϵ	Permittivity	[F/m]
λ	Flux linkage	[Wb]
μ	Permeability	[H/m]
ω	Angular velocity	[rad/s]
ϕ	Angular variable (rotor coordinates)	[rad]
ρ	Mass density	[kg/m^3]
σ	Conductivity	[S/m]
σ	Tangential force density (Chapter 2)	[N/m^2]=[J/m^3]
θ	Rotor positional angle	[rad]
φ	Angular variable (stator coordinates)	[rad]

Latin subscripts

0	Free space
0	Initial (in the case of θ)
ag	Centre of the air gap
Al	Aluminium
c	Critical value (Chapter 2)
ci	Shielding cylinder inside
co	Shielding cylinder outside
Cu	Copper
d	d-axis

e	Eddy current
e	Electric (Chapter 2)
fc	Fuel cell (Chapter 2)
Fe	Iron
i	Inside
k	Kinetic (Chapter 2)
k	Space harmonic
m	Mechanical
m	Per mass unit
mc	Centre of the magnets
mi	Magnet inside = shielding cylinder outside
min	Minimum
mo	Magnet outside
n	Time harmonic
o	Outside
pitch	Indicates pitch angle
q	q-axis
r	Radial component
r	Relative
rem	Remanence of a permanent magnet
ro	Rotor outside
s	Stator
sc	Shielding cylinder
si	Stator inside
so	Slot opening
so	Stator outside
t	Full-pitch turn

tr	Transfer (Chapter 2)
v	Per volume unit
w	Winding
wc	Centre of the winding
x	$= a, b, c$; Indicates phases a, b and c
z	z-component
$i_s e_p$	$\underline{I}_s$ is in phase with $\underline{E}_p$
$i_s u_s$	$\underline{I}_s$ is in phase with $\underline{U}_s$

Greek subscripts

ϕ	Tangential component (rotor)
σ	Leakage
φ	Tangential component (stator)

Latin superscripts

rc	Rotor coordinates
sc	Stator coordinates

Greek superscripts

(ν)	Region number

Introduction

1.1 Energy storage in hybrid electric vehicles

In 1996, General Motors Corp. (GM) leased its first pure electric vehicle (EV-1) to customers in Arizona and California. The market reaction to these vehicles was disappointing: for example, in 1999, GM leased only 137 EV-1s. The year 2002 marked the end for EV-1 as GM pulled the plug. This was only one in a series of blows to the electric vehicle industry, following the discontinuance of the Ford Ranger EV and the Nissan Altra EV. In 2002, Ford Motor Co. also put its Th!nk Mobility subsidiary, maker of a plastic-bodied electric two-seater, up for sale.

The sales of hybrid electric vehicles, on the other hand, increased over the same time span and is still increasing [Jon03]. One of the reasons for this is that electric vehicles suffer from limitations that most customers simply found unacceptable. The worst of these is its range: the average electric vehicle can drive only around 80 km before it needs a recharge. Charging takes several hours, the batteries perform poorly in cold weather, have a very restricted lifespan and are expensive.

The range problem mentioned above is due to the low energy density of the energy storage device. Electrical energy storage technologies cannot yet compete with the extremely high energy densities of gasoline, diesel and LPG. For example, a standard petrol car's fuel tank of 50 l stores 2.35 GJ of energy, corresponding to an energy density of 47 GJ/m^3 (13 MWh/m^3). The best energy storage technologies available today (in terms of energy density) are electrochemical technologies (i.e. batteries), with an energy density of about an order of magnitude lower than this.

Hybrids on the other hand, having per definition at least two energy sources, demand a much lower energy density of the storage device than pure electric vehicles. The power density is critical, however, since power delivery rather than energy delivery is the main function of storage in such a vehicle. In a hybrid, the primary

1

(a)

(b)   (c)

Figure 1.1: Hybrid electric vehicles: (a) City bus; Commercially available hybrid electric passenger cars: (b) Toyota Prius; (c) Honda FCX.

energy source is sized for the average power and the secondary energy source (a storage device) for the peak power. This practice is referred to as "load levelling" or "peak shaving" since it levels or "shaves" the peaks of the power demand off the primary energy source, so that it only needs to supply the average.

Other advantages of hybrid electric vehicles include a reduction of emissions and improved efficiency since the internal combustion engine, if used, can be operated in the narrow rpm band, where it is most efficient. Regenerative braking, where braking energy is converted into electrical form and pumped back into the storage device, further improves efficiency.

Figure 1.1 shows three hybrid electric vehicles. Figure 1.1(a) shows a city bus with a LPG engine as the primary energy source and a flywheel energy storage system as its secondary energy source. Figures 1.1(b) and (c) show two commercially available hybrid passenger cars: the Toyota Prius and the Honda FCX [Ros03]. The Toyota Prius has a gasoline internal combustion engine (ICE) and a battery system as the primary and secondary energy sources, respectively. Fuel cells are used for the primary energy source in the Honda FCX, with supercapacitors as the secondary energy source.

Power and energy required of an energy storage technology

To form an idea of the requirements placed upon the energy storage technology in hybrid electric vehicles, a few examples of passenger cars, busses and light-rail ve-

hicles are discussed next.

Passenger cars

Heitner [Hei94] states that 50–60 Wh/kg and 750–1200 W/kg would meet the desired requirements of a hybrid electric passenger car (from the Idaho National Engineering Laboratory (INEL)). Rajashekara [Raj94] lists a higher specific energy requirement than [Hei94] at 100 Wh/kg at a lower specific power of 400 W/kg. He further notes that 2500 cycles are required as a minimum, and the cost should be no more than $75/kg. In addition, a 40–80% recharge capacity in 30 minutes should be reached. In 1994, when his article was publisehed, these requirements were not yet met.

Hunt *et al.* [Hun95] distinguishes between dual mode and power assist mode. In dual mode, the vehicle is completely powered by an energy storage device. In power assist mode, the energy storage device adds its power to that of the primary energy source.

In dual mode, the approximate requirements are 50–60 W per kilogram vehicle mass needed to accelerate from 0–96 km/h in 10–12 s. For a standard motor vehicle in the USA, this translates to approximately 60–100 kW. A storage capacity of around 10 kWh is required.

The peak power requirements in power assist mode are identical to those in dual mode, except that the average power of the primary energy source is subtracted. Typically in a standard motor vehicle, the average power is around 15–25 kW. Therefore, the peak power requirements for the secondary energy source is typically 35–85 kW. The Toyota Prius of Figure 1.1(b) operates mainly in power assist mode, and the secondary energy source provides 38.8 kW. This source is a battery bank of 1.8 kWh with a system weight of 70 kg, translating into a specific energy and power of 26 Wh/kg and 554 W/kg. More detail on the Toyota Prius can be found in [Her98].

The other vehicle shown in Figure 1.1, the Honda FCX, has hydrogen proton-exchange membrane fuel cells as its primary energy source. These deliver 78 kW average power, and with the peak power supplied by supercapacitors, the car can accelerate about as well as Honda's Civic [Ros03]. The car has a 156 l fuel tank mounted under the floor and the driving range is about 350 km.

Busses

Busses are subject to many accelerations and decelerations, making them prime candidates for being transformed into hybrid electric vehicles. Miller *et al.* [Mil97] describes a battery evaluation for a fuel cell/battery bus (25 passengers). The methanol-fuel, phosphoric acid fuel cell was rated at 50 kW. The peak charge power level for the batteries was 55 kW during regenerative braking and they delivered 70 kW dur-

ing discharge.[1] Two battery types were investigated: lead-acid ($\sim$1800 Wh, 31 Wh/kg, 180 W/kg) and NiCd ($\sim$1200 Wh, 195 W/kg). Miller *et al.* concluded that the NiCd technology was better than the lead-acid one because of its longer life, in spite of its higher initial cost.

The public transport bus built by CCM B.V. (Nuenen, the Netherlands) uses the EMAFER flywheel system as secondary energy source. The flywheel stores 6.7 MJ (1.9 kWh) of usable energy and has a continuous output power varying between 133 kW and 200 kW; the power transfer time is 40 s. The system weighs 800 kg, translating into a specific energy and power of 2.4 Wh/kg and 250 W/kg, respectively.[2]

Since 1988, the Magneto-Dynamic Storage (MDS) K3 system of Magnet-Motor GmbH (Starnberg, Germany) is operating in a diesel-electric city bus. Since 1992, 12 trolley busses with these flywheels have been in operation in Basel, Switzerland. The MDS K3 stores 7.2 MJ (2 kWh) of usable energy. The output power is 150 kW, and with a system mass of 400 kg this corresponds to 5 Wh/kg and 375 W/kg.

Light-rail vehicles

Light-rail vehicles and trains may also be converted into hybrid form. In this case, the primary energy source is the overhead lines and the secondary source is the energy storage device.

In light- and heavy-rail applications, the energy storage device may be removed from the vehicle and placed at the station. In this case, several vehicles can benefit from its presence in the system instead of only one.

Reiner and Gunselmann [Rei98] report on a demonstration project supported by the EU-LIFE program. It consists of a Magnet-Motor MDS system of 9 kWh and 900 kW. At the time of their publication the flywheel system was to be mounted in a substation of the Cologne public transportation system. In the project, the following assumption was made: at least twice the energy of the vehicle moving at full speed must be stored. For their application, the 50,000 kg vehicle was to be accelerated in 10 s to 50–80 km/h and decelerated again in 30 s. This means that the required energy and power is about 8.6 kWh and 1 MW. The MDS machine used was optimized for low no-load losses and high efficiency (92–95%). A very important requirement for light-rail vehicles like trams and metros is a high cycle life, since they can have up to 40 stop-and-go cycles per hour. The used MDS flywheel system achieves 14.4 Wh/kg and 1.5 kW/kg.

---

[1] A vehicle actually requires a higher power level during regenerative braking than during acceleration. It is assumed that [Mil97] investigated rates that are the other way round because of the bidirectionality limitation of batteries. This limitation will be discussed more thoroughly in Chapter 2.

[2] The system is capable of storing 14.4 MJ of usable energy and a continuous output power of 300 kW; this translates into a specific energy and power of 5 Wh/kg and 375 W/kg, respectively.

Research into high-power-density energy storage technologies

Increasing the energy storage capacities and energy densities of energy storage devices remains interesting for many applications.

From the discussion so far, however, we see that this does not apply for hybrid electric vehicles. Here, research into the increase of the power delivery capabilities and power densities of these storage technologies is more interesting.

Several other applications exist where high power is needed for a short time from the energy storage device.

Other high-power short-duration energy storage applications

One important application is in power quality; for example in voltage-sag ride through. The compensation of voltage sags is needed for sensitive equipment, like computer systems, which may trip or reset during a short blackout or brownout. Another example is in the paper industry, where a voltage sag may cause a downtime of several hours to recover from a paper tear and resynchronize the drives.

From detailed studies such as the classic EPRI Distribution Power Quality Study [EPR1] it is now well established that the vast majority of disturbances in line voltage are very brief: less than 1 second. Dorr *et al.* [Dor97] classify power line disturbances with a duration shorter than 10 ms as transient, those lasting between 10 ms and 3 s as momentary, and those with a duration longer than 3 s as steady-state. Other classifications are made by Dugan *et al.* [Dug96] and Styvaktakis, Bollen and Gu [Sty00]. A method for comparing different voltage dip surveys is presented in [Bol02].

In a joint publication of EPRI and Westinghouse Electric Corp. [Nel96], it is shown that 50 kJ of energy storage per MW of load will restore voltage to 90% for roughly 70% of balanced sags, 150 kJ per MW is required for roughly 90% of the balanced sags, 300 kJ per MW for 99%, etc. According to [Jou99] and [Zyl98], the majority of loads need support in the fractional-kVA to 300 kVA power range.

Industrial applications of short-duration high-power transfer from energy storage technologies include: solid-state lasers [Alb98], welding, induction heating, resistive and wave heating, electron heating [Bas97]), (robot) actuators [Oh99], pulsed magnets [Sch97], EM-forming, powder spraying [Dri97] and removal of surface layers by arcing, among others. Bulldozers and other high-power machinery traditionally equipped with hydraulic actuators may also be a potential application if electrical actuators are used.[3] Fairground attraction applications, which need very high accelerations for short times, for example to speed up roller-coaster carts, may also be included as an industrial application.

All-electric combat vehicles (AECVs) are another application. Magnet-Motor GmbH has supplied MDS systems for battle tanks in the past [Rei97], [Rei99]. In [Ehr93], they list the projected development of the specific energy and power of their MDS systems. These are:

---

[3]When one considers the large difference between the obtainable force density of hydraulic actuators and that of electrical actuators, the latter can only replace the former for certain low-power applications.

- 1991/2: 40 kJ/kg (11.4 Wh/kg) and 2.5 kW/kg;

- 1995: 80 kJ/kg (22.8 Wh/kg) and 2.5 kW/kg;

- 2000: 150 kJ/kg (41.7 Wh/kg) and 5–10 kW/kg;

- beyond 2000: 300 kJ/kg (83.3 Wh/kg) and 10 kW/kg.

Summary

Table 1.1 lists a summary of energy storage applications, including long-duration applications like support of renewable energy sources and utility support.

As mentioned earlier in this introduction, the research into the increase in power density and/or specific power of energy storage technologies for hybrid electric vehicles is very relevant and interesting. The power transfer times in hybrid electric vehicles range from several seconds to several minutes. (Table 1.1 lists 20 seconds and 7 minutes.)

This thesis is mainly concerned with short-duration power transfer, comparable to that of the energy storage device in a hybrid electric vehicle. All the applications in

App.	[kW]	[kWh]	[kW/kg]	[Wh/kg]	t_{tr} [s]
VSRT[a]	300	0.025			0.3
Industrial	$100–3\times10^6$	0.14–45	$(1.5–2.1)\times10^3$	3.8–5.6	0.006–5
AECV[b]	3000	16.7	7.5	41.7	20
Trams	1000	9	1.5	14.4	36
Busses	70–300	1.2–4	0.18–0.4	5–30	36–90
Cars	35–85	~ 1.8	0.4–1.2	25–100	160–420
UPS[c]	10–100	5–50			1 800–3 600
Ren. Sup.[d]	300	8–1000		45	10 000
Util. Sup.[e]	200–30 000	150–40 000			900–24 000

Table 1.1: Summary of typical requirements placed on energy storage technologies by several applications. Requirements for power, energy, specific power, specific energy and power transfer time are listed, sorted on power transfer time.

---

[a]For a 300 kW load (ride-through carries full load power) and assuming 300 kJ storage per MW load (covering 99% of balanced voltage sags [Nel96]).

[b]Magnet-Motor L3.

[c]See [Wei98] and [Wei99].

[d]Renewables support. Based on two representative examples: A photovoltaic system [Fla88] and a wind turbine [Hea94].

[e]Utility support: [Kun86], [Wal90], [Kot93], [Bal95], [Mil96] and [Tha99].

Table 1.1 are thus included in the scope of the thesis except UPS systems, renewable support and utility support.

1.2   Problem description

Firstly, this thesis is concerned with finding a suitable energy storage technology for use in a hybrid electric city bus. The result of this search is documented in Chapter 2: a flywheel energy storage system.

A project was started to design and build such a system for use in large hybrid electric vehicles like busses and trams. The project was conducted in collaboration with the Centre for Concepts in Mechatronics (CCM) B.V. (Nuenen, the Netherlands). This project follows the successful EMAFER[4] system, already mentioned in Section 1.1. The flywheel in the EMAFER system rotates at 15 000 rpm; the achievable energy and continuous power levels are 14.4 MJ and 300 kW, respectively. The follow-up system, called EμFER, was initiated to reduce the overall size and mass, to reduce the no-load losses and to develop a flatter profile than that of the EMAFER system. To reduce the required size and mass, the rotational speed of the flywheel of the EμFER system was increased to 30 000 rpm. The system stores 7.2 MJ and the desired continuous power output is 150 kW, with the machine losses (both at load and at no-load) as low as possible.

CCM was responsible for the power electronics, the mechanical and thermal design and the actual construction of the system. During the initial stages of the project and as a result of this collaboration, it was decided that the flywheel machine should be an external-rotor version, with a radial-flux electrical machine integrated into the flywheel itself.

In such a flywheel system, of which the most important requirements are low losses and a high power output with a high power density, several components pose an interesting challenge. Of these, the challenge of designing the electrical machine in the flywheel is met in this thesis.

A permanent-magnet machine topology was chosen for its high power density. The magnets are surface mounted and the rotor iron is solid. Both of these decisions were made for mechanical reasons. Such mechanical design aspects are not considered in the thesis; neither are thermal, control or system design aspects.[5]

Since the rotor rotates at very high speeds (up to 30 000 rpm) in a low-pressure atmosphere, the ways of cooling the rotor are very limited. This necessitated the need for very low rotor loss. To design a machine with very low rotor loss, an accurate means for calculating the loss is needed. Obtaining such a loss calculation from the magnetic field is a natural choice.

Although it is much easier to cool the stator than the rotor, the stator losses should also be minimized. The stator losses consist of two parts: the iron and copper

---

[4]EMAFER = **E**lectro-**M**echanical **A**ccumulator **F**or **E**nergy **R**e-**U**se.

[5]The fact that these issues are not discussed in the thesis does not mean that they are not important, but merely that they fall outside the chosen scope of the thesis.

losses. The iron losses are approximately two to three orders of magnitude larger than the copper losses at no load, and these losses are concentrated in the stator teeth. A slotless stator is therefore used in the machine, thereby drastically reducing the induced losses in the stator iron. One consequence of the use of a slotless stator is that the stator conductors are now directly exposed to the rotating magnetic field of the permanent magnets. Once again, an accurate way to calculate this field is clearly needed. Furthermore, it is recognized that several permanent-magnet configurations or arrays are possible in a permanent-magnet machine. A way to calculate the field due to such arrays is therefore also needed.

Another consequence of the use of a slotless stator is that it is a challenge to calculate the magnetic field due to the stator currents accurately. This is so because in conventional electrical machines with slotted stators, the stator currents can be modelled as a surface current density on the surface of the stator. In this slotless machine with its winding in the air gap, this approach is no longer valid, and the current density in the air gap has to be used directly.

It has been stated above that the machine must have very low rotor losses. The findings of other research on such losses in high-speed machines [Vee97], [Pol98] suggested that this could be achieved by using a shielding cylinder in the flywheel machine. This cylinder is used to shield the permanent magnets and the solid rotor iron from high-frequency magnetic fields originating from the stator. Since a close look at the induced eddy-current loss in the shielding cylinder is required, the magnetic field of the induced eddy currents in the cylinder should be included in a calculation method. If this is done, the skin effect in the shielding cylinder is included, which is very desirable.

All the calculation problems above were solved by the derivation of an analytical model of the electrical machine based on two-dimensional magnetic fields. This model consists of two parts: the permanent-magnet field and the stator current field, the latter including the effect of the eddy currents in the shielding cylinder. All relevant and interesting machine quantities were derived from these two fields or their combination. The analytical model includes three permanent-magnet arrays.

Analytical models are well suited for optimization since, even with the modern PCs of today, a closed-form expression evaluates much faster than a similar calculation with the finite element method. The final part of the problem is to use the analytical model for optimization of the machine. The optimization consists of two parts: maximizing the electromagnetic torque, and minimizing the losses in the machine.

Thesis objectives

With the foregoing problem description in mind, the main objectives of the thesis are:

1. *To find the most suitable energy storage technology for use in large hybrid electric vehicles like busses and trams.*

2. To design the electrical machine for the EμFER flywheel energy storage system.

As part of the machine design, the following is also a thesis objective:

3. To optimize the machine geometry for the given flywheel dimensions.

In order to meet objectives 1, 2 and 3, the last objective is introduced:

4. To derive a comprehensive analytical model of the electrical machine.

1.3   Thesis layout

The thesis is divided into three parts:

- *Background.* Chapters 2 and 3 discuss the background of the project and where the thesis work fits in.

- *The analytical model.* Chapters 4, 5, 6 and 7 contain the specifics of the derived analytical model.

- *Optimization.* Chapter 8 discusses the use of the analytical model for machine optimization.

An overview of energy storage technologies is presented in Chapter 2 in an attempt to find the most suitable technology for high-power, medium-energy applications like hybrid electric vehicles. Chapter 2 looks at four candidate technologies by formulating trends gathered from an extensive literature study. The most important criteria used in Chapter 2 are medium energy density and high power density. It is shown that the flywheel energy storage system satisfies these criteria and it is therefore a good choice for the applications discussed in Chapter 1.

Chapter 3 takes a general look at drive system topologies, converter choice and machine type for high-power flywheel energy storage systems. In this chapter it is also decided to limit the scope of the rest of the thesis to the electrical machine, which is then introduced as the EμFER machine.

Chapter 4 starts the second part of the thesis, which deals with the specifics of the analytical model. The use of the analytical method vs. the finite element method is discussed, whereafter the power of the magnetic vector potential is explained. How the vector potential can be used to obtain useful machine quantities is explained in sections on flux linkage, the Poynting vector and the Lorentz force.

Chapter 5 applies the method outlined in Chapter 4 to the permanent magnets. The field due to the permanent magnets is then used to find the no-load voltage, which is experimentally validated for the EμFER machine. Chapter 5 treats three different permanent magnet arrays.

Chapter 6 derives the magnetic field due to the stator currents in the air gap winding, also using the method outlined in Chapter 4. An analytical expression is first developed for the three-phase current density, whereafter it is used to find the

magnetic field. The eddy currents in the shielding cylinder cause a field in reaction to the stator current field. This effect is also included in the model. Directly from the magnetic vector potential, an expression for the stator self-inductance is derived, which is also developed for a locked rotor. After this, the Poynting vector is used to find an expression for the induced loss in the shielding cylinder, which is further developed into the locked-rotor machine resistance. The locked-rotor machine inductance and resistance are experimentally validated at the end of Chapter 6. Chapter 6 concludes with the machine voltage equation, within which all quantities are now known and therefore the machine has been described completely at this point.

Chapter 7 goes a step further by combining the two magnetic fields of Chapters 5 and 6 into one by using the assumption of linearity of the vector potential. From this combined field, the electromagnetic torque can be calculated, which is done by means of the Lorentz force and Poynting vector methods. The stator losses are also a combined field effect, and are discussed next. The calculated locked-rotor resistance is modified for high frequencies by means of a simple iron-loss model, which is experimentally validated.

Chapter 8 utilizes the full power of the analytical model by investigating some optimizations. The optimization criteria chosen are the electromagnetic torque, stator iron losses and the induced eddy current loss in the shielding cylinder. These are optimized with respect to the permanent magnet array, winding distribution, machine geometry and converter options.

Chapter 9 summarizes the most important conclusions reached in the thesis and makes suggestions for the direction, content and scope of future research.

CHAPTER 2 ⎯⎯⎯⎯⎯⎯⎯⎯⎯⎯⎯⎯⎯⎯⎯⎯

⎯⎯⎯⎯⎯⎯⎯⎯⎯⎯⎯⎯⎯ Energy storage technologies

2.1 Introduction

Several energy storage technologies are available today in various stages of development. However, as motivated in Chapter 1, in this thesis the focus is mainly on energy storage technologies with the ability to deliver high power, with power transfer times lasting up to a few minutes. This eliminates technologies like pumped hydro, compressed air, flow batteries, etc. These are more suited to deliver their energy over longer periods of time, for example in energy management applications like load levelling, peak shaving and arbitrage, where energy storage is used in daily cycles for economic gain. (See the web site of the Energy Storage Association, `http://www.energystorage.org`, for more information on these topics.)

Four technologies were selected in this chapter for closer investigation with the emphasis on power delivery, power density and specific power. They are:

1. electrochemical energy storage: batteries and fuel cells (Section 2.2);

2. electric field energy storage: metal-film capacitors, aluminium electrolytic capacitors and supercapacitors (Section 2.3);

3. magnetic field energy storage: superconducting electromagnets (Section 2.4); and

4. kinetic energy storage: flywheels (Section 2.5).

These four technologies were chosen since they have reached a level of maturity, are commercially available in some form or another, and more data was available on these than on other technologies.

In Section 2.6, a comparison of these technologies is made. Criteria for the comparison includes power, power density, specific power, energy, energy density, spe-

cific energy, lifetime, bidirectionality, cost, etc. Section 2.7 uses this comparison to
motivate the choice of the kinetic energy storage technology for application in a hy-
brid electric city bus.

2.2 Electrochemical energy storage

Electrochemical energy storage technologies can be divided into two types: batteries
and fuel cells. The next two subsections pay some attention to these technologies.

2.2.1 Batteries

Batteries convert the chemical energy stored inside them into electrical energy when
connected to an external load. They can be either primary (non-rechargeable) or sec-
ondary (rechargeable). The previous section indicates that the technologies consid-
ered in this chapter are required to be bidirectional. Primary batteries are therefore
not considered here.[1]

The lead-acid battery

The most common secondary battery today is still the lead-acid type, invented in
1859 by Planté. A lead-acid battery consists of two plates, one of lead and the other
of lead oxide, suspended in an electrolyte of sulphuric acid (H_2SO_4), as shown in
Figure 2.1 [Ter94]. During discharge both the anode and cathode are converted into
lead sulphate, $PbSO_4$. Charging restores the cathode to lead oxide and the anode to
lead.

Overcharging the lead-acid battery leads to generation of hydrogen gas at the
anode and oxygen at the cathode, necessitating vents to the outside atmosphere. The
reason for the hydrogen generation is that the potential of the anode gets too high.
This also occurs during a rapid charge of the battery, i.e. at a very high power level.

The valve-regulated lead-acid battery

The mix of hydrogen and oxygen occurinf inthe lead-acid battery whenit is over-
charged is explosive. This potentially dangerous situation was partially solved in the
1960s with the invention of the valve-regulated lead-acid (VRLA) battery [Nel01]. In
the VRLA, the system is completely sealed. The principle of operation is basically as
follows: the cathode goes into overcharge, releasing oxygen that readily diffuses to
the surface of the electrode, where it is recombined.

In the VRLA battery, the amount of material of the anode is higher than that
of the cathode. Because of this fact and the oxygen recombination the anode never
reaches the potential at which hydrogen is released. No gasses are given off, the

---

[1]Fuel cells are, however, included in this discussion although they are also primary batteries according
to this definition. The reason why they are included is because of the contemporary interest in them.
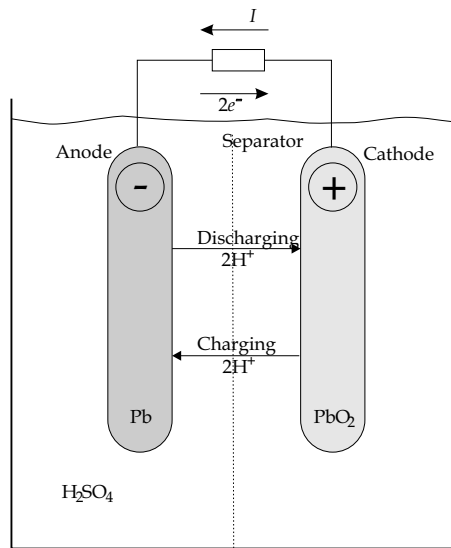
Figure 2.1: A schematic diagram of the lead-acid battery.

overall chemistry shows no net change, and all the excess electrical energy is converted into heat, which is dissipated. The situation just described is the ideal one. In reality, all VRLA batteries "give off relatively small quantities of gases under some conditions, and not just [in] abusive situations" [Nel01].

The thin metal film (TMF®) lead-acid battery

The TMF® lead-acid battery is a variation of the VRLA battery developed by Bolder Technologies Corporation in the USA [Nel97a], [Nel97b], [Bha99]. Since it is a VRLA battery, the highly porous separator carries 70% of the electrolyte and 30% is roughly evenly distributed between the two electrodes.

The TMF® battery differs from a conventional VRLA battery only in its construction. The plates are very thin (250 μm or less), spiral wound and very closely spaced [Nel97b]. This reduces the internal impedance significantly and results in low loss even at very high discharge currents.

Other battery types

Another type of battery based on the lead-acid chemistry is the bipolar lead-acid battery. One such system was developed by TNO in the Netherlands [Kol99].

Other types of batteries include nickel-cadmium, nickel-zinc, nickel-iron, sodium-sulphur, lithium-sulphur and many others. These batteries operate on the same basic principles as the lead-acid battery, but their chemistries are different. As a result some of these battery types exhibit better performance than the lead-acid or

VRLA battery types.

According to Nelson [Nel01], the battery chemistries of the NiCd cell and the VRLA are very similar, although the oxygen recombination functs better in the NiCd battery. He argues that this is due to the fact that a lot of research and development effort was invested in NiCd technology between 1940 and 1960. According to him, the VRLA battery may be improved substantially if the same R&D effort is put into it.

Companies developing high-power batteries[2] include Saft (France) [Owe99, Saf], and Sanyo (Japan) [San]. Saft developed high-power Li-ion and NiMH batteries specifically for hybrid electric vehicles. Sanyo developed the NiMH batteries that are used in the Toyota Prius of Figure 1.1(b). The 288 V battery bank, rated for 1.8 kWh and with a total system weight of 70 kg, delivers 38.8 kW to the drive system when needed.

Internal impedance

The structure of Figure 2.1 results in a high internal impedance, which is particularly due to the wet electrolyte and low contact area. It reduces power density and makes conventional lead-acid batteries not the best technology for use as a burst power source.[3]

The surface areas of VRLA and TMF$^{®}$ lead-acid batteries are larger than the conventional type, reducing the internal impedance, but not sufficiently to solve the problem altogether.

Another complication with lead-acid batteries is that they have a different internal impedance depending on whether they are charged or discharged. During charging the internal impedance is significantly higher than during discharging, because of the gas generation discussed above. More gas bubbles mean a smaller contact area between the electrodes and the electrolyte, which results in a higher impedance.

VRLA types, including the TMF$^{®}$ battery, perform better since less gas is generated, but the difference in impedance when charging and discharging remains. The 2 V, 1.2 Ah Bolder TMF$^{®}$ cell can be fully discharged in 1 s at 1 kA, and then recharged in a much longer period of 2–3 minutes [Nel97a].

As the ideal burst power source must be able both to deliver and absorb energy at very high rates, lead-acid batteries are not the best source of burst power. However, for some applications that do not need the energy storage element to be able to absorb the energy at as high a rate as it delivers it, like power line conditioning, lead-acid battery technologies seem promising.

---

[2]The reason why these companies are mentioned is because they represent the state of the art in battery technology today.

[3]An exact description of the complex internal impedance of lead-acid batteries is outside the scope of this thesis. Work has been done in this area at the RWTH Aachen in Germany [Kar01].

Lifetime

There are irreversible physical changes occurring inside the two electrodes of the lead-acid battery, which deteriorate performance and ultimately render the battery useless. Failure occurs between about 200-2000 cycles, depending on the design, duty cycle and the depth of the discharge-charge cycles.

Although it has a better construction with regards to internal impedance than the conventional lead-acid battery, the TMF® lead-acid battery does not have a significantly longer lifetime. It was reported that it took 1500 cycles at 100% depth of discharge (DoD) to reduce the battery to 80% of its initial capacity [Bha99].

Battery weight and specific power

All battery technologies require a construction with a high amount of chemically inactive material: grid metal, connectors, separators, and cell containers. In the lead-acid battery, this fact and the use of lead results in a battery with a high mass. This means that the specific power [W/kg] of lead-acid batteries is not very high. The VRLA and TMF® lead-acid batteries have higher values, but these are still not very high when compared with other energy storage technologies. Several research efforts in reducing the battery weight are being conducted; for instance the use of carbon fibre to form the grid structure in the cathode has been investigated in [Ter94].

2.2.2 Fuel cells

The history of fuel cells goes even further back than that of batteries: the principle of the hydrogen-oxygen cell was demonstrated in 1839 by Grove in England [Ter94]. Strictly speaking, fuel cells are not electrochemical energy storage devices in the same sense as batteries, since they do not store their own fuel and oxidant. Instead, they receive a constant supply of these two chemicals from an outside source, where it is stored. In contrast, a battery stores its fuel and oxidant internally.[4] In the lead-acid battery, the fuel (lead) is stored in the anode and the oxidant (lead oxide) is stored in the cathode.

Figure 2.2 shows a schematic diagram of an ion-membrane fuel cell, which is one of a number of different types of fuel cells that underwent development and refinement in the past [Mat87]. Hydrogen fuel is supplied from a gas chamber on the anode side and the oxidant, air or oxygen, is supplied from a gas chamber on the cathode side. The anode and cathode are separated by an ion-exchange membrane of about 1 mm thick which allows the positive hydrogen ions (H^+) to pass, but not the neutral oxygen (O_2) molecules. Electrons are separated from the supplied $2H_2$ by the catalyst-coated membrane, in the following chemical reaction:

$$2H_2 \longrightarrow 4H^+ + 4e^-, \tag{2.1}$$

---

[4]One may of course widen the definition of a fuel-cell-based energy storage system to include the storage tanks for the fuel and oxidant.

while the reaction at the cathode combines the electrons, the H^+-ions and the supplied oxygen to yield the waste product, water:

$$O_2 + 4H^+ + 4e^- \longrightarrow 2H_2O. \tag{2.2}$$
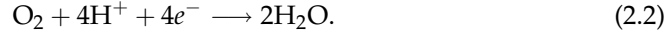
The energy converted into electrical form by an ion-membrane fuel cell in this way is equal to

$$E_{fc,elec} = neV_{fc}, \tag{2.3}$$

where n is the number of electrons, e the electron charge and V_{fc} the cell's electromotive force, 1.23V.

Fuel cells operate best when running continuously and cannot respond rapidly to load changes [Jou99]. Therefore they are not ideally suited as a burst power source. This is clearly seen in the commercially available Honda FCX of Figure 1.1(c). In this car, the main energy source is fuel cells, supplying the average power demand (period: typically minutes), while supercapacitors supply the peak (burst) power demand (seconds).
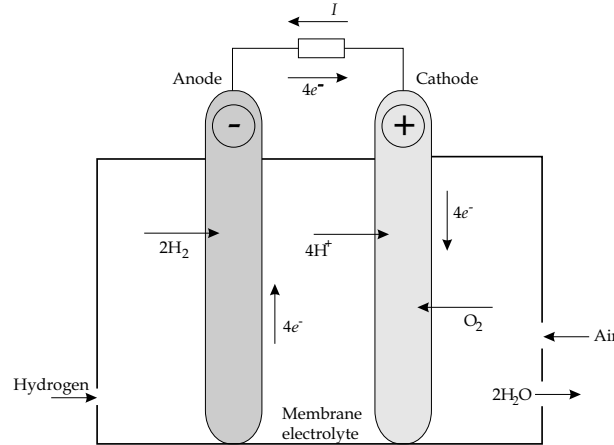
Figure 2.2: A schematic diagram of the ion-membrane fuel cell.

2.3 Electric field energy storage

2.3.1 Metal-film capacitors

The capacitance of a parallel plate capacitor is given by:

$$C = \frac{\epsilon_r \epsilon_0 A_e}{d}, \tag{2.4}$$

where ϵ_r is the dielectric constant or relative permittivity, ϵ_0 is the permittivity of vacuum, A_e is the effective area of one of the plates and d is the dielectric thickness. The energy stored in the capacitor's electric field is:

$$E_e = \frac{1}{2}CV^2, \tag{2.5}$$

where V is the voltage between the plates.

Metal-film capacitors have very high specific powers, typically between $100\,\text{kW/kg}$ and $1\,\text{MW/kg}$. This is at very low specific energies, i.e. below $0.1\,\text{Wh/kg}$. The reason for this is that the effective areas of the plates are not very large since they are in essence a parallel plate structure rolled up in a can. What is gained in low internal impedance and therefore specific power is paid for by a reduction of specific energy. The complete discharge time of parallel plate capacitors ranges from the μs to the ms region, which makes these capacitors a good candidate for burst power on the fast side of the time scale. The low amount of stored energy makes metal-film capacitors useful only for a limited number of applications, however.

2.3.2   Aluminium electrolytic capacitors

Electrolytic capacitors are very common in the power electronics industry today due to their high capacitance density $[\text{F/m}^3]$ in comparison to that of metal-film capacitors. They are called electrolytic capacitors because the dielectric is formed by an electrolytic process. The most common type of electrolytic capacitor in industry is the aluminium electrolytic capacitor, although several other different types exist like tantalum, niobium, zirconium and zinc. In an aluminium electrolytic capacitor, the dielectric is aluminium oxide (Al_2O_3), which is formed into a thin layer upon an aluminium plate by an electrolytic process, i.e., a current is passed through it in an appropriate solution. The thickness of the oxide layer depends on the formation voltage, which is typically 3–4 times higher than the rated voltage. The dielectric thickness is in the order of 1μm. A property of the oxide layer is that it is rectifying; it conducts in one direction and insulates in the other.

From (2.4) the capacitance can be increased by increasing the effective area A_e, and/or increasing ϵ_r, and/or decreasing d. Aluminium oxide has a relative permittivity of around 8, and tantalum pentoxide (Ta_2O_5) of about 27, however, tantalum electrolytic capacitors are more expensive. The effective area of both types can be increased by etching the oxide layers, which results in an increase in A_e of between 30–100 times [Kru]. The dielectric strength of the oxide layer in an aluminium electrolytic capacitor limits the voltage that it can withstand and therefore the maximum energy storage capacity. For example, a 800 V, 680 μF aluminium electrolytic capacitor stores just 217.6 J of energy when fully charged. The electrolyte also deteriorates with time and a typical capacitor used in a DC bus in industry will typically last for 2–3 years of before it needs replacing.

2.3.3   Supercapacitors

In 1853, Helmholtz observed that when a voltage is applied across two carbon electrodes suspended in a conductive fluid, no continuous current flows until a certain voltage threshold is reached. This is the principle upon which supercapacitors are based. Although a supercapacitor is an electrochemical device, it stores energy electrostatically, and not electrochemically like a battery, because no chemical reactions take place in the storage mechanism. The applied electric field causes the ions in the fluid to accumulate in a very thin layer bordering the electrode – it effectively polarizes the electrolyte [Pow]. The applied voltage on the positive electrode attracts the negative ions in the electrolyte while the voltage on the negative electrode attracts the positive ions in the electrolyte. This creates two layers of charge separation, one at the positive and one at the negative electrode – hence the name double layer capacitor. Porous carbon electrodes are used which can have a surface area of up to $10^4 \, \text{mm}^2/\text{g}$ [Die99]. This high area, combined with the extremely close spacing of the separated charges, typically in the order of 10 Å, results from (2.4) in the high capacitances that characterize these devices. The electrolyte breakdown voltage of supercapacitors is low (below 3 V), which limits their practical implementation to lower power requirements than that which batteries can provide.

Supercapacitors are fully bidirectional and have a very long life expectancy, up to 100 000 cycles, with a cost of approximately \$500/kW [Jou99]. These facts make supercapacitors a relatively attractive option for burst power applications with a low power demand [Dur99], [Pil95]. Although lowering of the equivalent series resistance of supercapacitors has been investigated [Pel99], [Bis99], it still remains fairly high ($\sim$15 mΩ for a 150 kJ-module) [Die99].

2.4   Magnetic field energy storage: Superconducting electromagnets

Inductors store energy in the magnetic field associated with the current flowing in their coils. The amount of stored energy is:

$$E_m = \frac{1}{2}LI^2, \tag{2.6}$$

where I is the current flowing in the coil. It is obvious from (2.6) that to maximize the stored energy, the current flowing in the coil should be as high as possible. This is the principle behind superconducting magnetic energy storage (SMES) systems. Due to the high resistance of non-superconductors, the coil current cannot be made high enough to store significant amounts of energy. Superconductors have three critical parameters: current density J, magnetic flux density B and temperature T. The safe operating region of a superconductor is approximately within the positive $\frac{1}{8}$ sphere on the graph of J vs B vs T, with J_c, B_c and T_c defining the critical points, i.e. the axis

intersections. If kept within these constraints, a superconducting material has zero resistance to DC current.

Practical superconductors are usually made from NbTi or Nb_3Sn multi-filaments embedded in a copper or aluminium stabilization matrix [Hor97], which is also used to absorb the energy in case the superconductor suddenly becomes normally conducting. The preferred material at present is Nb_3Sn as it is easier to work with. The critical values for $Nb_{47\%}Ti$ [Ter94] is

$$
\begin{aligned}
J_c &:= J|_{B=0,T=0} &=& \quad 10^4 \,\text{A/mm}^2 \\
B_c &:= B|_{J=0,T=0} &=& \quad 15\,\text{T} \\
T_c &:= T|_{J=0,B=0} &=& \quad 9.2\,\text{K}
\end{aligned}
\tag{2.7}
$$

A normal conductor in a transformer design, for example, would typically be used at $J = 3\,\text{A/mm}^2$, while (2.7) shows that for the $Nb_{47\%}Ti$-superconductor it is ∼3300 times higher. It can thus be seen that extremely high currents can be reached with SMES systems. If a normal conductor were to be used at the same current density and were to be constructed identically as one made of $Nb_{47\%}Ti$ as a comparison, from (2.6) it follows that the superconductor coil would be able to store approximately 10^7 times more energy. Due to the fact that high magnetic flux densities are utilized, air is used as the core in these systems. Windings can be solenoidal (which is cheaper, but has a high stray field), or toroidal (with zero external magnetic field, but it is expensive). The conductors in a SMES system are subjected to extremely large forces [Ter94]. A sound (and expensive) mechanical construction should therefore be used to counteract these forces [Hor97], [Hor99].

Research into high-temperature superconductors (HTS) is being conducted by several researchers [Boo88], [Kum91], [Moo99]. These are materials with a higher T_c than that of NbTi shown in (2.7). This allows the use of liquid nitrogen instead of liquid helium for the cryogenic coolant, which reduces cost substantially. The problem with HTS is that the materials are brittle ceramics, which makes it very difficult to manufacture practical conductors. Significant progress has been made by the American Superconductor Corporation with their BSCCO flexible wire in a metal matrix. It is a ceramic copper oxide compound containing bismuth, strontium, calcium, and a small amount of lead [Moo99]. One such coil made of this wire was used successfully in a SMES system as a dip protector on a paper mill [Sch99].

The specific powers of SMES systems are in the order of 200–1500 W/kg at specific energies of approximately that of double layer capacitors, placing them between aluminium electrolytic capacitors and double layer capacitors. This makes them suitable for complete discharges in 100 ms–60 s. These time values apply to both charge and recharge times, since SMES systems are fully bidirectional in their specific power capabilities. The factor limiting the specific power of SMES systems is the ac resistance of the coil due to the skin and proximity effects. If a sudden high energy withdrawal takes place, a large di/dt is forced onto the coil, of which the resistance then rises at localized points due to the above two effects. This in turn causes a temperature rise which can force the superconductor out of the safe operat-

ing area defined by (2.7). This quenches the coil (it becomes a normal conductor) at these localized spots. Extreme power dissipation then takes place at these spots and potentially destroys the coil.

SMES systems have a capital cost of around \$700–\$1000/kg and are available in the highest power levels of all the technologies considered here (up to 1 GW), according to [Jou99]. After fuel cells, they are the most expensive of all the options considered in this study. The cost of SMES systems are broken down into roughly the following: 10% cryogenics, 30% SMES coil and 60% power conversion [Kar99]. SMES systems have an almost unlimited number of discharge-charge cycles and can be fully discharged without any ill effects or reduction of the high efficiency (>95%) [Jou99].

2.5   Kinetic energy storage: Flywheels

Kinetic energy storage in the form of primitive flywheels has been known for centuries, but it is only since the development of high-strength composite materials and low-loss bearings that this method became a viable technical option.

The kinetic energy stored in a rotating mass is given by:

$$E_k = \frac{1}{2} I \omega^2 \quad \text{[J]},$$
(2.8)

where I is the moment of inertia and ω is the angular velocity. The moment of inertia is determined by the mass and geometry of the flywheel and is defined as:

$$I = \int x^2 dm_x \quad \text{[kg.m}^2\text{]},$$
(2.9)

where x is the distance from the axis of rotation to the differential mass dm_x.

2.5.1   The thin rim

In the special case of a thin rim flywheel ($r_i/r_o \rightarrow 1$, where r_i is the inside and r_o the outside radius), all the mass is concentrated in the infinitely thin outer rim. Thus, from (2.9) the moment of inertia for a thin-rim is $I = mr^2$, where m is the mass and r the radius of the flywheel. The stored energy in a thin-rim flywheel then becomes:

$$E_k = \frac{1}{2} mr^2 \omega^2 \quad \text{[J]}.$$
(2.10)

To obtain the specific energy, (2.10) is divided by the mass to give:

$$e_{k,m} = \frac{1}{2} r^2 \omega^2 \quad \text{[J/kg]}.$$
(2.11)

If equation (2.11) is multiplied by the mass density ρ of the flywheel, the energy density is obtained:

$$e_{k,v} = \frac{1}{2} \rho r^2 \omega^2 \quad \text{[J/m}^3\text{]}.$$
(2.12)

For a thin-rim flywheel, the material should withstand a tangential stress of σ_{min} for a given rotational velocity ω. This stress is given by [Gen85]:

$$\sigma_{min} = \rho r^2 \omega^2 \quad [\text{N/m}^2]. \tag{2.13}$$

From (2.12) and (2.13) the maximum achievable energy density with a particular material then becomes:

$$\hat{e}_{k,v} = \frac{1}{2}\sigma_{min} \quad [\text{J/m}^3]. \tag{2.14}$$

From (2.14) it is clear that in order to obtain a high energy density, a high strength material is needed. This is the reason why flywheel energy storage systems only recently became a viable option, since economically viable high-strength fibre composite materials are a fairly recent development, i.e. from the early 1980s [Gen85]. If (2.14) is divided by ρ, one obtains for the maximum obtainable specific energy:

$$\hat{e}_{k,m} = \frac{1}{2}\left(\frac{\sigma_{min}}{\rho}\right) \quad [\text{J/kg}]. \tag{2.15}$$

From (2.15) it can be seen that the specific energy is inversely proportional to the mass density of the flywheel material, as one would expect. The factor $1/2$ in (2.14) and (2.15) is only valid for thin-rim flywheels.

2.5.2 Other flywheel shapes

A more general expression for the maximum energy density, valid for all flywheel shapes, is obtained from (2.14):

$$\hat{e}_{k,v} = K\sigma_{min} \quad [\text{J/m}^3], \tag{2.16}$$

and for the maximum specific energy,

$$\hat{e}_{k,m} = K\frac{\sigma_{min}}{\rho} \quad [\text{J/kg}], \tag{2.17}$$

where K is the form factor or shape factor. It is dependent upon the flywheel geometry and comes essentially from the moment of inertia I [Gen85].

Figure 2.3 shows four different flywheel shapes with their respective form factors. The Laval disk, named after Carl de Laval, the Swedish engineer who invented it, has a form factor of $K = 1$. This flywheel shape has the property that the radial and tangential stress is equal at all points inside the flywheel. It is a theoretical geometry with $r_o \rightarrow \infty$. In practice it is thus not possible to have K exactly equal to 1.

A more manufacturable geometry, the solid disk, is shown in the second cross section of Figure 2.3, and has a K of below $2/3$. The thin rim, which like the Laval disk, also is a theoretical flywheel, has all of its mass concentrated in the infinitely
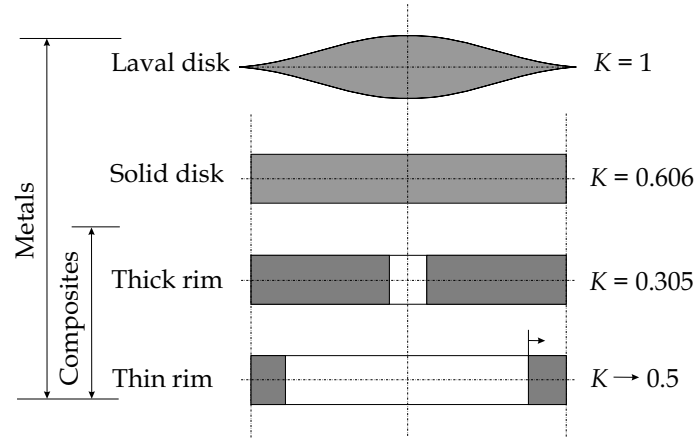
Figure 2.3: Four different flywheel shapes.

thin outer rim. It has a *K* of below 2/3. A disk with finite rim thickness has a significantly lower shape factor. For example, a flywheel with $r_o/r_i = 1.1$, which is an easy wheel to manufacture, has a form factor of only $K = 0.305$.

The first two flywheel geometries shown in Figure 2.3 are suitable only for isotropic materials like metals because they can withstand a high stress in both the tangential and radial directions. The last two geometries shown in Figure 2.3 are suitable for both isotropic and anisotropic materials. Anisotropic materials are materials with different strengths in different directions like glass and carbon fibre composite materials. From (2.16) it can be seen that to optimize the energy density of the flywheel, a high strength material should be used. If a high specific energy is also required, from (2.17) the material should also have a low mass density.

2.5.3   Metals vs composite materials

The use of metals as the flywheel material will thus result in a high energy density because of their high strength and the fact that they are isotropic, allowing geometries with *K* approaching 1. Metals will however result in a low specific energy due to their high mass density.

Anisotropic materials, typically fibre-reinforced epoxies, have higher tensile strengths than metals, but only in the fibres' longitudinal direction. Therefore they can only be used in flywheel geometries with form factors approaching 1/2. This limits the energy densities achievable with composite materials to energy densities that are the same or slightly less than those obtained with metals, but higher specific energies are achievable due to their low mass density.

Previous research [Tho93] has led to the summary of a comparison between metals and composite materials used in flywheels, shown in Table 2.1. The values in Table 2.1 have been calculated for the same amount of stored energy.

	Composite	Metal
Weight	1 pu	2–5 pu
Volume	2.5–5 pu	1 pu
Circumferential speed	1.5 pu	1 pu
Weight of safety enclosure	$0.5 \times$ flywheel weight	$2 \times$ flywheel weight

Table 2.1: A comparison between metal and composite flywheels for the same stored energy.

It can be seen from Table 2.1 that composite flywheels have an advantage over metal flywheels when it comes to weight, but a disadvantage when it comes to volume. This means that larger containment structures are necessary for composite flywheels. In spite of this, the failure mode of composite flywheels is much less destructive than that of metals and the containment structure is required to be only $\frac{1}{2}$ the weight of the flywheel, as opposed to 2 times the flywheel weight in the case of metal flywheels [Tho93]. The circumferential speed ($v_c = r\omega$) of composite flywheels is a factor 1.5 higher than that of metal flywheels, thus making the windage losses higher than in the case of metal flywheels.

The energy of flywheel systems lies between 15–150 Wh/kg and 2–11.9 kW/kg, which places them roughly in the 3.6–60 s full-discharge region. They are fully bidirectional in their specific power capabilities. Flywheels have the highest specific power capability of all the technologies compared in this study, even higher than that of aluminium electrolytic capacitors. They hold great promise as a burst power source in the complete discharge region of 3.6 s–60 s.

2.5.4   The future

According to Bitterly of US Flywheel Systems, a specific energy of 200 Wh/kg is possible for graphite fibre composite material in the near future [Bit98]. According to him, in the future, materials with a very high strength (in the order of $20\,000\,\mathrm{MN/m^2}$) may become available for use in flywheel manufacturing, increasing the energy densities significantly. These materials are very fine single-crystal whiskers, but have yet to be proven commercially. It is also predicted that the specific power of flywheel systems might be as high as 30 kW/kg in the future, the only limitation being the electrical machine [Bit98]. Flywheel energy storage systems are available in power ratings of more or less 10 kW–10 MW with a capital cost of about \$300/kW [Jou99], making it the cheapest technology considered here, after batteries. There are hardly any deteriorating effects[5] as in batteries, and a high number of deep discharge-charge cycles is obtainable ($\sim$10 000 [Jou99]). The efficiency of the power

---

[5]There is still mechanical wear when conventional bearings are used. The use of magnetic bearings solves this problem, but such bearings are generally not used in automotive applications.

electronics tend to limit the depth of discharge[6,7] to 95% [Bit98], which is considerably better than that of batteries, but less than supercapacitors or SMES (100% depth of discharge) [Bit98].[7]

2.6 Technology comparison

In the previous sections, we gave a brief overview of each of the the four main candidate technologies for a burst power source, namely electrochemical, electric field, magnetic field and kinetic energy storage technologies. In this section these four candidate technologies will be compared with regard to their suitability as a burst power source.

2.6.1 Compared data

Many comparisons between various energy storage technologies have already been done in the past [Gen85], [Tho93], [Ter94], [Nel97a], [Zyl98], [Jou99], [Dar99], [Die99], [Bak99], [Heb02]. It is a daunting task to completely evaluate energy storage technologies extensively, taking into account all factors. This has not been the aim of this chapter, but rather to give a brief overview of the main contender technologies from a burst power applications point of view.

From a literature survey, data for power, energy, specific power, specific energy, power density and energy density of the most feasible burst power sources were combined into Figures 2.4, 2.5 and 2.6 [Gen85], [Tho93], [Nel97a], [Bit98], [Jou99], [Die99].

2.6.2 Power vs energy

According to [Jou99], SMES systems are available with the highest power rating (1 GW) of the four technologies compared in this chapter. One cannot but wonder whether the power electronics were included in this high power rating, however. Flywheel and battery systems come second at a power level of 10 MW and supercapacitors have the lowest rating at 100 kW[8]. Battery systems are available with slightly higher stored energy levels than those of SMES, and both these levels are two orders of magnitude higher than that of supercapacitors. The flwyheel system made by Vista Tech, Inc. is available with a very high amount of stored energy (1 MWh).

---

[6]In practice, 75% is usually used in flywheels. A 75% drop in energy corresponds to half the maximum rotational speed.

[7]The power electronics not only limits the depth of discharge in flywheel systems, but also in SMES systems, battery systems, etc. It is therefore questionable whether the 100% depth of discharge of SMES systems that Bitterly claims, is really used in practice.

[8]This was what was found to be commercially available at the time of this writing. Of course several of these modules may be placed in series or parallel to increase the power level.
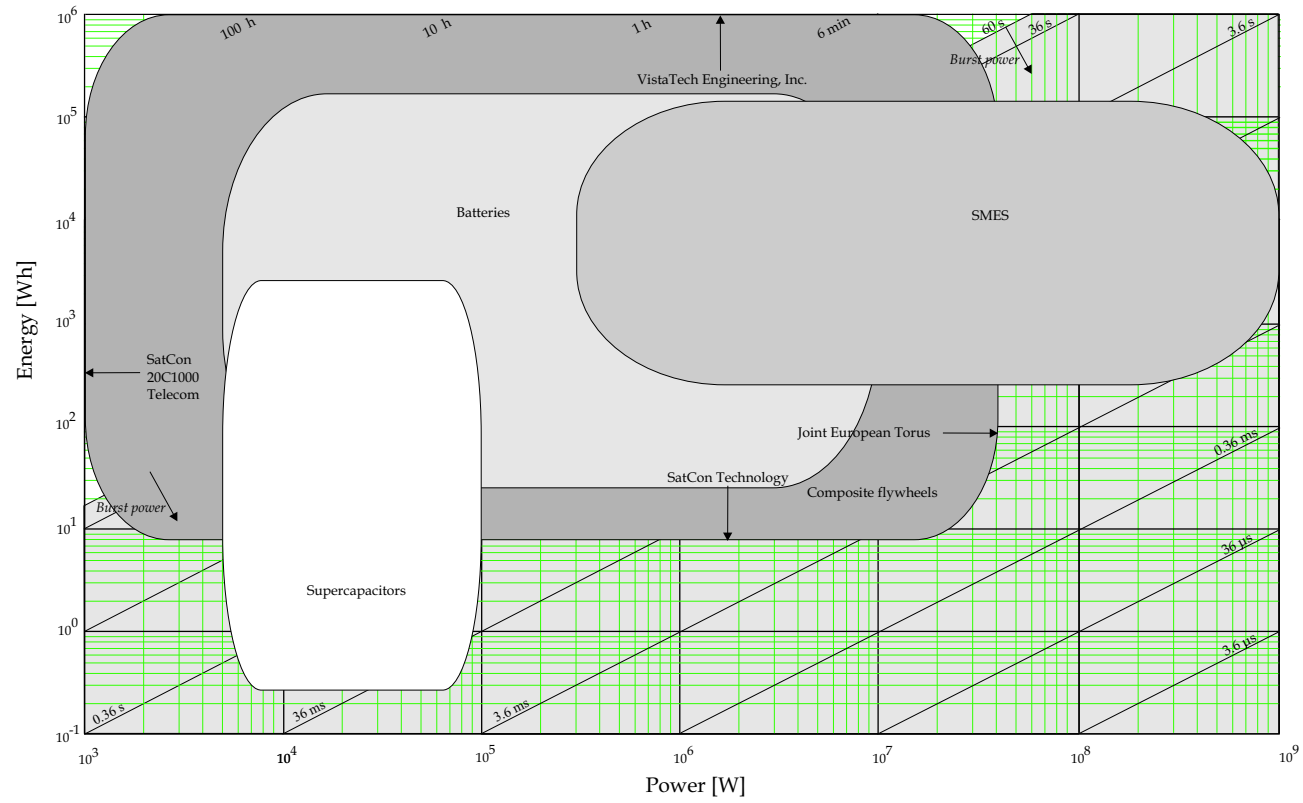
Figure 2.4: Power vs energy for the candidate technologies.

2.6.3   Power density vs energy density

Even less data are available on the power and energy densities of energy storage systems than on the specific quantities. Enough data could be gathered to construct Figure 2.5, however, which gives ample information to identify trends.

Batteries

Data from only one battery system manufacturer has been plotted in Figure 2.5; data of the high-power Li-ion systems of Saft, which can achieve power densities of $1.4\,\mathrm{MW/m^3}$. As these are electrochemical energy storage systems, one would expect them to have a very high energy density, which they do, as evidenced from Figure 2.5. These systems have the highest energy density just as in the case of specific energy, but flywheels already come quite close to the values achieved by electrochemical technologies. The flywheel data is for complete systems and was obtained from [Mar99].

Capacitors

The supercapacitor data used in Figure 2.5 was obtained from Siemens & Matshushita Components GmbH [Die99], for their 42 kJ and 150 kJ modules. The data on aluminium electrolytic capacitors was also obtained from Siemens & Matshushita Components GmbH [Pow] for their 6800 μF–33000 μF range. Supercapacitors do not score high on either axis of Figure 2.5, but the figures used are for complete modules, and in the case of the 150 kJ module, even electronic voltage sharing and protection circuitry are included. Aluminium electrolytic capacitors have a very high power density (around 650 kW/m^3) but at very low energy densities, typically $\sim$100 Wh/m^3. Metal-film capacitors have power densities higher than those of electrolytics, at lower energy densities due to the lower capacitance densities.

SMES

Data onf a single SMES system was available; the 2.7 MJ system made by American Semiconductor, which was also plotted. It can be seen that with the exception of electrolytic capacitors, it has the highest power density of the technologies shown in Figure 2.5. The data is for the electromagnet only, however, while the other technologies are listed as complete systems. When the total system is considered, the block will tend to move both to the left and downward, but the basic trend will remain the same, i.e. that SMES has the highest power density and the third highest energy density.

Figure 2.5: Power density vs energy density for the candidate technologies.
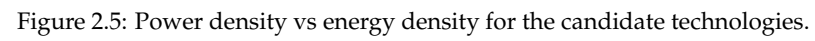
Composite flywheels

Composite flywheels perform worse with respect to energy per unit volume than the energy per unit mass, as can be seen from Figures 2.5 and 2.6. This can be explained from Table 2.1, where it can be seen that these composite flywheels require less mass but more volume for the same amount of stored energy than metal flywheels. This trend is also true for power: the power density of composite flywheels is worse relative to the other technologies than in the case of specific power.

2.6.4 Energy density comparison from first principles

The energy density of an electric energy storage device can be written from (2.5) as:

$$\hat{e}_{e,v} = \frac{\epsilon_r \epsilon_0 \hat{E}^2}{2}, \tag{2.18}$$

where $\hat{E}$ is the peak electric field intensity between the plates. Similarly, from (2.6) and (2.12) the energy densities of a magnetic storage device and a kinetic storage device can be written as:

$$\hat{e}_{m,v} = \frac{\hat{B}^2}{2\mu_0}, \tag{2.19}$$

and

$$\hat{e}_{k,v} = \frac{\rho \hat{v}_c^2}{2}, \tag{2.20}$$

where $\hat{B}$ is the peak magnetic flux density in the magnetic storage device and and $\hat{v}_c$ is the peak circumferential speed of the kinetic storage device. According to Driga [Dri93], from (2.18), (2.19) and (2.20), the stored energy ratios for the same volume is $\hat{e}_{e,v} : \hat{e}_{m,v} : \hat{e}_{k,v} = 1 : 10.9 : 131.9$; this is for:

- Electric: $\hat{E} = 1.6 \times 10^4 \, \text{V/mil}$, $\epsilon_r = 5\epsilon_0$;

- Magnetic: $\hat{B} = 12 \, \text{T}$;

- Kinetic:[9] $\hat{v}_c = 1150 \, \text{m/s}$, $\rho = 1800 \, \text{kg/m}^3$

Thus, the kinetic and magnetic energy storage devices store 131.9 and 10.9 times more energy than the electric energy device per cubic meter, respectively. This trend is confirmed by Figure 2.5, where flywheels have the highest energy density second only to that of batteries, followed my SMES and lastly by supercapacitors.

2.6.5 Summary: Power density vs energy density

Summarily, the following comments can be made regarding Figure 2.5:

---

[9]The high circumferential speed that Driga uses here suggests that these are projected values.

- Electrochemical technologies tend to have the highest energy densities of the compared technologies, but their power densities are limited due to the high impedance of wet-dry contact areas.

- Electric field technologies store less energy per cubic meter than the other three technologies, but have the highest power density.

- Magnetic field energy storage technologies store less energy per cubic meter than kinetic energy storage systems, but more than electric field technologies. They deliver more power per cubic meter than any of the other technologies except the electric field technologies.

- Due to the volume-inefficiency of composite flywheels as shown in Table 2.1, kinetic energy storage systems are second to batteries in stored energy per cubic meter, but higher than magnetic and electric field energy storage. They are third in power density, which is (similar to specific power) mainly limited by the electric machine.

2.6.6   Specific power vs specific energy

A comparison between the specific powers and energies of the various technologies is very difficult because these technologies are so different. For example, a battery and a supercapacitor have a DC output without any necessary power conversion while both SMES and flywheels need some form of power electronics to be able to compare them directly, adding mass to the system. To be really fair in a comparison, a system design study would have to be done for each application, choosing the specifications and comparing the energy storage system plus conversion and control for that set of specifications. This was not the aim of this study. Instead, an attempt was made to identify trends in the values and to gain a more qualitative understanding of what the different technologies are capable of.

Batteries

The specific energy of lead-acid batteries is around 30–40 Wh/kg at a specific power of up to 100 W/kg. Higher specific powers can be obtained, but at a reduced specific energy, as can bee seen in Figure 2.6.

The Ragone plots[10] shown in Figure 2.6 were obtained from [Gen85] and [Nel97a]. The data from [Gen85] is marked with an asterisk for identification. It can be seen that although conventional lead-acid batteries have undergone some progres during 1985–1997, no major breakthroughs were made in lead-acid technologies except the Bolder TMF® battery [Nel97a] and the TNO bipolar lead-acid battery [Kol99].

---

[10]The name "Ragone plot" is commonly used in battery technology. It relates specific power to specific energy.

Figure 2.6: Specific power vs specific energy for the candidate technologies.

The TMF$^{\circledR}$ battery is capable of achieving specific powers in excess of 4.4 kW/kg @ 7.3 Wh/kg. In fact, the 1.2 Ah cell is hypothetically expected to reach up to 12–15 kW/kg @ 3–4 Wh/kg, which corresponds to a discharge time of 1 s at a current level of 1 kA [Nel97a].

For the bipolar lead-acid battery, specific powers of up to 1 kW/kg at a specific energy of 8.3 Wh/kg at a laboratory scale have been demonstrated [Kol99]. From Figure 2.6 it can be seen that it is a good source of burst power for the approximate region of 3.6–20 s.

The high-power lithium ion technology of Saft (Alcatel) can achieve 1 kW/kg [Owe99], which is very high for Li-ion batteries and comparable with that achieved by the TNO bipolar lead-acid technology, but lower than that of the Bolder TMF$^{\circledR}$ (4 kW/kg). Lithium and Saft high-energy lithium-ion batteries have higher specific energies than lead-acid batteries, however. This makes them more suitable for slow-discharge applications.

SMES

Data on SMES systems is not readily available, and only values for the 2.7 MJ SMES made by American Superconductor is included in Figure 2.6. It should be noted that only the electromagnet data is plotted here, which is an unfair comparison, but a trend is nevertheless observable: SMES systems tend to have a higher specific power than battery technologies, but are rivalled by composite flywheels. A comparison taking the complete system mass into consideration would yield even lower specific powers for SMES.

Capacitors

Second to flywheels only, aluminium electrolytic capacitors have the highest specific power shown in Figure 2.6, but at very low specific energies, limiting them to high-power low-energy applications.

Metal-film capacitors have even higher specific powers than those of electrolytics (100 kW/kg–1 MW/kg; outside the scale of Figure 2.6) at an even lower specific energy (< 0.1 Wh/kg). They are thus only suited for very short power pulses.

Figure 2.6 shows that supercapacitors have specific powers (~4 kW/kg) [Die99] slightly below that of electrolytic capacitors, and their specific energies are between those of electrochemical storage devices and electrolytic capacitors. This makes supercapacitors a good power source for applications where full discharge is needed in approximately 1–60 s.

Composite flywheels

The data in Figure 2.6 on flywheels was obtained from [Gen85], [Bit98] and [Mar99]. It can be seen here that composite flywheels have the highest achievable specific power of all the compared technologies. For instance, 5.6 kW/kg (Trinity Flywheel

Batteries), 6.3 kW/kg (Satcon Technology Corporation) and 11.9 kW/kg (US Flywheel Systems). Bitterly of US Flywheel Systems projects that the specific power of flywheel systems can go as high as 30 kW/kg in future, the only limitation being the electric machine [Bit98]. Moreover, flywheels can have specific energies comparable with those of batteries, and Bitterly projects up to 200 Wh/kg based on increased strengths of graphite composites [Bit98].

2.6.7   Summary: Specific power vs specific energy

Summarily, the following comments can be made regarding Figure 2.6:

- Electrochemical technologies tend to have the highest specific energies, but their specific powers are limited due to the high impedance of wet-dry contact areas.

- Electric field technologies store less energy per kilogram than electrochemical technologies, but have a lower internal impedance than the former, giving them a higher specific power.

- Magnetic field energy storage technologies fit into a subset of the area occupied by electric field technologies in Figure 2.6.

- Kinetic energy storage systems deliver more power per kilogram than any other energy storage technology considered here and they also compare well with the high specific energy of batteries.

2.6.8   Other factors

Energy storage technologies may not only be compared in terms of power vs energy, power density vs energy density, and specific power vs specific energy (Figures 2.4–2.6), but also in terms of their cost, efficiency, bidirectionality, maintenance, depth of discharge, cycle life and other factors. A summary of such a comparison is listed in Table 2.2 [Jou99], [Dar99], [Heb02].

The reasons for the values in Table 2.2 can be explained by the working principles of each type of energy storage technology. This was one of the aims of this chapter. Another aim is to motivate the selection of kinetic energy storage for a hybrid electric city bus application. This is done in the next subsection.

Ref.	Item	Batteries	Fuel cells	Capacitors	Supercapacitors	SMES	Flywheels
[Jou99]	Cost [US$/kW]	100–200	1500	–	500	700–1000	300
[Dar99]		∼75	–	–	350–600	300–600	400–500^a; 30–100^b
[Heb02]		50–100^c	–	–	–	> 300	400–800
[Jou99]	Efficiency^d [%]	70–90	40–55	95	90	> 95	> 95
	Bidirectionality	Very bad	None	Good	Very good	Good	Very good
	Maintenance	High	–	Low	Low	Low	Low
	DoD [%]	70	–	100	100	100	95^e
	Cycle life	< 2000	–	> 10^5	> 10^6	> 10^6	> 10^6
[Heb02]	Life [service years]	3–5	–	–	–	∼20	> 20
	Practical time to hold a charge	Years	–	–	–	Days	Hours
	Annual sales [10^6 $]	∼7000	–	–	–	A few	∼2
	Number of US manufacturers	∼700	–	–	–	∼10	∼1
	Technology	Proven	–	–	–	Promising	Promising

Table 2.2: Energy storage technology comparison.

^{a}high speed

^{b}low speed

^{c}lead-acid

^{d}Von Jouanne *et al.* [Jou99] does not state which efficiency is meant here. The correct efficiency to compare is of course the turnaround efficiency, measured in the same domain (electrical).

^{e}usually operated at 75%

2.7 Selection of the kinetic energy storage technology for a hybrid electric city bus

The power and energy requirements for the bus[11] are 150 kW and 4 kWh, respectively. This is within the listed requirements of power and energy for busses in Table 1.1. Looking at Figure 2.4, one sees that SMES, batteries and composite flywheels are candidate energy storage systems.

Also from Table 1.1, the required energy storage technology should have a specific power of between 180 W/kg and 400 kW/kg, and a specific energy of 5–30 Wh/kg. From Figure 2.6, SMES does not meet these requirements and therefore only some battery technologies and composite flywheels remain as candidates. No requirements for power and energy density are set, but when Table 2.2 is considered, batteries are eliminated because of their bad bidirectionality, high maintenance and their low cycle life and lifetime. This leaves composite flywheels, which is not the cheapest technology, but nevertheless the one chosen for this application. It is envisaged that the high initial cost of the flywheel system will be offset over time because of its low maintenance cost and very high reliability.[12]

2.8 Summary

It was said in Chapter 1 that the goal of this thesis is to describe the design of an electrical machine for a flywheel energy storage system. This system is to be used for load levelling of hybrid electric city busses and light-rail vehicles. This chapter showed how flywheel (kinetic) energy storage systems fare against other contender technologies. The emphasis throughout the chapter was on the power delivery capabilities of each of the four energy storage technologies under consideration.

Sections 2.2–2.5 discussed four energy storage technologies as possible sources of high power delivery for short durations: They were:

1. electrochemical energy storage: batteries and fuel cells (Section 2.2);

2. electric field energy storage: metal-film capacitors, aluminium electrolytic capacitors and supercapacitors (Section 2.3);

3. magnetic field energy storage: superconducting electromagnets (Section 2.4); and

4. kinetic energy storage: flywheels (Section 2.5).

---

[11] If the requirements for a hybrid electric car instead of a bus would have to be met, supercapacitors would be an increasingly viable candidate for use as the energy storage technology.

[12] Once again, as with many of the other criteria, the reliability of a flywheel energy storage system is limited by the power electronics.

In Section 2.6 these four energy storage technologies were compared, and Section 2.7 concluded the chapter with the motivation of the choice of a flywheel for a hybrid electric city bus.

In Chapter 3, a flywheel energy storage system is introduced for this hybrid city bus application. The main challenge in such a system is the power level, and it will be shown that the most important factor influencing this is the electrical machine design. Such an electrical machine was designed for the flywheel. Chapter 3 introduces this electrical machine. In the rest of the thesis, the design will be discussed in more detail.

Introduction of the EμFER machine

3.1 Introduction

In Chapter 2, we motivated the choice of a kinetic energy storage system for a high-power, medium-energy storage application (power buffering in a hybrid electric vehicle). This chapter focusses on such flywheel energy storage systems, particularly with the aim of maximizing their power delivery capability. It takes a look at drive system topologies (Section 3.2), converter options (Section 3.3), and the selection of the electrical machine type (Section 3.6).

In Section 3.4, it will be shown that the power delivery capability of a flywheel energy storage system is mainly limited by the electrical machine design, whereafter Section 3.5 explains that the rest of the thesis will focus on the electrical machine. Section 3.6 takes a brief look at different possible machine types.

A machine has been designed for application in a flywheel energy storage system for a hybrid electric city bus and it has been constructed by the Centre for Concepts in Mechatronics (CCM) B.V. in the Netherlands.

Section 3.7 describes this flywheel energy storage system, called EμFER, in general. This is followed by a more detailed description of the designed electrical machine, which is the focus of the majority of the rest of this thesis. Section 3.8 summarizes the chapter.

3.2 Drive system topologies

The electrical machine to be introduced in Section 3.7 is intended for application in hybrid electric vehicles like light rail vehicles and city busses. Several topologies are possible for the drive systems of hybrid electric vehicles. It is, however, not the purpose of this thesis to provide a thoroughly detailed overview of hybrid drive

system topologies, but rather to state briefly into which system the electrical machine designed in this thesis fits.

Figure 3.1 shows the two main options for hybrid electric vehicle drive systems: series and parallel systems [Mag00, Jon02]. Both series and parallel hybrid systems may be configured in several different ways. Figure 3.1 shows only one possible configuration for each.

In the series hybrid topology of Figure 3.1(a), the traction is obtained by one drive shaft connected to the drive axle. Thus the energy flow of the flywheel system is added electrically to the drive shaft. One distinct advantage of the series hybrid topology is that the internal combustion engine (ICE) and traction machine can be mounted separately. In city busses, this makes it possible to have a low floor [Jon02]. Another advantage of the series hybrid topology is that the ICE may be run at the range of rotational velocities where it is most efficient, since there is no mechanical connection to the load.

In the parallel hybrid topology of Figure 3.1(b), the ICE is directly connected to the drive shaft through a gearbox. Thus, in contrast to how power is added in the series hybrid system, namely electrically, in the parallel hybrid system it is added mechanically. The parallel hybrid requires the ICE, gearbox and the traction machine to be mounted closely together.

When looking at the number of power conversion stages in the two topologies, one can observe the following:

- The series hybrid topology has three power conversion stages during nominal power transfer from the shaft of the ICE to the drive shaft, while the parallel hybrid topology has one.

- For power flow from the shaft of the ICE into the flywheel, the series hybrid topology requires three power conversion stages, and the parallel hybrid four.

- For power flow from the flywheel to the drive shaft, both the series hybrid and parallel hybrid topologies need four power conversion stages.

Not all power conversion stages have the same losses, however, meaning that merely counting the number of power conversions is not sufficient for a thorough comparison. Such a comparison is beyond the scope of this thesis. The purpose of this paragraph was simply to serve as an orientation and background to see where the EμFER electrical machine fits in. The bus in which it is used, utilizes the series hybrid topology.

3.3 Converter options

It is practical to use a DC bus in the chosen series hybrid system like the one shown in Figure 3.1(a). Thus the generator connected to the ICE is either a DC machine, or an ac machine with a controlled or uncontrolled rectifier. This part of the system is not under consideration in this thesis.
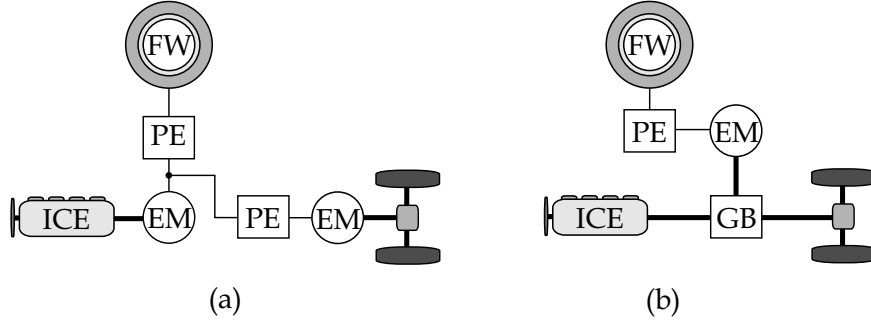
Figure 3.1: Drive system topologies: (a) series hybrid; (b) parallel hybrid. (ICE = internal combustion engine; EM = electrical machine; FW = flywheel; PE = power electronics; GB = gearbox.)

The practical options for the power converter connecting the flywheel electrical machine in Figure 3.1(a) to the DC grid can be divided into two broad categories: current source inverters (CSIs) and voltage source inverters (VSIs). Which of the two should be chosen for a flywheel drive depends on:

- the losses in the converter itself;

- the losses that the converter induces in the machine; and

- the electromagnetic torque or power output that can be realised with the converter for a specific machine.

The losses of the converter itself and those it induces in the machine will be discussed in Chapters 6, 7 and 8, after a method for calculating them has been developed.

Concerning the power level, one can easily show that the VSI is a better choice by considering a simple per-phase equivalent circuit of the machine, as the one shown in Figure 3.2(a). The voltage equation of Figure 3.2(a) is:

$$\underline{E}_p = \underline{U}_s + jX_s\underline{I}_s. \tag{3.1}$$

A phasor diagram of the machine of Figure 3.2(a) working at a lagging power factor (typical for a CSI) is shown in Figure 3.2(b). The power output of the circuit of Figure 3.2(a) is given by the well-known equation:

$$P = \frac{3\,U_s\,E_p}{X_s}\ \sin\delta, \tag{3.2}$$

where U_s and E_p are the rms values of the phasors $\underline{U}_s$ and $\underline{E}_p$, respectively, and δ is the power angle.

Figure 3.3 shows several more phasor diagrams. Figures 3.3(a)–(c) shows three operating strategies or control methods with the same no-load voltage $\underline{E}_p$:
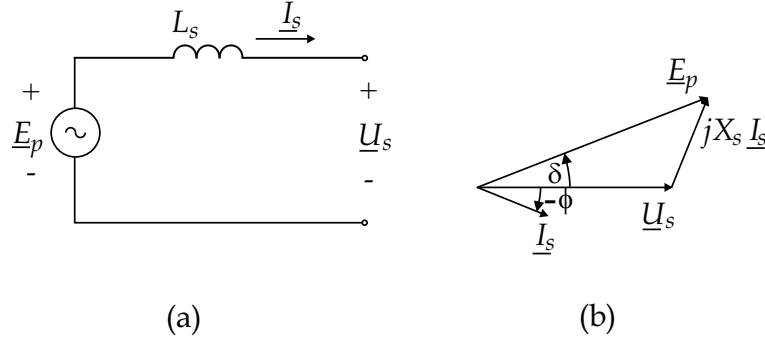
Figure 3.2: (a) Equivalent circuit of a PMSM; (b) phasor diagram for a lagging power factor.

Figure 3.3(a): lagging power factor; Figure 3.3(b): unity power factor; and Figure 3.3(c): $\underline{I}_s$ in phase with $\underline{E}_p$.

The lagging power factor case of Figure 3.3(a) is the mode of operation of the machine connected to a CSI. Due to the working principle of thyristors, the voltage across it must be positive before the current can start flowing after a gate pulse. This means that the current through a thyristor always lags the voltage, and this also applies for the CSI. There is always reactive power flow in such a system, necessitating an increase in the ratings of the semiconductors. In diode rectifiers, or CSIs with zero firing angle, this phase lag is typically small enough to be neglected; Figure 3.3(b) shows this situation.

When the current $\underline{I}_s$ is controlled (by a VSI, or uncontrolled in a diode bridge) such that it is in phase with the terminal voltage of the machine $\underline{U}_s$, unity power factor is achieved, as shown in Figure 3.3(b). In this case, no reactive power flows from the converter to the machine or vice versa.

In Figure 3.3(c), another control strategy is shown. Here, the current $\underline{I}_s$ is controlled to be in phase with the no-load voltage of the machine $\underline{E}_p$. In this case, the current leads the terminal voltage and the machine thus appears capacitive to the converter. The control strategy of Figure 3.3(c) can only be achieved with a VSI since
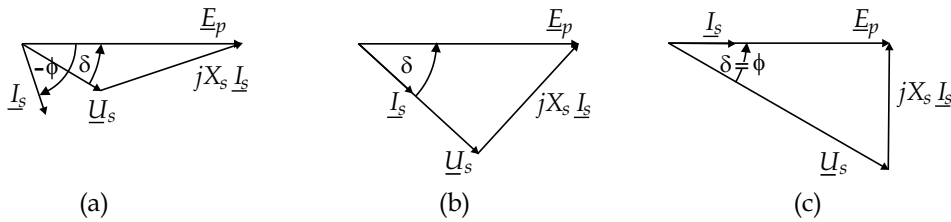
Figure 3.3: Phasor diagrams for the same no-load voltage: (a) lagging power factor; (b) unity power factor; (c) $\underline{I}_s$ in phase with $\underline{E}_p$.

the current leads $\underline{U}_s$. The VSI consists of controllable switches like IGBTs or GTOs and therefore the device current can lead its voltage.

It can be seen from Figure 3.3(a) that in the lagging power factor case, *by increasing the stator current* (this also changes the power factor and the load angle), the power output will collapse after a certain stator current value. The same is true for the unity power factor case in Figure 3.3(b), where a maximum power output is reached at $\delta = 45°$. It can be seen from Figure 3.3(b) that $U_s = E_p \cos \delta$, which gives for the power output of this case, from (3.2):

$$P_{i_s u_s} = \frac{3 E_p^2}{X_s} \cos \delta \sin \delta. \qquad (3.3)$$

The best control strategy of the above three for maximizing the power level for the same current between $\underline{E}_p$ and $\underline{U}_s$ is the case where the current $\underline{I}_s$ is controlled to be in phase with $\underline{E}_p$. In this case, theoretically no maximum power is reached for increasing δ. This can be seen from the fact that $U_s = \frac{E_p}{\cos \delta}$ from Figure 3.3(c). Thus the power output of the converter/machine for this control strategy is equal to:

$$P_{i_s e_p} = \frac{3 E_p^2}{X_s} \tan \delta. \qquad (3.4)$$

Equation (3.4) shows that the power gets asymptotically larger with increasing δ, and does not reach a maximum. The asymptote is at $\delta = 90°$. Figure 3.4 shows equations (3.3) and (3.4) normalised to $3E_p^2/X_s$. From Figure 3.4, one sees that the maximum power output of the unity power factor control strategy is $\frac{3}{2}E_p^2/X_s$ at $\delta = 45°$. At the same power angle, the power output of the control strategy where $\underline{I}_s$ is in phase with $\underline{E}_p$ is $3E_p^2/X_s$, twice that of the unity power factor case. This proves that this control strategy is able to withdraw/supply the highest power from/to the machine.[1]

To summarize, a CSI always results in a lagging power factor (for zero firing angle this lag is very small, i.e., only the commutation angle), which limits the maximum power that can be extracted from the machine. When a VSI is used, the unity power factor control strategy results in a higher power output than when a CSI is used. However, the control strategy that controls the stator current to be in phase with the no-load voltage results in the highest possible power extracted from the machine. Another, simpler, way to see this is to write the power output directly in phasor notation:

$$P = 3 \underline{E}_p \underline{I}_s^*, \qquad (3.5)$$

where $\underline{I}_s^*$ is the complex conjugate of $\underline{I}_s$. It may be seen directly from (3.5) that the maximum power for a constant value of $\underline{I}_s$ is reached when $\underline{E}_p$ is in phase with $\underline{I}_s$.[2]

---

[1]There is, of course, an effect on U_s in this control strategy: it steadily increases with increasing I_s. This cannot be done without limit, since at high U_s, the machine isolation might break down.

[2]By minimization of the losses, or maximizing the efficiency, one arrives at the same result.
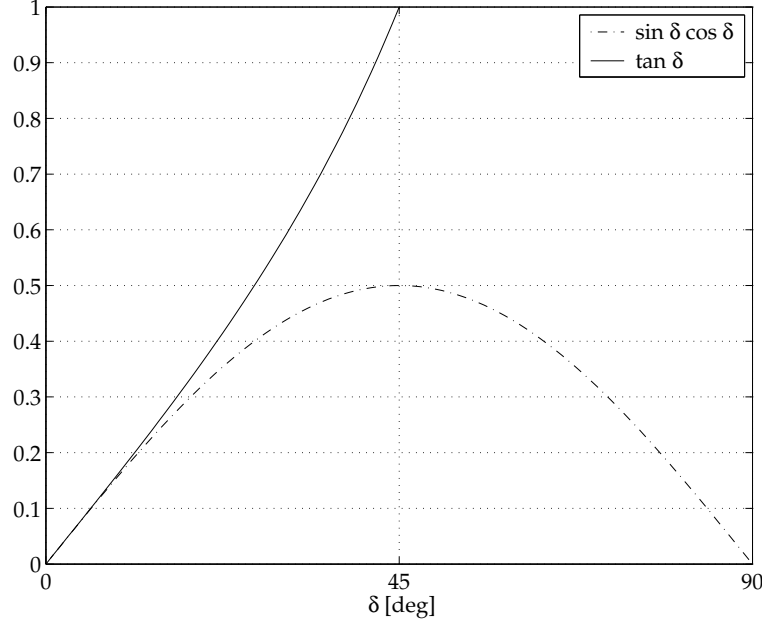
Figure 3.4: Normalized power output of two control strategies possible with a VSI: where $\underline{I}_s$ is in phase with $\underline{E}_p$ (solid line) and unity power factor (dotted line).

3.4 Energy and power limitations of a flywheel energy storage system

An important fact regarding flywheel machines is that the energy storage capacity is only limited mechanically, while the power delivery capabilities are limited mainly by the design of the electrical machine. This can be seen from (2.17), showing that the specific energy of the flywheel is a function of three mechanical parameters: the shape factor K, the minimum tensile strength σ_{min} for a given angular velocity ω, and the mass density ρ of the flywheel material. The electrical machine and the power electronics therefore do not play a role in the energy stored in the flywheel. (The rotor does add to the mass moment of inertia of the flywheel, but it contributes much less than the flywheel itself.)

On the other hand, the power level (both deliverable and absorbable) of such a system depends more on the mechanical properties of the flywheel than on the power electronics converter, the electrical machine and their interaction. Therefore one can say that the system's energy is mainly limited mechanically and its power is mainly limited electromagnetically and by the power electronics.

Thus, in order to increase the power level of such a system, one must focus on the design of the electrical machine and the power electronics converter. In Sec-

tion 3.3, it has been shown that the power level of a flywheel energy storage system can be increased by using a voltage source inverter (VSI) rather than a current source inverter (CSI). Furthermore, the achievable power level of a VSI is a direct function of the voltage and current rating of the switching devices used, the converter layout, and the maximum junction temperature of the switches. The switching losses can be reduced by utilizing resonant techniques to achieve soft switching of the devices. Furthermore, careful converter layout techniques will limit the stray impedances to a minimum. This only leaves the problem that the voltage and current rating of the switching devices of the converter limit its power capability, but this is an economic problem rather than one with the converter design. This is in contrast to the case of the electrical machine, where the design mainly determines the maximum power level that can be extracted from it.[3]

This means that the greatest challenge in increasing the power level of the complete system is the electrical machine design, a fact that has also been confirmed by [Bit98].

3.5 The focus of the rest of this thesis: The electrical machine

Up till now, this thesis had quite a broad scope. This scope is significantly narrowed from this section onwards however to include only the electrical machine. The reason for this is that the machine needed for the energy storage flywheel is a challenging one requiring special design and analysis techniques. The design requirements are:

- high power;

- low loss;

- low no-load loss; and

- high speed.

The choice of narrowing down the scope to the machine is strengthened by the argument in the previous section and [Bit98].

---

[3]As in the case of the converter, this is also only true up to the point where the material properties of the machine become the main limitation (e.g. the breakdown voltage of the conductors' insulation), at which stage improving the design will not lead to a higher power level anymore. Unlike in the case of the converter, however, much more may be achieved with respect to the machine design before the material limitations are felt.

3.6   Machine type selection

3.6.1   Introduction

In this section, electrical machine types are considered, with the emphasis on high-power energy extraction from energy storage flywheels. The mechanical and electrical requirements of the machine are discussed, whereafter a suitable machine type and topology are selected.

3.6.2   Mechanical requirements

Figure 2.3 shows that the best flywheel shape in terms of the shape factor is the Laval disk. As discussed in Chapter 2, however, this shape (or any shape with $K > 0.5$) requires an isotropic material like steel. When a composite material is chosen, one sees from Table 2.1 that the resulting flywheel requires 2–5 times less weight than a metal flywheel storing the same amount of energy, albeit at a larger volume. The shape requirement of the composite flywheel becomes an approximation of the thin rim, as shown in Figure 2.3. Since this flywheel shape results in a fairly large "hole" in the centre, this space might as well be used for the electrical machine, i.e., the machine has an external rotor construction.

   Further mechanical boundary conditions include the rotor iron outer radius (carbon fibre inner radius) due to the strength of the fibre, and the flywheel's axial length. The latter is quite short, resulting in a fairly flat machine. In spite of this fact, a radial flux machine is chosen (Chapter 2 also showed that mechanically, a radial flux topology is a better choice).[4]

3.6.3   Electrical requirements

The electrical requirements of the machine were listed in Section 3.5.

3.6.4   Machine type comparison

Acarnley *et al.* compared machine types for a flywheel [Aca96], as did Hofmann and Sanders [Hof96]. Table 3.1 lists a summary of these comparisons. It lists the advantages and disadvantages of synchronous reluctance, asynchronous and permanent-magnet synchronous machines (PMSMs).

   The greatest advantage of the synchronous reluctance machine is that there is no flux in the rotor at no load, and therefore ideally zero losses. The torque density of this machine type is lower than that of the PMSM, however. The tooth ripple effects during load can also cause substantial rotor loss at load. The windage losses will also be very high for a machine rotating at 30 000 rpm, although this disadvantage may easily be overcome by filling the rotor slots with nonmagnetic material.

---

[4]For discussions of axial flux machines in flywheels, see [Aca96] and [Sah01].

Synchronous reluctance	
Advantages	• Singly excited: negligible iron losses at no-load; ideal case: no rotor losses • Cheap rotor construction
Disadvantages	• Solid (non-laminated) rotor: L_d/L_q low $\Rightarrow$ low power factor and low torque density • Tooth ripple effects: high rotor eddy current losses • Windage losses (not such a problem in the EµFER machine since it rotates in a low pressure atmosphere)
Asynchronous	
Advantages	• Cheap rotor construction • Rotor suitable for disk geometry (metal flywheels)
Disadvantages	• Low power factor • High rotor losses • Typically a low torque density
PMSM	
Advantages	• High torque density • Low rotor losses
Disadvantages	• Magnets must be contained (axial flux topologies) • Demagnetization • Permanent magnets' dependency on temperature • High magnet cost • High no-load losses

Table 3.1: Flywheel machine type comparison [Aca96, Hof96].

A permanent magnet synchronous machine is chosen above an asynchronous machine because of the higher torque per unit volume and the lower rotor losses of the PMSM. It is very important to have the losses on the rotor as low as possible since the rotor rotates in vacuum at very high speed, which makes it difficult to cool.

3.6.5 The chosen machine type and topology

The chosen machine type for the flywheel is thus the PMSM, the main reasons being its high specific torque/torque density and the low rotor losses. The list of disadvantages in Table 3.1 may seem intimidating, but they are solvable. Magnet containment is no problem in external rotor, radial flux topologies since the magnets are supported by the rotor iron. It does have an influence on the rotor iron's mechanical properties, however, and on those of the carbon fibre. This is because the rotor iron carries the weight of the magnets and the shielding cylinder (if present), and

the carbon fibre carries the weight of the rotor iron, magnets and shielding cylinder. With careful design this is a challenge that can be met; it has been met in the past by several flywheel PMSM manufacturers. Demagnetization and magnet temperature problems may also be solved by good design and cooling of the rotor. High no-load losses may arise because the permanent magnets' flux cannot be switched off during no load, causing high dB/dt in the stator winding and iron, inducing eddy current losses. This is also a problem that can be reduced by good design, and it will be addressed in detail later in the thesis.

One way of reducing the no-load loss in the stator is to make the stator winding slotless and to use Litz wire stator conductors. Slotted and slotless stators have been compared in [Ark92] with respect to induced eddy current loss in the stator conductors and the stator iron. It was shown that if the diameter of the Litz wire strands is chosen appropriately, the losses can be significantly reduced.

In summary, the requirements of the electrical machine may now be written as:

- a flywheel shape approaching the thin rim is required ⇒ external rotor machine;

- although fixed dimensions require the machine to be quite flat, the aspect ratio still makes a radial flux topology viable;

- low rotor loss ⇒ use of a shielding cylinder on the rotor;

- high power density ⇒ PMSM; and

- low no-load loss ⇒ slotless, laminated stator with Litz wire conductors and very thin laminations.[5]

3.7 The EμFER machine

3.7.1 Introduction and system description

The EμFER flywheel energy storage system was initiated by CCM B.V. for use in large hybrid electric vehicles like city busses for power buffering. Figure 3.5 shows the drive system of the EμFER system for use in a hybrid electric city bus. The LPG internal combustion engine turns a DC generator connected to a DC grid, which forms the centre of the system. From the DC grid, the DC traction machine that turns the driving axle is fed through a DC/DC converter. The flywheel machine is also connected to the DC grid, through either a VSI or a CSI. In Figure 3.5, the average power is supplied by the diesel engine, which also charges the flywheel up slowly. During peak power demand, as in acceleration of the bus from standstill, the higher power level is supplied by the flywheel to the traction motor via the DC bus.

---

[5]The slotless stator reduces the power density listed in the previous requirement, but the density is still acceptable.

During braking, the kinetic energy of the city bus is converted into electrical form by the traction machine, thereby charging the flywheel up again (regenerative braking).

The specifications of the EµFER machine were fixed at: 150 kW nominal power (300 kW peak) and 7.2 MJ (2 kWh) usable stored energy, with the no-load losses as low as possible. The energy to power ratio of the EµFER system is 48 s when delivering/absorbing nominal power.
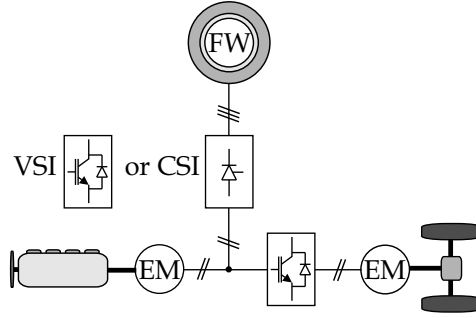
Figure 3.5: EµFER flywheel energy storage system for use in a hybrid electric city bus.

3.7.2 The use of a shielding cylinder

The effect of a shielding cylinder on the rotor losses in permanent-magnet machines has been investigated in [Vee97], [Abu97], [Pol98], [Zhu01a] and [Zhu01b], among others. This cylinder shields the permanent magnets and the rotor iron from high-frequency magnetic fields originating from the stator currents. One general conclusion was that for low rotational speeds, the addition of a shielding cylinder increases the losses, while for high rotational speeds, the addition of a shielding cylinder reduces them. In [Pol98], it is furthermore recommended that when a solid rotor iron is used, a shielding cylinder should always be used to reduce the rotor losses.

This can be seen from the skin depth:

$$\delta = \sqrt{\frac{2}{\omega \sigma \mu}} \, , \tag{3.6}$$

where ω is the frequency of excitation, σ is the conductivity and μ the permeability of the material under consideration. At the same frequency, the ratio between the skin depth of iron and copper is:

$$\frac{\delta_{Fe}}{\delta_{Cu}} = \sqrt{\frac{\sigma_{Cu}}{\sigma_{Fe}}} \sqrt{\frac{1}{\mu_{r,Fe}}} \, , \tag{3.7}$$

where $\mu_{r,Fe}$ is the relative permeability of iron.

The conductivity of copper is approximately 6.18 times larger than that of pure iron at room temperature, and therefore $\sqrt{\frac{\sigma_{Cu}}{\sigma_{Fe}}} = 2.49$. Depending on the processing, the permeability iron can be anywhere between 1000 to 5000 times higher than that of copper. Taking the number of 1000, we have: $\sqrt{\frac{1}{\mu_{r,Fe}}} = 0.0316$. Thus, $\frac{\delta_{Fe}}{\delta_{Cu}} = 0.0787$, or the skin depth in iron, is 12.7 times smaller than that in copper at the same frequency.

Furthermore, the resistance of a rectangular conductor is: $R = l/(\sigma A)$, where l is the current's path length, σ is the conductivity of the material and A the area through which the current flows. The ratio of the resistance of a rectangular iron conductor and that of an equivalent copper conductor is:

$$\frac{R_{Fe}}{R_{Cu}} = \frac{\sigma_{Cu}}{\sigma_{Fe}} \frac{\delta_{Cu}}{\delta_{Fe}} = \sqrt{\frac{\sigma_{Cu}}{\sigma_{Fe}}} \sqrt{\mu_{r,Fe}} = 2.49 \times 31.6 = 78.7 \tag{3.8}$$

from (3.7).

The metal of which the shielding cylinder is made can also be another nonmagnetic material like aluminium. This could have mechanical advantages, but the electrical properties are worse. More precisely, at room temperature, the conductivity of copper is 1.59 times higher than that of aluminium. Thus the ratio of the resistance of a rectangular aluminium conductor and that of an equivalent copper conductor is from (3.8):

$$\frac{R_{Al}}{R_{Cu}} = \sqrt{\frac{\sigma_{Cu}}{\sigma_{Al}}} = 1.26. \tag{3.9}$$

In the following discussion, the current is inductance limited; a change in the material's resistance then corresponds to a change in the induced loss in that material. From (3.8) it can be seen that there is a drastic reduction in induced rotor loss when the currents arising from induced voltages are dissipated in copper rather than in iron. From (3.9) it can be seen that this reduction is less when an aluminium shielding cylinder is used, but that it is still very significant. In either case, whether copper or aluminium is used, a shielding cylinder is required.

3.7.3   General machine description

Combining the facts discussed in Sections 3.6.5 and 3.7.2 above, the electrical machine becomes as that shown in Figure 3.6. On the inside of the stator iron is an electromagnetically inactive area that is used for bearings, cooling and other auxiliaries. The stator iron consists of a slotless cylinder that is laminated, i.e., it consists of very thin, closely stacked rings. On its outside, the stator winding region is located, which is described in the next section. On the outside of the mechanical air gap the electromagnetic shielding cylinder is located, followed by the permanent-magnet array and the solid rotor iron yoke. On the outside of the rotor iron, the carbon fibre flywheel is mounted.
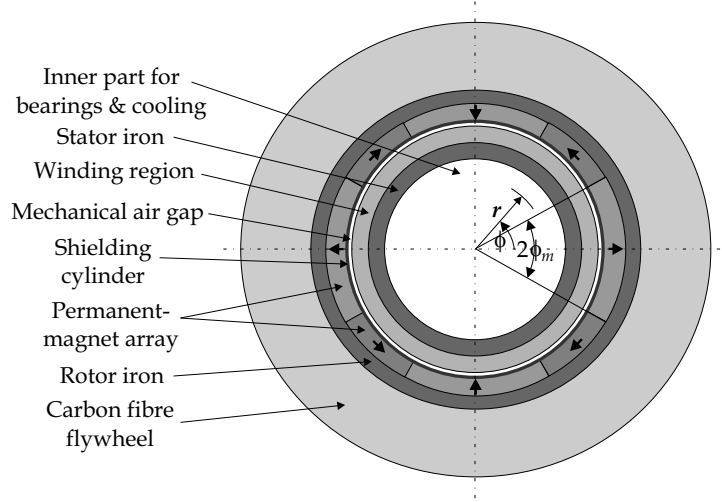
Figure 3.6: EμFER machine cross section with flywheel.

3.7.4 The stator winding distribution

General description of the winding

The stator winding distribution was designed to have a low space harmonic content, i.e., to closely approximate a sinusoidal winding distribution. In Figure 3.6, the winding region is the third region from the inside. The winding has two layers and is in fact constructed as a slotted structure, but the slots are made of a synthetic nonmetallic material. The second layer is short pitched by one slot, thus forming a 1-2-2-1 winding distribution. The winding parameters are:

- number of phases: $m = 3$;

- number of pole-pairs: $p = 2$;

- number of slots per pole per phase: $q = 3$;

- number of slots: $s = 2mpq = 36$;

- slot-opening angle: $\varphi_{so} = 0.8(\pi/18)$;

- pitch angle: $\varphi_{pitch} = \pi/18$; and

- 1 conductor per slot per layer

Figures 3.7(a) and (b) show photographs of the EμFER stator winding during the winding process, and Figure 3.7(c) shows a close-up of the end windings of the completed stator winding.

(a)   (b)

(c)
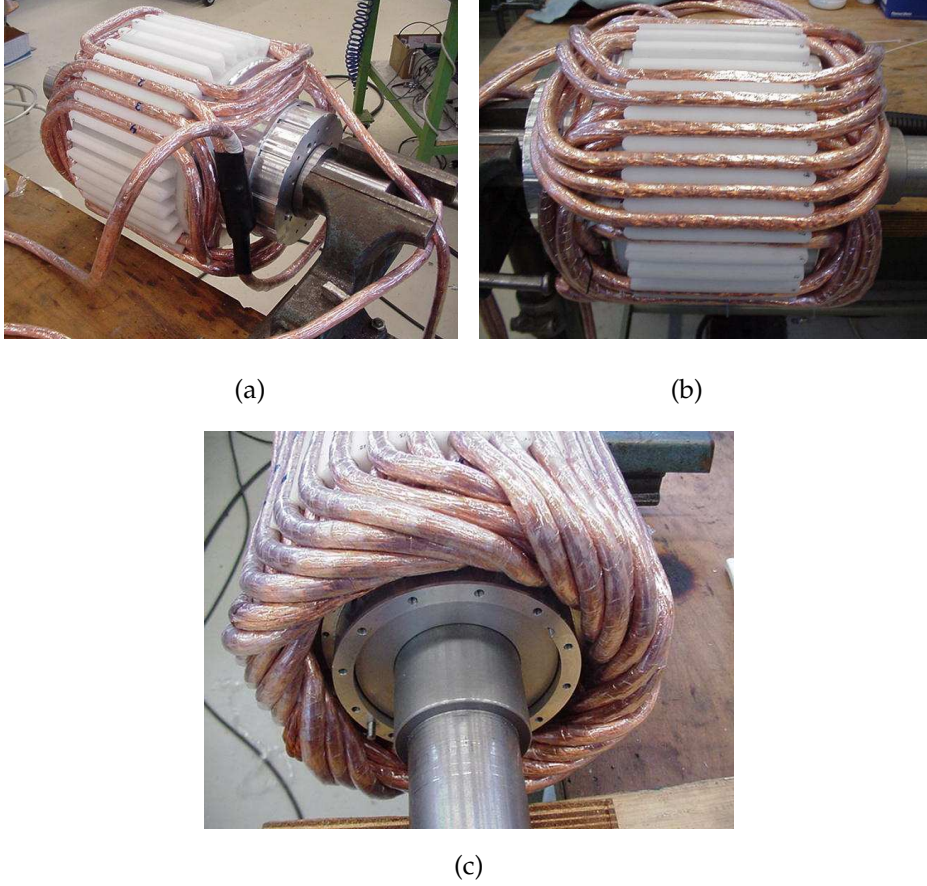
Figure 3.7: Photographs of the EμFER stator winding.

A mathematical description of the winding distribution

The EμFER machine was designed based on analytical field calculations. This choice will be motivated thoroughly in Chapter 4. To start such an analytical design process, we used the mathematical description of the stator winding shown in Figure 3.7. Since it is a three-phase winding, this may be done on a per-phase basis. For phase *a*, the winding distribution (the number of conductors per radian), can be written as the Fourier series:

$$n_{sa}(\varphi) = \sum_{k=1,3,5,\cdots}^{\infty} \hat{n}_{s,k} \cos(kp\varphi), \tag{3.10}$$

where k is the space harmonic, and the Fourier coefficient $\hat{n}_{s,k}$ is half the number of turns of the k-th space harmonic $N_{s,k}$. This can be seen by integrating (3.10) over half

a full pitch:

$$\tfrac{1}{2}N_{s,k} = kp \int\limits_{0}^{\pi/2kp} \hat{n}_{s,k} \cos(kp\varphi)\, d\varphi = \hat{n}_{s,k}. \tag{3.11}$$

The number of turns of the *k*-th space harmonic is related to the real number of turns *N* by [Sle92]:

$$N_{s,k} = \tfrac{4}{\pi} k_{w,k} N \tag{3.12}$$

where $k_{w,k}$ is the winding factor for the *k*-th space harmonic of the winding. (Winding factors are reviewed in Appendix A.) Figure 3.8 shows a linear depiction of the stator winding distribution and a plot of the function $n_{sa}(\varphi)$ as given by equation (3.10).

By making use of the fact that $\cos(-kp\varphi) = \cos(kp\varphi)$, equation (3.10) can be rewritten as:

$$n_{sa}(\varphi) = \overbrace{\sum_{\ddot{k}=-\infty}^{\infty} \hat{n}_{s,6\ddot{k}+1} \cos\big[(6\ddot{k}+1)p\varphi\big]}^{k=\cdots,-23,-17,-11,-5,1,7,13,19,25,\cdots} + \overbrace{\sum_{\dot{k}=0}^{\infty} \hat{n}_{s,6\dot{k}+3} \cos\big[(6\dot{k}+3)p\varphi\big]}^{k=3,9,15,21,27,\cdots}. \tag{3.13}$$

where $\ddot{k} \in \mathbb{Z}$ and $\dot{k} \in \mathbb{Z}^+$ are not the space harmonic anymore, but related to it as listed in Table 3.2, i.e.:

$$k = 6\ddot{k} + 1 \tag{3.14}$$

for the double-sided Fourier series, and:

$$k = 6\dot{k} + 3 \tag{3.15}$$

for the single-sided Fourier series.

It can be seen that the double-sided term in (3.13) represents all the non-triplen space harmonics and the single-sided term the triplens.
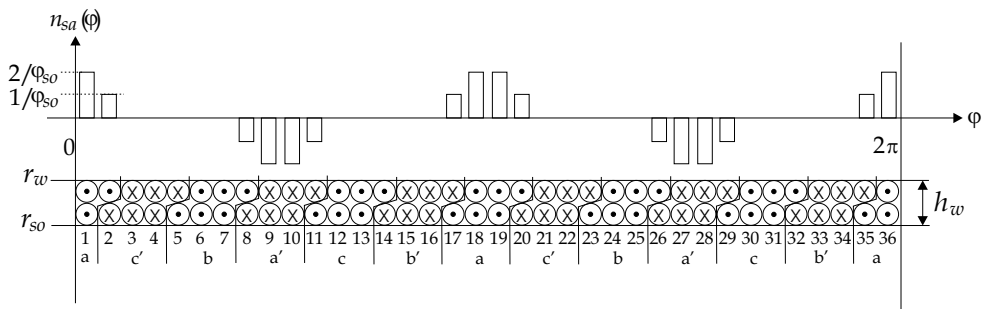
Figure 3.8: A linear depiction of the winding distribution of the flywheel machine of Figure 3.6. The winding distribution of phase *a*, given by equation (3.10), is also shown.

Double-sided	$\ddot{k}$	-4	-3	-2	-1	0	1	2	3	4
	$k = 6\ddot{k} + 1$	-23	-17	-11	-5	1	7	13	19	25
Single-sided	$\dot{k}$					0	1	2	3	4
	$k = 6\dot{k} + 3$					3	9	15	21	27

Table 3.2: Relationship between $\dot{k}$, $\ddot{k}$ and the space harmonic k.

The expressions for phases b and c are similar to (3.13), but shifted in phase by $-2\pi/3$ and $-4\pi/3$, respectively. Thus, for the three-phase winding distribution, we have:

$$n_{sa}(\varphi) = \sum_{\ddot{k}=-\infty}^{\infty} \hat{n}_{s,6\ddot{k}+1} \cos\left[(6\ddot{k}+1)p\varphi\right] + \sum_{\dot{k}=0}^{\infty} \hat{n}_{s,6\dot{k}+3} \cos\left[(6\dot{k}+3)p\varphi\right], \qquad (3.16a)$$

$$n_{sb}(\varphi) = \sum_{\ddot{k}=-\infty}^{\infty} \hat{n}_{s,6\ddot{k}+1} \cos\left[(6\ddot{k}+1)(p\varphi - \tfrac{2\pi}{3})\right] + \sum_{\dot{k}=0}^{\infty} \hat{n}_{s,6\dot{k}+3} \cos\left[(6\dot{k}+3)(p\varphi - \tfrac{2\pi}{3})\right],$$
$$\qquad (3.16b)$$

and

$$n_{sc}(\varphi) = \sum_{\ddot{k}=-\infty}^{\infty} \hat{n}_{s,6\ddot{k}+1} \cos\left[(6\ddot{k}+1)(p\varphi - \tfrac{4\pi}{3})\right] + \sum_{\dot{k}=0}^{\infty} \hat{n}_{s,6\dot{k}+3} \cos\left[(6\dot{k}+3)(p\varphi - \tfrac{4\pi}{3})\right]$$
$$\qquad (3.16c)$$

3.7.5   The mechanical construction

The machine and flywheel is mechanically constructed as shown in Figure 3.9, an axial cross section of the complete flywheel and electrical machine. The containment unit, flywheel, rotor, stator and the bearing unit are clearly shown.

3.7.6   The permanent-magnet array

In the 1980s, K. Halbach [Hal80], [Hal85] described a new approach for obtaining certain specified magnetization patterns with permanent magnets. The magnetic structures resulting from his work soon became known as Halbach arrays. These structures were first developed as elements in particle accelerators and advanced synchrotron light sources, but their potential for use in permanent-magnet machines was soon realized. See, among others, Marinescu and Marinescu [Mar92] and Trumper *et al.* [Tru93].

Figure 3.10 shows three different permanent-magnet arrays in linear form. The darker coloured region depicts the rotor iron and the lighter coloured region the permanent magnets; the arrows indicate the direction of magnetization. Figure 3.10(a) shows a standard radial array with a 100% magnet span for illustrative purposes. By

- Containment unit
- Carbon fibre flywheel
- Rotor
- Stator
- Bearing unit
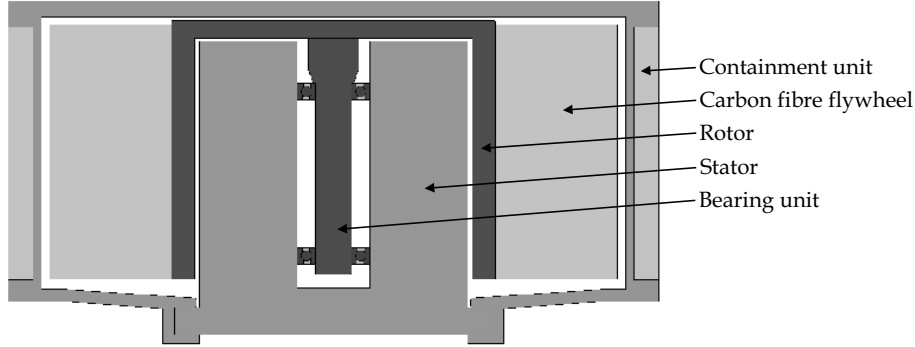
Figure 3.9: An axial cross section of the complete flywheel and electrical machine.

dividing every magnet into two equal parts and rotating every second magnet clockwise by 90°, the discrete Halbach array with two segments per pole of Figure 3.10(b) is obtained. Dividing each of these magnets in half again and rotating magnet numbers 2, 4, 6, ··· clockwise by 45°, the discrete Halbach array with four segments per pole of Figure 3.10(c) is obtained.

Halbach arrays with a different number of segments per pole, including uneven numbers like 3 or 5, are obtained in a similar manner as the above. Continuing the magnet dividing and rotating procedure *ad infinitum* so that there are an infinite number of segments per pole, the ideal Halbach array is obtained. This array has an ideal sinusoidally rotating magnetization vector [Ata97].

Halbach arrays result in a higher flux density in the air gap than standard radial arrays [Mar92], [Tru93], [Ata97]. This may potentially increase the torque & power density of the machine, and was therefore worth investigating for this project. For the thesis, three permanent-magnet arrays were investigated: the conventional radial array, a discrete Halbach array with two segments per pole, and an ideal Halbach array as a theoretical limit.

Traditionally, in Halbach arrays, the polar magnet spans are adjusted so that each magnet takes up equal space. Therefore, a discrete Halbach array with two segments per pole will customarily have radial magnets filling up 50% of the circumference, and tangential magnets filling up the other 50%.

The 80/20 discrete Halbach array investigated in this thesis is formed by making the span of the radial magnets such that they fill 80% of the circumference; the remaining 20% is used for the tangentially magnetized magnets, appropriately oriented for flux concentration on the inside of the array. In Chapter 8, the effect of varying the pole arc in the radial and discrete Halbach arrays will be investigated. For the discrete Halbach array with two segments per pole, the variation in pole arc corresponds to a variation of the 80/20 ratio introduced here.
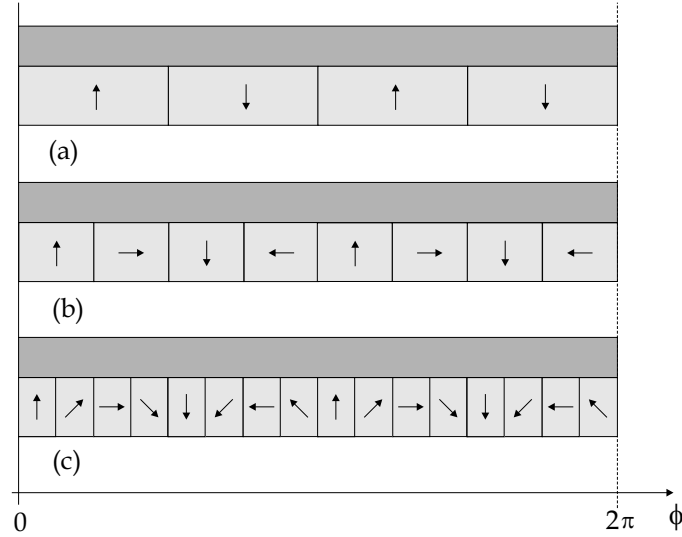
Figure 3.10: Cartesian versions of three different permanent-magnet arrays.

3.8 Summary

In this chapter, flywheel energy storage systems were discussed with the aim of maximizing their power delivery capability. Two of the most important drive system topologies were discussed in Section 3.2, followed by possible power converters (Section 3.3) and electrical machines (Section 3.6). It was mentioned in Section 3.4 that the energy storage capacity of a flywheel energy storage system is mainly limited by the mechanical properties and the construction of the flywheel itself, while the power delivery capability is limited mainly by the power electronics and electrical machine design.

Section 3.5 stated that the rest of this thesis focusses on the electrical machine design of such a system, after which Section 3.6 briefly investigated the machine type options.

Section 3.7 introduced the EμFER flywheel energy storage system, focusing on its electrical machine. The requirements of the EμFER machine discussed in Section 3.6 were realized into the chosen machine type and topology: an external rotor, radial flux PMSM with a shielding cylinder. A mathematical description of the winding distribution, which will be used in the rest of the thesis, was introduced. Section 3.7 also showed an axial cross section of the flywheel and electrical machine, showing the construction clearly. Section 3.7 closed by motivating the investigation of Halbach arrays to potentially increase the power density of the machine. The 80/20 discrete Halbach array with two segments per pole and the ideal Halbach array were also introduced in addition to the customary radial array. They will be extensively investigated in the rest of the thesis. Among other things, Chapter 8 will

take a look at the effects of varying the magnet span ratio of the radial and discrete Halbach arrays.

In the subsection describing the winding mathematically, Section 3.7, it was said that the chosen method of design in this thesis is the use of analytical field calculations. An outline of the analytical method to solve for the magnetic field and other interesting derived quantities will be discussed next in Chapter 4.

Outline of an analytical approach to the design of a slotless PMSM

4.1 Introduction

In the previous chapter, the EμFER machine was introduced for our case study. In the next four chapters, an analytical model will be derived for the design and analysis of PMSMs with air gap windings, including the effect of the eddy currents in the shielding cylinder. The analytical model will be applied to this EμFER machine throughout the course of these chapters. In Chapter 8, the EμFER machine will be optimized with the use of the model derived in Chapters 4 to 7. Also in Chapter 8, the analytical model will be generalized to other machine types and configurations.

In this chapter, the framework for deriving the analytical model is described. The magnetic field, or more specifically, the magnetic vector potential **A**, forms the heart of the analytical model. Together with the material properties, the vector potential contains all the information about the magnetic fields **B** and **H** in all machine regions. All other quantities needed for the machine's design and analysis are derived either directly from **A** or from **B** or **H**.

Section 4.2 starts off the chapter with motivating the choice of analytical field calculations as the design and analysis method instead of another approach like finite elements. In Section 4.3, previous work on analytical field calculations in machines is reviewed from publications found in literature. Section 4.4 discusses the derivation of a model for calculating the magnetic field by solving for the magnetic vector potential. Section 4.5 explains how this magnetic field links with the stator winding to obtain measurable quantities, while Sections 4.6 and 4.7 derive expressions for power and torque from the magnetic field quantities. Section 4.6 discusses how the Poynting vector can be used to calculate electromagnetic power in the air gap, from which mechanical power (torque) and the eddy current losses in the

shielding cylinder can be calculated. Section 4.7 examines another method whereby electromagnetic torque can be calculated: the Lorentz force equation. This simple method may be used to check the more complicated Poynting vector technique. The chapter is summarized in Section 4.8.

4.2   Design methodology: Analytically solving the two-dimensional magnetic field

4.2.1   The analytical method vs the finite element method

In this thesis, the method of analytical field calculations was chosen to design the EµFER machine. The reasons for this choice are as follows:

- *Lower computation time.* The analytical method has the important drawback of a longer initial time requirement compared to the finite element method (FEM). In spite of this longer time initially needed to develop a design and analysis framework for the machine, computation takes a fraction of the time required by the finite element method once an analytical model has been developed.

- *The geometry of the EµFER machine is well suited for an analytical approach.* The machine is cylindrical and it has a large air gap. These facts make it imperative that the behavior of the magnetic field has to be considered in at least the two most important dimensions: radially outward and tangentially. The machine is therefore directly analyzable in cylindrical coordinates, and ideally suited for the analytical method. The machine geometry can be analyzed well with a two-dimensional analytical field approach.

- *The analytical approach gives greater insight into the problem.* In R.L. Stoll's textbook on eddy current analysis [Sto74], the analytical approach is advocated exactly for this reason. Several studies are described in the book where ratios of quantities, for example problem dimensions, are later related to important design outputs. This provides powerful insight into the relationships between quantities, and one can quickly see trends and in such a manner that a deeper understanding of the problem is gained. Such insight is very difficult to obtain with the FEM, since every geometry change demands new meshing, solving and post-processing to take place. This method therefore requires many computations before relationships between quantities and trends can be identified.

For the reasons listed above, the analytical approach was chosen in this thesis.

4.2.2   Two-dimensional field approach

Solving for three-dimensional fields is a very difficult task analytically, and therefore the machine is simplified to the two-dimensional cross section of Figure 3.6.

Neglecting the magnetic field in the third dimension will introduce errors into the analytical model. (For example, the end windings are not included in the model, and they have an effect on the frequency behavior of the main-field inductance.) But as will be shown later, experimental results confirm that these errors are small. This is important to mention since the machine is quite flat with a large air gap and still a 2D-field model adequately describes its behavior.

The 2D-problem is approached with classical layer theory, where the machine is divided into layers or regions of interest. The magnetic field is then solved for each of these regions, from which all other important quantities are obtained. The first step in developing an analytical model for designing a machine such as the one shown in Figure 3.6 is therefore to define the regions of interest.

4.2.3 Definition of machine regions for an analytical approach to its design

In the the rest of this thesis, the stator inner radius r_{si} is set to zero to limit the number of regions in the machine. This is no problem as long as the stator iron does not saturate in the physical machine, since it is assumed that the permeability of the stator and rotor iron is infinite. (See the list of assumptions in the next section.)

Figure 4.1 shows a definition of the machine regions defined for the analytical field calculations of this thesis. The eddy currents in the shielding cylinder are included in the calculation, and thus the shielding cylinder is required to be a separate region. In classical layer theory, therefore, the system has six layers as indicated. In the next subsection, the outline of the analytical approach is further developed by introducing the stator and rotor angular coordinate systems.
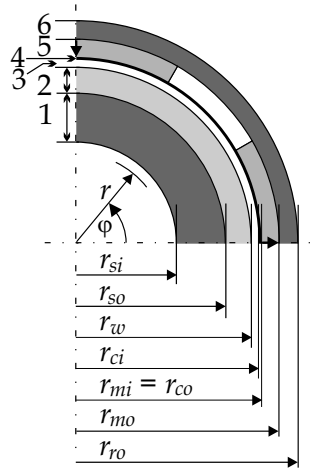
Figure 4.1: A quarter cross section of the flywheel machine for the analytical calculation of the magnetic field, showing the six defined layers.

4.2.4   The stator and rotor angular coordinate systems

In any PMSM, two reference systems can be identified: a stationary one fixed to the stator, and a rotary one fixed to the rotor. The former is generally called the *abc* system, and the latter the *dq*-system. Figure 4.2 shows the definitions of the reference systems and angular coordinates of the stator and rotor used in the rest of this thesis.

The stator angular coordinate is introduced as φ, measured from the *a*-axis in the *abc*-reference system of the stator, as shown in Figures 4.2(a) and (d). Figures 4.2(b) and (e) show the same angle φ, now in the semi-four-phase $\alpha\beta$-system obtained by the Clarke transformation $\boldsymbol{C}_{23}$.

The rotor angular coordinate ϕ, measured from the *d*-axis in the *dq*-system fixed to the rotor, is shown in Figures 4.2(c) and (f). Variables in the *abc*-system can be transformed into the *dq*-system by first doing the Clarke transformation and then rotating the result by the rotor positional angle by means of a rotation matrix $-\boldsymbol{C}_{rot}(p\theta)$. The combination of these two transformations is known as the Park transformation $\boldsymbol{C}_{23,rot}(p\theta)$.

The rotor positional angle θ is introduced as the angle between the *dq*- and *abc*- or $\alpha\beta$-systems as:

$$\theta \equiv \varphi - \phi, \tag{4.1}$$

as can be seen from Figures 4.2(c) and (f). The *dq*-system rotates at a mechanical angular velocity of ω_m with respect to the *abc*- or $\alpha\beta$-systems, or:

$$\theta(t) = \int \omega_m \, dt + \theta_0/k = \omega_m t + \theta_0/k, \tag{4.2}$$

where θ_0 is the initial rotor position.

Figure 4.2 also shows the effect of the number of pole pairs on the reference systems and the angular coordinates. This effect can be seen by comparing the difference in Figures 4.2(a)–(c) and Figures 4.2(d)–(f). The former is drawn for a three-phase, two-pole machine and the latter for a three-phase, four-pole machine. It can be clearly seen that by doubling the number of poles, the angles between the axes of all the reference systems are halved (in mechanical radians). However, considering the angles to be measured in electrical radians, i.e. by multiplying all angular variables by the pole-pair number p, this effect disappears. Therefore, if φ, ϕ, θ and ω_m is replaced by $p\varphi$, $p\phi$, $p\theta$ and $p\omega_m$ respectively, Figures 4.2(a)–(c) stay valid for all p. Also, equations (4.1) and (4.2) stay valid for all p. This is the convention that will be followed in the rest of this thesis.

4.3   Literature review of 2D magnetic field calculations

Analytical field calculations are not new. In fact, the 2D-solution to Poisson's equation has been known since early in the previous century [Hag29]. However, since the availability of high energy product rare-earth permanent magnets like Samarium Cobalt (SmCo) in the 1970s and Neodymium Iron Boron (NdFeB) in the 1980s, the
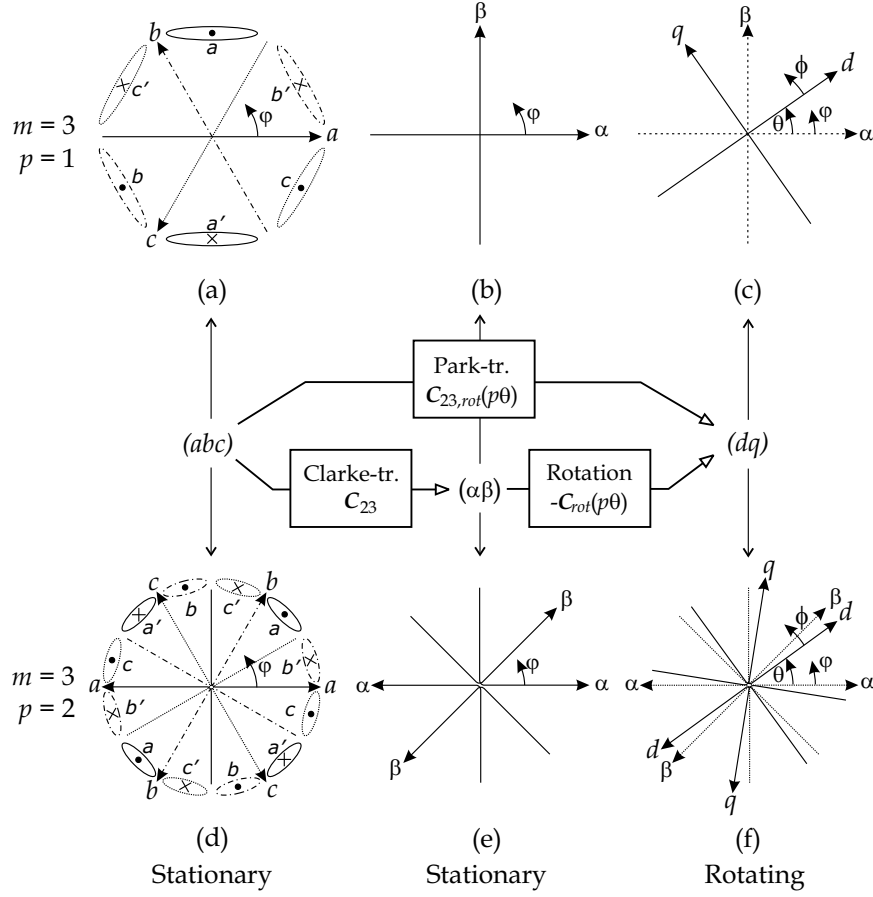
Figure 4.2: The different reference systems in the machine.

analytical calculation of the magnetic field in permanent-magnet-excited machines has received renewed interest in recent literature. Before these magnets were in use in machines, the air gaps were small and one-dimensional field calculations were adequate. These rare-earth permanent magnets resulted in larger useable air gaps since their coercive force is so high. These large air gaps resulted in curvature effects of the field and therefore one-dimensional analysis was no longer adequate.

For recent literature see, for example, [Bou84], [Wat92], [Zhu93a], [Kim98a], [Pol98], [Mos98a], [Ras00] and [Zhi00] for a description of the analytical calculation of the 2D **B**-field in permanent magnet machines in cylindrical coordinates due to radially magnetized permanent magnets, and [Mos98b] in Cartesian coordinates. In [Bou84], [Mos98a], [Mos98b] and [Ras00], equivalent surface current densities are used to replace the permanent magnets, while in [Wat92], [Zhu93a], [Kim98a] and [Pol98] the magnetization is used directly.

In [Zhu93a], the permanent magnets are considered to be surface mounted, as in [Bou84], [Wat92], [Kim98a], [Mos98a], [Mos98b], [Ras00] and [Pol98]. [Zhu93a] is the first part of a four-part series devoted to the analytical calculation of magnetic fields in permanent magnet machines. As already mentioned, the first part describes the field due to the magnets. The other three parts consider the magnetic field due to the stator currents [Zhu93b], the effects of stator slotting on the field [Zhu93c], and the combination of fields due to the magnets and stator currents, resulting in the field in a loaded machine [Zhu93d]. In [Zhu94], Zhu *et al.* further develops their analytical model to predict the magnetic field due to inset magnets. In [Zhu02], several improvements on [Zhu93a] are documented: internal and external rotors are now included in their model, as well as both radial and parallel magnetization. (The field due to both radial and parallel magnetization has also been solved in [Bou84].)

Watterson *et al.* developed an analytical field calculation model specifically as an optimization tool for a machine with a solid permanent-magnet rotor and slotless stator [Wat92]. Kim *et al.* discussed the solution of the 2D-magnetic field in cylindrical coordinates in a machine with rotor eccentricity in [Kim98a]. In [Kim98b], they included the stator slotting effect on the field in the model. Zhilichev [Zhi00] combines analytical field calculations with corrections from the finite element method where necessary, resulting in a hybrid method. Both slotless and slotted stators are included, although the emphasis is on the treatment of the slots. In this thesis, the effect of stator slotting on the field is of no importance since the case-study machine introduced in Chapter 3 is slotless.

In [Bou84], [Zhu93a]—[Zhu93d], [Zhu94], [Kim98b], [Zhi00] and [Zhu02], the magnetic scalar potential is used to obtain the magnetic field of the magnets, while in [Wat92], [Pol98], [Mos98a] and [Mos98b], the magnetic vector potential is used. In [Ras00], a combination of both approaches is used. In this thesis, the vector potential approach is used, and the motivation for this choice is discussed in the next section.

4.4   Derivation of a calculation model for the magnetic field

4.4.1   Motivation for the use of the magnetic vector potential

One tool in the analysis and design of a permanent-magnet machine is to be able to predict the magnetic flux density **B** and field intensity **H** due to the various field sources in all the machine regions.

Vector fields, like **B** and **H**, are position dependant. With every such field a potential may be associated, where the field relates to the potential and some combination of its positional derivatives. Depending on the nature of the vector field, this potential can either be a scalar potential or a vector potential.

A vector field can either be solenoidal, or irrotational, or both. A vector field **X**

is said to be solenoidal if:

$$\nabla \cdot \mathbf{X} = 0, \tag{4.3}$$

and irrotational if:

$$\nabla \times \mathbf{X} = \mathbf{0}. \tag{4.4}$$

Solenoidal vector fields may be represented by a vector potential, and irrotational vector fields by a scalar potential [Hau89], [Ham99].

The relationships between magnetic fields and the potentials associated with them are listed in Table 4.1. In Table 4.1 one can see that it is straightforward to obtain the vector field once its associated potential has been obtained.

Ampère's Law ($\nabla \times \mathbf{H} = \mathbf{J}$) shows that $\mathbf{H}$ is only irrotational in regions where there is no current density. However, it is possible to use the magnetic scalar potential in regions where a non-zero current density exists by introducing the electric vector potential $\mathbf{T}$ [Ham99]. This potential is defined by rewriting Ampères Law as follows:

$$\nabla \times (\mathbf{H} - \mathbf{T}) = \mathbf{0}, \tag{4.5}$$

where the electric vector potential $\mathbf{T}$ is defined implicitly by:

$$\mathbf{J} \equiv \nabla \times \mathbf{T}, \tag{4.6}$$

similar to the definition of the magnetic vector potential. By introducing the electric vector potential, the condition for obtaining the magnetic field in all regions therefore changes from $\mathbf{J} = \mathbf{0}$ to $\nabla \cdot \mathbf{J} = \mathbf{0}$, which is not a severely restricting constraint. The magnetic flux density $\mathbf{B}$ is always solenoidal, for all $\mathbf{J}$, due to the law of conservation of magnetic flux ($\nabla \cdot \mathbf{B} = 0$).

Choosing whether to use the magnetic scalar or vector potential to solve for the field thus reduces to imposing a non-limiting constraint upon $\mathbf{J}$ or no constraint at all. Either choice will lead to good results, as shown in literature. In this thesis, however, the magnetic vector potential is chosen. Later in this chapter it will be shown that the machine inductances and other parameters can be obtained from the vector potential directly, thereby further motivating this choice. Before discussing the derivation of the vector form of Poisson's equation, we first list the assumptions made in the rest of the thesis in the next subsection.

Vector field	Associated scalar potential	Associated vector potential	Relationship	Condition
$\mathbf{H}$	V_m	–	$\mathbf{H} = -\nabla V_m$	if $\mathbf{J} = \mathbf{0}$
$\mathbf{H} - \mathbf{T}$	V_m	–	$\mathbf{H} - \mathbf{T} = -\nabla V_m$	if $\nabla \cdot \mathbf{J} = 0$
$\mathbf{B}$	–	$\mathbf{A}$	$\mathbf{B} = \nabla \times \mathbf{A}$	none

Table 4.1: Relationship between potentials and magnetic fields.

4.4.2 List of assumptions

In the rest of the work presented in this thesis, the following assumptions were made:

1. linearity, i.e., the vector potentials of different sources may simply be added together algebraically: $\mathbf{A}_{total} = \mathbf{A}_{magnets} + \mathbf{A}_{stator\ currents}$;

2. symmetry, i.e., $\mathbf{A}(r, \varphi) = -\mathbf{A}(r, \varphi + \frac{\pi}{p})$;

3. the relative permeability of the stator and rotor iron is infinite, i.e., it does not saturate;

4. the relative permeability of all non-iron parts (the winding, shielding cylinder and the magnets) is equal to 1;

5. the magnets do not demagnetize; and

6. all materials are isotropic.

4.4.3 Derivation of the vector form of Poisson's equation

As shown in Section 4.4.1, since $\mathbf{B}$ is always solenoidal, finding $\mathbf{B}$ is equivalent to finding the vector potential $\mathbf{A}$. This section is therefore dedicated to the derivation of the vector form of Poisson's equation in order to find $\mathbf{A}$.

In Appendix B, the equations of Maxwell are listed for stationary media. In Section B.3, the field equation for the magnetoquasistatic (MQS) approximation is listed as:

$$-\nabla \times \mathbf{H} + \mathbf{J} = -\mathbf{J}_{ext}, \tag{4.7a}$$

$$\nabla \times \mathbf{E} + \frac{\partial \mathbf{B}}{\partial t} = \mathbf{0}, \tag{4.7b}$$

$$\nabla \cdot \mathbf{J}_{ext} = 0, \tag{4.7c}$$

and

$$\nabla \cdot \mathbf{B} = 0. \tag{4.7d}$$

The static part is given by (4.7a) and the dynamic part by (4.7b).

The constitutive relations for a linear isotropic medium are:

$$\mathbf{J} = \sigma \mathbf{E}, \tag{4.8a}$$

which is Ohm's Law, and

$$\mathbf{B} = \mu \mathbf{H} + \mathbf{B}_{rem}, \tag{4.8b}$$

where σ is the conductivity, μ the permeability and $\mathbf{B}_{rem}$ the remanent flux density of the material, respectively.

By use of (4.8b), Ampère's Law (equation (4.7a)) can be rewritten as:

$$\nabla \times \mathbf{H} = \mathbf{J} + \mathbf{J}_{ext}$$

$$\nabla \times \left[\frac{1}{\mu} \left(\mathbf{B} - \mathbf{B}_{rem} \right) \right] = \mathbf{J} + \mathbf{J}_{ext} \tag{4.9}$$

$$\nabla \times \mathbf{B} = \mu \mathbf{J} + \mu \mathbf{J}_{ext} + \nabla \times \mathbf{B}_{rem}.$$

Since **B** is solenoidal from (4.7d), it can be written in terms of the vector potential as:

$$\mathbf{B} = \nabla \times \mathbf{A}. \tag{4.10}$$

Substituting this into (4.9), one obtains:

$$\nabla \times (\nabla \times \mathbf{A}) = \mu \mathbf{J} + \mu \mathbf{J}_{ext} + \nabla \times \mathbf{B}_{rem}. \tag{4.11}$$

The left-hand side of this equation can be rewritten from the vector identity as:

$$\nabla \times (\nabla \times \mathbf{A}) = \nabla (\nabla \cdot \mathbf{A}) - \nabla^2 \mathbf{A}. \tag{4.12}$$

By choosing the Gaussian gauge:

$$\nabla \cdot \mathbf{A} = 0, \tag{4.13}$$

and using (4.12), equation (4.11) is rewritten as:

$$-\nabla^2 \mathbf{A} = \mu \mathbf{J} + \mu \mathbf{J}_{ext} + \nabla \times \mathbf{B}_{rem}. \tag{4.14}$$

The final step is to substitute the constitutive relation (4.8a) in conjunction with:

$$\mathbf{E} = -\frac{\partial \mathbf{A}}{\partial t} \tag{4.15}$$

into (4.14). This results in:

$$-\nabla^2 \mathbf{A} + \mu \sigma \frac{\partial \mathbf{A}}{\partial t} = \mu \mathbf{J}_s + \nabla \times \mathbf{B}_{rem}, \tag{4.16}$$

where the external current density $\mathbf{J}_{ext}$ has been replaced by the stator current density $\mathbf{J}_s$.

Equation (4.16) stands central in this thesis. This is because it relates the vector potential (including the eddy-current effects on it) to the two main field sources in the machine: the permanent-magnet array described by $\mathbf{B}_{rem}$, and the stator current density described by $\mathbf{J}_s$.

In Chapter 5, the Poisson equation (4.16) will be used to derive **A** due to the three permanent-magnet arrays: (i) the radial array; (ii) the discrete Halbach array with two segments per pole; and (iii) the ideal Halbach array. In Chapter 5, eddy current effects upon **A** are neglected, and therefore Poisson's equation for magnetoquasistatic fields with $\partial \mathbf{A}/\partial t = \mathbf{0}$ is used since it is assumed that the shielding

cylinder shields the magnets and therefore no eddy currents can flow in them. The stator current density is also set equal to zero in Chapter 5, thereby simplifying (4.16) to:

$$-\nabla^2 \mathbf{A} = \nabla \times \mathbf{B}_{rem}, \tag{4.17}$$

where the right-hand side is only nonzero in the magnet regions.

Chapter 6 investigates the field due to the stator currents, including the influence of the reaction field of the eddy currents in the shielding cylinder. In this case, equation (4.16) simplifies to:

$$-\nabla^2 \mathbf{A} + \mu\sigma\frac{\partial \mathbf{A}}{\partial t} = \mu\mathbf{J}_s, \tag{4.18}$$

where $\mathbf{J}_s$ is only nonzero in the stator current region and $\mu\sigma\partial\mathbf{A}/\partial t$ is only nonzero in the shielding cylinder region.

In order to solve for $\mathbf{A}$ from equation (4.16), we set up boundary value problems by writing boundary condition equations for the layers shown in Figure 4.1. In writing these equations, it is recognized that the only two relevant boundary conditions are those implied by Ampère's Law and the flux conservation law. These boundary conditions are discussed next.

4.4.4   Boundary conditions

The boundary condition implied by Ampère's Law (4.7a) states that the tangential component of the magnetic field intensity on one side of the boundary is equal to that of the other side plus a surface current density, or mathematically [Hau89]:

$$\hat{\mathbf{n}} \times \left(\mathbf{H}^{(\nu)} - \mathbf{H}^{(\nu+1)} \right) = \mathbf{K}^{(\nu)}, \tag{4.19}$$

where $\hat{\mathbf{n}}$ is the unit normal vector, $\mathbf{H}^{(\nu)}$ denotes the magnetic field intensity in region ν and $\mathbf{K}^{(\nu)}$ the surface current density at the boundary interface between regions ν and $\nu + 1$.

The boundary condition implied by the magnetic flux conservation law (4.7d) states that the normal component of the flux density on one side of a region boundary is equal to that on the other, or mathematically:

$$\hat{\mathbf{n}} \cdot (\mathbf{B}^{(\nu)} - \mathbf{B}^{(\nu+1)}) = 0. \tag{4.20}$$

4.4.5   Poisson's equation in cylindrical coordinates for two-dimensional magnetic fields

Due to the geometry of the machine, as shown in cross-sectional form in Figure 4.1, the most appropriate coordinate system within which to solve for $\mathbf{A}$ is clearly the circular cylindrical coordinate system, hereafter simply called the cylindrical coordinate system. Although this coordinate system is three dimensional with coordinates

r, ϕ and z, a two-dimensional simplification of the magnetic field in the machine is used in this thesis. This two-dimensional simplification of the magnetic field implies that:

7. the vector potential has only a z-component; and

8. it is dependent on only r and ϕ,

which has been added to the list of assumptions in Section 4.4.2.

From the above two assumptions, the vector potential can be written as:

$$\mathbf{A}(r,\phi) = A_z(r,\phi)\hat{\mathbf{i}}_z, \tag{4.21}$$

which, from (4.10), results in the following expression for the flux density:

$$\mathbf{B}(r,\phi) = B_r(r,\phi)\hat{\mathbf{i}}_r + B_\phi(r,\phi)\hat{\mathbf{i}}_\phi. \tag{4.22}$$

From (4.22) and (4.21), the relationship between the magnetic vector potential and the magnetic flux density (4.10) becomes:

$$B_r\hat{\mathbf{i}}_r + B_\phi\hat{\mathbf{i}}_\phi = \frac{1}{r}\frac{\partial A_z}{\partial \phi}\hat{\mathbf{i}}_r - \frac{\partial A_z}{\partial r}\hat{\mathbf{i}}_\phi. \tag{4.23}$$

Also from (4.22) and (4.21), the Poisson equation (4.16) is significantly simplified to:

$$\frac{\partial^2 A_z}{\partial r^2} + \frac{1}{r^2}\frac{\partial^2 A_z}{\partial \phi^2} + \frac{1}{r}\frac{\partial A_z}{\partial r} + \mu\sigma\frac{\partial A_z}{\partial t} = -\mu J_{s,z} - \frac{B_{rem,\phi}}{r} - \frac{\partial B_{rem,\phi}}{\partial r} + \frac{1}{r}\frac{\partial B_{rem,r}}{\partial \phi}. \tag{4.24}$$

In Chapters 5 and 6, this partial differential equation will be solved in the simplified forms of (4.17) for Chapter 5 and (4.18) for Chapter 6.

We have now outlined a method to obtain the 2D-magnetic field in the machine in cylindrical coordinates due to the two main field sources. In order for this magnetic field to do useful work, it must link with the stator winding. This flux linkage is the next subject of attention.

4.5 From magnetic field to linked flux

4.5.1 General definition

The amount of magnetic flux linking with a coil is called the flux linkage, and defined as:

$$\lambda \equiv \iint\limits_{S} \mathbf{B} \cdot d\mathbf{a}, \tag{4.25}$$

where $\mathbf{B}$ is the density of the magnetic flux linking with a coil formed by the surface of integration S.

As shown in [Hau89], [Pol97] and [Gie97], by the use of Stokes' Integral Theorem, one can obtain the flux linkage of a coil directly from the magnetic vector potential. From (4.10), (4.25) and Stoke's Integral Theorem, we may write for the flux linkage:

$$\lambda = \iint\limits_S \mathbf{B} \cdot d\mathbf{a} = \iint\limits_S \nabla \times \mathbf{A} \cdot d\mathbf{a} = \oint\limits_C \mathbf{A} \cdot d\mathbf{s}, \qquad (4.26)$$

where C is the closed contour forming a boundary for S, i.e., the contour C follows along the conductor making up the coil.

Figure 4.3 depicts an integration surface S and its bounding curve C to evaluate (4.26) on the stator surface of an external rotor four-pole machine, as introduced in Chapter 3. In Figure 4.3, the curve C is formed by a single full-pitch turn, i.e., from $\varphi = 0$ to $\varphi = \pi/2$ rad, although for illustrative purposes, any angle would suffice. The curve C is made up of four parts: C_{xy1}, C_{z1}, C_{xy2} and C_{z2}.

Since the vector potential was assumed to have only a z-component and to be independent of z, or $\mathbf{A} = A_z(r, \varphi)\hat{\mathbf{i}}_z$, the following two remarks regarding the contour integral are made:

- $\mathbf{A}$ has no r- or φ-components. Therefore, the contour integrals along C_{xy1} and C_{xy2} in the XY-plane are zero:

$$\int\limits_{C_{xy1}} \mathbf{A} \cdot d\mathbf{s} = \int\limits_{C_{xy2}} \mathbf{A} \cdot d\mathbf{s} = 0; \qquad (4.27)$$

- $\mathbf{A}$ is constant in the Z-direction. Therefore, the contour integrals along C_{z1} and C_{z2} are equal to the value at that particular value of r and φ, times l_s, the stator
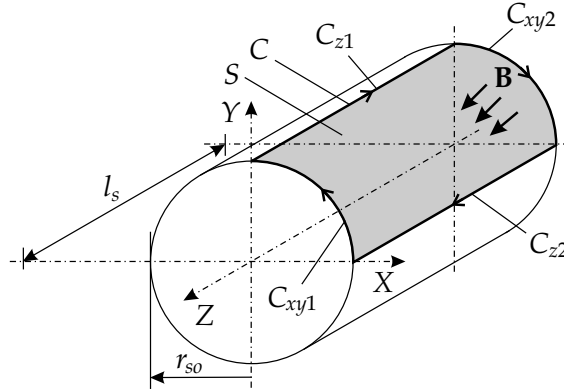
Figure 4.3: Contour integral for calculating the flux linked with a single full-pitch turn on the stator surface of an external rotor PMSM.

axial length (stack length), or:

$$\int_{C_{z1}} \mathbf{A} \cdot d\mathbf{s} = -l_s A_z \left(r, \varphi + \tfrac{\pi}{p} \right) = \int_{C_{z2}} \mathbf{A} \cdot d\mathbf{s} = l_s A_z(r, \varphi), \qquad (4.28)$$

where Assumption 2 (symmetry) of Section 4.4.2 has been used.

From (4.26), (4.27) and (4.28), the total flux linked by a full-pitch turn at a radius r and angle φ is simply:

$$\lambda_t(r, \varphi) = 2l_s A_z(r, \varphi). \qquad (4.29)$$

Since the cylinder in Figure 4.3 represents the stator iron of the machine introduced in Chapter 3, the flux linking with the contour C in the figure is $\lambda_t(r_s, 0)$.

4.5.2 Possible flux linkages

The magnetic field caused by permanent-magnet excitation in a PMSM needs to interact, or link, with the stator winding if useful energy is to be transferred. Similarly, the flux due to the currents flowing in the stator winding also links with the winding itself. Furthermore, eddy currents are induced in the shielding cylinder due to high-frequency magnetic fields originating from the stator currents. These currents in the shielding cylinder also link with the stator winding, and in [Pol98] this is treated explicitly by modelling the shielding cylinder as an infinite series of "windings". In this thesis, the magnetic field due to the stator currents includes the effect of the reaction field due to the induced eddy currents in the shielding cylinder. Therefore, it is unnecessary to model the flux linkage of the shielding cylinder explicitly. This is also true of the flux linkage of the stator winding due to the currents in the shielding cylinder, since it is already included in the field due to the stator currents.

In Chapter 5, the magnetic field due to the permanent magnets is discussed, including other important quantities derived from this field. One of these is the flux linkage of the stator winding due to the permanent magnets: from it, the no-load voltage of the machine can be calculated.

An important quantity derived from the flux linkage of the stator winding due to the currents in itself is the stator main-field self-inductance. The calculation of this inductance is discussed in Chapter 6.

4.6 The Poynting vector

4.6.1 Introduction

In Appendix B, the Theorem of Poynting is given and worked out for rotating systems. This theorem may be used to relate the power density in the air gap of a machine to various components, i.e., dissipated and mechanical components.

The Poynting vector in the frequency domain is defined as:

$$\hat{\mathbf{S}} \equiv \tfrac{1}{2} \left(\hat{\mathbf{E}} \times \hat{\mathbf{H}}^* \right) \quad [\text{W/m}^2], \qquad (4.30)$$

where the real-valued vector $\mathbf{E}$ may be written in terms of $\hat{\mathbf{E}}$ and its complex conjugate $\hat{\mathbf{E}}^*$ as:

$$\mathbf{E} = \mathrm{Re}\left\{\hat{\mathbf{E}}e^{j\omega t}\right\} = \tfrac{1}{2}\left(\hat{\mathbf{E}}e^{j\omega t} + \hat{\mathbf{E}}^* e^{-j\omega t}\right). \tag{4.31}$$

A similar expression as (4.31) is valid for the relationship between $\mathbf{H}$ and $\hat{\mathbf{H}}$ and other real-valued and complex-valued vectors, including the Poynting vector of (4.30).

When the rotor rotates, the stator "observes" the fields differently than the rotor does and vice versa. A way is thus needed to describe the electromagnetic problem in the rotor coordinate system as well as in the stator coordinate system. Such a method may be obtained by using results from the theory of special relativity introduced by Einstein. When using these results, the Theorem of Poynting may be written in two coordinate systems [Blo75]: the so-called R-system (the rotor) and the L-system (the stator). The R stands for "rest" and indicates that the R-system is in rest with respect to the matter that is moving; in our case, the rotor. The L-system stands still (i.e. the stator) and observes the matter and consequentially the R-system as moving with respect to itself.

One requirement of the theory of special relativity is that the velocity must be constant. In rotational systems, this is not the case since the direction changes. With circumferential velocities small in relation to the speed of light in vacuum, however, the approximation of constant velocity holds [Bla73], [Shi73].

4.6.2   The Theorem of Poynting

Integral form in the frequency domain: R-system

This section actually does not list the Theorem of Poynting, but the more useful conservation of energy relation derived from it. (See Appendix B for more information.) Quantities in the R-system are indicated by placing primes on the symbols; for example, $\hat{\mathbf{S}}$ in the L-system becomes $\hat{\mathbf{S}}'$ in the R-system.

In the R-system, i.e., in rotor coordinates, this is in integral form in the frequency domain:

$$-\mathrm{Re}\left\{\oint_S \hat{\mathbf{S}}' \cdot d\mathbf{a}\right\} - \tfrac{1}{2}\mathrm{Re}\left\{\int_V \sigma\hat{\mathbf{E}}' \cdot \hat{\mathbf{E}}'^* \, dv\right\} = \tfrac{1}{2}\mathrm{Re}\left\{\int_V \hat{\mathbf{E}}' \cdot \hat{\mathbf{J}}'^*_{ext} \, dv\right\}, \tag{4.32}$$

where S is the bounding surface of V, i.e. $S = \partial V$, and $\hat{\mathbf{J}}'_{ext}$ is the external current density. (The external current density is external to the volume V.)

In rotor coordinates, we have therefore:

$$\langle P'_{source}\rangle - \langle P'_{diss,sc}\rangle = \langle P'_{ext}\rangle, \tag{4.33}$$

meaning that the average air gap power minus the power dissipated in the shielding cylinder is equal to the average power passing through the surface S.

Integral form in the frequency domain: *L*-system

The conservation of energy in the frequency domain in the *L*-system is:

$$
- \operatorname{Re} \left\{ \oint_S \hat{\mathbf{S}} \cdot d\mathbf{a} \right\} - \tfrac{1}{2}\operatorname{Re} \left\{ \int_V \hat{\mathbf{H}} \cdot j\omega \mathbf{B}_{rem} \, dv \right\} - \tfrac{1}{2}\operatorname{Re} \left\{ \int_V \sigma \hat{\mathbf{E}} \cdot \hat{\mathbf{E}}^* \, dv \right\}
$$

$$
- \tfrac{1}{2}\operatorname{Re} \left\{ \int_V (\sigma \mu \mathbf{v}_c \times \hat{\mathbf{H}}) \cdot \hat{\mathbf{E}}^* \, dv \right\} = \tfrac{1}{2}\operatorname{Re} \left\{ \int_V \hat{\mathbf{E}} \cdot \hat{\mathbf{J}}_{ext}^* \, dv \right\}. \quad (4.34)
$$

In stator coordinates, we have therefore:

$$
\langle P_{source} \rangle - \langle P_{mech} \rangle - \langle P_{diss,sc} \rangle - \langle P_{mech,sc} \rangle = \langle P_{ext} \rangle. \quad (4.35)
$$

One can see from a comparison of (4.33) and (4.35) that there are more power terms in stator coordinates. The reason why this is so is explained in Chapter 7 and Appendix B; the former explains the existence of more power terms by investigating the combination of space and time harmonic components and the latter by deriving them from the field equations.

4.6.3   The placement of the integration surface *S*

It is obvious that the placement of the integration surface *S* is a very important aspect of the problem of calculating power balances in the machine. The integration surface *S* has the form of a cylinder, very similar to the shaded area in Figure 4.3. The difference with Figure 4.3 is that the shaded area in the case of the surface integral of the Poynting vector spans the whole circumference: it calculates the power moving through the entire surface.

In this thesis, the surface is located at two different places:

- Firstly, in the derivation of the power balances in Appendix B, the surface is placed *just outside the magnets*. The reason for this is that if we go further outwards, the permeability becomes infinite per definition and the Poynting Theorem as listed in (4.32) and (4.34) is no longer valid.[1]

  When the surface is located just outside the magnets, the external power is zero (in both the *L*- and *R*-systems.) For the *R*-system, this means that the air gap power is equal to the dissipated power in the shielding cylinder; see (B.47). For the *L*-system, apart from the dissipated power in the shielding cylinder there is also a mechanical power component delivered to the cylinder and one delivered to the permanent magnets; see (B.48).

- In the rest of the thesis, the integration surface *S* is placed in the centre of the air gap. This makes $\sigma = 0$ inside the integration volume of equations (4.32) and

---

[1]Another term should be added in this case; see equation (B.33) in Appendix B.

(4.34), and the remanence zero in (4.34). The power balances (4.33) and (4.35) therefore simply become:

$$\langle P_{source} \rangle = \langle P_{ext} \rangle. \tag{4.36}$$

The above discussion leads to the following very important conclusions for the calculation of the air gap power (the integration surface S is in the center of the air gap).

- In rotor coordinates, the air gap power is:

$$\langle P'_{source} \rangle = \langle P'_{diss,sc} \rangle, \tag{4.37}$$

- and in stator coordinates, the air gap power is:

$$\langle P_{source} \rangle = \langle P_{mech} \rangle + \langle P_{diss,sc} \rangle + \langle P_{mech,sc} \rangle. \tag{4.38}$$

Finding the above power components is thus equal to finding the source power flowing from the stator to the rotor through the air gap. This is simply the real part of the closed surface integral of the complex Poynting vector:

$$\langle P_{source} \rangle = -\text{Re} \left\{ \oint_S \hat{\mathbf{S}} \cdot d\mathbf{a} \right\}. \tag{4.39}$$

Obtaining $\langle P'_{source} \rangle$ is similar to (4.39), but with $\hat{\mathbf{S}}$ replaced by $\hat{\mathbf{S}}'$. Chapter 7 will show that $\langle P'_{diss,sc} \rangle = \langle P_{diss,sc} \rangle$.

In the thesis, therefore, the air gap power is calculated directly from the Poynting vector as in (4.39). The breakup into mechanical and loss components is found by interpretation, not calculation. The next section discusses the calculation of (4.39).

4.6.4   Application to the two-dimensional magnetic field

It is assumed in this thesis that the magnetic field **H** has only r- and ϕ-components, as can be seen from (4.22). Furthermore, from Faraday's Law (4.7b) and the fact that **A** has only a z-component, the induced electric field also has only a z-component. The Poynting vector can thus be written from (4.30) as:

$$\hat{\mathbf{S}} = \begin{vmatrix} \hat{\mathbf{i}}_r & \hat{\mathbf{i}}_\phi & \hat{\mathbf{i}}_z \\ 0 & 0 & \bar{E}_z \\ \bar{H}_r^* & \bar{H}_\phi^* & 0 \end{vmatrix} = -\bar{E}_z \bar{H}_\phi^* \hat{\mathbf{i}}_r + \bar{E}_z \bar{H}_r^* \hat{\mathbf{i}}_\phi \tag{4.40}$$

Therefore, the Poynting vector in the machine also has only r- and ϕ-components. When one wants to calculate the power that flows from the stator to the rotor (or the other way round), only the radial component plays a role. This follows from the choice that the integration surface S is a cylinder, similar as in Figure 4.3. From

equation (4.39) it then follows that the surface integral is only nonzero for the radial component of $\hat{\mathbf{S}}$.

The closed surface integral of the Poynting vector $\hat{\mathbf{S}}$ in (4.39) is the average power crossing the air gap from the stator to the rotor. It is, from (4.40):

$$- \oint_S \hat{\mathbf{S}} \cdot d\mathbf{a} = -\tfrac{1}{2} \int_0^{l_s} \int_0^{2\pi} (-\bar{E}_z \bar{H}_\phi^*)\, r\, d\phi\, dl = \pi r l_s\, \bar{E}_z \bar{H}_\phi^*, \qquad (4.41)$$

where r is the location of the integration surface S. The most obvious location for S is in the centre of the mechanical air gap, or $r = r_{ag} = (r_w + r_{ci})/2$. In this way, one can calculate the power crossing the air gap from the stator to the rotor.[2] In Chapter 6, the locked rotor machine impedance and the losses in the shielding cylinder will be calculated from (4.41). The electromagnetic torque will also be calculated from (4.41) (in Chapter 7).

4.7 Lorentz force

4.7.1 Definition

Another way[3] to calculate electromagnetic torque is by use of the Lorentz force, which is directly applicable in the EμFER machine since the conductors are situated in the air gap. The Lorentz force is the force experienced by a conductor situated in a magnetic field, and given by:

$$\mathbf{f} = \mathbf{J} \times \mathbf{B}, \qquad (4.42)$$

where $\mathbf{f}$ [N/m^3] is the electromagnetic force density, $\mathbf{J}$ [A/m^2] is the current density and $\mathbf{B}$ [T] the magnetic flux density. The total force $\mathbf{F}$ [N] may be obtained from (4.42) by calculating the integral over the volume, and the electromagnetic torque [Nm] may be obtained from $\mathbf{F}$ by:

$$\mathbf{T} = \mathbf{r} \times \mathbf{F}, \qquad (4.43)$$

where $\mathbf{r}$ is the radial position vector.

The reason for using both the Poynting vector and Lorentz force method is that the latter provides some verification of the former. It was felt that verification is necessary since the use of the Poynting vector, as in this thesis, is not widely found in literature.

---

[2]Equation (4.41) was written in stator coordinates. In rotor coordinates, it has the same form, but all quantities are primed, as shown in the previous section.

[3]There is, of course, other methods to calculate forces and torques; for example, by using the Maxwell stresses. However, this method is more complex than the Lorentz force method, and it leads to the same result: the electromagnetic force, which can then be translated into the torque. Similarly to the Lorentz force method, the Maxwell stress method does not provide any information on dissipated power. Therefore, by using the Poynting vector and the Lorentz force methods, all power components are calculated, and there is no need for another (more complicated) method.

4.7.2   Application to the two-dimensional magnetic field

For the machine under discussion in this thesis, the only component of the stator current density $\mathbf{J}_s$ is the axial or *z*-component $J_{s,z}\hat{\mathbf{i}}_z$. Furthermore, the only two components of the magnetic field due to the permanent magnets are the radial and tangential components $B_r\hat{\mathbf{i}}_r$ and $B_\phi\hat{\mathbf{i}}_\phi$, respectively. From (4.42) this means that the electromagnetic force density $\mathbf{f}$ also has radial and tangential components:

$$\mathbf{f} = f_r\hat{\mathbf{i}}_r + f_\phi\hat{\mathbf{i}}_\phi = -J_{s,z}B_\phi\hat{\mathbf{i}}_r + J_{s,z}B_r\hat{\mathbf{i}}_\phi. \tag{4.44}$$

The only component of $\mathbf{f}$ that contributes to useful torque is obviously $f_\phi\hat{\mathbf{i}}_\phi$. Therefore, the electromagnetic torque of the machine can be written as:

$$T_e = l_s \int\limits_{r_{so}}^{r_w} \int\limits_0^{2\pi} r^2 B_r(r,\phi) J_{s,z}(r,\varphi)\, dr\, d\varphi. \tag{4.45}$$

It should be noted that the magnetic flux density in (4.45) is written in the rotor coordinate system because its source is the permanent magnets, while the current density is written in the stator angular coordinate system. Transforming either one to the other will lead to the same result since the electromagnetic torque on the stator is equal to that on the rotor (see equation (4.1)).

Equation (4.45) will be used in Chapter 7 to obtain the electromagnetic torque of the machine.

4.8   Summary

This chapter outlined the analytical approach to the design and analysis of a slotless PMSM.

The choice of the analytical design methodology was motivated in Section 4.2, while Section 4.3 discussed literature on 2D-field calculations. Section 4.4 showed how to obtain an analytical model for calculating of the magnetic field in the machine, while Section 4.5 explained how this field links with the stator winding

Sections 4.6 and 4.7 discussed two powerful techniques to calculate electromagnetic power in the air gap (the Poynting vector) and electromagnetic torque (the Lorentz force).

The techniques outlined here will be used in detail in Chapters 5, 6 and 7 to obtain the fields and derived quantities of the EμFER machine introduced in Chapter 3.

The assumptions regarding the vector potential and material properties made in this chapter are valid for the remainder of the thesis. They are summarized as:

1. linearity, i.e., the vector potentials of different sources may simply be added together algebraically: $\mathbf{A}_{total} = \mathbf{A}_{magnets} + \mathbf{A}_{stator\ currents}$;

2. symmetry, i.e., $\mathbf{A}(r,\varphi) = -\mathbf{A}(r,\varphi + \frac{\pi}{p})$;

3. the relative permeability of the stator and rotor iron is infinite, i.e., it does not saturate;

4. the relative permeability of all non-iron parts (the winding, shielding cylinder and the magnets) is equal to 1;

5. the magnets do not demagnetize;

6. all materials are isotropic.

7. the vector potential has only a z-component; and

8. the vector potential only depends on r and ϕ.

CHAPTER 5

The field due to the permanent magnets and derived quantities

5.1 Introduction

In Chapter 3, the EμFER case study machine was introduced. Particularly, in Section 3.7.6, different possible permanent-magnet arrays for the excitation field of the machine were mentioned. There it was said that here, three permanent-magnet arrays will be discussed in detail: the radial array, the discrete Halbach array with two segments per pole and the ideal Halbach array.

The analytical method to solve for the magnetic field was motivated in Chapter 4, and in particular, the layer theory approach to solving for the field was mentioned. The six layers identified for this were shown in Figure 4.1, including the eddy current reaction field in the shielding cylinder. For the field due to the magnets, the reaction field is not important since there is no relative movement between the magnets and the shielding cylinder. All space-harmonic field components penetrate the cylinder into the air gap. For this reason, the six layers can be reduced to four, as shown in Figure 5.1. In this chapter, the magnetic field will be calculated for these four regions, and useful quantities derived from this field.

The method for calculating the magnetic field was outlined in Chapter 4, i.e. solving for the magnetic vector potential by means of the vector form of Poisson's equation (4.16). The method to calculate the magnetic field due to the magnets is further refined in Section 5.2, which also describes the form of the solution and a general procedure to solve for any array. In Sections 5.3, 5.4 and 5.5, this general solution is applied and worked out for the three arrays mentioned above. These three sections are preceded by a discussion on changing the value of the remanent flux density of the permanent magnets in the analytical model to conform better to reality (Section 5.2.4). Section 5.6 compares the analytically calculated magnetic field
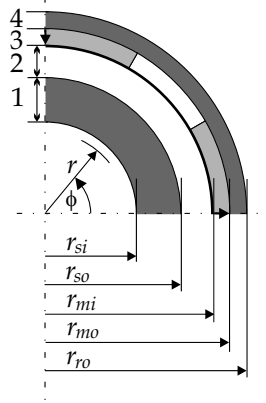
Figure 5.1: A quarter cross section of the flywheel machine for the analytical calculation of the magnetic field due to the permanent magnets, showing the four layers of interest for this case.

of the radial array with a finite element method calculation.

Concerning the derived quantities, Section 5.7 discusses the no-load voltage of the machine from the flux linkage of the stator winding due to the permanent magnets. This is verified experimentally in Section 5.8. Section 5.9 summarizes and concludes the chapter.

5.2 Solution of the magnetic field

5.2.1 Introduction

Chapter 4 showed that the magnetic field can be obtained by solving Poisson's equation (4.16) for the magnetic vector potential **A**. It was also shown that equation (4.16) can be simplified to (4.17) when solving for the field due to the magnets.

By applying the 2D-simplifications listed in Chapter 4 to (4.16), equation (4.24) is obtained. Now by setting to zero the terms $\mu\sigma\frac{\partial A_z}{\partial t}$ and $\mu J_{s,z}$ in (4.24), one obtains:

$$\frac{\partial^2 A_z}{\partial r^2} + \frac{1}{r^2}\frac{\partial^2 A_z}{\partial \phi^2} + \frac{1}{r}\frac{\partial A_z}{\partial r} = -\frac{B_{rem,\phi}}{r} - \frac{\partial B_{rem,\phi}}{\partial r} + \frac{1}{r}\frac{\partial B_{rem,r}}{\partial \phi}. \tag{5.1}$$

This chapter discusses the solution of equation (5.1) for the three permanent-magnet arrays mentioned in the introduction.

Table 5.1 lists the four machine regions, also shown in Figure 5.1, within which is solved for **A**. The regions are denoted by ν and counted from the inside out. The governing equation in each region is also written in its general form in Table 5.1 since

ν	Description	Range for r	$\mu_r^{(\nu)}$	Governing equation
1	Stator iron	$r_{si} \leq r < r_{so}$	$\mu_r^{(1)} = \infty$	$-\nabla^2 \mathbf{A} = \mathbf{0}$
2	Winding region & mechanical air gap	$r_{so} \leq r < r_{mi}$	$\mu_r^{(2)} = 1$	$-\nabla^2 \mathbf{A} = \mathbf{0}$
3	Permanent magnet region	$r_{mi} \leq r < r_{mo}$	$\mu_r^{(3)} = 1$	$-\nabla^2 \mathbf{A} = \nabla \times \mathbf{B}_{rem}$
4	Rotor iron	$r_{mo} \leq r \leq r_{ro}$	$\mu_r^{(4)} = \infty$	$-\nabla^2 \mathbf{A} = \mathbf{0}$

Table 5.1: Machine regions defined for calculating the vector potential from equation (5.1).

it is shorter. The only region where there is a magnetic field source is the permanent-magnet region ($\nu = 3$). In the other three regions, the Poisson equation (5.1) simplifies to the corresponding Laplace equation:

$$\frac{\partial^2 A_z}{\partial r^2} + \frac{1}{r^2}\frac{\partial^2 A_z}{\partial \phi^2} + \frac{1}{r}\frac{\partial A_z}{\partial r} = 0. \tag{5.2}$$

In solving for A_z from (5.1) and (5.2), the four regions listed in Table 5.1 are used to set up boundary conditions from (4.19) and (4.20). These can be written by applying the 2D-simplifications of Chapter 4 to (4.19) and (4.20) to obtain:

$$H_\phi^{(\nu)}(r_\nu, \phi) - H_\phi^{(\nu+1)}(r_\nu, \phi) = -K_z^{(\nu)}(r_\nu, \phi), \tag{5.3}$$

for Ampère's Law, and:

$$B_r^{(\nu)}(r_\nu, \phi) - B_r^{(\nu+1)}(r_\nu, \phi) = 0, \tag{5.4}$$

for the flux conservation law.

5.2.2 Form of the solution

Poisson's equation is solved by solving the associated Laplace equation first. The Laplace equation is solved by the method of separation of variables, as documented in many textbooks on differential equations. See, for example, [Jef90]. The solution is a product of r^k and r^{-k} terms for the r-part and $\sin(k\phi)$ and $\cos(k\phi)$ terms for the ϕ-part of the solution, where k is an arbitrary constant, or:

$$(d_1 r^k + d_2 r^{-k})(c_3 \cos(k\phi) + c_4 \sin(k\phi)). \tag{5.5}$$

The following steps are made to construct a solution to Laplace's equation from (5.5):

- The magnetization vector's direction is chosen as in the d-axis: the $\cos(k\phi)$-term may then be eliminated from the solution.

- The regions wherein the equations are to be solved were already denoted by ν. This notation is used as a superscript (ν) in the solution of A_z: i.e., $A_z^{(\nu)}$.

- The solution is formed by taking a sum of solutions over an infinite number of boundary condition constants $C_k^{(\nu)}$ and $D_k^{(\nu)}$, where k is odd.

- The radius r is normalized with respect to r_ν, the radius at the interface between regions ν and $\nu + 1$.

- Use is made of the periodicity of A_z with the poles of the machine: ϕ is then replaced by $p\phi$.

Therefore, the solution to Laplace's equation (5.2) in a region ν can now be written as:

$$A_z^{(\nu)}(r, \phi) = \sum_{k=1,3,5,\cdots}^{\infty} \widehat{A}_{z,k}^{(\nu)}(r) \sin(kp\phi) \tag{5.6a}$$

where:

$$\widehat{A}_{z,k}^{(\nu)}(r) = C_k^{(\nu)} \left(\frac{r}{r_\nu} \right)^{-kp} + D_k^{(\nu)} \left(\frac{r}{r_\nu} \right)^{kp}, \tag{5.6b}$$

and $C_k^{(\nu)}$ and $D_k^{(\nu)}$ are the boundary condition constants.

In the solution to Poisson's equation (5.1), equation (5.6) forms a homogeneous part of the solution. The particular solution still has to be obtained. It is assumed that the particular solution for the ν-th region has the same Fourier-series form as (5.6a):

$$A_{part,z}^{(\nu)}(r, \phi) = \sum_{k=1,3,5,\cdots}^{\infty} \widehat{A}_{part,z,k}^{(\nu)}(r) \sin(kp\phi). \tag{5.7}$$

Therefore, the solution to Poisson's equation (5.1) can be written as:

$$A_z^{(\nu)}(r, \phi) = \sum_{k=1,3,5,\cdots}^{\infty} \widehat{A}_{z,k}^{(\nu)}(r) \sin(kp\phi) \tag{5.8a}$$

where:

$$\widehat{A}_{z,k}^{(\nu)}(r) = C_k^{(\nu)} \left(\frac{r}{r_\nu} \right)^{-kp} + D_k^{(\nu)} \left(\frac{r}{r_\nu} \right)^{kp} + \widehat{A}_{part,z,k}^{(\nu)}(r). \tag{5.8b}$$

5.2.3   Solution procedure

The solution procedure for different machine regions may be obtained for any permanent-magnet array by finding expressions for $H_\phi^{(\nu)}(r_\nu, \phi)$, $H_\phi^{(\nu+1)}(r_\nu, \phi)$, $B_r^{(\nu)}(r_\nu, \phi)$ and $B_r^{(\nu+1)}(r_\nu, \phi)$ from the solution of the vector potential, equations (5.6) and (5.8), and substituting them back into the boundary condition equations (5.3) and (5.4).

The magnetic field intensity in a region ν ($H_\phi^{(\nu)}$) is related to the flux density in that region ($B_\phi^{(\nu)}$) by equation (4.8b), which is valid for all material types. A relative

permeability is defined for each region under consideration ($\mu_r^{(\nu)}$), and assumptions 3 and 4 made in Chapter 4 are used to simplify $\mu_r^{(\nu)}$ in all four regions to either 1 or ∞, as listed in Table 5.1.

5.2.4 The value of the remanent flux density

$(\widehat{B}_{rem})$ **setting 1**

The assumption in the previous section that the relative permeability of the permanent magnets is equal to one was made to simplify the analytical field calculations. The resulting air gap flux density can be partly adjusted for a realistic relative permeability of larger than 1 (typically $\mu_r = 1.05$ for NdFeB) by using a lower remanent flux density in the calculation. The flux density that is obtained when the line drawn from the point (H_c, 0) with a slope of μ_0 intersects the B-axis results in a realistic value; see Figure 5.2(a).

$(\widehat{B}_{rem})$ **setting 2**

To simplify the analytical field calculations even further, another assumption is made: B_{rem} is assumed to be proportional to $1/r$. This is a reasonable assumption since the magnets are relatively thin. If the physical case of a constant remanent flux density were to be used in the analytical calculations, the particular solution would be proportional to r and contain a term $1/((kp)^2 - 1)$ for $kp \neq 1$. (In [Zhu93a], this solution was used.) When $B_{rem} \propto (1/r)$ is assumed, the particular solution is independent of r and valid for all kp. The latter option is simpler and thus chosen in the solution presented here. To remedy the effect of this assumption on the resulting air gap flux density, $\widehat{B}_{rem}$ is chosen to be the data sheet value in the centre of the magnets, as shown in Figure 5.2(b).
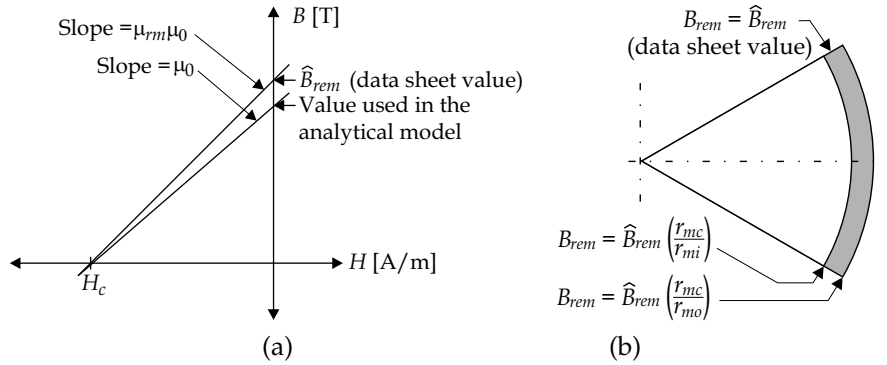
Figure 5.2: Setting of the value of the remanent flux density: (a) $(\widehat{B}_{rem})$ setting 1: due to the difference in μ_r of the magnets in reality and in the analytical model; (b) $(\widehat{B}_{rem})$ setting 2: due to the assumption that $B_{rem} \propto (1/r)$.

5.3   Radial array

5.3.1   Magnetization

Figure 5.3 shows a schematic cross-sectional view of a four-pole version of this array. The remanent flux density of the radial array is in the radial direction only: the ϕ-component is zero everywhere. There is also only one segment per pole in this array, with the inter-segment space filled with air.

   The remanent flux density of the magnets in the array shown in Figure 5.3 can be described by the vector:

$$\mathbf{B}_{rem} = B_{rem,r}\hat{\mathbf{i}}_r, \tag{5.9}$$

with:

$$B_{rem,r}(r,\phi) = \begin{cases} \widehat{B}_{rem}\left(\frac{r_{mc}}{r}\right) & \text{if } -\phi_m \leq \phi \leq \phi_m \\ -\widehat{B}_{rem}\left(\frac{r_{mc}}{r}\right) & \text{if } \frac{\pi}{2} - \phi_m \leq \phi \leq \frac{\pi}{2} + \phi_m \\ \widehat{B}_{rem}\left(\frac{r_{mc}}{r}\right) & \text{if } \pi - \phi_m \leq \phi \leq \pi + \phi_m \\ -\widehat{B}_{rem}\left(\frac{r_{mc}}{r}\right) & \text{if } \frac{3\pi}{2} - \phi_m \leq \phi \leq \frac{3\pi}{2} + \phi_m \\ 0 & \text{otherwise} \end{cases} \tag{5.10}$$
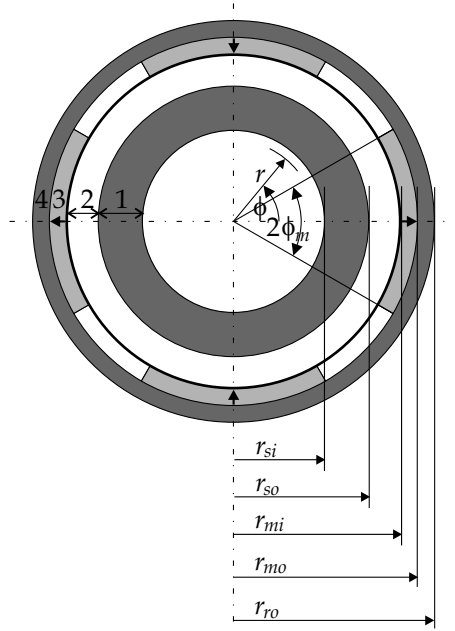
Figure 5.3: A cross section of the flywheel machine with radial magnetization showing regions for the calculation of the field due to the permanent magnets.

In (5.10), the centre radius of the magnets is given by:

$$r_{mc} \equiv \frac{r_{mi} + r_{mo}}{2}, \tag{5.11}$$

as can also be seen from Figure 5.2(b).

It is more convenient to rewrite the remanence by approximation by the use of a Fourier series representation of (5.10) as:

$$B_{rem,r}(r, \phi) = \sum_{k=1,3,5,\cdots}^{\infty} \widehat{B}_{rem,r,k}(r) \cos(kp\phi); \tag{5.12a}$$

$$\widehat{B}_{rem,r,k}(r) = \frac{4 r_{mc} \widehat{B}_{rem}}{\pi r k} \sin(kp\phi_m), \tag{5.12b}$$

which is valid for all kp, as opposed to (5.10), which is only valid for a four-pole machine like the EμFER.

5.3.2 Solution

For a remanence as given by (5.12), the particular solution of Poisson's equation (5.1) in the magnet region ($\nu = 3$) is given by:

$$A_{part,z}^{(3)}(r, \phi) = \sum_{k=1,3,5,\cdots}^{\infty} \widehat{A}_{part,z,k}^{(3)}(r) \sin(kp\phi); \tag{5.13a}$$

$$\widehat{A}_{part,z,k}^{(3)}(r) = \frac{4 r_{mc} \widehat{B}_{rem}}{\pi p k^2} \sin(kp\phi_m). \tag{5.13b}$$

Equation (5.13b) is a constant, i.e., independent of r. This is a direct consequence of (5.10).

Here we give only the solutions of the vector potential in the most interesting regions in the machine, i.e., the winding, mechanical air gap and the permanent magnet regions. The solutions in the stator and rotor iron regions are similar. In the equations listed below, K_{rad} is a constant, defined as equal to the peak value of the particular solution (5.13b):

$$K_{rad} = \frac{4 r_{mc} \widehat{B}_{rem}}{\pi p k^2} \sin(kp\phi_m). \tag{5.14}$$

The vector potential is now listed as follows:

Winding & mechanical air gap ($\nu = 2$):

$$A_z^{(2)}(r, \phi) = \sum_{k=1,3,5,\cdots}^{\infty} \widehat{A}_{z,k}^{(2)}(r) \sin(kp\phi); \tag{5.15a}$$

$$\widehat{A}_{z,k}^{(2)}(r) = \frac{K_{rad}}{2\left[\left(\frac{r_{so}}{r_{mo}}\right)^{2kp} - 1\right]} \left\{ \left[\left(\frac{r_{so}}{r_{mo}}\right)^{2kp} - \left(\frac{r_{so}}{r_{mi}}\right)^{2kp}\right] \left(\frac{r}{r_{mi}}\right)^{-kp} \right.$$

$$\left. + \left[\left(\frac{r_{mi}}{r_{mo}}\right)^{2kp} - 1\right] \left(\frac{r}{r_{mi}}\right)^{kp} \right\}. \quad (5.15b)$$

Permanent-magnet region ($\nu = 3$):

$$A_z^{(3)}(r,\phi) = \sum_{k=1,3,5,\cdots}^{\infty} \widehat{A}_{z,k}^{(3)}(r) \sin(kp\phi); \quad (5.16a)$$

$$\widehat{A}_{z,k}^{(3)}(r) = \frac{K_{rad}}{2} \left[\frac{1 - \left(\frac{r_{so}}{r_{mi}}\right)^{2kp}}{\left(\frac{r_{so}}{r_{mo}}\right)^{2kp} - 1} \right] \left(\frac{r_{mi}}{r_{mo}}\right)^{kp} \left[\left(\frac{r}{r_{mo}}\right)^{-kp} + \left(\frac{r}{r_{mo}}\right)^{kp} \right] + K_{rad}. \quad (5.16b)$$

5.3.3 Results of the magnetic field solution

In the radial array, the results of the magnetic field solution were calculated for a polar magnet span that fills 80% of the circumference, i.e. $2\phi_m = 0.8\pi/p$.

Figures 5.4 and 5.5 show the results of the calculations of this section. The magnetic field lines are shown in Figure 5.4 and the radial and tangential components
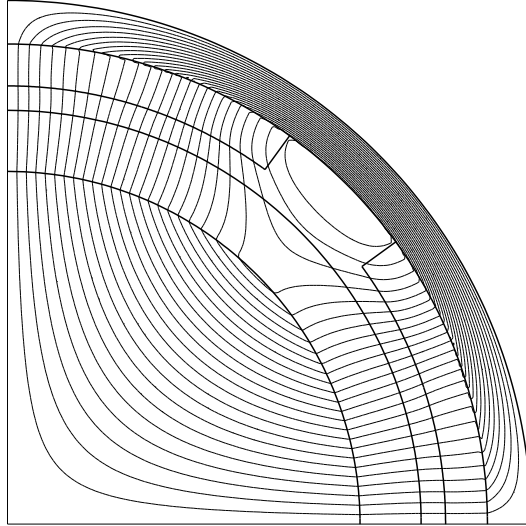
Figure 5.4: Magnetic field lines due to radial array excitation.

of the flux density in Figure 5.5. From Figure 5.5 it can be seen that the flux density decreases with increasing radius. This is because the area through which the flux passes, increases with increasing radius.

Figure 5.5: (a) Radial and (b) tangential components of the flux density at several different radii due to radial array excitation.

5.4 Discrete Halbach array with two segments per pole

5.4.1 Introduction

As discussed in Chapter 3, many other permanent-magnet arrays than the radially magnetized array can be used in PMSMs. It was mentioned that the use of discrete and ideal Halbach arrays as the machine excitation was considered by several researchers, both theoretically and experimentally. In this section, one of these arrays will be investigated analytically with respect to the magnetic field produced by it: the discrete Halbach array with two segments per pole.

See [Mar92], [Ata97] and [Ofo95] for treatments of analytical field calculations of permanent-magnet arrays other than the radial array. Rasmussen *et al.* [Ras00] replaced the permanent magnets with equivalent current densities in the bulk of the magnets and surface current densities on the surfaces. In this way, magnetization dependencies upon position may be modelled as well as both radial and tangential

components of the magnetization vector. By use of the method of Rasmussen *et al.*, one may solve for the field of several permanent-magnet arrays. Since the solution due to **J** is already obtained in [Ras00], this same solution can also be used to solve for the field due to the stator current distribution. Although their method is powerful, it is more physical to use the magnetization or remanence directly to model permanent magnets. This latter approach has been chosen in this thesis, and was already used in the previous section for calculating the field due to the radial array. This section continues with this approach.

5.4.2 Magnetization

The magnetization of the discrete Halbach array differs from that of the radial array of Figure 5.3 in that properly oriented tangentially magnetized magnets are inserted in the air spaces between the radial magnets of Figure 5.3. These magnets can be seen in Figure 5.6, which shows a schematic cross-sectional view of a four-pole version of this array.

The remanence of the magnets in the array shown in Figure 5.6 can again be described by the remanence vector of (5.9), but now also with a tangential component:

$$\mathbf{B}_{rem} = B_{rem,r}\hat{\mathbf{i}}_r + B_{rem,\phi}\hat{\mathbf{i}}_\phi, \tag{5.17}$$

Figure 5.6: A cross section of the flywheel machine with a discrete Halbach array with two segments per pole showing regions for the calculation of the field due to the permanent magnets.

The radial component of the remanence vector of the discrete Halbach array with two segments per pole is the same as that of the radial array, equation (5.12), which is repeated here:

$$B_{rem,r}(r,\phi) = \sum_{k=1,3,5,\cdots}^{\infty} \widehat{B}_{rem,r,k}(r)\cos(kp\phi); \tag{5.18a}$$

$$\widehat{B}_{rem,r,k}(r) = \frac{4r_{mc}\widehat{B}_{rem}}{\pi r k}\ \sin(kp\phi_m). \tag{5.18b}$$

The tangential component is given by:

$$B_{rem,\phi}(r,\phi) = \sum_{k=1,3,5,\cdots}^{\infty} \widehat{B}_{rem,\phi,k}(r)\sin(kp\phi); \tag{5.19a}$$

$$\widehat{B}_{rem,\phi,k}(r) = \frac{4r_{mc}\widehat{B}_{rem}}{\pi r k}\ \cos(kp\phi_m). \tag{5.19b}$$

5.4.3 Solution

The solution of the vector potential for the discrete Halbach array with two segments per pole can be constructed by summing two solutions:

$$A_z^{(\nu)}(r,\phi) = A_{z,rad}^{(\nu)}(r,\phi) + A_{z,tang}^{(\nu)}(r,\phi), \tag{5.20}$$

where $A_{z,rad}^{(\nu)}(r,\phi)$ is the vector potential due to the radially magnetized magnets and $A_{z,tang}^{(\nu)}(r,\phi)$, the vector potential due to the tangentially magnetized magnets.

It follows from (5.20) that the particular solution for this array is also the sum of two particular solutions:

$$A_{part,z}^{(3)}(r,\phi) = A_{part,z,rad}^{(3)}(r,\phi) + A_{part,z,tang}^{(3)}(r,\phi), \tag{5.21}$$

where $A_{part,z,rad}^{(3)}(r,\phi)$ is the particular solution of the vector potential due to the radially magnetized magnets and $A_{part,z,tang}^{(3)}(r,\phi)$ the particular solution of the vector potential due to the tangentially magnetized magnets. The particular solution of the vector potential due to the tangentially magnetized magnets is zero, however. From (5.21) this means that the particular solution of the vector potential due to the whole array is equal to that of the radial array, equation (5.13).

In the equations for the vector potential listed below, K_{tang} is a constant, defined by:

$$K_{tang} = \frac{4r_{mc}\widehat{B}_{rem}}{\pi p k^2}\cos(kp\phi_m), \tag{5.22}$$

similar to K_{rad} defined in (5.14) for the radially magnetized magnets.

The vector potential in the winding, the mechanical air gap and the permanent-magnet regions due to the tangential magnets is now listed as follows:

Winding & mechanical air gap ($\nu = 2$):

$$A_{z,tang}^{(2)}(r,\phi) = \sum_{k=1,3,5,\cdots}^{\infty} \widehat{A}_{z,k,tang}^{(2)}(r) \sin(kp\phi); \tag{5.23a}$$

$$\widehat{A}_{z,k,tang}^{(2)}(r) = \frac{K_{tang}}{2} \left[\frac{\left(\frac{r_{mi}}{r_{mo}}\right)^{-kp} + \left(\frac{r_{mi}}{r_{mo}}\right)^{kp} - 2}{\left(\frac{r_{so}}{r_{mo}}\right)^{-kp} - \left(\frac{r_{so}}{r_{mo}}\right)^{kp}} \right] \left[\left(\frac{r}{r_{so}}\right)^{-kp} + \left(\frac{r}{r_{so}}\right)^{kp} \right]. \tag{5.23b}$$

Permanent-magnet region ($\nu = 3$):

$$A_{z,tang}^{(3)}(r,\phi) = \sum_{k=1,3,5,\cdots}^{\infty} \widehat{A}_{z,k,tang}^{(3)}(r) \sin(kp\phi); \tag{5.24a}$$

$$\widehat{A}_{z,k,tang}^{(3)}(r) = \frac{K_{tang}}{2} \left[\frac{2\left(\frac{r_{so}}{r_{mo}}\right)^{kp} - \left(\frac{r_{so}}{r_{mi}}\right)^{kp} - \left(\frac{r_{so}}{r_{mi}}\right)^{-kp}}{-\left(\frac{r_{so}}{r_{mo}}\right)^{-kp} + \left(\frac{r_{so}}{r_{mo}}\right)^{kp}} \right] \left(\frac{r}{r_{mo}}\right)^{-kp}$$

$$+ \frac{K_{tang}}{2} \left[\frac{2\left(\frac{r_{so}}{r_{mo}}\right)^{-kp} - \left(\frac{r_{so}}{r_{mi}}\right)^{kp} - \left(\frac{r_{so}}{r_{mi}}\right)^{-kp}}{-\left(\frac{r_{so}}{r_{mo}}\right)^{-kp} + \left(\frac{r_{so}}{r_{mo}}\right)^{kp}} \right] \left(\frac{r}{r_{mo}}\right)^{kp}. \tag{5.24b}$$

From (5.20), the total solution for the field due to this array is obtained by summing the result due to the tangential magnets ((5.23) and (5.24) above), to the result due to the radial magnets ((5.15) and (5.16)).

5.4.4   Results of the magnetic field solution

Similar as for the radial array, the results for the discrete Halbach array with two segments per pole were calculated for a polar magnet span that fills 80% of the circumference, i.e. $2\phi_m = 0.8\pi/p$. This means that the polar span of the tangential magnets was $0.2\pi/p$ in the results presented here.

Figures 5.7 and 5.8 show the results of the calculations of this section. The magnetic field lines are shown in Figure 5.7 and the radial and tangential components of the flux density in Figure 5.8. The field lines in Figure 5.7 clearly show that the flux density in the rotor back iron is reduced due to the tangentially magnetized magnets. The peaks of the radial component of the flux density at the sides of the radially magnetized magnets are also reduced by the tangentially magnetized magnets, as can be seen in Figure 5.8.
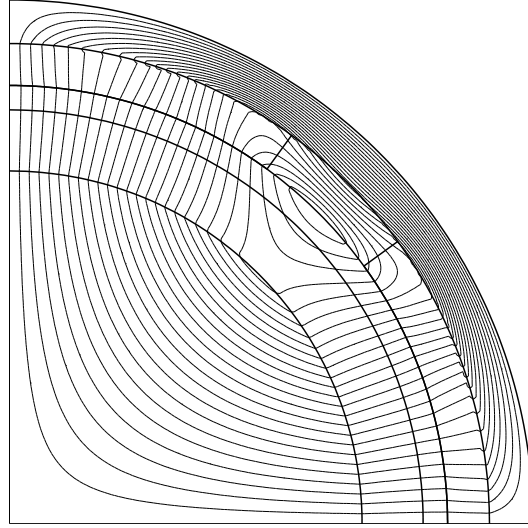
Figure 5.7: Magnetic field lines due to the excitation of the discrete Halbach array with two segments per pole.
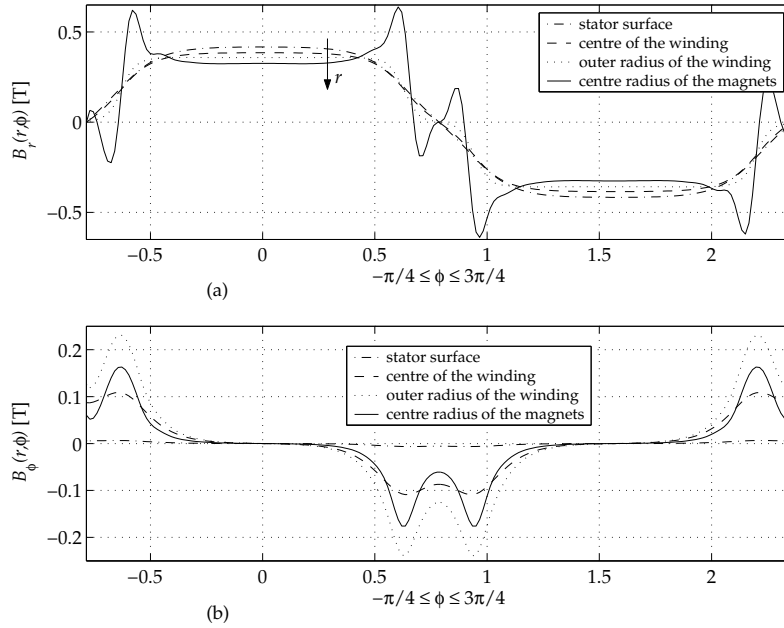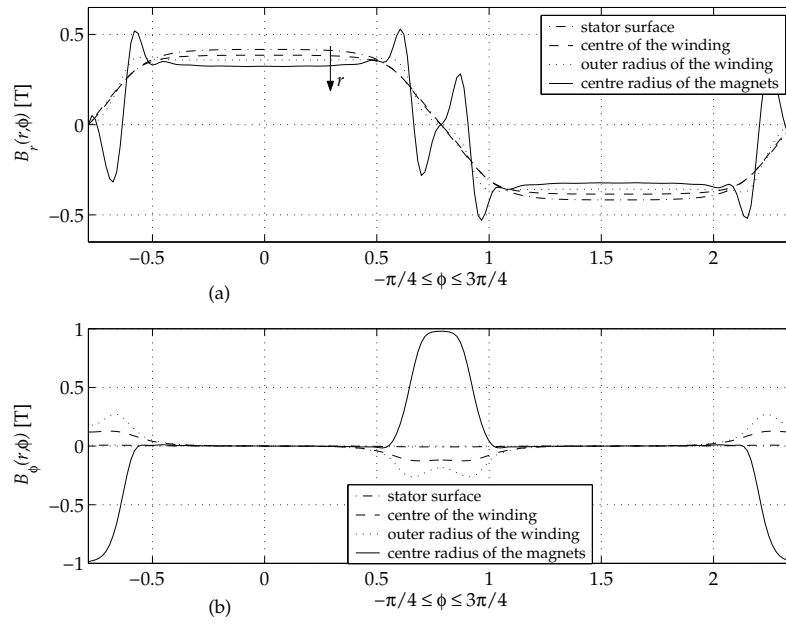

Figure 5.8: (a) Radial and (b) tangential components of the flux density at several different radii due to discrete Halbach array excitation.

5.5   Ideal Halbach array

5.5.1   Magnetization

Figure 5.9 shows a schematic cross-sectional view of a four-pole version of this array, where it can be seen that the magnetization of the ideal Halbach array varies sinusoidally with ϕ, and not discretely as in the arrays of Figures 5.3 and 5.6.

The remanence of the magnets in the array shown in Figure 5.9 can again be described by the remanence vector of (5.9), with the components [Ata97]:

$$B_{rem,r}(r,\phi) = \widehat{B}_{rem}\cos(p\phi), \tag{5.25a}$$

and

$$B_{rem,\phi}(r,\phi) = \widehat{B}_{rem}\sin(p\phi), \tag{5.25b}$$

respectively.

5.5.2   Solution

For a remanence as given by (5.25), the particular solution of Poisson's equation (5.1) in the magnet region ($\nu = 3$) is given by [Ata97]:

$$A_{part,z}^{3}(r,\phi) = \widehat{A}_{part,z}^{3}(r)\sin(p\phi); \tag{5.26a}$$

$$\widehat{A}_{part,z}^{3}(r) = \begin{cases} \dfrac{r\widehat{B}_{rem}}{p-1} & \text{if } p \neq 1 \\ -r\ln\left(\dfrac{r}{r_a}\right)\widehat{B}_{rem} & \text{if } p = 1, \end{cases} \tag{5.26b}$$

where r_a is an arbitrary constant.

The vector potential in the winding, the mechanical air gap and the permanent-magnet regions in the machine is now listed as follows:

Winding & mechanical air gap ($\nu = 2$):

$$A_z^{(2)}(r,\phi) = \widehat{A}_z^{(2)}(r)\sin(p\phi); \tag{5.27a}$$

$$\widehat{A}_z^{(2)}(r) =$$

$$\begin{cases} \dfrac{\frac{\widehat{B}_{rem}}{p-1}\left[r_{mo}\left(\frac{r_{so}}{r_{mo}}\right)^{2p} - r_{mi}\left(\frac{r_{mi}}{r_{mo}}\right)^{p}\left(\frac{r_{so}}{r_{mi}}\right)^{2p}\right]}{\left[\left(\frac{r_{so}}{r_{mo}}\right)^{2p} - 1\right]\left(\frac{r_{mi}}{r_{mo}}\right)^{p}}\left[\left(\frac{r}{r_{mi}}\right)^{-p} + \left(\frac{r_{so}}{r_{mi}}\right)^{-2p}\left(\frac{r}{r_{mi}}\right)^{p}\right] & \text{if } p \neq 1 \\ \dfrac{\widehat{B}_{rem}r_{mo}^{2}}{r_{so}^{2} - r_{mo}^{2}}\ln\left(\dfrac{r_{mi}}{r_{mo}}\right)\left[\dfrac{r_{so}^{2}}{r} + r\right] & \text{if } p = 1 \end{cases} \tag{5.27b}$$
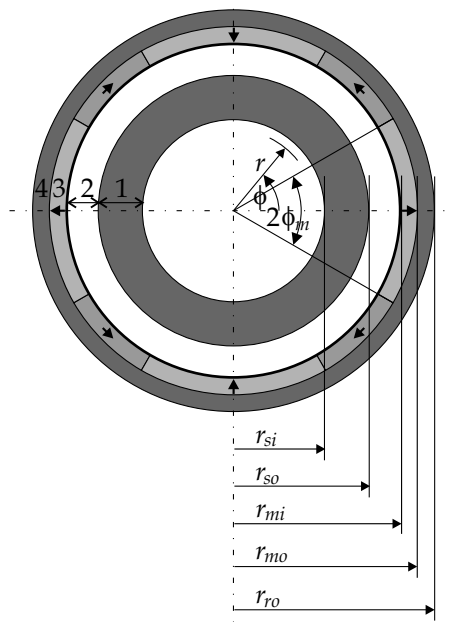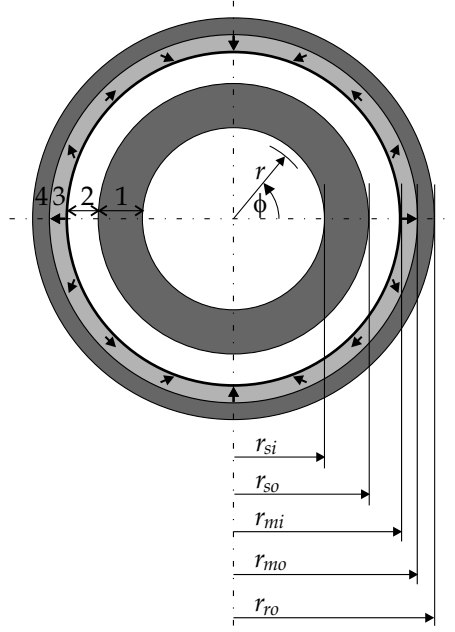
Figure 5.9: A cross section of the flywheel machine with an ideal Halbach array showing regions for the calculation of the field due to the permanent magnets.

Permanent-magnet region ($\nu = 3$):

$$A_z^{(3)}(r,\phi) = \widehat{A}_z^{(3)}(r)\sin(p\phi); \tag{5.28a}$$

$$\widehat{A}_z^{(3)}(r) = \begin{cases} \dfrac{\left[\frac{-r_{mi}\widehat{B}_{rem}}{p-1}\left(\frac{r_{mi}}{r_{mo}}\right)^p\left(\frac{r_{so}}{r_{mi}}\right)^{2p}\left[\left(\frac{r}{r_{mo}}\right)^{-p}+\left(\frac{r}{r_{mo}}\right)^p\right]\right]}{\left[\left(\frac{r_{so}}{r_{mo}}\right)^{2p}-1\right]} \\ \quad + \dfrac{\frac{r_{mo}\widehat{B}_{rem}}{p-1}\left[\left(\frac{r_{so}}{r_{mo}}\right)^{2p}\left(\frac{r}{r_{mo}}\right)^{-p}+\left(\frac{r}{r_{mo}}\right)^p\right]}{\left[\left(\frac{r_{so}}{r_{mo}}\right)^{2p}-1\right]} + \dfrac{r\widehat{B}_{rem}}{p-1} & \text{if } p \neq 1 \\[2em] \dfrac{\widehat{B}_{rem}r}{r_{so}^2-r_{mo}^2}\left[r_{so}^2\ln\left(\frac{r_{mi}}{r}\right)+r_{mo}^2\ln\left(\frac{r}{r_{mo}}\right)+r_{so}^2r_{mo}^2 r^{-2}\ln\left(\frac{r_{mi}}{r_{mo}}\right)\right] & \text{if } p = 1 \end{cases} \tag{5.28b}$$

5.5.3 Results of the magnetic field solution

Figures 5.10 and 5.11 show the results of the calculations of this section. The magnetic field lines are shown in Figure 5.10 and the radial and tangential components of the flux density in Figure 5.11. As can be expected, only the fundamental harmonic of the field is present in both the radial and tangential components.
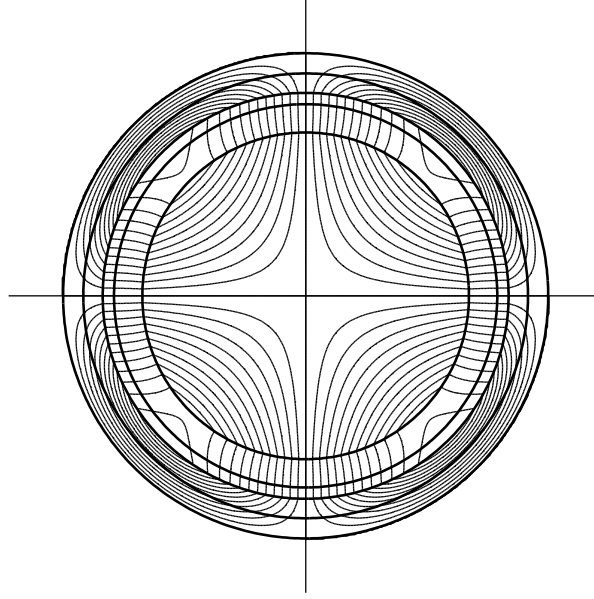
Figure 5.10: Magnetic field lines due to the excitation of the ideal Halbach array.

5.6   Magnetic field verification with the FEM

Figure 5.12 shows a comparison between a calculation done with the analytical method derived in this chapter and one with the finite element method (FEM). It shows a plot of the radial component of the flux density due to the permanent magnets for a pole pitch in the centre of the air gap for a sample geometry. The FEM-calculation was done with the FLUX2D® package of CEDRAT S.A. (France). Figure 5.12(a) shows $B_r(r, \phi)$ for the radial array and Figure 5.12(b) for the discrete Halbach array with two segments per pole.

   The calculations in FLUX2D® were done with realistic values of the relative permeabilities of iron and of the permanent magnets of $\mu_{r,Fe} = 2500$ and $\mu_{r,magnets} = 1.04$, respectively. The data of magnet type 677 AP (axial pressed) was used for the calculations of Figure 5.12. This magnet is made by Vacuumschmelze GmbH, Germany, and the remanent flux density given in the data sheet is 1.13 T at 20°C. The coercivity H_{cB} for the 677 AP magnet type is -860 kA/m at 20°C from the data sheet.

   In the analytical method, the remanent flux density has to be changed, as ex-
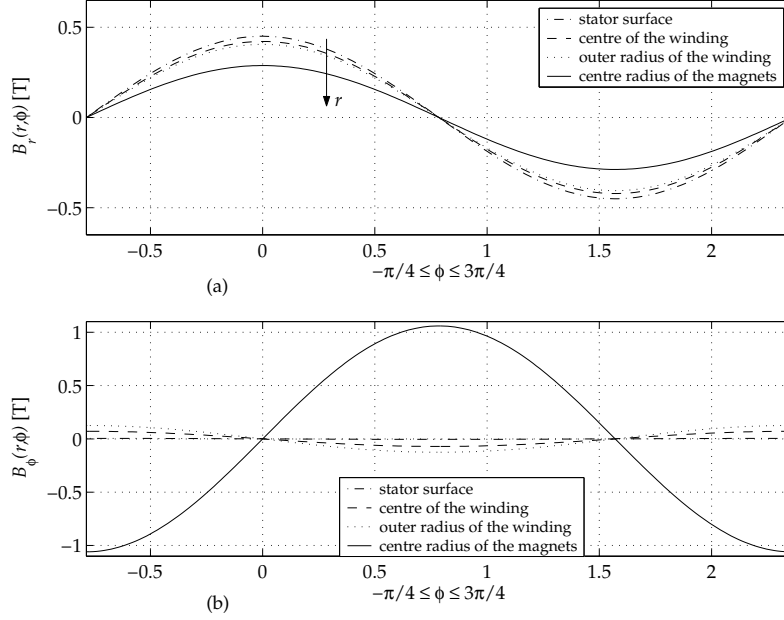
Figure 5.11: (a) Radial and (b) tangential components of the flux density at several different radii due to ideal Halbach array excitation.

plained in Section 5.2.4, to account for the relative permeability of the magnets, which is higher than one. This is $\widehat{B}_{rem}$ setting 1, resulting in $\widehat{B}_{rem} = -\mu_0(-860 \times 10^3) = 1.08$ T. The other change in the remanence, $\widehat{B}_{rem}$ setting 2 of Section 5.2.4 (to account for the $1/r$-dependency of $\widehat{B}_{rem}$), is already incorporated into (5.12).

For the radial array, the peak value of the flux density calculated with FLUX2D is 0.15% higher than that calculated by the analytical method. For the discrete Halbach array, FLUX2D gives a 1.16% higher peak value. The shape of the flux density curve is slightly different with the two methods, with the largest difference for the discrete Halbach array. In spite of these minor differences, the result of the analytical method compares well with that of the finite element method.

5.7 The flux linkage of the stator winding due to the permanent magnets: No-load voltage

5.7.1 Introduction

In this chapter, the previous sections have discussed the magnetic fields for the three permanent-magnet arrays. In this section, a practically useful quantity will be derived from these fields due to the permanent-magnet arrays: the no-load voltage of the machine.
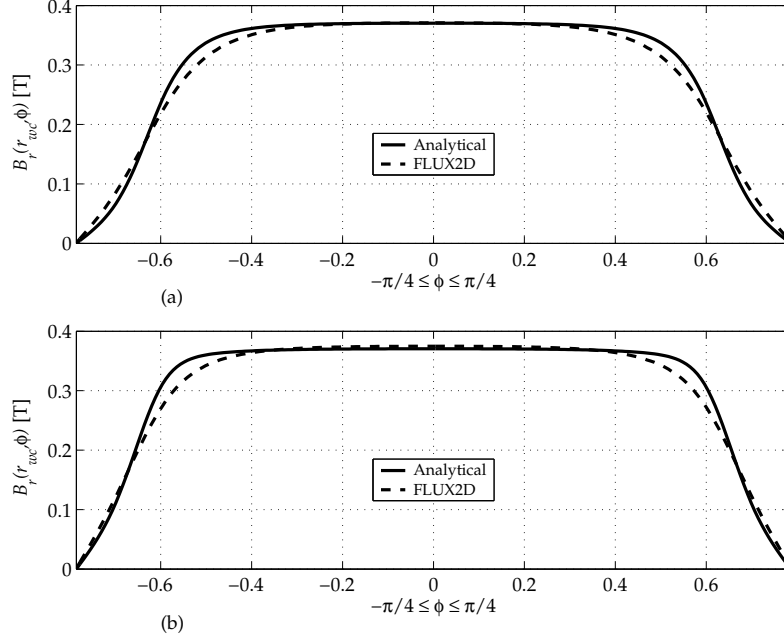
Figure 5.12: Comparison of the radial component of the flux density calculated with
the analytical method and the FEM: (a) radial array; (b) discrete Halbach
array with two segments per pole.

5.7.2   Notation and machine regions

Since the flux linkages of the different permanent-magnet arrays are used together
in this section, a notational system for differentiating between them is needed first.
Table 5.2 lists this notational system, where the subscripts *rad*, *dh*2 and *ih* are added
to the vector potential $A_z^{(\nu)}$ to denote the different field sources: the radial array, the
discrete Halbach array with two segments per pole and the ideal Halbach array.

It should also be recalled from (4.1) that the stator and rotor angular coordi-
nates are related to one another by the rotor angular position θ by: $\varphi = \phi + \theta$. Since
the permanent-magnet arrays are on the rotor, their fields are described in the rotor
angular coordinate system (r, ϕ, z), which rotates at synchronous speed around the
stator angular coordinate system (r, φ, z). To obtain the flux linkage of the wind-
ing due to the permanent magnets, the transformation (4.1) is therefore applied to
transform the rotor field to the stator.

Permanent magnet array	Notation
permanent magnets: radial array	$A_{z,rad}^{(\nu)}(r,\phi)$
perm. magnets: discrete Halbach array with 2 segments per pole	$A_{z,dh2}^{(\nu)}(r,\phi)$
permanent magnets: ideal Halbach array	$A_{z,ih}^{(\nu)}(r,\phi)$

Table 5.2: The notation for the vector potential due to the three different permanent-magnet arrays.

5.7.3 The stator voltage equation

The voltage equation of the stator winding can be written as:[1]

$$\vec{u}_s(t) = R_s\vec{i}_s(t) + \frac{d\vec{\lambda}_s(t)}{dt}, \tag{5.29}$$

where R_s is the stator resistance and

$$\vec{u}_s(t) = \begin{bmatrix} u_{sa}(t) \\ u_{sb}(t) \\ u_{sc}(t) \end{bmatrix}, \quad \vec{i}_s(t) = \begin{bmatrix} i_{sa}(t) \\ i_{sb}(t) \\ i_{sc}(t) \end{bmatrix}, \quad \text{and} \quad \vec{\lambda}_s(t) = \begin{bmatrix} \lambda_{sa}(t) \\ \lambda_{sb}(t) \\ \lambda_{sc}(t) \end{bmatrix} \tag{5.30}$$

are the stator voltages, currents and flux linkages, respectively. The flux linking with the stator winding can be broken down into three distinct parts, as mentioned in Chapter 4. Two of these flux linkages arise from the two different sources of magnetic flux, i.e., the permanent magnets ($\vec{\lambda}_{sm}$) and the stator currents ($\vec{\lambda}_{ss}$). The third part of the flux linkage of the stator is due to the leakage flux of the end windings ($\vec{\lambda}_{s\sigma}$). The leakage flux in the air gap and the "slots" is included in the main air gap flux, since the EμFER machine has an air gap winding.

Writing the total flux linkage of the stator winding explicitly as the sum of these different parts, one obtains the stator voltage equation:

$$\vec{u}_s(t) = R_s\vec{i}_s(t) + \frac{d\vec{\lambda}_{sm}(t)}{dt} + \frac{d\vec{\lambda}_{ss}(t)}{dt} + \frac{d\vec{\lambda}_{s\sigma}(t)}{dt}. \tag{5.31}$$

5.7.4 The flux linkage of an arbitrary winding distribution

In Section 4.5, the flux linking with a full-pitch turn at radius r and angular coordinate φ was shown to be given simply by (4.29): $\lambda_t(r,\varphi) = 2l_s A_z(r,\varphi)$. Generally, single full-pitch turns are not used in practical machines, and therefore the flux linking with a physical winding has to be developed from $\lambda_t(r,\varphi)$. This can be done by

---

[1]In this chapter, the notation $\vec{u}_s$ is introduced for vectors without directional meaning. For example, the stator voltage vector $\vec{u}_s$ comprises the three components of the three phases *a*, *b* and *c*, but it is not oriented in some direction in space. This is in contrast with vectors with a directional meaning, like the magnetic flux density **B**. For these, the boldface notation is retained.

integrating the product of $\lambda_t(r, \varphi)$ and the winding distribution described in Chapter 3. Therefore, the flux linked with phase a of an air gap winding with arbitrary distribution $n_{sa}(\varphi)$ at any radius r is from (3.10) and (4.29):

$$\lambda_{sa}(r) = p \int\limits_0^{\pi/p} n_{sa}(\varphi)\lambda_t(r,\varphi)d\varphi = 2pl_s \int\limits_0^{\pi/p} n_{sa}(\varphi)A_z(r,\varphi)d\varphi. \qquad (5.32)$$

The flux linked with phases b and c of the air gap winding is similar to (5.32), with $n_{sa}(\varphi)$ replaced by $n_{sb}(\varphi)$ and $n_{sc}(\varphi)$, respectively.

The fields due to the three permanent-magnet arrays obtained earlier in the chapter are linked with the stator winding. Thus, $A_{z,rad}^{(2)}(r,\phi)$, $A_{z,dh2}^{(2)}(r,\phi)$ and $A_{z,ih}^{(2)}(r,\phi)$ are substituted into (5.32).

5.7.5   Radial array

For the radial array, equation (5.32) is rewritten as:

$$\lambda_{sma,rad}(r) = 2pl_s \int\limits_0^{\pi/p} n_{sa}(\varphi)A_{z,rad}^{(2)}(r,\phi)d\varphi. \qquad (5.33)$$

Since the field due to the permanent magnets also contains triplen space harmonics, as is evident from (5.15a), both the double-sided and single-sided Fourier series of (3.16a) must be used for the winding distribution $n_{sa}(\varphi)$ in (5.33). Furthermore, the expression for the vector potential in the winding region due to the radial array, equation (5.15a), must be rewritten in terms of $\ddot{k} \in \mathbb{Z}$ and $\dot{k} \in \mathbb{Z}^+$ to comply with (3.16a).

However, it should be recalled that (3.16a) is just a way to rewrite (3.10) so that the triplen and non-triplen harmonics can easily be separated. When considering three-phase currents that can either be balanced or not, this approach makes sense. When considering the field due to the permanent magnets, however, there is no need to distinguish between the triplen and non-triplen harmonics. Therefore, the simpler notation of (3.10) is chosen to work out the flux linkage of the stator winding due to the permanent magnets.

Thus, from (3.10) and (5.15a), equation (5.33) may be written as:

$$\lambda_{sma,rad}(r) = \sum_{k=1,3,5,\cdots}^{\infty} \sum_{l=1,3,5,\cdots}^{\infty} 2pl_s\hat{n}_{s,k}\widehat{A}_{z,rad,l}^{(2)}(r) \int\limits_0^{\pi/p} \cos(kp\varphi)\sin(lp\phi)\,d\varphi. \qquad (5.34)$$

In (5.34), the rotor angular coordinate ϕ needs to be substituted with the stator angular coordinate φ by means of (4.1). The resulting integral is always zero except when $k = l$. Therefore, the flux linked with phase a of an air gap winding with distribution

$n_{sa}(\varphi)$ at radius r is:

$$\lambda_{sma,rad}(r,\theta) = \sum_{k=1,3,5,\cdots}^{\infty} 2pl_s\hat{n}_{s,k}\widehat{A}_{z,rad,k}^{(2)}(r) \int_0^{\pi/p} \cos(kp\varphi)\sin\left[kp(\varphi-\theta)\right] \, d\varphi, \quad (5.35)$$

now an explicit function of the rotor angular position θ. When integrated, equation (5.35) is simply:

$$\lambda_{sma,rad}(r,\theta) = -\pi\, l_s \sum_{k=1,3,5,\cdots}^{\infty} \hat{n}_{s,k}\widehat{A}_{z,rad,k}^{(2)}(r)\sin(kp\theta), \quad (5.36)$$

where the peak value of the vector potential $\widehat{A}_{z,rad,k}^{(2)}(r)$ is obtained from (5.15b).

For phases b and c, the flux linkage is similar to that of phase a, but displaced at angles of $2\pi/3p$ and $4\pi/3p$, respectively. Therefore, the flux linkage of the stator winding due to the radial permanent-magnet array is:

$$\vec{\lambda}_{sm,rad}(r,\theta) = -\pi\, l_s \sum_{k=1,3,5,\cdots}^{\infty} \hat{n}_{s,k}\widehat{A}_{z,rad,k}^{(2)}(r) \begin{bmatrix} \sin(kp\theta) \\ \sin\left[kp\left(\theta - \frac{2\pi}{3p}\right)\right] \\ \sin\left[kp\left(\theta - \frac{4\pi}{3p}\right)\right] \end{bmatrix} \quad (5.37)$$

Equation (5.37) can be considered to be a function of time by making use of (4.2). Thus, $\vec{\lambda}_{sm,rad}(r,\theta) = \vec{\lambda}_{sm,rad}(r,\theta(t)) = \vec{\lambda}_{sm,rad}(r,t)$ with θ replaced by $\omega_m t$. The time derivative of the flux linkage is the no-load voltage:

$$\frac{\partial\vec{\lambda}_{sm,rad}(r,t)}{\partial t} = -\pi\, l_s\, \omega_m \sum_{k=1,3,5,\cdots}^{\infty} kp\,\hat{n}_{s,k}\widehat{A}_{z,rad,k}^{(2)}(r) \begin{bmatrix} \cos(kp\omega_m t) \\ \cos\left[kp\left(\omega_m t - \frac{2\pi}{3p}\right)\right] \\ \cos\left[kp\left(\omega_m t - \frac{4\pi}{3p}\right)\right] \end{bmatrix}.$$
$$(5.38)$$

Since the machine has a slotless stator, the flux linkages of the outer and inner layers of the winding are different, as is evident from the fact that $\vec{\lambda}_{sm,rad}$ is a function of r. The value of r at which the flux linkage is chosen to be determined lies at the centre of the winding, or $r = r_{wc}$, to obtain an average value. The radius at the centre of the winding is defined by:

$$r_{wc} \equiv \frac{r_{so} + r_w}{2}. \quad (5.39)$$

Thus the flux linkage is now a function of time only and (5.38) becomes:

$$\vec{e}_{p,rad}(t) = \frac{d\vec{\lambda}_{sm,rad}(t)}{dt}$$

$$= -\pi\, l_s\, \omega_m \sum_{k=1,3,5,\cdots}^{\infty} kp\,\hat{n}_{s,k}\widehat{A}_{z,rad,k}^{(2)}(r_{wc}) \begin{bmatrix} \cos(kp\omega_m t) \\ \cos\left[kp\left(\omega_m t - \frac{2\pi}{3p}\right)\right] \\ \cos\left[kp\left(\omega_m t - \frac{4\pi}{3p}\right)\right] \end{bmatrix}. \quad (5.40)$$

Equation (5.40) is the no-load voltage of the machine fitted with a radial array.

5.7.6 Discrete Halbach array with two segments per pole

Similar to (5.40), the time derivative of the flux linkage of the stator winding due to the discrete Halbach array with two segments per pole is:

$$\vec{e}_{p,dh2}(t) = -\pi\, l_s\, \omega_m \sum_{k=1,3,5,\cdots}^{\infty} kp\, \hat{n}_{s,k} \widehat{A}^{(2)}_{z,dh2,k}(r_{wc}) \begin{bmatrix} \cos(kp\omega_m t) \\ \cos\left[kp\left(\omega_m t - \frac{2\pi}{3p}\right)\right] \\ \cos\left[kp\left(\omega_m t - \frac{4\pi}{3p}\right)\right] \end{bmatrix}, \quad (5.41)$$

where the peak value of the vector potential $\widehat{A}^{(2)}_{z,dh2,k}(r_{wc})$ is obtained from (5.23b) and (5.15b).

5.7.7 Ideal Halbach array

Similar to (5.40), the time derivative of the flux linkage of the stator winding due to the ideal Halbach array is:

$$\vec{e}_{p,ih}(t) = -\pi\, l_s\, \omega_m\, p\, \hat{n}_{s,1} \widehat{A}^{(2)}_{z,ih}(r_{wc}) \begin{bmatrix} \cos(p\omega_m t) \\ \cos\left[p\left(\omega_m t - \frac{2\pi}{3p}\right)\right] \\ \cos\left[p\left(\omega_m t - \frac{4\pi}{3p}\right)\right] \end{bmatrix}, \quad (5.42)$$

where the peak value of the vector potential $\widehat{A}^{(2)}_{z,ih}(r_{wc})$ is obtained from (5.27b). Because the magnetic field of the ideal Halbach array contains only a fundamental harmonic component, it only links with the fundamental space harmonic of the winding. This can be seen from the fact that the integral $\int_0^{\pi/p} \cos(kp\varphi)\sin(p\varphi)d\varphi$ is nonzero only for $k = 1$.

5.7.8 Results of the no-load voltage calculation

Figure 5.13 shows the radial component of the flux density at the centre of the air gap for the three permanent-magnet arrays under discussion in this chapter.

Figure 5.14 shows the no-load voltages of the EμFER machine rotating at 30 000 rpm for the flux densities of Figure 5.13. In Figure 5.14(a) the line-neutral voltages $e_{pa,rad}(t)$, $e_{pa,dh2}(t)$ and $e_{pa,ih}(t)$, calculated from (5.40), (5.41), and (5.42) are shown. Figure 5.14(b) shows the line-line voltages $e_{pab,rad}(t)$, $e_{pab,dh2}(t)$, and $e_{pab,ih}(t)$, respectively. The line-line voltage corresponds to the measured voltage between two line terminals of the machine, and is calculated as the difference between two line-neutral voltages: $e_{pab}(t) = e_{pa}(t) - e_{pb}(t)$.

The magnet parameters used for the calculations of Figure 5.14 are the same as those used in Section 5.6.
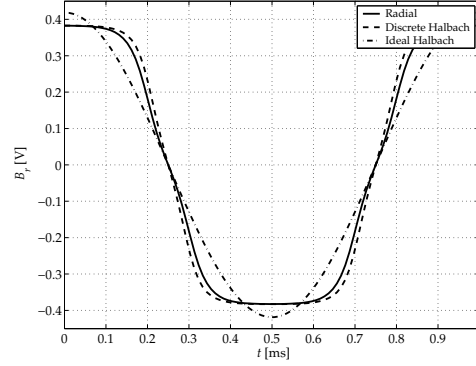
Figure 5.13: Radial component of the flux density at the centre of the air gap, i.e., at r_{wc}, for the three permanent-magnet arrays.

(a)

(b)
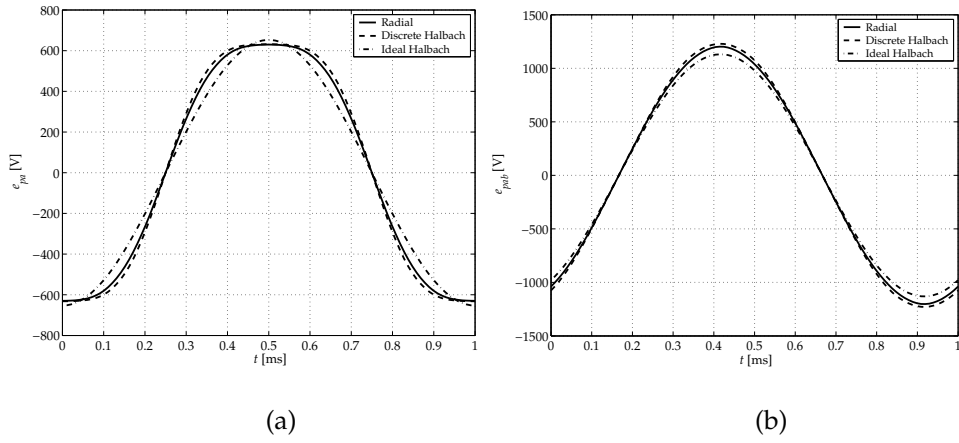
Figure 5.14: No-load voltage of the EμFER machine at a rotational speed of 30 000 rpm for the three arrays: (a) line-neutral voltages $e_{pa,rad}(t)$, $e_{pa,dh2}(t)$ and $e_{pa,ih}(t)$; (b) line-line voltages $e_{pab,rad}(t)$, $e_{pab,dh2}(t)$ and $e_{pab,ih}(t)$.

When one looks at the no-load voltage waveforms of Figure 5.14, the higher-order harmonics do not appear to play a significant role. This is particularly so in the line-line voltages of Figure 5.14(b). In fact, at first glance, the line-line voltage only seems to consist of the fundamental harmonic, but this is not the case. (It is only true for the ideal Halbach array.) When the amplitudes at the different harmonics are plotted on a logarithmic scale, they can be clearly distinguished. Moreover, the effect of the tangential magnets in the discrete Halbach array and the effect of the winding distribution can be investigated in this way.

Figure 5.15 shows the normalized harmonic content of the flux density, winding distribution and the no-load voltage, both the line-neutral voltages (Figures 5.15(a)

and (c)) and the line-line voltages (Figures 5.15(b) and (d)).

The space harmonics at which the flux density, winding distribution and no-load voltage are zero may be investigated from Figure 5.15. For example, the winding distribution is seen to be zero for $k = 9, 27, \cdots$ The reason for this comes from the Fourier series used to represent it. This may be clearly seen from equation (A.15) in Appendix A, where a direct Fourier analysis of the winding distribution was done. (It may also be seen from the winding factor representation.) In (A.15), the Fourier coefficient b_k is zero for multiples of 9 since the arguments of all eight sine functions making up b_k are divided by 9. If the Fourier coefficient is zero, the whole function, in this case the winding distribution, is also zero.

Also, from Figures 5.15(a) and (b), one can see that the radial component of the flux density in the centre of the air gap for the radial array is zero for $k = 5, 15, 25, \cdots$ Once again this is a consequence of the Fourier-series representation of the flux density. Equation (5.12b) shows this clearly, where, since $2\phi_m = 0.8\pi/p$, $\phi_m = \pi/5$, and therefore the argument of the sine function in (5.12b) is $2k\pi/5$. This explains the fact that $B_{r,rad,k}(r_{wc}, t)$ is zero for all k that are multiples of 5.

For the discrete Halbach array, $B_{r,dh2,k}(r_{wc}, t) \neq 0$ for all k, as can be seen from (5.18b) and (5.19b).

The product of the winding distribution and the flux density results in the no-load voltage, up to a factor, as can be seen in (5.40), for example. (Recall that the radial component of the flux density is obtained from the vector potential of (5.40) by (4.23).) Therefore the no-load voltages of the two arrays will reflect the properties of their flux densities. This is clearly seen in Figures 5.15(a) and (c), where the line-neutral no-load voltages of the two arrays are shown. For the line-line voltage, the fact that the triplen harmonics are zero is added, since in this thesis only balanced three-phase currents are considered.

Thus, the harmonic content of Figures 5.15(a)—(d) can be summarized as follows:

- $\hat{n}_{s,k} = 0$ for $k = 9, 27, \cdots$

- radial array:

    - $B_{r,k} = 0$ for $k = 5, 15, 25, \cdots$
    - $e_{pa,k} = 0$ for $k = 9, 27, \cdots$, and $k = 5, 15, 25, \cdots$
    - $e_{pab,k} = 0$ for $k = 3, 9, 15, 21, \cdots$, and $k = 5, 15, 25, \cdots$

- discrete Halbach array with two segments per pole:

    - $B_{r,k} \neq 0$ for all k
    - $e_{pa,k} = 0$ for $k = 9, 27, \cdots$
    - $e_{pab,k} = 0$ for $k = 3, 9, 15, 21, \cdots$

For the ideal Halbach array:
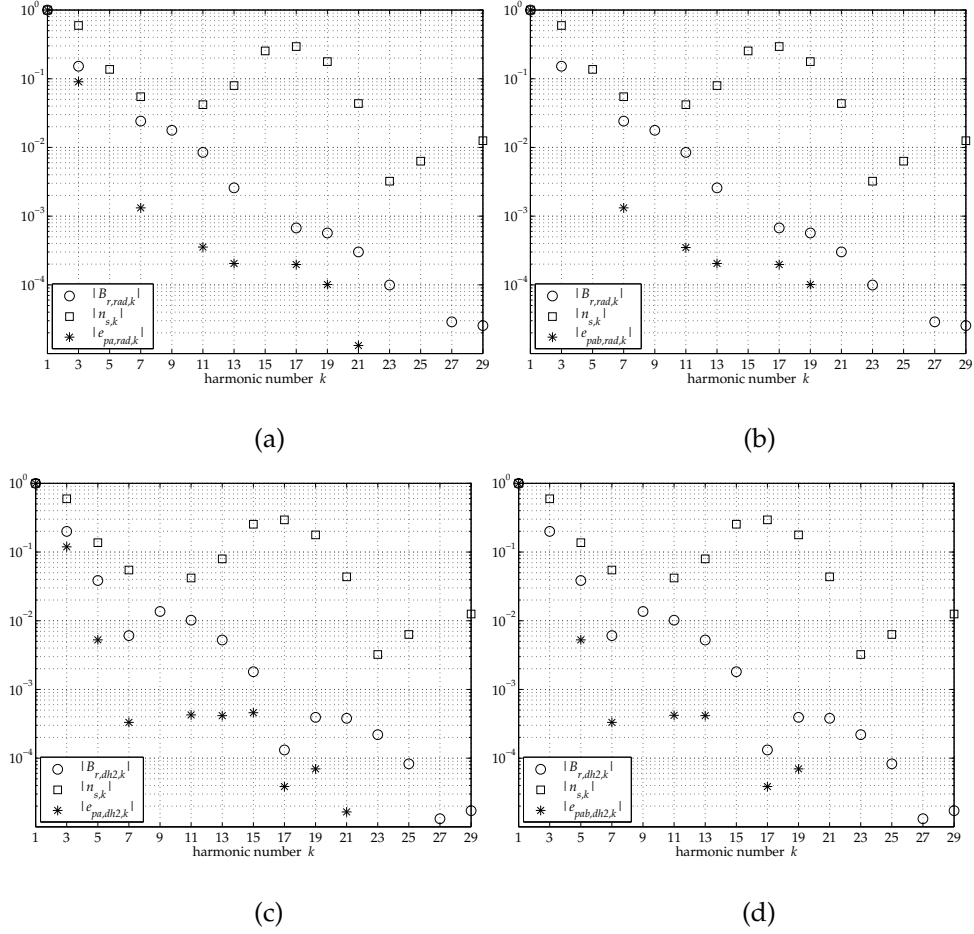
Figure 5.15: Normalized harmonic spectrum of the flux density, winding distribution and the no-load voltage: (a) line-neutral voltage, radial array; (b) line-line voltage, radial array; (c) line-neutral voltage, discrete Halbach array; (d) line-line voltage, discrete Halbach array.

- $\hat{n}_{s,k} = 0$ for $k = 9, 27, \cdots$

- $B_{r,k} = 0$ for all $k \neq 1$

- $e_{pa,k} = 0$ for all $k \neq 1$

- $e_{pab,k} = 0$ for all $k \neq 1$

The harmonic behavior described above is a direct consequence of the winding distribution and the polar magnet arc $2\phi_m$. These are physical properties of the machine that may be varied to obtain certain desired harmonic properties of its no-load voltage. As shown above, the choice of permanent-magnet array is also a very

important factor to consider for controlling the harmonic content of the no-load voltage.

5.8   Experimental verification of the no-load voltage

The EµFER machine is constructed with a radial array. The reasons for this choice will become clear in Chapter 8, where it will be shown that only a small amount of torque is gained when the discrete Halbach array is used instead of the radial array.

Figure 5.16 compares an experimental measurement of the no-load voltage of the EµFER machine with the prediction by the analytical model. For this measurement, the flywheel was manually turned at a rotational speed of 159.1 rpm. This resulted in a stator fundamental frequency of $f_s = 5.2645$ Hz. The peak value of the analytically predicted no-load voltage is 4.3% higher than the measured result. This difference may be explained by the leakage field into the third dimension, which the analytical model does not take into account.

Since both the frequency and amplitude of the no-load voltage are linear functions of the rotational speed, the analytical predictions will also be accurate at the operating speeds of between 15 000 and 30 000 rpm.
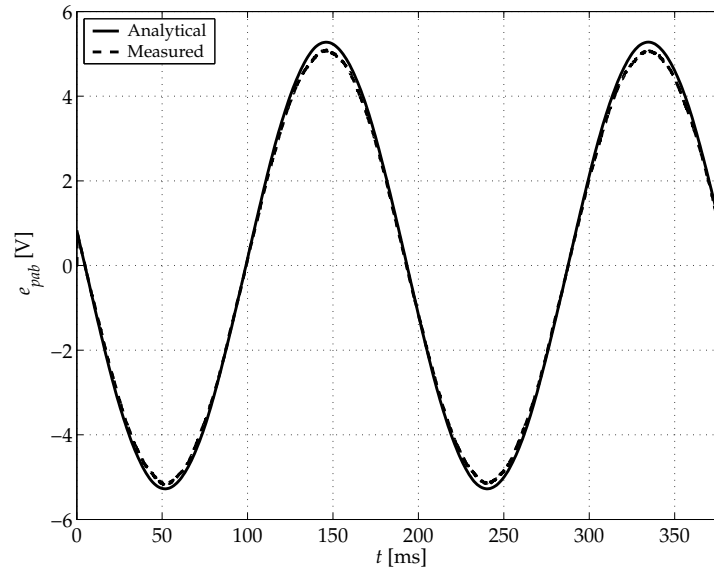
Figure 5.16: Measured and predicted no-load voltage of the EµFER machine at a rotational speed of 159.1 rpm.

5.9   Summary and conclusions

This chapter focused on the field due to the permanent magnets and useful quantities derived from this field. The chapter started with describing a method for solving for the magnetic field in Section 5.2.

Sections 5.3—5.5 presented magnetic field solutions for the three permanent-magnet arrays introduced in Chapter 3.

The analytically calculated flux density of the radial array was verified with the FEM in Section 5.6.

Section 5.7 started the discussion on the derived field quantities by looking at the flux linkage of the stator winding, leading to the machine's no-load voltage. Section 5.7 also showed how the harmonic content of the no-load voltage can be controlled by means of three parameters:

- the winding distribution (number of slots, slot width, etc.);

- the polar magnet arc $2\phi_m$; and

- the permanent-magnet array.

The no-load voltage was verified experimentally in Section 5.8 for the EμFER machine (which has a radial array) at a low rotational speed. Since both the frequency and amplitude of the no-load voltage are linear functions of the rotational speed, the analytical predictions will also be accurate at high rotational speeds.

The field due to the stator currents and derived quantities

6.1 Introduction

This chapter continues the development of an analytical model for the analysis and design of external rotor slotless PMSMs. The ideas developed in this chapter will once again be applied to the EμFER machine introduced in Chapter 3. In Chapter 5, a simplified approach was developed for the field due to the permanent magnets. This approach rested upon classical layer theory, outlined in Chapter 4, and was applied to the four-layer cross section of Figure 5.1.

In this chapter, the shielding cylinder is included in the analysis. Since the cylinder experiences a high-frequency magnetic field, eddy currents will flow in it. These induced eddy currents in the cylinder also give rise to a magnetic field, effectively in "reaction" to the stator currents' excitation. Hence the term "reaction field" of the eddy currents in the shielding cylinder. This reaction field opposes the excitation field of the stator currents, and therefore forms a "shield" for the high-frequency fields so that they do not penetrate the magnets or rotor iron. Hence the term "shielding cylinder".

The six-layer cross section of the EμFER machine of Figure 4.1 stands central in this chapter.

The current density in the air gap winding is the source of excitation under investigation in this chapter, including the effect of the reaction field due to the eddy currents in the shielding cylinder. Since the stator winding is located in the air gap in an ironless structure, the stator current density $\mathbf{J}_s$ may be used directly in the Poisson equation (4.16).

In Section 6.2, the chapter starts with a literature review of work done by others relevant to the two main contributions of this chapter: (i) the stator winding excitation (air gap winding); and (ii) the influence of the eddy-current reaction field upon

the field due to the stator currents. The field due to the air gap winding currents is described in Sections 6.3—6.5, starting with the development of the current density from the winding distribution (Section 6.3). Section 6.4 applies this to calculate the field of the stator currents in all six regions due to the current density in the air gap winding, including the effect of the reaction field of the eddy currents in the shielding cylinder on this field. Some results of this field calculation is documented in Section 6.5.

For a free rotor, the quantities derived from the magnetic field are the stator main-field inductance (Section 6.6) and the induced eddy-current loss in the shielding cylinder (Section 6.8). The latter will be illustrated with three stator current waveforms. The end-winding leakage inductance is briefly mentioned in Section 6.7, but it is not calculated since the end windings are not included in the 2D-model. This inductance is measured in Section 6.10, however.

For the locked-rotor tests, the locked-rotor machine impedance will be derived in Section 6.9. Section 6.10 presents and discusses an experimental verification of the locked-rotor machine impedance. Section 6.11 lists the machine's voltage equation, of which all quantities will by then be developed. The chapter is summarized and concluded in Section 6.12.

6.2 Literature review

6.2.1 Literature review on air gap winding excitation

Some researchers have calculated the magnetic field in the air gap of machines with slotted stators due to the stator currents; these are, among others, [Hug77], [Pol97] and [Zhu93b] (with improvements in [Zhu02]). The approach here is to use an equivalent surface current density, located at the stator surface. For a slotless stator, this approach is not valid, and the field due to the current density in the air gap needs to be calculated directly, which has been done in [Ata98] and [Sri95].

In this chapter, the field due to the current flowing in the air gap winding of a PMSM is calculated. As in [Ata98] and [Sri95], the current density is obtained here by a Fourier-series approximation of the current density for the whole winding region, developed directly from the three-phase winding distribution. The definition of the current density introduced here is slightly different from that in [Ata98]. Another difference between [Ata98] and the work in this thesis is the way in which the machine inductance is calculated. In [Ata98], the magnetic field energy is used to obtain the inductance, while in this thesis, the inductance is calculated directly from the magnetic vector potential, as has been shown in Chapter 4. The reason for this is that it is simpler to use the magnetic vector potential for the field solutions in this thesis than the field energy method.

6.2.2 Literature review on eddy-current reaction fields

The effect of eddy currents upon the field was not considered in the references cited above. In fact, the combination of a current density excitation in an air gap winding and the reaction field of the eddy currents in the shielding cylinder has not been described in literature. However, several researchers have looked at eddy current fields with excitation sources other than a current density. Strictly speaking, the excitation source is unimportant for the calculation of the eddy-current reaction field. However, one aim of this thesis is to develop an analytical model of the complete case-study machine introduced in Chapter 3, and therefore the combination of both these concepts is important.

In the 1960s and 1970s, several textbooks on analytical solutions in electromagnetics were published. Some of these authors also addressed eddy currents, like J. Lammeraner [Lam66] and R.L. Stoll [Sto74]. Since then, many other publications have also addressed the analytical calculation of the magnetic field due to eddy currents. See for example [Ant91], [Ng96], [Den97], [Den98], [Abu99], [Zhu01b] and [Bol02]. Some of the works cited presented their results in Cartesian coordinates ([Lam66], [Sto74], [Ng96] and [Abu99]), while [Ant91], [Den97], [Den98], [Zhu01b] and [Bol02] presented them in cylindrical coordinates. The latter also account for curvature-effects. However, none of these authors solved a six-layer system and as already mentioned, none used a current density in the air gap as excitation. The contribution of this chapter then mainly lies in these aspects of the problem.

6.3 The stator current density

6.3.1 Introduction

To start the analysis, one needs an expression for the current density in the air gap winding. To obtain the current density, the product of the winding distribution and the stator current may be divided by the radius at the centre of the winding and the winding height. For phase *a* this is:

$$J_{sa}(\varphi, t) = \frac{n_{sa}(\varphi) i_{sa}(t)}{h_w r_{wc}}, \tag{6.1}$$

where r_{wc} is given by (5.39). The current densities of the other two phases are identical except for the subscripts of n_{sa} and i_{sa}.

In the following two subsections, expressions for i_{sa} and J_{sa} are developed. The winding distribution n_{sa} was already obtained in Chapter 3, Section 3.7.

6.3.2 Stator current waveforms

In this thesis, only balanced three-phase conditions are considered. Therefore, all triplen harmonics in the stator current waveforms are zero. In terms of the constant

$\ddot{n} \in \mathbb{Z}$, related to the time harmonic by:

$$n = 6\ddot{n} + 1, \tag{6.2}$$

similar to (3.14), the stator current i_{sa} is written as:

$$i_{sa}(t) = \sum_{\ddot{n}=-\infty}^{\infty} \hat{i}_{s,6\ddot{n}+1} \cos\left[(6\ddot{n}+1)\omega_s t\right]. \tag{6.3}$$

For phase *b* this is:

$$i_{sb}(t) = \sum_{\ddot{n}=-\infty}^{\infty} \hat{i}_{s,6\ddot{n}+1} \cos\left[(6\ddot{n}+1)(\omega_s t - \tfrac{2\pi}{3})\right]. \tag{6.4}$$

Phase *c* has same the expression, but with $\frac{2\pi}{3}$ replaced by $\frac{4\pi}{3}$. The double-sided Fourier series in (6.3) and (6.4) contain only non-triplen time harmonic components of the stator current waveforms, exactly as given in Table 3.2 for the space harmonics of the winding distribution.

6.3.3 Stator current density

The stator current density can be obtained from (3.16), (6.1) and (6.3). For phase *a* we have in harmonic component form:

$$J_{sa,6\ddot{k}+1,6\ddot{n}+1}(\varphi, t) = \frac{1}{h_w r_{wc}} \left\{ \hat{n}_{s,6\ddot{k}+1} \cos\left[(6\ddot{k}+1)p\varphi\right] \right\} \cdot$$
$$\left\{ \hat{i}_{s,6\ddot{n}+1} \cos\left[(6\ddot{n}+1)\omega_s t\right] \right\}. \tag{6.5}$$

By rearranging the terms in (6.5) and by doing the double summation, one obtains for the current density of phase *a*:

$$J_{sa}(\varphi, t) = \frac{1}{h_w r_{wc}} \left\{ \sum_{\ddot{k}=-\infty}^{\infty} \sum_{\ddot{n}=-\infty}^{\infty} \hat{n}_{s,6\ddot{k}+1} \hat{i}_{s,6\ddot{n}+1} \cos\left[(6\ddot{k}+1)p\varphi\right] \cos\left[(6\ddot{n}+1)\omega_s t\right] \right\}. \tag{6.6}$$

Similarly, the current density of phase *b* is from (6.4):

$$J_{sb}(\varphi, t) = \frac{1}{h_w r_{wc}} \left\{ \sum_{\ddot{k}=-\infty}^{\infty} \sum_{\ddot{n}=-\infty}^{\infty} \hat{n}_{s,6\ddot{k}+1} \hat{i}_{s,6\ddot{n}+1} \cos\left[(6\ddot{k}+1)(p\varphi - \tfrac{2\pi}{3})\right] \right.$$
$$\left. \cdot \cos\left[(6\ddot{n}+1)(\omega_s t - \tfrac{2\pi}{3})\right] \right\}. \tag{6.7}$$

The expression for phase *c* is similar to (6.7), but with the term $\frac{2\pi}{3}$ replaced by $\frac{4\pi}{3}$.

Equations (6.6), (6.7) and the expression for $J_{sc}(\varphi, t)$ can be rewritten by use of the identity:

$$\cos u \cos v = \tfrac{1}{2}\left[\cos(u - v) + \cos(u + v)\right].$$ (6.8)

Thus, for phase *a*:

$$J_{sa}(\varphi, t) = \frac{1}{h_w r_{wc}} \cdot$$

$$\left\{ \sum_{\ddot{k}=-\infty}^{\infty} \sum_{\ddot{n}=-\infty}^{\infty} \frac{1}{2} \hat{n}_{s,6\ddot{k}+1} \hat{i}_{s,6\ddot{n}+1} \left\{ \cos\left[(6\ddot{k}+1)p\varphi - (6\ddot{n}+1)\omega_s t\right] \right. \right.$$

$$\left. \left. + \cos\left[(6\ddot{k}+1)p\varphi + (6\ddot{n}+1)\omega_s t\right] \right\} \right\}.$$ (6.9)

For phase *b* this is:

$$J_{sb}(\varphi, t) = \frac{1}{h_w r_{wc}} \cdot$$

$$\left\{ \sum_{\ddot{k}=-\infty}^{\infty} \sum_{\ddot{n}=-\infty}^{\infty} \frac{1}{2} \hat{n}_{s,6\ddot{k}+1} \hat{i}_{s,6\ddot{n}+1} \left\{ \cos\left[(6\ddot{k}+1)p\varphi - (6\ddot{n}+1)\omega_s t - 6(\ddot{k}-\ddot{n})\tfrac{2\pi}{3}\right] \right. \right.$$ (6.10)

$$\left. \left. + \cos\left[(6\ddot{k}+1)p\varphi + (6\ddot{n}+1)\omega_s t - [6(\ddot{k}+\ddot{n})+2]\tfrac{2\pi}{3}\right] \right\} \right\},$$

with a similar expression for phase *c*.

The sum of these current densities results in the total current density in the stator winding of the machine:

$$J_s(\varphi, t) = J_{sa}(\varphi, t) + J_{sb}(\varphi, t) + J_{sc}(\varphi, t).$$ (6.11)

Both clockwise and anticlockwise rotating travelling waves are contained in (6.11): the travelling wave rotates clockwise if $\ddot{k} \geq 0 \wedge \ddot{n} \geq 0$ or $\ddot{k} < 0 \wedge \ddot{n} < 0$, and anticlockwise if $\ddot{k} < 0 \wedge \ddot{n} \geq 0$ or $\ddot{k} \geq 0 \wedge \ddot{n} < 0$.

The total current density J_s may be obtained by inspection from (6.9) and (6.10). By comparing the first cosine term in both equations, one sees that they are identical except for the term $6(\ddot{k}-\ddot{n})\tfrac{2\pi}{3}$. Therefore, the sum of these three cosine terms (phase *c* also) may be represented by this simplification:

$$\cos\left[x - y\right] + \cos\left[x - y - 6(\ddot{k}-\ddot{n})\tfrac{2\pi}{3}\right] + \cos\left[x - y - 6(\ddot{k}-\ddot{n})\tfrac{4\pi}{3}\right]$$

$$= \begin{cases} 3\cos\left[x - y\right] & \text{if } 6(\ddot{k}-\ddot{n}) \text{ is a multiple of 3} \\ 0 & \text{otherwise} \end{cases}$$ (6.12)

The above reasoning may be applied to the whole of J_s as:

$$J_s(\varphi, t) = \begin{cases} 3J_{sa}(\varphi, t) & \text{if } 6(\ddot{k}-\ddot{n}) = 3L, \ L \in \mathbb{Z}, \\ & \text{i.e., if } 2(\ddot{k}-\ddot{n}) = L \\ 0 & \text{otherwise} \end{cases}$$ (6.13)

Similarly, from the second cosine term in (6.9) and (6.10) may be deduced:

$$
J_s(\varphi, t) = \begin{cases} 3J_{sa}(\varphi, t) & \text{if } 6(\ddot{k} + \ddot{n}) + 2 = 3M, \ M \in \mathbb{Z}, \\ & \text{i.e. if } 2(\ddot{k} + \ddot{n}) + \frac{2}{3} = M \\ 0 & \text{otherwise} \end{cases} \tag{6.14}
$$

The conditional in (6.13) is true for all $\ddot{k}$ and $\ddot{n}$, while that in (6.14) is false for all $\ddot{k}$ and $\ddot{n}$. Therefore, only the first cosine term contributes to the total current density, and J_s may be written as:

$$
J_s(\varphi, t) = \sum_{\ddot{k}=-\infty}^{\infty} \sum_{\ddot{n}=-\infty}^{\infty} \left\{ \frac{3}{2} \frac{\hat{n}_{s,6\ddot{k}+1} \hat{i}_{s,6\ddot{n}+1}}{h_w r_{wc}} \right\} \left\{ \cos\left[(6\ddot{k}+1)p\varphi - (6\ddot{n}+1)\omega_s t\right] \right\}. \tag{6.15}
$$

Equation (6.15) is written in the *stator reference frame*. For the rotor reference frame, the stator angular variable φ should be replaced with the rotor angular variable ϕ by means of equations (4.1) and (4.2):

$$
\varphi = \phi + \theta = \phi + \omega_m t + \theta_0 / (6\ddot{k} + 1), \tag{6.16}
$$

where θ_0 is the initial rotor positional angle and ω_m the fundamental of the mechanical angular frequency. Substituting (6.16) into (6.15) results in the stator current density as seen by the rotor, i.e. in the *rotor reference frame:*

$$
J_s(\phi, t) = \sum_{\ddot{k}=-\infty}^{\infty} \sum_{\ddot{n}=-\infty}^{\infty} \left\{ \frac{3}{2} \frac{\hat{n}_{s,6\ddot{k}+1} \hat{i}_{s,6\ddot{n}+1}}{h_w r_{wc}} \right\} \left\{ \cos\left[(6\ddot{k}+1)p\phi + 6(\ddot{k} - \ddot{n})\omega_s t + p\theta_0\right] \right\}. \tag{6.17}
$$

6.4   Solution of the magnetic field

6.4.1   Introduction

In Chapter 4, the Poisson equation with eddy-current effects upon the field, equation (4.16), was introduced. For the permanent magnet field of Chapter 5, equation (4.16) was simplified to (4.17).

In this chapter, the permanent magnet excitation is set to zero and the field due to the stator currents is solved, including the effect in all the regions of the eddy currents in the shielding cylinder. Therefore, equation (4.16) is simplified to (4.18), or:

$$
-\nabla^2 \mathbf{A} + \mu\sigma \frac{\partial \mathbf{A}}{\partial t} = \mu \mathbf{J}_s. \tag{6.18}
$$

With the 2D-simplifications discussed in Chapter 4, this equation is:

$$
\frac{\partial^2 A_z}{\partial r^2} + \frac{1}{r^2} \frac{\partial^2 A_z}{\partial \phi^2} + \frac{1}{r} \frac{\partial A_z}{\partial r} + \mu\sigma \frac{\partial A_z}{\partial t} = -\mu J_{s,z}. \tag{6.19}
$$

Table 6.1 lists the machine regions shown in Figure 4.1(a), with the relative permeability of the material and the governing equation used to solve for **A** from (6.19) in each of these regions. As can be seen from Table 6.1, for regions 1, 3, 5 and 6, the Poisson equation simply becomes the Laplace equation $-\nabla^2\mathbf{A} = \mathbf{0}$, and therefore it has the same solution form, differing only in the boundary conditions. Regions 2 and 4 (stator winding and shielding cylinder) demand special care in their solution.

In the next few sections, a solution to the complete system is systematically developed. The result is an expression for the k-th space and n-th time harmonic components of the vector potential in all six regions of the machine, as a function of the two positional coordinates r and φ (or ϕ), and time t.

The solution procedure is identical to that outlined in Section 5.2.3 for the field due to the magnets. The form of the solution is also similar to (5.8), with two important differences:

- The solution developed in this chapter is in terms of both the space and time harmonics k and n, whereas the solution in Chapter 5 was only in terms of the space harmonic.

- The trigonometric expression of (5.8a) is written in this chapter in the complex exponential form. This is done to facilitate the calculation of a derived quantity (the Poynting vector) for the stator current field later on in this chapter and for the combined field in Chapter 7. The real part of the complex vector potential $\bar{A}_z$ is the part with physical significance:

$$A_z(r,\phi,t) \equiv \mathrm{Re}\big\{\bar{A}_z(r,\phi,t)\big\}. \tag{6.20}$$

ν	Description	Range for r	$\mu_r^{(\nu)}$	Governing equation
1	Stator iron	$r_{si} \leq r < r_{so}$	∞	$-\nabla^2\mathbf{A} = \mathbf{0}$
2	Winding region	$r_{so} \leq r < r_w$	1	$-\nabla^2\mathbf{A} = \mu\mathbf{J}_s$
3	Mechanical air gap	$r_w \leq r < r_{ci}$	1	$-\nabla^2\mathbf{A} = \mathbf{0}$
4	Shielding cylinder	$r_{ci} \leq r < r_{co}$	1	$-\nabla^2\mathbf{A} + \mu\sigma\frac{\partial\mathbf{A}}{\partial t} = \mathbf{0}$
5	Permanent magnets	$r_{co} \leq r < r_{mo}$	1	$-\nabla^2\mathbf{A} = \mathbf{0}$
6	Rotor iron	$r_{mo} \leq r \leq r_{ro}$	∞	$-\nabla^2\mathbf{A} = \mathbf{0}$

Table 6.1: Machine regions defined for the calculation of the vector potential from equation (4.16) due to the stator currents, including the reaction field due to the eddy currents in the shielding cylinder.

6.4.2 Solution in Region 4: The shielding cylinder

Introduction

It is important to choose the correct coordinate system within which to solve the system of PDEs. Since the shielding cylinder is fixed to the rotor, the obvious choice for the solution in the cylinder itself, region 4, is the rotor coordinate system. This means that also the excitation $\mathbf{J}_s$, as expressed in the rotor coordinate system by equation (6.17), needs to be used, even though the winding is physically stationary.

The fundamental space and time harmonic of the stator current density will then appear as stationary in the solution, since the whole coordinate system is rotating with this travelling wave.

It is also important to note that if the rotor coordinate system is used to obtain the solution in the shielding cylinder, that the *whole system* of PDEs needs to be solved in this coordinate system to satisfy the boundary conditions.

From Table 6.1, the governing equation for the shielding cylinder region is for the complex vector potential $\bar{\mathbf{A}}$:

$$\nabla^2 \bar{\mathbf{A}} = \mu\sigma \frac{\partial \bar{\mathbf{A}}}{\partial t}, \tag{6.21}$$

which can be rewritten in cylindrical coordinates from (6.19) as:

$$\frac{\partial^2 \bar{A}_z}{\partial r^2} + \frac{1}{r^2} \frac{\partial^2 \bar{A}_z}{\partial \varphi^2} + \frac{1}{r} \frac{\partial \bar{A}_z}{\partial r} = \mu\sigma \frac{\partial \bar{A}_z}{\partial t}, \tag{6.22}$$

the time and space harmonic component of which is:

$$\frac{\partial^2 \bar{A}_{z,6\ddot{k}+1,6\ddot{n}+1}}{\partial r^2} + \frac{1}{r^2} \frac{\partial^2 \bar{A}_{z,6\ddot{k}+1,6\ddot{n}+1}}{\partial \varphi^2} + \frac{1}{r} \frac{\partial \bar{A}_{z,6\ddot{k}+1,6\ddot{n}+1}}{\partial r} = \mu\sigma \frac{\partial \bar{A}_{z,6\ddot{k}+1,6\ddot{n}+1}}{\partial t}. \tag{6.23}$$

In (6.23), $\ddot{k}$ and $\ddot{n}$ are related to the space and time harmonics k and n by (3.14) and (6.2), respectively.

Before the solution is constructed, the current density has to be changed to complex exponential form as motivated in Section 6.4.1.

Current density for when the rotor rotates synchronously with the stator field

The stator current density in rotor coordinates was given by (6.17). The rotor coordinate solution is *the* solution, and it may also be seen as the case where the rotor rotates synchronously with the stator field. Equation (6.17) was written in trigonometric form. We obtain for the k-th space and n-th time harmonic in complex harmonic form:

$$J_{s,6\ddot{k}+1,6\ddot{n}+1}(\phi, t) = \left\{ \frac{3}{2} \frac{\hat{n}_{s,6\ddot{k}+1} \hat{\bar{\imath}}_{s,6\ddot{n}+1}}{h_w r_{wc}} \right\} \mathrm{e}^{-j\left[(6\ddot{k}+1)p\phi + 6(\ddot{k}-\ddot{n})\omega_s t + p\theta_0\right]}. \tag{6.24}$$

The k-th space and n-th time harmonic of equation (6.17) is the real part of (6.24).

Current density for a locked rotor

The locked-rotor form of (6.24) is, by use of (6.16) with $\omega_m = 0$:

$$J_{s,6\ddot{k}+1,6\ddot{n}+1}(\varphi, t) = \left\{ \frac{3}{2} \frac{\hat{n}_{s,6\ddot{k}+1}\hat{i}_{s,6\ddot{n}+1}}{h_w r_{wc}} \right\} \mathrm{e}^{-j\left[(6\ddot{k}+1)p\varphi - 6(\ddot{n}-1)\omega_s t\right]}. \tag{6.25}$$

Assumed solution for a synchronously rotating rotor

The assumed solution of $\bar{A}_z$ for a synchronously rotating rotor is chosen to comply with the stator current density for this case, equation (6.24):

$$\bar{A}_z(r, \phi, t) = \sum_{\ddot{k}=-\infty}^{\infty} \sum_{\ddot{n}=-\infty}^{\infty} \hat{\bar{A}}_{z,6\ddot{k}+1,6\ddot{n}+1}(r) \left\{ \frac{3}{2} \frac{\hat{n}_{s,6\ddot{k}+1}\hat{i}_{s,6\ddot{n}+1}}{h_w r_{wc}} \right\} \mathrm{e}^{-j\left[(6\ddot{k}+1)p\phi + 6(\ddot{k}-\ddot{n})\omega_s t + p\theta_0\right]}. \tag{6.26}$$

The space and time harmonic component of (6.26) is:

$$\bar{A}_{z,6\ddot{k}+1,6\ddot{n}+1}(r, \phi, t) = \hat{\bar{A}}_{z,6\ddot{k}+1,6\ddot{n}+1}(r) \left\{ \frac{3}{2} \frac{\hat{n}_{s,6\ddot{k}+1}\hat{i}_{s,6\ddot{n}+1}}{h_w r_{wc}} \right\} \mathrm{e}^{-j\left[(6\ddot{k}+1)p\phi + 6(\ddot{k}-\ddot{n})\omega_s t + p\theta_0\right]}, \tag{6.27}$$

with partial time derivative:

$$\frac{\partial}{\partial t}\bar{A}_{z,6\ddot{k}+1,6\ddot{n}+1}(r, \phi, t) =$$
$$- 6j(\ddot{k}-\ddot{n})\omega_s \hat{\bar{A}}_{z,6\ddot{k}+1,6\ddot{n}+1}(r) \left\{ \frac{3}{2} \frac{\hat{n}_{s,6\ddot{k}+1}\hat{i}_{s,6\ddot{n}+1}}{h_w r_{wc}} \right\} \mathrm{e}^{-j\left[(6\ddot{k}+1)p\phi + 6(\ddot{k}-\ddot{n})\omega_s t + p\theta_0\right]}. \tag{6.28}$$

Equation (6.28) may be rewritten from (6.27) as:

$$\frac{\partial}{\partial t}\bar{A}_{z,6\ddot{k}+1,6\ddot{n}+1}(r, \phi, t) = -6j(\ddot{k}-\ddot{n})\omega_s \bar{A}_{z,6\ddot{k}+1,6\ddot{n}+1}(r, \phi, t). \tag{6.29}$$

Substituting (6.29) into the right-hand side of (6.23) results in:

$$\mu\sigma \frac{\partial}{\partial t}\bar{A}_{z,6\ddot{k}+1,6\ddot{n}+1}(r, \phi, t) \equiv \bar{\tau}^2_{6\ddot{k}+1,6\ddot{n}+1}\bar{A}_{z,6\ddot{k}+1,6\ddot{n}+1}(r, \phi, t), \tag{6.30}$$

where a constant $\bar{\tau}^2_{6\ddot{k}+1,6\ddot{n}+1}$ has been defined as:

$$\bar{\tau}^2_{6\ddot{k}+1,6\ddot{n}+1} \equiv -6j\mu\sigma(\ddot{k}-\ddot{n})\omega_s. \tag{6.31}$$

Assumed solution for a locked rotor

To comply with the stator current density for a locked rotor, equation (6.25), the *k*-th space and *n*-th time harmonic of the assumed solution of $\bar{A}_z$ is for this case:

$$\bar{A}_{z,6\ddot{k}+1,6\ddot{n}+1}(r, \varphi, t) = \hat{\bar{A}}_{z,6\ddot{k}+1,6\ddot{n}+1}(r) \left\{ \frac{3}{2} \frac{\hat{n}_{s,6\ddot{k}+1}\hat{i}_{s,6\ddot{n}+1}}{h_w r_{wc}} \right\} \mathrm{e}^{-j\left[(6\ddot{k}+1)p\varphi - (6\ddot{n}+1)\omega_s t\right]}. \tag{6.32}$$

In this case, the the right-hand side of (6.23) is:

$$\mu\sigma\frac{\partial}{\partial t}\bar{A}_{z,6\ddot{k}+1,6\ddot{n}+1}(r,\varphi,t) \equiv \bar{\tau}^2_{6\ddot{n}+1}\bar{A}_{z,6\ddot{k}+1,6\ddot{n}+1}(r,\varphi,t), \qquad (6.33)$$

where the constant $\bar{\tau}^2_{6\ddot{n}+1}$ is not a function of the space harmonic anymore as in (6.31):

$$\bar{\tau}^2_{6\ddot{n}+1} \equiv j\mu\sigma(6\ddot{n}+1)\omega_s. \qquad (6.34)$$

In the next subsection it will be shown that due to the different constants $\bar{\tau}^2_{6\ddot{k}+1,6\ddot{n}+1}$ and $\bar{\tau}^2_{6\ddot{n}+1}$ of (6.31) and (6.34), the solution of the differential equations in Region 4 is different for the rotating and locked-rotor cases.

6.4.3   Solution in Region 4 for a synchronously rotating rotor

As in Chapter 5, here product solutions also form the basis of the solutions. If a product solution is assumed for the vector potential in the shielding cylinder for a synchronously rotating rotor, i.e.,

$$\bar{A}_{z,6\ddot{k}+1,6\ddot{n}+1}(r,\phi,t) = \bar{R}_{6\ddot{k}+1,6\ddot{n}+1}(r)\bar{F}_{6\ddot{k}+1,6\ddot{n}+1}(\phi,t), \qquad (6.35)$$

then equation (6.23) can be rewritten as:

$$\left[\frac{r^2}{\bar{R}_{6\ddot{k}+1,6\ddot{n}+1}}\frac{d^2\bar{R}_{6\ddot{k}+1,6\ddot{n}+1}}{dr^2} + \frac{r}{\bar{R}_{6\ddot{k}+1,6\ddot{n}+1}}\frac{d\bar{R}_{6\ddot{k}+1,6\ddot{n}+1}}{dr}\right]$$
$$+ \left[\frac{1}{\bar{F}_{6\ddot{k}+1,6\ddot{n}+1}}\frac{d^2\bar{F}_{6\ddot{k}+1,6\ddot{n}+1}}{d\phi^2}\right] = \bar{\tau}^2_{6\ddot{k}+1,6\ddot{n}+1}r^2, \quad (6.36)$$

which is separated into two ordinary differential equations. Therefore these two ordinary differential equations can be written as:

$$\frac{1}{\bar{F}_{6\ddot{k}+1,6\ddot{n}+1}}\frac{d^2\bar{F}_{6\ddot{k}+1,6\ddot{n}+1}}{d\phi^2} \equiv -(6\ddot{k}+1)^2, \qquad (6.37)$$

and:

$$r^2\frac{d^2\bar{R}_{6\ddot{k}+1,6\ddot{n}+1}}{dr^2} + r\frac{d\bar{R}_{6\ddot{k}+1,6\ddot{n}+1}}{dr} - \left[\bar{\tau}^2_{6\ddot{k}+1,6\ddot{n}+1}r^2 + (6\ddot{k}+1)^2\right]R_{6\ddot{k}+1,6\ddot{n}+1} = 0. \quad (6.38)$$

Equation (6.38) is a modified Bessel equation [McL55].

Solution for $\bar{R}$

From (6.31) it can be seen that if the space and time harmonics are equal to one another, i.e. $6\ddot{k}+1 = 6\ddot{n}+1$, then $\bar{\tau}^2_{6\ddot{k}+1,6\ddot{n}+1} = 0$. This leads to the modified Bessel equation (6.38), reducing to a non-Bessel equation. In fact, it reduces to the same

differential equation as the one obtained in the solution of the magnetic fields due to the permanent magnets in Chapter 5. Therefore, the solution to (6.38) is separated into the two cases where $\ddot{k} = \ddot{n}$ and $\ddot{k} \neq \ddot{n}$. Thus, a general solution to (6.38) can be written as:

$$\bar{R}_{6\ddot{k}+1,6\ddot{n}+1}(r) = \begin{cases} \bar{c}_{6\ddot{k}+1,6\ddot{n}+1} I_{6\ddot{k}+1}(\bar{\tau}_{6\ddot{k}+1,6\ddot{n}+1}r) + \bar{d}_{6\ddot{k}+1,6\ddot{n}+1} K_{6\ddot{k}+1}(\bar{\tau}_{6\ddot{k}+1,6\ddot{n}+1}r) \\ \qquad\qquad\qquad\qquad\qquad\qquad\qquad\qquad\qquad \text{if } \ddot{k} \neq \ddot{n} \\[2mm] \bar{c}_{6\ddot{k}+1,6\ddot{n}+1} \left(\dfrac{r}{r_4}\right)^{-|6\ddot{k}+1|p} + \bar{d}_{6\ddot{k}+1,6\ddot{n}+1} \left(\dfrac{r}{r_4}\right)^{|6\ddot{k}+1|p} \quad \text{if } \ddot{k} = \ddot{n}, \end{cases}$$

$$(6.39)$$

where $I_{6\ddot{k}+1}$ and $K_{6\ddot{k}+1}$ are modified Bessel functions of the first and second kind of order $6\ddot{k} + 1$, and $\bar{c}_{6\ddot{k}+1,6\ddot{n}+1}$ and $\bar{d}_{6\ddot{k}+1,6\ddot{n}+1}$ are constants to be determined from the boundary conditions. Bessel functions are briefly summarized in Appendix C.

Solution for $\bar{F}$

The general solution to (6.37) was discussed in Chapter 5 and may be written in many forms. By choosing a form similar to the solution of the vector potential (6.27), we have:

$$\bar{R}_{6\ddot{k}+1,6\ddot{n}+1}(\phi,t) = a_{6\ddot{k}+1,6\ddot{n}+1} e^{-j\left[(6\ddot{k}+1)p\phi + 6(\ddot{k}-\ddot{n})\omega_s t + p\theta_0\right]}, \tag{6.40}$$

with $a_{6\ddot{k}+1,6\ddot{n}+1}$ a boundary condition constant.

Product solution $\bar{R}\bar{F}$

The k-th space and n-th time harmonic of the solution to Poisson's equation (6.23) in the shielding cylinder ($\nu = 4$) is, from (6.35), (6.39) and (6.40):

$$\bar{A}_{z,6\ddot{k}+1,6\ddot{n}+1}(r,\phi,t) = \hat{\bar{A}}_{z,6\ddot{k}+1,6\ddot{n}+1}(r) \left\{ \frac{3}{2} \frac{\hat{n}_{s,6\ddot{k}+1}\hat{\bar{i}}_{s,6\ddot{n}+1}}{h_w r_{wc}} \right\} e^{-j\left[(6\ddot{k}+1)p\phi + 6(\ddot{k}-\ddot{n})\omega_s t + p\theta_0\right]};$$

$$(6.41a)$$

$$\hat{\bar{A}}_{z,6\ddot{k}+1,6\ddot{n}+1}(r) = \begin{cases} \bar{C}^{(\nu)}_{6\ddot{k}+1,6\ddot{n}+1} I_{6\ddot{k}+1}(\bar{\tau}_{6\ddot{k}+1,6\ddot{n}+1}r) + \bar{D}^{(\nu)}_{6\ddot{k}+1,6\ddot{n}+1} K_{6\ddot{k}+1}(\bar{\tau}_{6\ddot{k}+1,6\ddot{n}+1}r) \\ \qquad\qquad\qquad\qquad\qquad\qquad\qquad\qquad\qquad \text{if } \ddot{k} \neq \ddot{n} \\[2mm] \bar{C}^{(\nu)}_{6\ddot{k}+1,6\ddot{n}+1} \left(\dfrac{r}{r_4}\right)^{-|6\ddot{k}+1|p} + \bar{D}^{(\nu)}_{6\ddot{k}+1,6\ddot{n}+1} \left(\dfrac{r}{r_4}\right)^{|6\ddot{k}+1|p} \quad \text{if } \ddot{k} = \ddot{n}, \end{cases}$$

$$(6.41b)$$

where the boundary condition constants $a_{6\ddot{k}+1,6\ddot{n}+1}\bar{c}_{6\ddot{k}+1,6\ddot{n}+1}$ and $a_{6\ddot{k}+1,6\ddot{n}+1}\bar{d}_{6\ddot{k}+1,6\ddot{n}+1}$ have been replaced by $\bar{C}^{(\nu)}_{6\ddot{k}+1,6\ddot{n}+1}$ and $\bar{D}^{(\nu)}_{6\ddot{k}+1,6\ddot{n}+1}$, respectively.

The fact that the solution is different for the two cases in (6.41b) has the consequence that the boundary condition constants are different, not only in Region 4, but in all the regions. This is not explicitly indicated in the solutions of the different regions in this chapter, but implicitly in the indices of the boundary condition constants. If this was not done, i.e., if different boundary condition constants were

introduced for the two different cases, the equations would have been unnecessarily complicated by more symbols. The fact that the solution in the winding region, discussed in Section 6.4.5, also has two cases in its solution, makes this argument even stronger.

6.4.4   Solution in Region 4 for a locked rotor

Since the constant $\bar{\tau}_{6\ddot{n}+1}$ of (6.34) does not contain the space harmonic, it is valid for all $\ddot{k}$ and $\ddot{n}$. This means the differential equation for $\bar{R}$ is a modified Bessel equation for all $\ddot{k}$ and $\ddot{n}$ and the solution for a locked rotor do not have two cases as in Section 6.4.3 for a synchronously rotating rotor. From (6.32) and (6.41b) the solution is:

$$\bar{A}_{z,6\ddot{k}+1,6\ddot{n}+1}(r,\varphi,t) = \hat{\bar{A}}_{z,6\ddot{k}+1,6\ddot{n}+1}(r) \left\{ \frac{3}{2} \frac{\hat{n}_{s,6\ddot{k}+1}\hat{i}_{s,6\ddot{n}+1}}{h_w r_{wc}} \right\} e^{-j\left[(6\ddot{k}+1)p\varphi - 6(\ddot{n}+1)\omega_s t\right]};$$
(6.42a)

$$\hat{\bar{A}}_{z,6\ddot{k}+1,6\ddot{n}+1}(r) = \bar{C}^{(\nu)}_{6\ddot{k}+1,6\ddot{n}+1} I_{6\ddot{k}+1}(\bar{\tau}_{6\ddot{k}+1,6\ddot{n}+1}r) + \bar{D}^{(\nu)}_{6\ddot{k}+1,6\ddot{n}+1} K_{6\ddot{k}+1}(\bar{\tau}_{6\ddot{k}+1,6\ddot{n}+1}r).$$
(6.42b)

6.4.5   Solution in Region 2: The stator winding

Introduction

In the stator winding, the governing equation for this region is, from Table 6.1:

$$\nabla^2 \bar{\mathbf{A}} = -\mu \bar{\mathbf{J}}_s,$$
(6.43)

which can be rewritten in cylindrical coordinates and with the assumptions made earlier in this chapter as:

$$\frac{\partial^2 \bar{A}_z}{\partial r^2} + \frac{1}{r^2}\frac{\partial^2 \bar{A}_z}{\partial \phi^2} + \frac{1}{r}\frac{\partial \bar{A}_z}{\partial r} = -\mu \bar{J}_s,$$
(6.44)

the time and space harmonic component of which is:

$$\frac{\partial^2 \bar{A}_{z,6\ddot{k}+1,6\ddot{n}+1}}{\partial r^2} + \frac{1}{r^2}\frac{\partial^2 \bar{A}_{z,6\ddot{k}+1,6\ddot{n}+1}}{\partial \phi^2} + \frac{1}{r}\frac{\partial \bar{A}_{z,6\ddot{k}+1,6\ddot{n}+1}}{\partial r} = -\mu \bar{J}_{s,6\ddot{k}+1,6\ddot{n}+1}.$$
(6.45)

Homogeneous solution

The solution to the Poisson equation (6.45) can be written as the sum of a homogeneous and a particular solution as follows:

$$\bar{A}_{z,6\ddot{k}+1,6\ddot{n}+1}(r,\phi) = \bar{A}_{hom,z,6\ddot{k}+1,6\ddot{n}+1}(r,\phi) + \bar{A}_{part,z,6\ddot{k}+1,6\ddot{n}+1}(r,\phi),$$
(6.46)

where the homogeneous solution $\bar{A}_{hom,z,6\ddot{k}+1,6\ddot{n}+1}(r,\phi)$ satisfies the Laplace equation associated with (6.45), i.e.:

$$\frac{\partial^2 \bar{A}_{z,6\ddot{k}+1,6\ddot{n}+1}}{\partial r^2} + \frac{1}{r^2}\frac{\partial^2 \bar{A}_{z,6\ddot{k}+1,6\ddot{n}+1}}{\partial \phi^2} + \frac{1}{r}\frac{\partial \bar{A}_{z,6\ddot{k}+1,6\ddot{n}+1}}{\partial r} = 0, \qquad (6.47)$$

and the particular solution $\bar{A}_{part,z,6\ddot{k}+1,6\ddot{n}+1}(r,\phi)$ satisfies (6.45).

The homogeneous solution is similar to (5.6), but now the more general exponential form is chosen instead of the trigonometric form. It is given (without the subscript *hom*) by:

$$\bar{A}^{(\nu)}_{z,6\ddot{k}+1,6\ddot{n}+1}(r,\phi,t) = \hat{\bar{A}}^{(\nu)}_{z,6\ddot{k}+1,6\ddot{n}+1}(r) \left\{ \frac{3}{2}\frac{\hat{n}_{s,6\ddot{k}+1}\hat{\bar{i}}_{s,6\ddot{n}+1}}{h_w r_{wc}} \right\} e^{-j\left[(6\ddot{k}+1)p\phi+6(\ddot{k}-\ddot{n})\omega_s t+p\theta_0\right]};$$

$$(6.48a)$$

$$\hat{\bar{A}}^{(\nu)}_{z,6\ddot{k}+1,6\ddot{n}+1}(r) = \bar{C}^{(\nu)}_{6\ddot{k}+1,6\ddot{n}+1}\left(\frac{r}{r_2}\right)^{-|6\ddot{k}+1|p} + \bar{D}^{(\nu)}_{6\ddot{k}+1,6\ddot{n}+1}\left(\frac{r}{r_2}\right)^{|6\ddot{k}+1|p}, \qquad (6.48b)$$

where ν again indicates the region, in this case $\nu = 2$.

Particular solution

In the solution to Poisson's equation (6.45), equation (6.48) forms the homogeneous part of the solution, $\bar{A}^{(\nu)}_{hom,z,6\ddot{k}+1,6\ddot{n}+1}(r,\phi,t)$. The particular solution may be written as:

$$\bar{A}^{(\nu)}_{part,z,6\ddot{k}+1,6\ddot{n}+1}(r,\phi,t) = \hat{\bar{A}}^{(\nu)}_{part,z,6\ddot{k}+1}(r) \left\{ \frac{3}{2}\frac{\hat{n}_{s,6\ddot{k}+1}\hat{\bar{i}}_{s,6\ddot{n}+1}}{h_w r_{wc}} \right\} e^{-j\left[(6\ddot{k}+1)p\phi+6(\ddot{k}-\ddot{n})\omega_s t+p\theta_0\right]}.$$

$$(6.49)$$

Therefore, the *k*-th space and *n*-th time harmonic component of the solution to Poisson's equation (6.45) can be written as:

$$\bar{A}^{(\nu)}_{z,6\ddot{k}+1,6\ddot{n}+1}(r,\phi,t) = \hat{\bar{A}}^{(\nu)}_{z,6\ddot{k}+1,6\ddot{n}+1}(r) \left\{ \frac{3}{2}\frac{\hat{n}_{s,6\ddot{k}+1}\hat{\bar{i}}_{s,6\ddot{n}+1}}{h_w r_{wc}} \right\} e^{-j\left[(6\ddot{k}+1)p\phi+6(\ddot{k}-\ddot{n})\omega_s t+p\theta_0\right]};$$

$$(6.50a)$$

$$\hat{\bar{A}}^{(\nu)}_{z,6\ddot{k}+1,6\ddot{n}+1}(r) = \bar{C}^{(\nu)}_{6\ddot{k}+1,6\ddot{n}+1}\left(\frac{r}{r_2}\right)^{-|6\ddot{k}+1|p}$$

$$+ \bar{D}^{(\nu)}_{6\ddot{k}+1,6\ddot{n}+1}\left(\frac{r}{r_2}\right)^{|6\ddot{k}+1|p} + \hat{\bar{A}}^{(\nu)}_{part,z,6\ddot{k}+1}(r). \quad (6.50b)$$

For an excitation as given by (6.25), the *k*-th space and *n*-th time harmonic component of the peak value of the particular solution in the winding region ($\nu = 2$) is:

$$\hat{\bar{A}}^{(\nu)}_{part,z,6\ddot{k}+1}(r) = \begin{cases} \dfrac{\mu r^2}{\left[(6\ddot{k}+1)p\right]^2-4} & \text{if } (6\ddot{k}+1)p \neq 2 \\[2mm] \frac{1}{4}\mu r^2\left(-\ln(r)+\frac{1}{4}\right) & \text{if } (6\ddot{k}+1)p = 2 \end{cases} \qquad (6.51)$$

It can be seen that the peak value is the same for all time harmonics.

Solution for a locked rotor

Equation (6.50) was developed for a synchronously rotating rotor. To obtain the corresponding solution for a locked rotor, the term $e^{-j\left[(6\ddot{k}+1)p\phi+6(\ddot{k}-\ddot{n})\omega_s t+p\theta_0\right]}$ is replaced by $e^{-j\left[(6\ddot{k}+1)p\varphi-(6\ddot{n}+1)\omega_s t\right]}$.

6.4.6   Solution in Regions 1, 3, 5 and 6

The k-th space and n-th time harmonic component of the general solution to the Laplace equation (6.47) is given by (6.48). This solution is valid in regions 1, 3, 5 and 6.

6.4.7   Conclusive remarks

It should be remembered that the solution in the winding region had two cases: one for $(6\ddot{k}+1)p \neq 2$ and one for $(6\ddot{k}+1)p = 2$, and the solution in the shielding cylinder also had two cases: one for $\ddot{k} \neq \ddot{n}$ and one for $\ddot{k} = \ddot{n}$. This leads to four different cases, each for which the *entire* system of boundary condition constants of the solutions to the PDEs in all six regions had to be solved. The boundary condition constants were solved from the boundary condition equations (5.3) and (5.4) in MAPLE® V. The complete system of solutions was implemented in MATLAB® 5.

In summary, the solutions in the different regions are, for a synchronously rotating rotor:

- Regions 1,3,5 and 6: $\bar{A}^{(\nu)}_{z,6\ddot{k}+1,6\ddot{n}+1}(r,\phi,t)$ given by (6.48);

- Region 2: $\bar{A}^{(\nu)}_{z,6\ddot{k}+1,6\ddot{n}+1}(r,\phi,t)$ given by (6.50) for two different cases: $(6\ddot{k}+1)p \neq 2$ and $(6\ddot{k}+1)p = 2$; and

- Region 4: $\bar{A}^{(\nu)}_{z,6\ddot{k}+1,6\ddot{n}+1}(r,\phi,t)$ given by (6.41) for the two different cases $\ddot{k} \neq \ddot{n}$ and $\ddot{k} = \ddot{n}$ of equation (6.51).

For each of the four different cases, the whole system of PDEs was solved in all six regions. The boundary condition constants therefore reflect these different cases. A summary is shown in Figure 6.1.

For the solution for a locked rotor, the difference between cases $\ddot{k} \neq \ddot{n}$ and $\ddot{k} = \ddot{n}$ disappears, i.e., only the first line of (6.41b) is valid with $\bar{\tau}_{6\ddot{k}+1,6\ddot{n}+1}$ replaced by $\bar{\tau}_{6\ddot{n}+1}$. In Figure 6.1, only the top branch is now valid. The final change is to replace the term $e^{-j\left[(6\ddot{k}+1)p\phi+6(\ddot{k}-\ddot{n})\omega_s t+p\theta_0\right]}$ with $e^{-j\left[(6\ddot{k}+1)p\varphi-6(\ddot{n}+1)\omega_s t\right]}$.

$$\bar{C}^{(\nu)}_{6\ddot{k}+1,6\ddot{n}+1},\bar{D}^{(\nu)}_{6\ddot{k}+1,6\ddot{n}+1} \begin{array}{l} \nearrow \quad \ddot{k} \neq \ddot{n} \begin{array}{l} \nearrow (6\ddot{k}+1)p \neq 2 \\ \searrow (6\ddot{k}+1)p = 2 \end{array} \\ \searrow \quad \ddot{k} = \ddot{n} \begin{array}{l} \nearrow (6\ddot{k}+1)p \neq 2 \\ \searrow (6\ddot{k}+1)p = 2 \end{array} \end{array}$$

for $\nu = 1, 2, 3, 4, 5, 6$ and $\ddot{k}, \ddot{n} \in \mathbb{Z}$
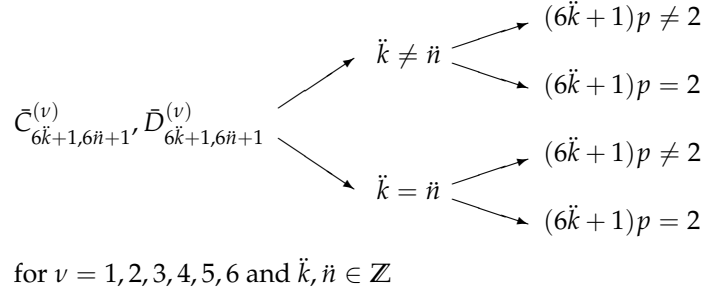
Figure 6.1: Summary of different cases for a synchronously rotating rotor for the boundary condition constants.

6.5 Results of the magnetic field solution

Investigating the magnetic flux density at a DC current in the stator winding gives some insight into the effect of the slotless winding and its distribution on the magnetic field.

For the solution of the system of PDEs for DC currents, equation (6.41) for $\ddot{k} = \ddot{n}$ should be used, since in this case, the time harmonic actually does not exist. The differential equation in the shielding cylinder region is thus a non-Bessel equation. The lower branch of Figure 6.1 is used to determine the boundary condition constants for DC currents.

Figure 6.2 shows the magnetic flux density at four different radii for a locked rotor due to the currents $i_a = 0$, $i_b = 260.6\text{A} = -i_c$ flowing in the air gap winding. The slotting effect of the 1-2-2-1 winding distribution of Figure 3.8 on the magnetic field can clearly be identified in Figure 6.2.

For a synchronously rotating rotor, Figure 6.3 shows the magnetic field lines due to AC stator currents in the air gap winding. In Figure 6.3(a), the flux lines for the fundamental space harmonic $k = 1$ and fundamental time harmonic $n = 1$ are shown, while Figure 6.3(b) shows the same space harmonic with the fifth time harmonic component. It can clearly be seen from Figure 6.3(b) that the shielding cylinder almost perfectly shields the magnets even at frequencies as low as the fifth time harmonic, while in Figure 6.3(a), the magnetic field passes through the cylinder, as would be expected. This result was calculated for a typical current waveform of a current source inverter (CSI) for a rotational speed of the flywheel of 30 000 rpm.

For the field calculation of Figure 6.3, the radial and tangential components of the flux density at several different radii for a synchronously rotating rotor are shown in Figure 6.4. Figure 6.4 shows the flux density for three different time harmonics: (a) $n = 1$, (b) $n = 5$, and (c) $n = 11$. In all three, the space harmonic components were added for $k = 1, 5, 7, 11, 13$. The calculation of Figure 6.4 was done at two radii: r_{wc} in the centre of the air gap and r_{mc} in the centre of the permanent-magnet array.
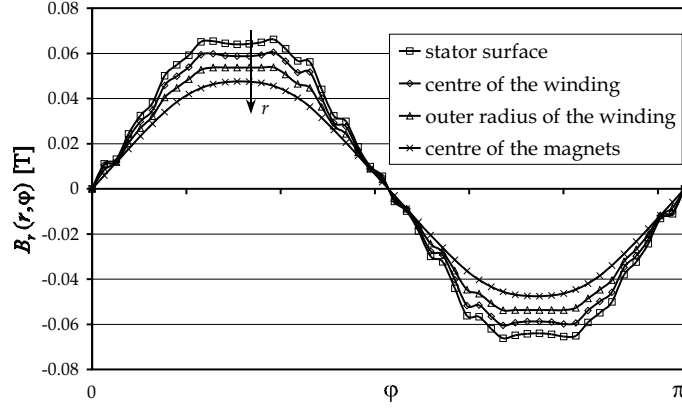
Figure 6.2: Radial component of the flux density at several different radii for a locked rotor due to the currents $i_a = 0$, $i_b = 260.6\text{A} = -i_c$ flowing in the air gap winding.

Figure 6.4 shows the shielding effect of the shielding cylinder in another way than Figure 6.3. In Figure 6.4(a) for $n = 1$, the field at the centre of the winding contains higher space harmonics, which are filtered out at the centre of the magnets,
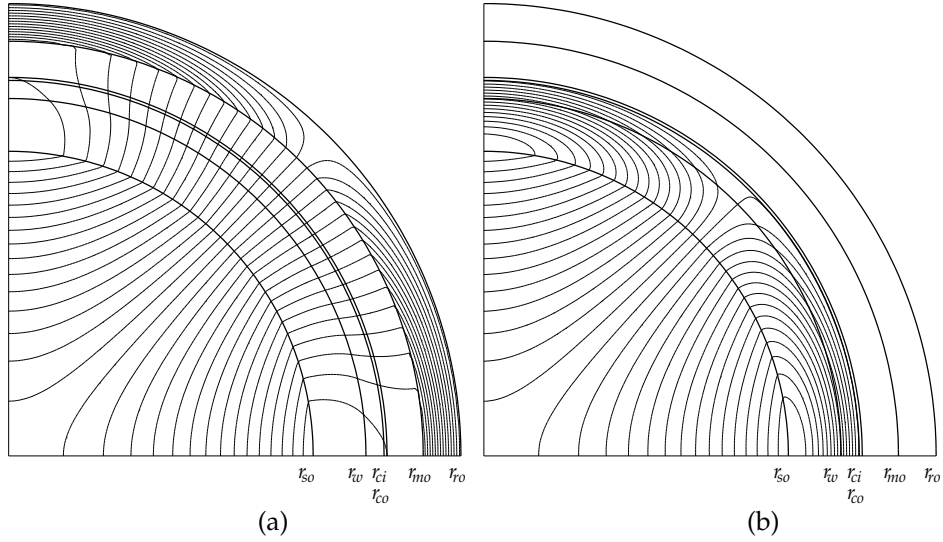
Figure 6.3: Magnetic field lines for a synchronously rotating rotor due to AC stator currents in the air gap winding, including the eddy-current reaction field of the shielding cylinder, for: (a) $k = 1$, $n = 1$; (b) $k = 1$, $n = 5$.

hence only the fundamental space harmonic is present. Similarly, Figure 6.4(b) for $n = 5$ shows that higher space harmonics are present in the field at r_{wc}, but only the fifth space harmonic is allowed to pass through the shielding cylinder, as is evident from the waveform at r_{mc}. This effect also occurs in Figure 6.4(c), but the eleventh space harmonic is too small to see.

The magnetic field calculation model is hereby concluded. As in Chapter 5 for the permanent-magnet field, the next section starts with the derivation of useful quantities from this field. Particularly, the subject under attention in the next section is the flux linkage of the stator winding due to the field just derived, from which the stator main-field inductance naturally follows.
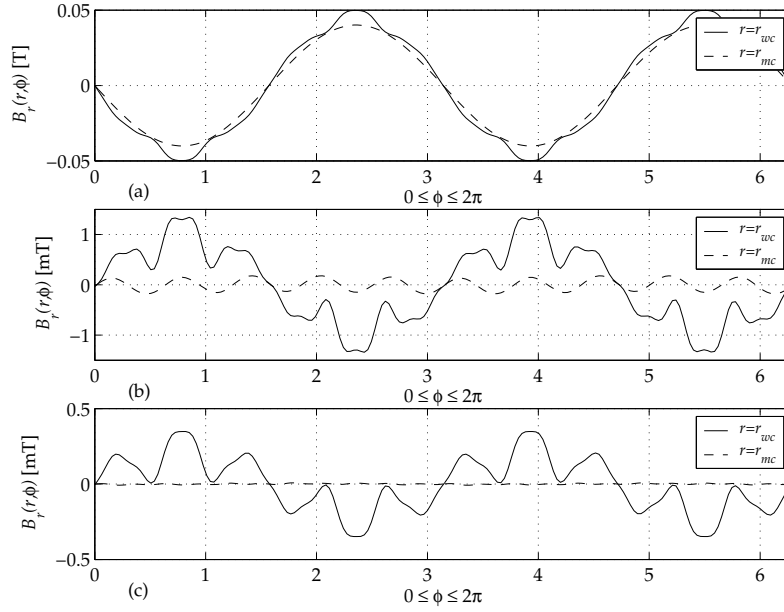
Figure 6.4: Magnetic flux density for a synchronously rotating rotor due to AC stator currents in the air gap winding, including the eddy-current reaction field of the shielding cylinder. Results for two radii are shown: at the centre of the winding and at the centre of the permanent magnets. These results were calculated as the sum of space harmonics $k = 1, 5, 7, 11, 13$. Time harmonics are: (a) $n = 1$; (b) $n = 5$; and (c) $n = 11$.

6.6   The stator main-field inductance

6.6.1   Introduction

For the calculation of the flux linkage, equation (5.32) is valid for any magnetic field source, as discussed in Chapter 5. Therefore, for the flux linkage of the stator winding due to the stator currents, the vector potential due to the stator currents should be substituted into (5.32). In the next two subsections, this flux linkage is worked out, leading to the machine's main-field inductance. The next subsection discusses the calculation and the one after that presents the calculated machine inductance for the EμFER machine.

Assumptions

Two assumptions are made for the inductance calculations. They are:

- *Symmetry.* For the inductance, symmetry is assumed. This means that the inductance of one phase is equal to that of the others and that the mutual inductances are also equal for all three phases. For this assumption, the flux linkage may be written in a general form as follows:

$$\begin{bmatrix} \lambda_{ssa} \\ \lambda_{ssb} \\ \lambda_{ssc} \end{bmatrix} = \begin{bmatrix} L & M & M \\ M & L & M \\ M & M & L \end{bmatrix} \begin{bmatrix} i_{sa} \\ i_{sb} \\ i_{sc} \end{bmatrix} \tag{6.52}$$

- *Balanced three-phase currents.* For balanced three-phase currents, the triplen terms are zero and the non-triplen mutual inductance terms are all equal to each other. Thus, equation (6.52) may be written as:

$$\begin{bmatrix} \lambda_{ssa} \\ \lambda_{ssb} \\ \lambda_{ssc} \end{bmatrix} = \begin{bmatrix} L-M & 0 & 0 \\ 0 & L-M & 0 \\ 0 & 0 & L-M \end{bmatrix} \begin{bmatrix} i_{sa} \\ i_{sb} \\ i_{sc} \end{bmatrix} \tag{6.53}$$

Since the non-triplens have already been neglected in this thesis, the flux linkage resulting from the method documented in the next sections is of the form (6.53).

6.6.2   Calculation

The vector potential in the air gap due to the stator currents was written in complex form in this chapter. For the flux linkage, the real part is explicitly used, given by (6.20). Thus in this section, the real part of $\bar{A}^{(\nu)}_{z,6\ddot{k}+1,6\ddot{n}+1}(r,\phi,t)$ will be used, indicated by $A^{(\nu)}_{z,6\ddot{k}+1,6\ddot{n}+1}(r,\phi,t)$, where $\nu = 2$.

The flux linkage of winding a due to the stator currents is, from (5.32):

$$\lambda_{ssa,6\ddot{k}+1,6\ddot{n}+1}(t) = 2p\,l_s \int_0^{\pi/p} n_{sa}(\varphi)\, A^{(2)}_{z,6\ddot{k}+1,6\ddot{n}+1}(r_{wc}, \varphi, t)\, d\varphi, \tag{6.54}$$

where the flux linkage integral is located at $r = r_{wc}$, the centre of the winding. From (3.10) and (6.25), equation (6.54) may be written, in stator coordinates, as:

$$\lambda_{ssa,6\ddot{k}+1,6\ddot{n}+1}(t) = 2pl_s\hat{n}_{s,k} \left\{ \frac{3}{2} \frac{\hat{n}_{s,6\ddot{k}+1}\hat{i}_{s,6\ddot{n}+1}}{h_w r_{wc}} \right\} \hat{A}^{(2)}_{z,6\ddot{k}+1,6\ddot{n}+1}(r_{wc}) \cdot$$

$$\cdot \int_0^{\pi/p} \cos\left[(6\ddot{k}+1)p\varphi\right] \cos\left[(6\ddot{k}+1)p\varphi - (6\ddot{n}+1)\omega_s t\right] d\varphi. \tag{6.55}$$

If (6.55) is integrated, one obtains:

$$\lambda_{ssa,6\ddot{k}+1,6\ddot{n}+1}(t) = \pi l_s \left\{ \frac{3}{2} \frac{\hat{n}^2_{s,6\ddot{k}+1}}{h_w r_{wc}} \right\} \hat{A}^{(2)}_{z,6\ddot{k}+1,6\ddot{n}+1}(r_{wc})\, \hat{i}_{s,6\ddot{n}+1} \cos\left[(6\ddot{n}+1)\omega_s t\right]$$

$$= \pi l_s \left\{ \frac{3}{2} \frac{\hat{n}^2_{s,6\ddot{k}+1}}{h_w r_{wc}} \right\} \hat{A}^{(2)}_{z,6\ddot{k}+1,6\ddot{n}+1}(r_{wc})\, i_{sa,6\ddot{n}+1}(t). \tag{6.56}$$

The last line follows from (6.3). The stator self-inductance of phase a is therefore:

$$L_{ssa,6\ddot{k}+1,6\ddot{n}+1} = \pi l_s \left\{ \frac{3}{2} \frac{\hat{n}^2_{s,6\ddot{k}+1}}{h_w r_{wc}} \right\} \hat{A}^{(2)}_{z,6\ddot{k}+1,6\ddot{n}+1}(r_{wc}). \tag{6.57}$$

The frequency dependency of L_{ssa} is implicitly contained in the peak value of the vector potential $\hat{A}^{(2)}_{z,6\ddot{k}+1,6\ddot{n}+1}(r_{wc})$, which actually comes from the boundary condition constants in terms of which it is obtained (see (6.41b)). These constants are a function of the constant $\bar{\tau}_{6\ddot{k}+1,6\ddot{n}+1}$ of (6.31), which is a function of frequency.

The vector potential in (6.57) was obtained from the total current density of the winding, which is the sum of the three current densities due to the three phases, from (6.11). This means that (6.57) is of the form of the matrix in (6.53), and therefore a vector notation for the three-phase flux linkage of the stator winding due to the stator currents may be introduced as:

$$\vec{\lambda}_{ss,6\ddot{k}+1,6\ddot{n}+1}(t) = L_{ss,6\ddot{k}+1,6\ddot{n}+1}\, \vec{i}_{s,6\ddot{n}+1}(t). \tag{6.58}$$

Since the matrix in (6.53) is zero for the non-diagonal terms, the inductance of (6.58) is simply a scalar, given by (6.57). The sum over all space and time harmonic components of the flux linkage (6.58) is needed for the voltage equation of (5.29). It is given by:

$$\frac{d\vec{\lambda}_{ss}(t)}{dt} = \sum_{\ddot{k}=-\infty}^{\infty} \sum_{\ddot{n}=-\infty}^{\infty} L_{ss,6\ddot{k}+1,6\ddot{n}+1} \frac{d}{dt} \vec{i}_{s,6\ddot{n}+1}(t). \tag{6.59}$$

6.6.3 Results

For the EμFER machine, the inductance $L_{ssa,6\ddot{k}+1,6\ddot{n}+1}$ of (6.57) is listed in Table 6.2. The space harmonic components are listed in the rows and the time harmonic components in the columns. It can clearly be seen that the space harmonics only have a small influence on the inductance; the 5th space harmonic component for $n = 1$ is approximately 1000 times smaller than the fundamental space harmonic component, and even smaller for the higher space harmonics. This is due to the fact that the winding is situated in the air gap on a slotless stator.

One can also see from Table 6.2 that the inductance changes to a lower value when the frequency changes from the 1st time harmonic to the 5th, and then stays fairly constant for the time harmonic components above the 5th. This is due to the fact that the shielding cylinder almost completely shields at the 5th time harmonic, as can be seen also from Figure 6.3. Any increase in frequency above this does not significantly change the shielding effect. The total inductance (sum of the space harmonic components up to $k = 19$ in Table 6.2) is 38.5 μH for $n = 1$ and 4.69 μH for $n = 19$.

Practically, this means that the converter connected to the EμFER machine will "see" 38.5 μH for the fundamental time harmonic of the current, since the rotor turns synchronously with this field. All higher-order harmonics will "see" the lower value of 4.69 μH. For a CSI this inductance plus the end-winding leakage inductance will therefore be the inductance to be reckoned with for commutation intervals, since these are in the order of microseconds.

$k \backslash n$	1	5	7	11	13	17	19
1	38.42	4.649	4.647	4.641	4.638	4.631	4.627
5	0.0338	0.0729	0.0339	0.0338	0.0338	0.0337	0.0337
7	0.0032	0.0032	0.0054	0.0032	0.0032	0.0032	0.0032
11	0.0009	0.0009	0.0009	0.0012	0.0009	0.0009	0.0009
13	0.0024	0.0024	0.0024	0.0024	0.0029	0.0024	0.0024
17	0.0205	0.0205	0.0205	0.0205	0.0205	0.0225	0.0205
19	0.0061	0.0061	0.0061	0.0061	0.0061	0.0061	0.0065

Table 6.2: The k-th and n-th component of the main-field inductance L_{ss} [μH] for the EμFER machine, calculated from (6.57).

6.7 Leakage inductance

The flux linkage of the stator winding due to leakage flux is, for non-triplen harmonics:

$$\vec{\lambda}_{s\sigma}(t) = L_{s\sigma}\vec{i}_s(t), \tag{6.60}$$

where the stator leakage inductance is given by:

$$L_{s\sigma} = L_{s\sigma a} - M_{s\sigma ab}. \tag{6.61}$$

In (6.61), due to symmetry, $M_{s\sigma ab}$ is equal to the mutual leakage inductance between every pair of phases, and $L_{s\sigma a} = L_{s\sigma b} = L_{s\sigma c}$.

The time derivative of (6.60) is:

$$\frac{d\vec{\lambda}_{s\sigma}(t)}{dt} = L_{s\sigma}\frac{d\vec{i}_s(t)}{dt}. \tag{6.62}$$

In general, the leakage inductance in electrical machines consists of the slot leakage, air gap leakage and end-winding leakage. Since the machine under consideration is slotless, what is conventionally the slot leakage inductance is now included in (6.57). The air gap leakage inductance is also included in the main-field inductance $L_{ss,k,n}$ of equation (6.57) because the calculation of $L_{ss,k,n}$ takes the two-dimensional air gap field into account. The only component of the leakage inductance of the flywheel machine is therefore the end-winding leakage inductance. Since the end windings of the machine are in the third dimension, the analytical field model cannot take them into account.

6.8 Induced loss in the shielding cylinder due to the field of the stator currents

6.8.1 Introduction

In the previous two sections, the stator inductance was discussed. The stator main-field inductance of Section 6.6 was calculated directly from the vector potential in the winding region. Another important quantity is the loss in the shielding cylinder due to the eddy currents flowing there. Like the inductance this is also a quantity derived from the magnetic field of the stator currents only, and it is therefore included in this chapter.

Several researchers have published on analytical calculation of loss in the shielding cylinders of PMSMs. The loss may be calculated by either taking the volume integral of the current density in the shielding cylinder [Zhu01a], [Vee97], or the surface integral of the Poynting vector, as in [Den97], [Den98], [Abu99] and [Zhu01b]. Since the solutions for the vector potential obtained in this chapter contain complex Bessel functions, avoiding the volume integral is highly recommended.

Poynting's Theorem, listed in Appendix B, may be used to obtain the loss in the shielding cylinder since it describes the total power crossing the air gap. When one calculates in rotor coordinates, the only power component is the power dissipated in the shielding cylinder. This is because in rotor coordinates, the coordinate system rotates synchronously with the fundamental harmonic of the stator field and therefore it cannot "see" the power it transfers to the field of the magnets. In Chapter 7, the calculation is repeated in stator coordinates in order to calculate the power associated

with the fundamental time and space harmonic and to convert it into electromagnetic torque.

6.8.2   Calculation

The calculation starts by finding the surface integral of the Poynting vector introduced in equation (4.41) of Section 4.6, but here in rotor coordinates:

$$- \oint_S \hat{\mathbf{S}}' \cdot d\mathbf{a} = \pi r' l_s \, \bar{E}'_z \bar{H}'^*_\phi, \tag{6.63}$$

where the electric and magnetic fields are both obtained from the vector potential. In the space and time harmonic form used in this chapter, this works out to:

$$- \oint_S \hat{\mathbf{S}}'_{6\ddot{k}+1,6\ddot{n}+1} \cdot d\mathbf{a} = \frac{-\pi r' l_s}{\mu_0} \left[6j(\ddot{k} - \ddot{n})\omega_s \right] \left\{ \frac{3}{2} \frac{\hat{n}_{s,6\ddot{k}+1} \hat{i}_{s,6\ddot{n}+1}}{h_w r_{wc}} \right\}^2$$
$$\cdot \left(\hat{\bar{A}}'^{(4)}_{z,6\ddot{k}+1,6\ddot{n}+1}(r') \right) \left[\frac{d}{dr'} \left(\hat{\bar{A}}'^{(4)}_{z,6\ddot{k}+1,6\ddot{n}+1}(r') \right) \right]^*, \tag{6.64}$$

where the peak value of the vector potential $\hat{\bar{A}}'_{z,6\ddot{k}+1,6\ddot{n}+1}(r')$ is given by the case where $\ddot{k} \neq \ddot{n}$ in (6.41b), since the case for $\ddot{k} = \ddot{n}$ works out to zero. The location of the integration surface S is chosen in the centre of the air gap: $r = r_{ag}$.

From Chapter 4 and Appendix B, the only possible interpretation of the power terms in (6.64) is the dissipation in the shielding cylinder. The average power crossing the air gap from the stator to the rotor, $\langle P'_{\delta,sc,6\ddot{k}+1,6\ddot{n}+1} \rangle = \langle P'_{source,sc,6\ddot{k}+1,6\ddot{n}+1} \rangle$, can therefore be written as:

$$\langle P'_{\delta,sc,6\ddot{k}+1,6\ddot{n}+1} \rangle = \langle P'_{diss,sc,6\ddot{k}+1,6\ddot{n}+1} \rangle = \text{Re} \left\{ - \oint_S \hat{\mathbf{S}}'_{6\ddot{k}+1,6\ddot{n}+1} \cdot d\mathbf{a} \right\}, \tag{6.65}$$

where $\langle P'_{diss,sc,6\ddot{k}+1,6\ddot{n}+1} \rangle$ is the k-th space n-th time harmonic of the average power dissipated in the shielding cylinder.

6.8.3   Results for typical current waveforms

Figure 6.5 shows an example of typical current waveforms of a CSI connected to the machine. Realistic waveforms for a small firing angle of $\alpha = 1°$ and a larger one of $\alpha = 42°$ are shown.[1] In these two waveforms, the line inductance is nonzero and a boost converter pre-stage is connected between the DC bus and the CSI. The latter

---

[1]For $\alpha = 42°$, the power level is 134 kW at a DC-link current of 400 A. The current waveform for $\alpha = 1°$ has been given the same DC-link current level of 400 A; for this equal current the power level at $\alpha = 1°$ is 164 kW.
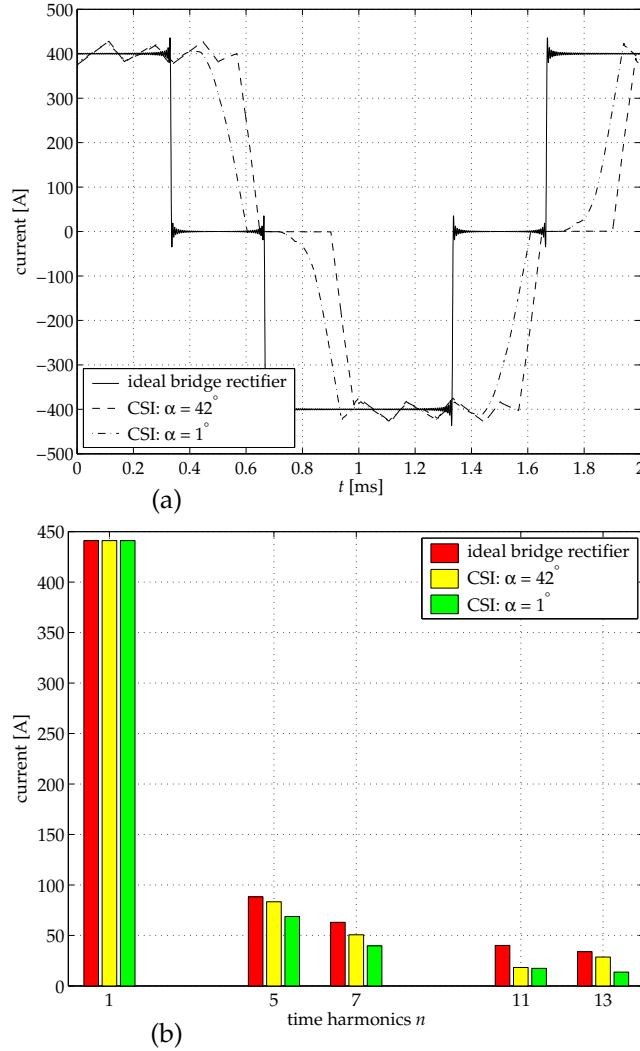
Figure 6.5: Three current waveforms for calculating the induced eddy-current loss in the shielding cylinder: (a) as a function of time; and (b) spectral content

causes the ripple in the current waveforms. Also shown is a waveform of an ideal diode bridge rectifier with zero line inductance. This unrealistic waveform represents the worst case in terms of time harmonic content. The waveforms of Figure 6.5 correspond to a flywheel rotational speed of 15 000 rpm.

The eddy-current loss induced in the shielding cylinder for the three waveforms of Figure 6.5, calculated by (6.64) and (6.65), are listed in Table 6.3.

As in the case of inductance (see Table 6.2), the space harmonic plays a less important role in the shielding cylinder loss than the time harmonic. The total loss

$k \setminus n$	1	5	7	11	13
Ideal bridge rectifier					
1	0	61.48	31.37	13.79	9.871
5	4.319	0	0.0964	0.0357	0.0313
7	0.2599	0.0115	0	0.0027	0.0015
11	0.0327	0.0011	0.0007	0	0.0002
13	0.0567	0.0026	0.0009	0.0006	0
CSI: $\alpha = 42°$					
1	0	55.13	20.29	2.861	7.046
5	4.335	0	0.0624	0.0074	0.0223
7	0.2609	0.0103	0	0.0006	0.0011
11	0.0328	0.0010	0.0005	0	0.0002
13	0.0569	0.0023	0.0006	0.0001	0
CSI: $\alpha = 1°$					
1	0	53.53	17.81	3.728	2.304
5	6.187	0	0.0547	0.0097	0.0073
7	0.3723	0.0100	0	0.0007	0.0004
11	0.0468	0.0009	0.0004	0	0.0001
13	0.0812	0.0022	0.0006	0.0002	0

Table 6.3: The k-th and n-th component of the induced eddy-current loss [W] in the shielding cylinder for the waveforms of Figure 6.5.

in the case of the ideal rectifier is 121.4 W, while for the CSI with $\alpha = 42°$ and $\alpha = 1°$, it is 90.13 W and 84.15 W, respectively.

This section and Section 6.6 discussed two derived quantities from the stator field: inductance and induced loss in the shielding cylinder. The inductance was derived in stator coordinates and the induced loss in the shielding cylinder in rotor coordinates. They were both derived for a rotor that is free to turn. The next section takes a look at the locked-rotor situation. The locked-rotor tests are widely used to determine machine parameters as a function of frequency. To compare the analytically calculated results with the locked-rotor tests, the solutions for the inductance and the Poynting vector have to be transformed to the case in standstill.

6.9   The locked-rotor machine impedance

6.9.1   Introduction

In Section 6.6, the stator main-field inductance was calculated directly from the vector potential in the winding region. It was shown in Table 6.2 that the machine inductance decreases at high frequencies, where the shielding cylinder shields the magnets and rotor iron.

The magnetic field also influences the resistance measured at the stator terminals, causing an increase with frequency. This resistance consists of two parts: the stator winding resistance, and the reflected resistance of the rotor due to the magnetic field effects. As shown in the next section, the resistance of the Litz wire used in the stator winding is constant up to very high frequencies since the strands are very thin (0.1 mm).

After showing that the stator Litz wire resistance may be neglected when determining the frequency-dependent resistance effects, the locked-rotor impedance is developed. For this, the discrete time harmonics are converted into a continuous function of frequency in Section 6.9.3.

6.9.2 Stator Litz wire resistance

The stator winding layout was shown in Figure 3.8. There is one conductor per slot per layer, and these conductors are made up of Litz wire cables, as described in Chapter 5, where the induced loss in the Litz wire winding was calculated. The diameter of one Litz strand is chosen as 0.1 mm.

The skin depth is given by equation (3.6) and repeated here:

$$\delta = \sqrt{\frac{2}{\omega\sigma\mu}} = \sqrt{\frac{1}{\pi f \sigma \mu}} \ . \tag{6.66}$$

For the fundamental frequency of the stator, $f_s = 1000$ Hz, the skin depth of copper is:

$$\delta_{Cu,1kHz} = \sqrt{\frac{1}{1000\pi \cdot 5.8 \times 10^7 \cdot 4\pi \times 10^{-7}}} = 2.09 \text{ mm}. \tag{6.67}$$

At first, 0.1 mm strand-diameter Litz wire for the stator winding's conductors seems too small considering the large skin depth of (6.67). This apparently too small a choice can also be seen from the AC resistance of one strand.

To calculate the AC resistance of a single isolated conductor, one can derive a differential equation from Maxwell's equations for the current density in the conductor as a function of the radius [Lam66]. This differential equation is a modified Bessel equation, similar to (6.38), but with much simpler boundary conditions. From the solution to this equation, i.e., the current density, the wire's impedance can be obtained. The expression for this impedance is:

$$Z_{strand}(f) = R_{strand} + j2\pi f L_{strand} = \frac{j^{\frac{3}{2}} k_\tau}{2\pi r_0 \sigma} \frac{I_0\left(j^{\frac{3}{2}} k_\tau r_0\right)}{I_1\left(j^{\frac{3}{2}} k_\tau r_0\right)} \quad [\Omega/\text{m}], \tag{6.68}$$

where r_0 is the outer radius of the strand conductor; I_0 and I_1 are modified Bessel functions[2] of the first kind of order 0 and 1, respectively; and k_τ is a constant similar to (6.31), and defined by:

$$k_\tau \equiv \sqrt{2\pi f \sigma \mu}. \tag{6.69}$$

---

[2]See Appendix C for a brief overview of Bessel functions.

The resistance R_{strand} can be extracted from (6.68) by taking its real part by a computer package capable of working with (modified) Bessel functions with complex arguments, like MATLAB$^{\circledR}$ 5. Another way is to rewrite (6.68) in terms of the Kelvin functions to obtain a real function for the resistance [Lam66], [McL55].

Figure 6.6 shows the AC resistance, calculated with (6.68) and normalized to the DC resistance, of a single strand of Litz wire as a function of frequency. Figure 6.6 shows that the choice of 0.1 mm results in a Litz wire resistance that is constant and equal to the DC resistance up to a few hundred kHz. The main frequency-dependent part of the stator resistance is therefore the real part of the reflected impedance of the rotor.

The skin depth and AC resistance arguments given above do not motivate the choice of the strand diameter of 0.1 mm. The choice has not been based on these arguments, however, but rather on the induced loss in the strands due to the rotating field of the permanent magnets. This will be discussed in Chapter 7, Section 7.6. Particularly, equation (7.53) shows that this induced loss is a function of the strand diameter squared, which explains the choice of 0.1 mm better.

6.9.3   Inductance

The stator self-inductance of phase *a*, given by (6.57), may be transformed for the locked-rotor solution into a continuous function of frequency by choosing the base frequency f_s very small in the solution so that (6.34), repeated here:

$$\bar{\tau}_{6\ddot{n}+1}^2 = j\mu\sigma(6\ddot{n}+1)\omega_s, \tag{6.70}$$

becomes:

$$\bar{\tau}^2(f) = j\mu\sigma 2\pi f. \tag{6.71}$$

This transforms the *k*-th space harmonic of the inductance into:

$$L_{ssa,6\ddot{k}+1}(f) = \pi l_s \left\{\frac{3}{2}\frac{\hat{n}_{s,6\ddot{k}+1}^2}{h_w r_{wc}}\right\} \hat{A}_{z,6\ddot{k}+1}^{(2)}(r_{wc},f). \tag{6.72}$$

6.9.4   Reflected resistance of the rotor

In Appendix B, an expression for the locked rotor machine resistance is derived from Poynting's Theorem (equation (B.52)). There, $\langle P_{source}\rangle$ was introduced as the average power delivered to the rotor from the stator. Since the rotor is locked, rotor and stator coordinates are the same. The only power component of $\langle P_{source}\rangle$ is the power dissipated in the shielding cylinder, i.e., the eddy-current loss $\langle P_{diss,sc}\rangle$ (see Section 6.8.2 and Appendix B for more information). Its *k*-th space harmonic may be written from (6.65) as:

$$\langle P_{diss,sc,6\ddot{k}+1}(f)\rangle = -\text{Re}\left\{\oint_S \hat{\bar{\mathbf{S}}}_{6\ddot{k}+1}(f) \cdot d\mathbf{a}\right\}, \tag{6.73}$$
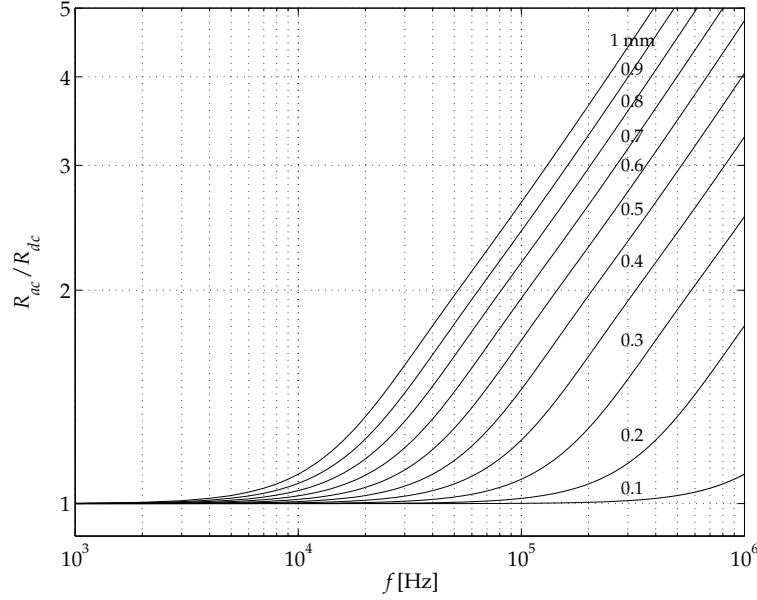
Figure 6.6: R_{ac} of a single Litz wire strand as a function of frequency, normalized with respect to R_{dc}, calculated from (6.68); strand diameters range from 0.1 mm to 1.0 mm.

which is, from (6.64):

$$\langle P_{diss,sc,6\ddot{k}+1}(f) \rangle = \text{Re} \left\{ \frac{\pi r l_s}{\mu_0} (j2\pi f) \left\{ \frac{3}{2} \frac{\hat{n}_{s,6\ddot{k}+1} \hat{i}_s(t)}{h_w r_{wc}} \right\}^2 \right.$$
$$\left. \cdot \left(\hat{A}_{z,6\ddot{k}+1}^{(4)}(r_{ag}, f) \right) \left[\frac{d}{dr} \left(\hat{A}_{z,6\ddot{k}+1}^{(4)}(r_{ag}, f) \right) \right]^* \right\}. \tag{6.74}$$

An equivalent resistance may be defined for the power dissipation of (6.74), as shown in Appendix B, equation (B.52). From equation (B.52), the equivalent resistance is twice the power dissipation divided by an equivalent peak current squared. The equivalent per-phase resistance is one third of this:

$$R_{s,1\phi,6\ddot{k}+1}(f) = \frac{2}{3} \frac{\langle P_{diss,sc,6\ddot{k}+1}(f) \rangle}{|\hat{\hat{i}}(f)|^2}, \tag{6.75}$$

where $\hat{\hat{i}}(f)$ is an equivalent peak current, conveniently chosen as 1 A.

6.10 Experimental verification of the locked rotor machine impedance

6.10.1 Introduction

The inductance of (6.72) does not contain the end-winding leakage inductance, as already mentioned. To obtain a proper comparison, this inductance has to be added to $L_{ssa}(f)$ (the inductance $L_{ssa}(f)$ is the sum of the space harmonics of $L_{ssa,6\ddot{k}+1}(f)$). From the measurements, the per-phase end-winding leakage inductance is: $L_{s\sigma a} = 5.95\ \mu$H.[3]

Similarly, the resistance $R_{s,1\phi,6\ddot{k}+1}(f)$ of (6.75) does not contain the DC resistance R_{dc}. It was determined experimentally as: $R_{dc} = 2.566$ mΩ per phase (at room temperature).[4]

The method used to measure the machine impedance is described in the next section, whereafter the results are compared with the analytical predictions.

6.10.2 The controlled current-injection (CCI) method

To measure the locked-rotor machine impedance, current is injected into the stator winding from a PWM converter. The voltage waveform applied to the machine terminals only contains certain harmonics (the fundamental switching frequency plus its harmonic components), but the experiment can be performed at several appropriately chosen frequencies. Figure 6.7 shows the circuit diagram for this method.

For low frequencies, a square wave current was modulated by the converter, while at high frequencies (higher than 500 Hz), the current ripple was used directly. Thus, for frequencies below 500 Hz, the fundamental and 3rd, 5th, 7th, etc. harmonic components were present in the current waveform and for frequencies higher than 500 Hz, even harmonics were also present. The converter is simply shown as a block in Figure 6.7, although it included a series inductor for frequencies below 500 Hz and a series inductor and capacitor for frequencies above 500 Hz. The current levels varied from a 50 A peak value at low frequencies (square wave) to a peak value of 4 A (triangular waveform) at high frequencies.

As shown in Figure 6.7, the line-line voltage $u_{sbc}(t)$ and the line current $i_{sb}(t)$ were measured and sampled. These signals were measured and recorded onto disk for the different switching frequencies, whereafter the FFT algorithm was used to transform the signals into the frequency domain: $\bar{U}_{sbc}(f)$ and $\bar{I}_{sb}(f)$. The machine impedance at frequency f is then given by:

$$\bar{Z}(f) = \frac{\bar{U}_{sbc}(f)}{\bar{I}_{sb}(f)}, \tag{6.76}$$

---

[3]The per-phase end-winding leakage inductance was not directly measured. It was taken to be that part of the inductance that the analytical model did not account for. More precisely, it was taken to be the level shift in the inductance vs frequency graph between the measured and calculated values.

[4]The DC resistance was also calculated; it agrees with the measured value.
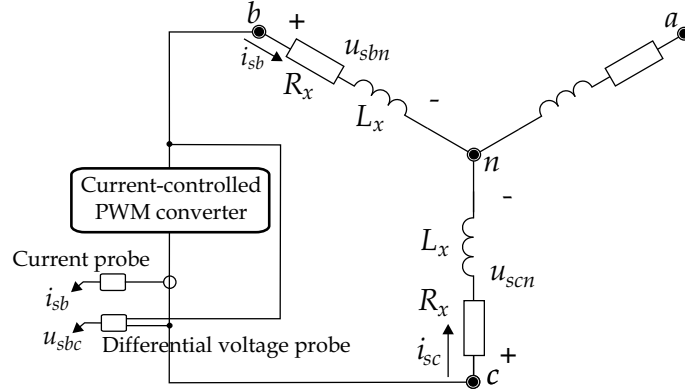
Figure 6.7: Circuit diagram for measuring machine impedance with controlled current injection.

and from Figure 6.7 the impedance is also equal to:

$$\bar{Z}(f) = 2R_x(f) + 4j\pi f L_x(f). \tag{6.77}$$

Therefore, the resistance and inductance can be calculated from (6.77) as:

$$R_x(f) = \frac{1}{2}\operatorname{Re}(\bar{Z}_x(f)), \tag{6.78}$$

and

$$L_x(f) = \frac{1}{4\pi f}\operatorname{Im}(\bar{Z}_x(f)), \tag{6.79}$$

respectively.

6.10.3 Results

Figure 6.8 shows a comparison of results of the analytically calculated and the measured per-phase machine impedance. Figure 6.8(a) shows the DC resistance, the analytically predicted frequency-dependent per-phase resistance of (6.75) and the measured resistance of (6.78). Figure 6.8(b) shows the end-winding leakage inductance, the analytically predicted frequency-dependent per-phase inductance of (6.72) and the measured inductance of (6.79).

In Figure 6.8(a), the analytically calculated resistance agrees well with the measured data up to about 300 Hz. The greatest differences in the measured and calculated resistance occur in the points of transition. The rise in the calculated resistance above about 20 kHz is due to the skin effect in the shielding cylinder. However, at these high frequencies, the loss due to eddy currents in the stator iron have already completely dominated the reflected resistance. The losses in the stator iron start playing a significant role above about 300 Hz. Since stator iron loss is a combined
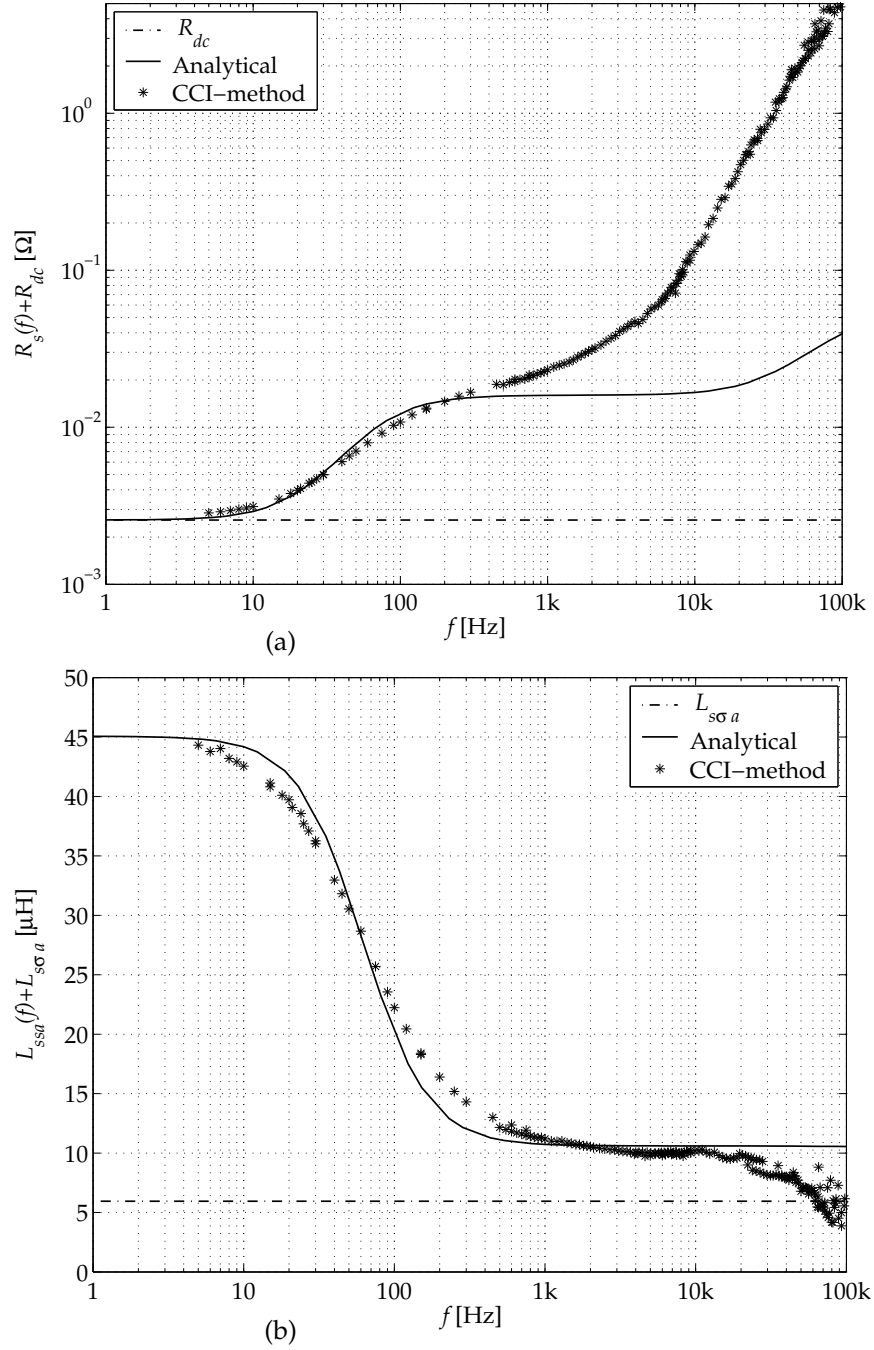
Figure 6.8: Comparison of results of the analytically calculated and the measured impedance: (a) per-phase resistance; and (b) per-phase inductance.

field effect, it will be discussed in Chapter 7, where the difference between the two graphs of Figure 6.8(a) at high frequencies will again be investigated.

In Figure 6.8(b), the analytically predicted inductance agrees well with the measured result over the whole frequency range, except above approximately 20 kHz. As in the case of the stator resistance, the greatest differences in the measured and calculated resistance occur at the points of transition. These differences are larger in the case of the inductance, however. Most likely this is due to frequency-dependent effects in the end windings, which are not modelled since they occur in the third dimension.

6.11   The stator voltage equation

The stator voltage equation was introduced in Chapter 5, in equation (5.31). At this stage, after the discussions on total stator resistance, no-load voltage and stator main-field inductance are completed, this voltage equation can be rewritten as:

$$
\vec{u}_s(t) = R_{dc}\,\vec{i}_s(t) + \sum_{\ddot{k}=-\infty}^{\infty} \sum_{\ddot{n}=-\infty}^{\infty} R_{s,6\ddot{k}+1,6\ddot{n}+1}\,\vec{i}_{s,6\ddot{n}+1}(t) + \vec{e}_{pa}(t)
$$
$$
+ \sum_{\ddot{k}=-\infty}^{\infty} \sum_{\ddot{n}=-\infty}^{\infty} L_{ss,6\ddot{k}+1,6\ddot{n}+1}\,\frac{d}{dt}\,\vec{i}_{s,6\ddot{n}+1}(t) + L_{s\sigma}\frac{d\vec{i}_s(t)}{dt}, \quad (6.80)
$$

where the resistance $R_{s,6\ddot{k}+1,6\ddot{n}+1}$ is obtained similarly to (6.75).

Equation (6.80) inherently contains the effect of the eddy currents in the shielding cylinder, since this effect is included in the magnetic field. Therefore, there is no need to define a winding or a voltage equation for the shielding cylinder. There is also no voltage equation for the field winding because the excitation is achieved with permanent magnets. Therefore, although it is short, equation (6.80) is the only voltage equation needed and provides a complete description of the machine.

6.12   Summary and conclusions

6.12.1   Summary

This chapter focused on the magnetic field due to the stator currents, including the effect on this field of the eddy currents in the shielding cylinder. Section 6.2 started the chapter with a literature review of work done by others relevant to the two main contributions of this chapter: (i) the stator winding excitation (air gap winding); and (ii) the influence of the eddy-current reaction field on the field due to the stator currents.

The field due to the air gap winding currents was described in Sections 6.3 (development of the stator current density), 6.4 (the magnetic field) and 6.5 (results).

For a free rotor, the quantities derived from the magnetic field were the stator main-field inductance (Section 6.6), and the induced eddy-current loss in the shielding cylinder (Section 6.8). The latter was illustrated with three stator current waveforms. Section 6.7 mentioned the end-winding leakage inductance, but it was not calculated, since it is not included in the 2D-model. It is measured in Section 6.10, however.

For the locked-rotor tests, the locked-rotor machine impedance was derived in Section 6.9. Section 6.10 presented and discussed an experimental verification of the locked-rotor machine impedance, while Section 6.11 listed the stator voltage equation.

6.12.2   Conclusions

Some of the important conclusions reached in this chapter are:

- Double-sided and single-sided Fourier series are a good way to describe a periodic waveform where the triplens need to be separated from the other harmonic components.

- The solution of the vector potential in the shielding cylinder enforces two cases: one for $k \neq n$ and one for $k = n$. The solution in the winding also requires two cases: one for $kp \neq 2$ and the other for $kp = 2$. This causes four overall cases for which the entire system of PDEs in all six layers had to be solved.

- The shielding cylinder already shields completely at the 5th time harmonic component (5 kHz). In fact, the transition from no shielding to complete shielding takes place between approximately 20 Hz and 200 Hz for the EμFER geometry.

- The Litz wire winding of the stator has an essentially constant resistance up to approximately 100 kHz. Therefore, all frequency-dependent resistance effects originate in the rotor, with the exception of the induced iron loss in the stator yoke. This will be investigated in Chapter 7 since it is a combined field effect.

- The Theorem of Poynting provides a convenient and powerful way of calculating the induced eddy-current loss in the shielding cylinder.

- Experimental verification validates the analytical model derived in this thesis. Both the experimental locked-rotor resistance and inductance are in good agreement with the analytically predicted results. (The calculated locked-rotor resistance does not agree at high frequencies; this will be reexamined in Chapter 7.)

- The machine needs only one voltage equation to completely describe it since the effects of the shielding cylinder are already included in the magnetic field.

The combined field and derived quantities

7.1 Introduction

Chapters 5 and 6 described the magnetic field due to the permanent magnets and the stator currents. The first assumption made in Chapter 4 is that of linearity of the magnetic vector potential. This means that the field of Chapter 5 may be algebraically added to the field of Chapter 6: $\mathbf{A}_{total} = \mathbf{A}_{magnets} + \mathbf{A}_{stator\ currents}$.

This chapter focuses on this combined field.

Section 7.2 shows the details of combining the two fields into one, whereafter Section 7.3 starts the discussion of quantities derived from this field by looking at electromagnetic torque. Both the Poynting vector method and the Lorentz force method will be used to obtain the torque.

Electrical machines are designed to convert electrical power into mechanical power and vice versa. The electromagnetic torque of Section 7.3 is the way in which useful conversion takes place. However, some of the electromagnetic power inevitably also goes to waste in the form of heat. These losses are induced both in the stator and in the rotor.

The rotor loss consists only of the eddy-current loss in the shielding cylinder and is only a function of the stator current field. It was therefore discussed as a derived field quantity in Chapter 6. (Had stator slots been present, the permanent magnets in combination with the stator teeth would have caused a pulsating field in the shielding cylinder and thus extra loss. The machine under discussion in this thesis does not have slots however, and therefore this effect does not occur.)

The stator losses, on the other hand, are a function of both the stator current and the permanent-magnet fields, i.e., the combined field. The way in which the fields can be combined is not the same for all materials, however. In the stator, two electromagnetically active materials are present: copper (in the winding) and iron

(in the stator yoke). Assumption 1 of Chapter 4 is actually only valid in magnetically linear materials, and to find $\mathbf{A}_{total}$ in Section 7.2, this has indeed been assumed. In the determination of stator losses, however, this assumption has to be revised. In iron close to saturation, the **B** and **H** fields are not linearly related anymore and a mere sum of the two potentials $\mathbf{A}_{magnets}$ and $\mathbf{A}_{stator\ currents}$ is no longer valid.

However, one may neglect the stator current field for the following two reasons:

- *Field magnitude.* The magnitude of the stator field is much lower than that of the rotor (approximately an order of magnitude).

- *Low armature reaction.* The reason for a low armature reaction comes from the fact that the machine has a very small inductance. This causes the phase angle between the rotor and stator fields to be small; the rotor field is therefore not heavily influenced by the stator field.

In Section 7.4, therefore, only the field due to the permanent magnets is considered when determining the induced stator iron loss. Section 7.5 revisits the frequency-dependent stator resistance by including the effect of the stator iron losses on this frequency-dependent resistance.

The stator current field can also be neglected when determining the stator copper loss. Hence for the induced eddy current loss in the stator winding, discussed in Section 7.6, the field due to the stator currents is also neglected.

Section 7.7 summarizes and concludes the chapter.

7.2 The combined field

7.2.1 Introduction

This section is devoted to finding the combined field. We recall that the magnetic vector potential in the air gap due to the permanent magnets (region 2 in Chapter 5) was given by:

- for the *radial array:* equation (5.15);

- for the *discrete Halbach array with two segments per pole:* equation (5.23); and

- for the *ideal Halbach array:* equation (5.27).

These expressions were written as $\sin(\cdot)$ functions, while in Chapter 6, the vector potential due to the stator currents was written as a complex exponential function $e^{j(\cdot)}$. The vector potential due to the stator currents (region 3 in Chapter 6) had two solutions:

- in *rotor coordinates:* equation (6.48), where the boundary condition constants of the solution for the synchronously rotating rotor are used; and

- in *stator coordinates:* equation (6.48), where the term $\mathrm{e}^{-j\left[(6\ddot{k}+1)p\phi+6(\ddot{k}-\ddot{n})\omega_s t\right]}$ is replaced with $\mathrm{e}^{-j\left[(6\ddot{k}+1)p\varphi-(6\ddot{n}+1)\omega_s t\right]}$ and the boundary condition constants of the locked-rotor solution are used.

The next subsection discusses the details of adding the two fields together.

7.2.2 Addition of the vector potentials

Firstly, from now on we will indicate the field due to the magnets generically by the subscript *m*, which can be one of *rad*, *dh*2 or *ih*. The field due to the stator currents is indicated by the subscript *s*.

The second step is to convert the trigonometric function $\sin(\cdot)$ used for the field due to the magnets to the complex exponential function $\mathrm{e}^{j(\cdot)}$. To do this, we make use of the Euler formula:

$$\mathrm{e}^{j\beta} \equiv \cos\beta + j\sin\beta, \tag{7.1}$$

which means that the *k*-th space harmonic of the real-valued vector potential of Chapter 5, equation (5.8), can be obtained from the complex-valued version of this chapter, equation (7.3), by:

$$\sin\beta = \mathrm{Re}\left\{\mathrm{e}^{j\left(\beta-\frac{\pi}{2}\right)}\right\}, \tag{7.2}$$

for the space harmonics $k = 1, 5, 7, 11, \cdots$

Thirdly, the space harmonics of the field due to the magnets *k* are converted to the form $k = 6\ddot{k} + 1$ of (3.14). The consequence of this is that the triplen space harmonics of the permanent-magnet field are ignored. It may be seen both from the Poynting vector and Lorentz force methods that the product of a field with triplen harmonics with a field with zero triplens results in a field with zero triplen harmonics. Thus the triplen harmonics of the permanent-magnet field can be removed right from the start.

7.2.3 Rotor coordinates

The field due to the permanent magnets was already given in rotor coordinates in (5.15), (5.23) and (5.27) and therefore the *k*-th space harmonic of the magnetic vector potential due to the magnets is from (3.14) and (7.2):

$$\bar{A}_{z,m,6\ddot{k}+1}^{(2)}(r,\phi) = \hat{\bar{A}}_{z,m,6\ddot{k}+1}^{(2)}(r)\,\mathrm{e}^{-j\left[(6\ddot{k}+1)p\phi-\frac{\pi}{2}\right]}, \tag{7.3}$$

in rotor coordinates in complex exponential form. The term $\hat{\bar{A}}_{z,m,6\ddot{k}+1}^{(2)}(r)$ in (7.3) (the peak value or *r*-part of the product solution) is given by (5.15b), (5.23b) and (5.27b).

The k-th space and n-th time harmonic component of the vector potential due to the stator currents in the air gap is given by (6.48):

$$\bar{A}^{(3)}_{z,s,6\ddot{k}+1,6\ddot{n}+1}(r,\phi,t) = \hat{\bar{A}}^{(3)}_{z,s,6\ddot{k}+1,6\ddot{n}+1}(r)\left\{\frac{3}{2}\frac{\hat{n}_{s,6\ddot{k}+1}\hat{\bar{i}}_{s,6\ddot{n}+1}}{h_w r_{wc}}\right\}e^{-j\left[(6\ddot{k}+1)p\phi+6(\ddot{k}-\ddot{n})\omega_s t+p\theta_0\right]}.$$

(7.4)

In (6.48), the initial rotor position θ_0 was set to zero, but in this chapter it is not.

The sum of equations (7.3) and (7.4) is the total vector potential in the air gap:

$$\bar{A}^{(3)}_{z,tot,6\ddot{k}+1,6\ddot{n}+1}(r,\phi,t) = \bar{A}^{(2)}_{z,m,6\ddot{k}+1}(r,\phi) + \bar{A}^{(3)}_{z,s,6\ddot{k}+1,6\ddot{n}+1}(r,\phi,t),$$

(7.5)

where the region numbering of the total field has been chosen as the region numbering of the stator field. (See Table 6.1).

7.2.4   Stator coordinates

The k-th space harmonic of the magnetic vector potential due to the magnets is in stator coordinates:

$$\bar{A}^{(2)}_{z,m,6\ddot{k}+1}(r,\varphi,t) = \hat{\bar{A}}^{(2)}_{z,m,6\ddot{k}+1}(r)\,e^{-j\left[(6\ddot{k}+1)p\varphi-(6\ddot{k}+1)\omega_s t-p\theta_0-\frac{\pi}{2}\right]},$$

(7.6)

from equations (7.3) and (6.16).

The stator coordinate version of equation (7.4) is from (6.16):

$$\bar{A}^{(3)}_{z,s,6\ddot{k}+1,6\ddot{n}+1}(r,\varphi,t) = \hat{\bar{A}}^{(3)}_{z,s,6\ddot{k}+1,6\ddot{n}+1}(r)\left\{\frac{3}{2}\frac{\hat{n}_{s,6\ddot{k}+1}\hat{\bar{i}}_{s,6\ddot{n}+1}}{h_w r_{wc}}\right\}e^{-j\left[(6\ddot{k}+1)p\varphi-(6\ddot{n}+1)\omega_s t\right]}.$$

(7.7)

The k-th space and n-th time harmonic of the total vector potential in stator coordinates is given by the sum of (7.6) and (7.7):

$$\bar{A}^{(3)}_{z,tot,6\ddot{k}+1,6\ddot{n}+1}(r,\varphi,t) = \bar{A}^{(2)}_{z,m,6\ddot{k}+1}(r,\varphi) + \bar{A}^{(3)}_{z,s,6\ddot{k}+1,6\ddot{n}+1}(r,\varphi,t).$$

(7.8)

7.3   Electromagnetic torque

7.3.1   Introduction

In this section, we start off the discussion on the quantities derived from the combined field with the electromagnetic torque. Two methods are used to calculate the electromagnetic torque developed by the machine: the Poynting vector method and the Lorentz force method. The Poynting vector method is preceded by a literature review of the use of the Poynting vector in electrical machines.

7.3.2 Literature review: Use of the Poynting vector in electrical machines

The Poynting vector cannot only be used to find the loss induced in the shielding cylinder, as in in [Den97], [Den98], [Abu99], [Zhu01b] and Chapter 6, but also to find the complete air gap power and consequently the electromagnetic torque.

Slepian [Sle19], [Sle42] first introduced the use of the Poynting vector in electrical machines. The aim of his work was to develop a tool to visualize the energy flow in the air gap. Darrieus [Dar36], Dahlgren [Dah50] and Harrison [Har66] subsequently also demonstrated the usefulness of the Poynting vector in machines. These authors treated the subject in a fairly general way.

Applied to specific machine types, Hawthorne developed expressions for DC and synchronous machines [Haw53], [Haw54]. Induction machines were investigated by Alger and Oney [Alg53], [Alg54], Poloujadoff and Perret [Pol71] and Cray [Cra84]. Palit unified the theory into a model that is valid for all machine types in [Pal80a], whereafter he applied the general theory to six machine types [Pal80b]. His work was extended in [Pal82].

In [Gut98], Gutt and Grüner use the Poynting vector to define the power density as a general utilization factor. Permanent-magnet synchronous machines were treated explicitly in [Xia96] by Xiaojuan *et al*. The magnets were modelled by equivalent surface current densities on the surfaces of the magnets, and three torque calculation methods were investigated: (i) from the Maxwell stresses, (ii) the energy method and (iii) the Poynting vector. In this section, two methods for computing torque will be used and compared: the Poynting vector method and the Lorentz force method.

7.3.3 The Poynting vector method

The Poynting vector method gives the total power crossing the air gap from the stator to the rotor. Equation (4.41) was used in Chapter 6 to obtain the induced eddy current loss in the shielding cylinder. In this chapter, the interest is in all the power crossing the air gap, including the electromagnetic torque. Therefore, the total vector potential of (7.5) must be used. From equation (4.41) of Section 4.6, the surface integral of the Poynting vector $\hat{\mathbf{S}}_{tot}$ of the total field is given by:

$$\oint_S \hat{\mathbf{S}}_{tot} \cdot d\mathbf{a} = -\pi r l_s \, \bar{E}_{z,tot} \bar{H}_{\phi,tot}^*, \tag{7.9}$$

where r is the radius of the integration surface S. To find the power crossing the air gap, the integration radius is set equal to the radius at the centre of the air gap: $r \equiv r_{ag} = (r_w + r_{ci})/2$.

In (7.9), $\bar{E}_{z,tot}$ and $\bar{H}_{\phi,tot}^*$ are the electric and magnetic fields due to the sum of the vector potentials due to the permanent magnet array and the stator currents, respectively. The * in $\bar{H}_{\phi,tot}^*$ denotes the complex conjugate of $\bar{H}_{\phi,tot}$.

The rest of this subsection revolves around equation (7.9). It will be worked out in both rotor and stator coordinates to find the total power crossing the air gap from the stator to the rotor.

7.3.4 Rotor coordinates

From (4.15) and (7.5) the k-th space and n-th time harmonic of the electric field in the air gap is given by:[1]

$$\bar{E}^{(3)}_{z,tot,6\ddot{k}+1,6\ddot{n}+1}(r,\phi,t) = -\frac{\partial}{\partial t}\bar{A}^{(3)}_{z,tot,6\ddot{k}+1,6\ddot{n}+1}(r,\phi,t), \tag{7.10}$$

which can be written from (7.3) and (7.4) as:

$$\bar{E}^{(3)}_{z,tot,6\ddot{k}+1,6\ddot{n}+1}(r,\phi,t) = \quad 0 \quad + $$
$$\left[-6j(\ddot{k}-\ddot{n})\omega_s\right]\hat{A}^{(3)}_{z,s,6\ddot{k}+1,6\ddot{n}+1}(r)\left\{\frac{3}{2}\frac{\hat{n}_{s,6\ddot{k}+1}\hat{i}_{s,6\ddot{n}+1}}{h_w r_{wc}}\right\}\mathrm{e}^{-j\left[(6\ddot{k}+1)p\phi+6(\ddot{k}-\ddot{n})\omega_s t+p\theta_0\right]}, \tag{7.11}$$

since the time derivative of the vector potential due to the permanent magnets, equation (7.3), is zero.

From (4.23) and (7.5) the k-th space and n-th time harmonic of the complex conjugate of the magnetic field in the air gap is given by:

$$\bar{H}^{(3)*}_{\phi,tot,6\ddot{k}+1,6\ddot{n}+1}(r,\phi,t) = -\frac{1}{\mu_0}\left(\frac{\partial}{\partial r}\bar{A}^{(3)}_{z,tot,6\ddot{k}+1,6\ddot{n}+1}(r,\phi,t)\right)^*, \tag{7.12}$$

which becomes, from (7.3) and (7.4):

$$\bar{H}^{(3)*}_{\phi,tot,6\ddot{k}+1,6\ddot{n}+1}(r,\phi,t) = -\frac{1}{\mu_0}\left[\frac{d}{dr}\hat{A}^{(2)}_{z,m,6\ddot{k}+1}(r)\right]^*\mathrm{e}^{j\left[(6\ddot{k}+1)p\phi\right]}$$
$$-\frac{1}{\mu_0}\left[\frac{d}{dr}\hat{A}^{(3)}_{z,s,6\ddot{k}+1,6\ddot{n}+1}(r)\right]^*\left\{\frac{3}{2}\frac{\hat{n}_{s,6\ddot{k}+1}\hat{i}_{s,6\ddot{n}+1}}{h_w r_{wc}}\right\}\mathrm{e}^{j\left[(6\ddot{k}+1)p\phi+6(\ddot{k}-\ddot{n})\omega_s t+p\theta_0\right]}. \tag{7.13}$$

The total power crossing the air gap from the stator to the rotor is therefore

---

[1] Following the convention in this thesis, primes should be used in rotor coordinates. This is not done in this chapter, however, to make the equations more readable. The context indicates whether quantities are measured in rotor or stator coordinates. Where really needed, the superscripts *rc* and *sc* instead of primes are used to indicate rotor and stator coordinates, respectively.

obtained by substituting (7.11) and (7.13) into (7.9) and taking the real part:

$$
\begin{aligned}
P^{rc}_{\delta,6\ddot{k}+1,6\ddot{n}+1}(t) = \mathrm{Re}&\left\{ \frac{-\pi r_{ag}l_s}{\mu_0} \left[6j(\ddot{k}-\ddot{n})\omega_s\right] \left\{ \frac{3}{2}\frac{\hat{n}_{s,6\ddot{k}+1}\hat{i}_{s,6\ddot{n}+1}}{h_w r_{wc}} \right\} \right. \\
&\left. \cdot \hat{A}^{(3)}_{z,s,6\ddot{k}+1,6\ddot{n}+1}(r_{ag}) \left[\frac{d}{dr}\hat{A}^{(2)}_{z,m,6\ddot{k}+1}(r)\right]^{*}_{r=r_{ag}} e^{-j\left[6(\ddot{k}-\ddot{n})\omega_s t+p\theta_0\right]} \right\} \\
+ \mathrm{Re}&\left\{ \frac{-\pi r_{ag}l_s}{\mu_0} \left[6j(\ddot{k}-\ddot{n})\omega_s\right] \left\{ \frac{3}{2}\frac{\hat{n}_{s,6\ddot{k}+1}\hat{i}_{s,6\ddot{n}+1}}{h_w r_{wc}} \right\}^{2} \right. \\
&\left. \cdot \hat{A}^{(3)}_{z,s,6\ddot{k}+1,6\ddot{n}+1}(r_{ag}) \left[\frac{d}{dr}\hat{A}^{(3)}_{z,s,6\ddot{k}+1,6\ddot{n}+1}(r)\right]^{*}_{r=r_{ag}} \right\}.
\end{aligned}
\tag{7.14}
$$

It can clearly be seen that the two terms in (7.14) arise from different parts of the total electric and magnetic fields. They may be represented as:

- Power term 1 $\equiv P^{rc}_1(t) \propto E_{z,s}H_{\phi,m}$, i.e., the product of the electric field due to the stator currents with the magnetic field due to the magnets; and

- Power term 2 $\equiv P^{rc}_2 \propto E_{z,s}H_{\phi,s}$, i.e., the product of the electric and magnetic fields due to the stator currents.

$P^{rc}_1(t)$ consists only of *time-dependent* components for nonequal space and time harmonics. These terms have an average value of zero.

P^{rc}_2 consists only of *constant* components for nonequal space and time harmonics. In the next subsection it will become clear that these terms represent the power dissipated in the shielding cylinder on the rotor.

The average value of the power crossing the air gap is therefore equal to P^{rc}_2:

$$
\langle P^{rc}_{\delta,6\ddot{k}+1,6\ddot{n}+1}\rangle = P^{rc}_{2,6\ddot{k}+1,6\ddot{n}+1} = -\pi r_{ag}l_s \bar{E}^{(3)}_{z,s,6\ddot{k}+1,6\ddot{n}+1}\bar{H}^{(3)*}_{\phi,s,6\ddot{k}+1,6\ddot{n}+1}.
\tag{7.15}
$$

Table 7.1 lists the average value of the k-th space and n-th time harmonic component of the power crossing the air gap in rotor coordinates calculated by equations (7.14) and (7.15). This result was calculated for the waveform of the CSI with $\alpha = 42°$ of Figure 6.5 and a radial array. This power is the power dissipated in the shielding cylinder, also calculated in Chapter 6.

One would expect constant power to be transferred from the stator to the rotor when $\ddot{k} = \ddot{n}$, but (7.14) shows that the total power crossing the air gap is zero for equal space and time harmonics *in rotor coordinates*.

In stator coordinates, this expectation is fulfilled, however. The difference between the results in the two coordinate systems may be understood by noticing that in rotor coordinates, the integration surface rotates synchronously with the stator field for $\ddot{k} = \ddot{n}$. In stator coordinates, the integration surface stands still and relative movement effects are included in the power terms. The air gap power calculation in stator coordinates is the focus of the next subsection.

$|k| \setminus |n|$	1	5	7	11	13
1	0	55.13	20.29	2.861	7.046
5	4.335	0	0.0624	0.0074	0.0223
7	0.2609	0.0103	0	0.0006	0.0011
11	0.0328	0.0010	0.0005	0	0
13	0.0569	0.0023	0.0006	0	0

Table 7.1: The average value of the *k*-th and *n*-th component of the power crossing the air gap [W] in rotor coordinates calculated by equations (7.14) and (7.15). This result was calculated for the waveform of the CSI with $\alpha = 42°$ of Figure 6.5 and a radial array.

7.3.5 Stator coordinates

The total electric field in stator coordinates may be obtained from (7.6) and (7.7) as:

$$\bar{E}^{(3)}_{z,tot,6\ddot{k}+1,6\ddot{n}+1}(r, \varphi, t) =$$
$$- \left[j(6\ddot{k}+1)\omega_s \right] \hat{A}^{(2)}_{z,m,6\ddot{k}+1}(r) \, \mathrm{e}^{-j\left[(6\ddot{k}+1)p\varphi - (6\ddot{k}+1)\omega_s t - p\theta_0 \right]}$$
$$- \left[j(6\ddot{n}+1)\omega_s \right] \hat{A}^{(3)}_{z,s,6\ddot{k}+1,6\ddot{n}+1}(r) \left\{ \frac{3}{2} \frac{\hat{n}_{s,6\ddot{k}+1} \hat{i}_{s,6\ddot{n}+1}}{h_w r_{wc}} \right\} \mathrm{e}^{-j\left[(6\ddot{k}+1)p\varphi - (6\ddot{n}+1)\omega_s t \right]}. \quad (7.16)$$

Similarly, the total magnetic field in stator coordinates is:

$$\bar{H}^{(3)*}_{\varphi,tot,6\ddot{k}+1,6\ddot{n}+1}(r, \varphi, t) = -\frac{1}{\mu_0} \left[\frac{d}{dr} \hat{A}^{(2)}_{z,m,6\ddot{k}+1}(r) \right]^* \mathrm{e}^{j\left[(6\ddot{k}+1)p\varphi - (6\ddot{k}+1)\omega_s t - p\theta_0 \right]}$$
$$- \frac{1}{\mu_0} \left[\frac{d}{dr} \hat{A}^{(3)}_{z,s,6\ddot{k}+1,6\ddot{n}+1}(r) \right]^* \left\{ \frac{3}{2} \frac{\hat{n}_{s,6\ddot{k}+1} \hat{i}_{s,6\ddot{n}+1}}{h_w r_{wc}} \right\} \mathrm{e}^{j\left[(6\ddot{k}+1)p\varphi - (6\ddot{n}+1)\omega_s t \right]}. \quad (7.17)$$

As in (7.14) for rotor coordinates, different power terms may be identified when substituting (7.16) and (7.17) into (7.9) and taking the real part. In a compact representation, these four terms are:

- $P_1^{sc} \propto E_{z,m} H_{\varphi,m}$;

- $P_2^{sc}(t) \propto E_{z,m} H_{\varphi,s}$;

- $P_3^{sc}(t) \propto E_{z,s} H_{\varphi,m}$; and

- $P_4^{sc} \propto E_{z,s} H_{\varphi,s}$.

When fully written out, these expressions are:

$$P^{sc}_{1,6\ddot{k}+1,6\ddot{n}+1} = \mathrm{Re}\left\{ \frac{-\pi r_{ag}l_s}{\mu_0} \left[j(6\ddot{k}+1)\omega_s \right] \right.$$
$$\left. \cdot \hat{A}^{(2)}_{z,m,6\ddot{k}+1}(r_{ag}) \left[\frac{d}{dr}\hat{A}^{(2)}_{z,m,6\ddot{k}+1}(r) \right]^*_{r=r_{ag}} \right\}, \quad (7.18)$$

$$P^{sc}_{2,6\ddot{k}+1,6\ddot{n}+1}(t) = \mathrm{Re}\left\{ \frac{-\pi r_{ag}l_s}{\mu_0} \left[j(6\ddot{k}+1)\omega_s \right] \left\{ \frac{3}{2} \frac{\hat{n}_{s,6\ddot{k}+1}\hat{i}_{s,6\ddot{n}+1}}{h_w r_{wc}} \right\} \right.$$
$$\left. \cdot \hat{A}^{(2)}_{z,m,6\ddot{k}+1}(r_{ag}) \left[\frac{d}{dr}\hat{A}^{(3)}_{z,s,6\ddot{k}+1,6\ddot{n}+1}(r) \right]^*_{r=r_{ag}} e^{j\left[6(\ddot{k}-\ddot{n})\omega_s t + p\theta_0\right]} \right\}, \quad (7.19)$$

$$P^{sc}_{3,6\ddot{k}+1,6\ddot{n}+1}(t) = \mathrm{Re}\left\{ \frac{-\pi r_{ag}l_s}{\mu_0} \left[j(6\ddot{n}+1)\omega_s \right] \left\{ \frac{3}{2} \frac{\hat{n}_{s,6\ddot{k}+1}\hat{i}_{s,6\ddot{n}+1}}{h_w r_{wc}} \right\} \right.$$
$$\left. \cdot \hat{A}^{(3)}_{z,s,6\ddot{k}+1,6\ddot{n}+1}(r_{ag}) \left[\frac{d}{dr}\hat{A}^{(2)}_{z,m,6\ddot{k}+1}(r) \right]^*_{r=r_{ag}} e^{-j\left[6(\ddot{k}-\ddot{n})\omega_s t + p\theta_0\right]} \right\}, \quad (7.20)$$

and

$$P^{sc}_{4,6\ddot{k}+1,6\ddot{n}+1} = \mathrm{Re}\left\{ \frac{-\pi r_{ag}l_s}{\mu_0} \left[j(6\ddot{n}+1)\omega_s \right] \left\{ \frac{3}{2} \frac{\hat{n}_{s,6\ddot{k}+1}\hat{i}_{s,6\ddot{n}+1}}{h_w r_{wc}} \right\}^2 \right.$$
$$\left. \cdot \hat{A}^{(3)}_{z,s,6\ddot{k}+1,6\ddot{n}+1}(r_{ag}) \left[\frac{d}{dr}\hat{A}^{(3)}_{z,s,6\ddot{k}+1,6\ddot{n}+1}(r) \right]^*_{r=r_{ag}} \right\}. \quad (7.21)$$

The k-th space and n-th time harmonic of the total power crossing the air gap is then simply:

$$P^{sc}_{\delta,6\ddot{k}+1,6\ddot{n}+1}(t) = P^{sc}_{1,6\ddot{k}+1,6\ddot{n}+1} + P^{sc}_{2,6\ddot{k}+1,6\ddot{n}+1}(t) + P^{sc}_{3,6\ddot{k}+1,6\ddot{n}+1}(t) + P^{sc}_{4,6\ddot{k}+1,6\ddot{n}+1}. \quad (7.22)$$

Power component 1 is always zero[2]: $P^{sc}_{1,6\ddot{k}+1,6\ddot{n}+1} = 0$, while the other three components represent the sum of the mechanical power delivered to the rotor and the power dissipated on the rotor. This may be written as:

$$P^{sc}_{\delta,6\ddot{k}+1,6\ddot{n}+1}(t) = P^{sc}_{diss,6\ddot{k}+1,6\ddot{n}+1} + P^{sc}_{mech,6\ddot{k}+1,6\ddot{n}+1}(t), \quad (7.23)$$

---

[2]This is because there is no interaction between the E and H fields of the magnets. For the power terms $P^{sc}_{2,6\ddot{k}+1,6\ddot{n}+1}$ and $P^{sc}_{3,6\ddot{k}+1,6\ddot{n}+1}$, there is interaction between the rotor and stator fields. For the power component due to only the stator field, $P^{sc}_{4,6\ddot{k}+1,6\ddot{n}+1}$, the interaction is due to the relative movement between the fields, i.e. for some combinations of space and time harmonics, the field rotates clockwise at a certain speed and for other combinations anticlockwise at another speed. For $P^{sc}_{1,6\ddot{k}+1,6\ddot{n}+1}$, this effect does not occur since all space harmonic fields rotate in the same direction.

where $P_{diss,6\ddot{k}+1,6\ddot{n}+1}$ is the k-th space and n-th time harmonic of the power dissipated and $P_{mech,6\ddot{k}+1,6\ddot{n}+1}$ the k-th space and n-th time harmonic of the mechanical power delivered from the stator to the rotor.

As in the case of rotor coordinates, from the definition of the complex Poynting vector in Appendix B, we are only interested in the average value[3] of the air gap power:

$$\langle P^{sc}_{\delta,6\ddot{k}+1,6\ddot{n}+1}\rangle = P^{sc}_{diss,6\ddot{k}+1,6\ddot{n}+1} + \langle P^{sc}_{mech,6\ddot{k}+1,6\ddot{n}+1}\rangle. \tag{7.24}$$

The time-dependent components in (7.22) are $P^{sc}_{2,6\ddot{k}+1,6\ddot{n}+1}(t)$ and $P^{sc}_{3,6\ddot{k}+1,6\ddot{n}+1}(t)$ for nonequal space and time harmonics. The average values of these two power components are zero when $\ddot{k} \neq \ddot{n}$, i.e., the only nonzero average values are for equal space and time harmonics. These are the interaction terms between the stator and the rotor with zero relative movement between the two and therefore they only consist of mechanical power.

The Power term $P^{sc}_{4,6\ddot{k}+1,6\ddot{n}+1}$ represents power delivered to the shielding cylinder from the stator winding, since it is only due to the electric and magnetic fields of the stator current. It contains both mechanical and dissipation terms. This is because, as in $P^{sc}_{2,6\ddot{k}+1,6\ddot{n}+1}(t)$ and $P^{sc}_{3,6\ddot{k}+1,6\ddot{n}+1}(t)$, relative movement between rotor and stator fields is present, for when $\ddot{k} \neq \ddot{n}$. The difference with $P^{sc}_{2,6\ddot{k}+1,6\ddot{n}+1}(t)$ and $P^{sc}_{3,6\ddot{k}+1,6\ddot{n}+1}(t)$ is that the average values of the power for these relative-movement terms are nonzero in the case of $P^{sc}_{4,6\ddot{k}+1,6\ddot{n}+1}$. To distinguish between the mechanical and loss components of power term $P^{sc}_{4,6\ddot{k}+1,6\ddot{n}+1}$, the rotor slip must be introduced.

7.3.6 P^{sc}_4 and the slip

The relationship between the two power components of $P^{sc}_{4,6\ddot{k}+1,6\ddot{n}+1}$ can be found by introducing the slip:[4]

$$s_{6\ddot{k}+1,6\ddot{n}+1} = \frac{6(\ddot{n} - \ddot{k})}{6\ddot{n} + 1}. \tag{7.25}$$

Table 7.2 lists the slip for up to the 13th space and time harmonic.

In terms of the slip, $P^{sc}_{4,6\ddot{k}+1,6\ddot{n}+1}$ is rewritten as:

$$\begin{aligned}
P^{sc}_{4,6\ddot{k}+1,6\ddot{n}+1} &= P^{sc}_{diss,4,6\ddot{k}+1,6\ddot{n}+1} + P^{sc}_{mech,4,6\ddot{k}+1,6\ddot{n}+1} \\
&= s_{6\ddot{k}+1,6\ddot{n}+1} P^{sc}_{4,6\ddot{k}+1,6\ddot{n}+1} + (1 - s_{6\ddot{k}+1,6\ddot{n}+1}) P^{sc}_{4,6\ddot{k}+1,6\ddot{n}+1}.
\end{aligned} \tag{7.26}$$

Power term $P^{sc}_{4,6\ddot{k}+1,6\ddot{n}+1}$ is zero for equal space and time harmonics, thus both its dissipation and mechanical components are zero for $\ddot{k} = \ddot{n}$.

---

[3]Since $P_{diss,6\ddot{k}+1,6\ddot{n}+1}$ is constant, $\langle P_{diss,6\ddot{k}+1,6\ddot{n}+1}\rangle = P_{diss,6\ddot{k}+1,6\ddot{n}+1}$.

[4]The validity of the usage of the slip may be found in any text that treats induction machines like [Sle92]. The shielding cylinder and stator winding in combination act as an induction machine since there are rotating fields originating from the stator that differ in rotational speed from the mechanical rotational speed of the shielding cylinder.

$|k| \setminus |n|$	1	5	7	11	13
$s_{6\ddot{k}+1,6\ddot{n}+1}$					
1	0	1.2	0.8571	1.091	0.9231
5	6	0	1.714	0.5455	1.385
7	-6	2.4	0	1.636	0.4615
11	12	-1.2	2.571	0	1.846
13	-12	3.6	-0.8571	2.182	0
$1 - s_{6\ddot{k}+1,6\ddot{n}+1}$					
1	1	-0.2	0.1429	-0.0909	0.0769
5	-5	1	-0.7143	0.4546	-0.3846
7	7	-1.4	1	-0.6364	0.5385
11	-11	2.2	-1.571	1	-0.8462
13	13	-2.6	1.857	-1.182	1

Table 7.2: The k-th and n-th component of the slip calculated by (7.25).

7.3.7 The average air gap power

Equation (7.24) is the average air gap power in stator coordinates. The dissipation and mechanical components may be written by distinguishing between the equal and nonequal space and time harmonics cases. The dissipation component is:

$$P_{diss,6\ddot{k}+1,6\ddot{n}+1}^{sc} = \begin{cases} 0 & \text{if } \ddot{k} = \ddot{n} \\ s_{6\ddot{k}+1,6\ddot{n}+1} P_{4,6\ddot{k}+1,6\ddot{n}+1}^{sc} & \text{if } \ddot{k} \neq \ddot{n}, \end{cases} \tag{7.27}$$

and the mechanical component is:

$$\langle P_{mech,6\ddot{k}+1,6\ddot{n}+1}^{sc} \rangle = \begin{cases} \langle P_{2,6\ddot{k}+1,6\ddot{n}+1}^{sc} \rangle + \langle P_{3,6\ddot{k}+1,6\ddot{n}+1}^{sc} \rangle & \text{if } \ddot{k} = \ddot{n} \\ (1 - s_{6\ddot{k}+1,6\ddot{n}+1}) P_{4,6\ddot{k}+1,6\ddot{n}+1}^{sc} & \text{if } \ddot{k} \neq \ddot{n}. \end{cases} \tag{7.28}$$

Table 7.3 lists the average mechanical power $\langle P_{2,6\ddot{k}+1,6\ddot{n}+1}^{sc} \rangle + \langle P_{3,6\ddot{k}+1,6\ddot{n}+1}^{sc} \rangle$, the power term $P_{4,6\ddot{k}+1,6\ddot{n}+1}^{sc}$, and its dissipation and mechanical components.

The following observations may be made from Tables 7.1 and 7.3:

- The higher harmonics of the average mechanical power due to stator-rotor interaction are negligible in comparison with the fundamental ($k = 1$, $n = 1$) component.

- The 5th space and 5th time harmonic of the average mechanical power due to stator-rotor interaction is zero. This is a direct consequence of the 5th space harmonic of the winding distribution being zero. However, the other components are also very small, as mentioned above. This leads to the following observation:

$|k| \setminus |n|$	1	5	7	11	13
$\langle P^{sc}_{2,6\ddot{k}+1,6\ddot{n}+1}\rangle + \langle P^{sc}_{3,6\ddot{k}+1,6\ddot{n}+1}\rangle$					
1	-1.766×10^5	0	0	0	0
5	0	0	0	0	0
7	0	0	32.72	0	0
11	0	0	0	-4.145	0
13	0	0	0	0	-4.425
$P^{sc}_{4,6\ddot{k}+1,6\ddot{n}+1}$					
1	0	45.95	23.68	2.622	7.633
5	0.7224	0	0.0364	0.0136	0.0161
7	-0.0435	0.0043	0	0.0003	0.0024
11	0.0027	-0.0009	0.0002	0	0
13	-0.0047	0.0006	-0.0007	0	0
$s_{6\ddot{k}+1,6\ddot{n}+1}P^{sc}_{4,6\ddot{k}+1,6\ddot{n}+1}$					
1	0	55.13	20.29	2.861	7.046
5	4.335	0	0.0624	0.0074	0.0223
7	0.2609	0.0103	0	0.0006	0.0011
11	0.0328	0.0010	0.0005	0	0
13	0.0569	0.0023	0.0006	0	0
$(1 - s_{6\ddot{k}+1,6\ddot{n}+1})P^{sc}_{4,6\ddot{k}+1,6\ddot{n}+1}$					
1	0	-9.189	3.383	-0.2384	0.5872
5	-3.612	0	-0.0259	0.0062	-0.0062
7	-0.3044	-0.0060	0	-0.0002	0.0013
11	-0.0300	-0.0019	-0.0003	0	0
13	-0.0616	-0.0017	-0.0014	0	0

Table 7.3: The average value of the k-th and n-th component of the power crossing the air gap [W] in stator coordinates. This result was calculated for the waveform of the CSI with $\alpha = 42°$ of Figure 6.5 and a radial array. The dissipation and mechanical components of $P^{sc}_{4,6\ddot{k}+1,6\ddot{n}+1}$ are also listed.

- The space harmonics play only a minor role in all the power terms.

- The average air gap power in rotor coordinates is equal to the dissipation part of $P^{sc}_{4,6\ddot{k}+1,6\ddot{n}+1}$ in stator coordinates. This may be written as:

$$P^{rc}_{2,6\ddot{k}+1,6\ddot{n}+1} = s_{6\ddot{k}+1,6\ddot{n}+1}P^{sc}_{4,6\ddot{k}+1,6\ddot{n}+1}. \tag{7.29}$$

This is the power dissipated in the shielding cylinder, also calculated in Chapter 6. Equation (7.29) proves that the power dissipated in the shielding cylinder is equal in stator and rotor coordinates. We have, therefore, in the notation of Chapter 4 (where primes indicate rotor coordinates) just shown that

$\langle P'_{diss,sc} \rangle = \langle P_{diss,sc} \rangle$ where $\langle P'_{diss,sc} \rangle = P_2^{rc}$ and $\langle P_{diss,sc} \rangle = sP_4^{sc}$.

- The air gap power term $P_{4,6\ddot{k}+1,6\ddot{n}+1}^{sc}$ is negative for the same combination of space and time harmonics where the slip is negative. This means that when it is multiplied by the slip, all the resulting terms are positive. This is the third entry in Table 7.3, i.e., the dissipated power. Dissipated power should always be positive; this is therefore a good way to check the calculated result.

7.3.8 The Lorentz force method

Another method to calculate the electromagnetic torque of the machine is by means of the Lorentz force, as explained in Chapter 4. This method is ideal for the EμFER machine since it calculates the force on a conductor in a magnetic field. An expression, (4.45), has been obtained for the torque:

$$T_e = l_s \int\limits_{r_{so}}^{r_w} \int\limits_0^{2\pi} r^2 B_{r,mag}(r,\phi) J_{z,s}(r,\varphi) \, dr \, d\varphi. \tag{7.30}$$

in the complex notation used in this chapter, equation (7.30) becomes:

$$T_{e,6\ddot{k}+1,6\ddot{n}+1}(t) = l_s \int\limits_{r_{so}}^{r_w} \int\limits_0^{2\pi} r^2 B_{r,m,6\ddot{k}+1}^{(2)}(r,\varphi,t) J_{z,s,6\ddot{k}+1,6\ddot{n}+1}(\varphi,t) \, dr \, d\varphi, \tag{7.31}$$

where:

$$B_{r,m,6\ddot{k}+1}^{(2)}(r,\varphi,t) = \mathrm{Re}\left\{ \bar{B}_{r,m,6\ddot{k}+1}^{(2)}(r,\varphi,t) \right\}, \tag{7.32}$$

and:

$$J_{z,s,6\ddot{k}+1,6\ddot{n}+1}(\varphi,t) = \mathrm{Re}\left\{ \bar{J}_{z,s,6\ddot{k}+1,6\ddot{n}+1}(\varphi,t) \right\}. \tag{7.33}$$

The k-th space harmonic of the flux density due to the magnets is in stator coordinates, from (4.23):

$$\bar{B}_{r,m,6\ddot{k}+1}^{(2)}(r,\varphi,t) = \frac{1}{r}\left[\frac{\partial}{\partial \phi} \bar{A}_{z,m,6\ddot{k}+1}^{(2)}(r,\varphi,t) \right] \tag{7.34}$$

which becomes, from (7.6):

$$\bar{B}_{r,m,6\ddot{k}+1}^{(2)}(r,\varphi,t) = \frac{-j(6\ddot{k}+1)p}{r} \hat{\bar{A}}_{z,m,6\ddot{k}+1}^{(2)}(r) \, e^{-j\left[(6\ddot{k}+1)p\varphi - (6\ddot{k}+1)\omega_s t - p\theta_0\right]}. \tag{7.35}$$

The three-phase stator currents result in a current density travelling wave, of which the k-th space and n-th time harmonic component is written as:

$$\bar{J}_{z,s,6\ddot{k}+1,6\ddot{n}+1}(\varphi,t) = \left\{ \frac{3}{2} \frac{\hat{n}_{s,6\ddot{k}+1}\hat{\bar{i}}_{s,6\ddot{n}+1}}{h_w r_{wc}} \right\} e^{-j\left[(6\ddot{k}+1)p\varphi - (6\ddot{n}+1)\omega_s t\right]} \tag{7.36}$$

from (6.15), but now written in complex exponential form. Equation (6.15) is the sum over the space and time harmonics of the real part of (7.36). From (7.35) and (7.36), the integral over φ in (7.31) can be written as:

$$\int_0^{2\pi} \cos\left[(6\ddot{k}+1)p\varphi - (6\ddot{k}+1)\omega_s t - p\theta_0\right] \cos\left[(6\ddot{k}+1)p\varphi - (6\ddot{n}+1)\omega_s t\right] d\varphi. \quad (7.37)$$

Performing the integral, one obtains:

$$\pi \sin\left[6(\ddot{k}-\ddot{n})\omega_s t - p\theta_0\right]. \quad (7.38)$$

The second integral in (7.31) is $\int_{r_{so}}^{r_w} r\hat{A}_{z,m,6\ddot{k}+1}^{(2)}(r)\, dr$. It can be worked out in general when recalling from (5.6b) that the r-dependent part of the vector potential in the air gap due to the permanent magnets[5] can be written as:

$$\hat{A}_{z,m,6\ddot{k}+1}^{(2)}(r) = C_{6\ddot{k}+1}^{(2)} \left(\frac{r}{r_{mi}}\right)^{-|6\ddot{k}+1|p} + D_{6\ddot{k}+1}^{(2)} \left(\frac{r}{r_{mi}}\right)^{|6\ddot{k}+1|p}. \quad (7.39)$$

Working out this integral results in the following general expression for the *k*-th space and *n*-th time harmonic component of the electromagnetic torque on the stator:

$$T_{e,6\ddot{k}+1,6\ddot{n}+1}(t) = -\pi(6\ddot{k}+1)pl_s \sin\left[6(\ddot{k}-\ddot{n})\omega_s t - p\theta_0\right] \left\{\frac{3}{2}\frac{\hat{n}_{s,6\ddot{k}+1}\hat{i}_{s,6\ddot{n}+1}}{h_w r_{wc}}\right\}$$

$$\cdot \begin{cases} \frac{r_{mi}^{|6\ddot{k}+1|p}C_{6\ddot{k}+1}^{(2)}}{2-|6\ddot{k}+1|p}\left(r_w^{2-|6\ddot{k}+1|p} - r_{so}^{2-|6\ddot{k}+1|p}\right) + \frac{r_{mi}^{-|6\ddot{k}+1|p}D_{6\ddot{k}+1}^{(2)}}{2+|6\ddot{k}+1|p}\left(r_w^{2+|6\ddot{k}+1|p} - r_{so}^{2+|6\ddot{k}+1|p}\right) \\ \hspace{8cm} \text{if } |6\ddot{k}+1|p \neq 2, \\ r_{mi}^2 C_{6\ddot{k}+1}^{(2)}\ln\left(\frac{r_w}{r_{so}}\right) + \frac{D_{6\ddot{k}+1}^{(2)}}{r_{mi}^2}\left(r_w^4 - r_{so}^4\right) \hspace{1cm} \text{if } |6\ddot{k}+1|p = 2. \end{cases}$$

$$(7.40)$$

Equation (7.40) is valid for all three permanent-magnet arrays, as long as the appropriate boundary condition constants $C_{6\ddot{k}+1}^{(2)}$ and $D_{6\ddot{k}+1}^{(2)}$ are substituted into it. From (7.40) it can be seen that the torque is constant when the space and time harmonics are equal, and pulsating (a function of time) when $\ddot{k} \neq \ddot{n}$. The effect of the rotor offset angle θ_0 (the angle between the magnetic axes of the permanent-magnet field and the stator current field) is also seen in (7.40). When $\theta_0 = 0$, the torque is zero for equal space and time harmonics and when $\theta_0 = \pm\frac{\pi}{4}$, the torque is maximum.

Table 7.4 lists the mechanical power (the electromagnetic torque times the rotational velocity) for the same current waveform and permanent magnets as in Tables 7.1 and 7.3. It may be seen from Table 7.4 that the mechanical power for equal

---

[5]There is no bar in $\hat{A}_{z,m,6\ddot{k}+1}^{(2)}(r)$ because in Chapter 5, the boundary condition constants were all real.

space and time harmonics is equal to the result of the Poynting vector method shown in Table 7.3.

Each of the two methods provides unique information with respect to the other method. The Poynting vector method results, in addition to mechanical power terms, also in dissipation power terms that cannot be calculated by the Lorentz force method. The Lorentz force method, on the other hand, provides information about the torque ripple[6] that the Poynting vector method, as used in this thesis, does not provide.

The torque ripple for the current waveform and magnets used for Tables 7.1, 7.3 and 7.4 is shown in Figure 7.1. The average value of the torque, $\langle T_e \rangle$, is also shown.

$|k| \setminus |n|$	1	5	7	11	13
$T_{e,6\ddot{k}+1,6\ddot{n}+1}\omega_m$					
1	-1.766×10^5	33388	-20258	7299	-11457
5	0	0	0	0	0
7	285.3	-53.94	32.72	-11.79	18.51
11	100.3	-18.96	11.50	-4.145	6.51
13	-68.20	12.89	-7.824	2.819	-4.425

Table 7.4: The mechanical power obtained with the Lorentz force method from (7.40).

7.4 Induced losses in the stator iron

7.4.1 Introduction

Arguably the most difficult parameter to predict in any electrical machine is the iron losses. This is mainly due to the following facts:

- iron is a magnetically nonlinear material;

- its magnetic properties may be anisotropic (important when rotating fields are considered);

- manufacturing of laminations strongly influence the magnetic properties;

- temperature; and

- pressure or forces on the iron.

This list is only a partial list of the factors influencing the electromagnetic properties of iron.

Although a lot of research has gone into the calculation of the iron losses in (slotted) laminated cores of electrical machines, this will not be reviewed here. (For a thorough literature review, see [Pol98].)

---

[6]It should be recalled that the time-varying terms of the Poynting vector have been neglected in this thesis. This is documented in Appendix B.
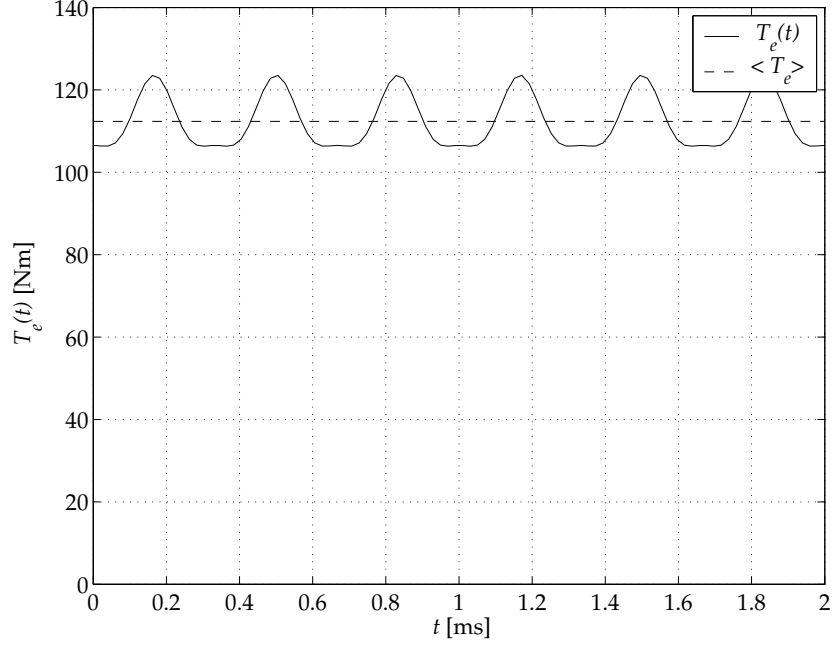
Figure 7.1: Electromagnetic torque $T_e(t)$ calculated by the Lorentz force method for the same current waveform and magnets used for Tables 7.1, 7.3 and 7.4. The torque ripple is clearly visible, and the average value of the torque, $\langle T_e \rangle$, is also shown.

To summarize, previous research can be divided into two categories:

- *The classical approach.* Here, the total iron loss is considered to be the sum of the hysteresis loss and eddy current loss:

$$P_{Fe} = P_{Fe,h} + P_{Fe,e}, \tag{7.41}$$

where the hysteresis loss is proportional to frequency and the the peak flux density to the power of a number S:

$$P_{Fe,h} \propto \omega \widehat{B}^S, \tag{7.42}$$

where S is the Steinmetz constant. Its value depends on material properties and its range is: $1.5 < S < 2.3$.

The eddy current loss is proportional to the square of the flux density and either proportional to the frequency squared or to the power of 3/2. The former case is for the case where the reaction field of the eddy currents does not influence the applied field (i.e. at low frequencies), while in the latter (high-

frequency) case it does:

$$P_{Fe,e} \propto \begin{cases} \omega^2 \widehat{B}^2 & \text{for small } \omega \\ \omega^{\frac{3}{2}} \widehat{B}^2 & \text{for large } \omega \end{cases} \tag{7.43}$$

- *The modern approach.* In practice, machines exhibit losses that are not accounted for by (7.43). Therefore, in addition to the the hysteresis and eddy current loss, a third loss component is added: the anomalous loss. Thus, (7.41) becomes:

$$P_{Fe} = P_{Fe,h} + P_{Fe,e} + P_{Fe,a}. \tag{7.44}$$

Many researchers have put serious efforts into finding analytical expressions for $P_{Fe,a}$, with varying degrees of success. This is not under consideration in this thesis, however. More attention is paid to the eddy current loss, since the largest component in (7.44) at high frequencies is usually $P_{Fe,e}$. The next subsection takes a look at calculating the eddy current loss in the stator iron. This is followed by a discussion of a simple but effective method to estimate the total iron loss P_{Fe} from material data provided by the manufacturer.

7.4.2 Eddy current loss

Appendix D documents the derivation of an equation for the calculation of the stator eddy current loss. A function:

$$F(\xi) \equiv \frac{3}{\xi} \frac{\sinh \xi - \sin \xi}{\cosh \xi - \cos \xi}, \tag{7.45}$$

has been introduced for this purpose, where the variable ξ is the ratio of the lamination thickness to the skin depth, or:

$$\xi \equiv \frac{2b}{\delta}. \tag{7.46}$$

The stator iron volume:

$$V_{s,Fe} = \pi \left(r_{so}^2 - r_{si}^2 \right) l_s, \tag{7.47}$$

is needed for the calculation, given as:

$$P_{s,Fe,e} = \sum_{k=1,3,5,\cdots}^{\infty} \frac{1}{6} V_{s,Fe} \widehat{B}_{sy,k}^2 \sigma \pi^2 f_k^2 (2b)^2 F_k(\xi_k). \tag{7.48}$$

From equation (7.48), the eddy current loss in the stator yoke is a function of the peak yoke flux density squared. The dependency on the lamination thickness $2b$ and the frequency is given by the function $F(\xi)$ from equation (7.45). For low frequencies, and thus small ξ, $F(\xi) \approx 1$, the dependencies on lamination thickness and frequency are:

$$P_{s,Fe,e} \propto (2b)^2 f^2. \tag{7.49}$$

For high frequencies, $F(\xi) \approx \frac{3}{\xi}$, the dependencies become:

$$P_{s,Fe,e} \propto (2b)f^{\frac{3}{2}}. \tag{7.50}$$

The flux density in the winding is to be as high as possible since this increases the power density of the machine. However, the flux density in the yoke should be minimized because of the squared dependency of the stator loss on it. It can be decreased by increasing the yoke thickness $b_{sy} \equiv (r_{so} - r_{si})$, i.e., by decreasing r_{si}, the stator inner radius. By algebraic manipulation of the term $V_{s,Fe}\widehat{B}^2_{sy,k}$ in (7.48):

$$V_{s,Fe}\widehat{B}^2_{sy,k} = \pi \left(r^2_{so} - r^2_{si} \right) l_s \left(\frac{\widehat{\Phi}_{sy,k}}{(r_{so} - r_{si})l_s} \right)^2 = \frac{\pi\widehat{\Phi}^2_{sy,k}}{l_s} \frac{(r_{so} - r_{si})(r_{so} + r_{si})}{(r_{so} - r_{si})^2}$$

$$= \frac{\pi\widehat{\Phi}^2_{sy,k}}{l_s} \frac{b_{sy} + 2r_{si}}{b_{sy}}, \tag{7.51}$$

one sees that the loss is not a function of the yoke thickness squared, but $(b_{sy} + 2r_{si})/b_{sy}$, which means that the reduction in loss gets asymptotically less as b_{sy} increases. Figure 7.2 shows the eddy current loss in the stator yoke of the EμFER machine as a function of b_{sy}.

Another possibility for reducing the eddy current loss is to make the laminations thinner; the chosen thickness is a tradeoff between low losses and cost.

For the dimensions of the EμFER machine, Table 7.5 lists the eddy current loss in the stator iron at 30 000 rpm. This is done as a function of the first 13 space
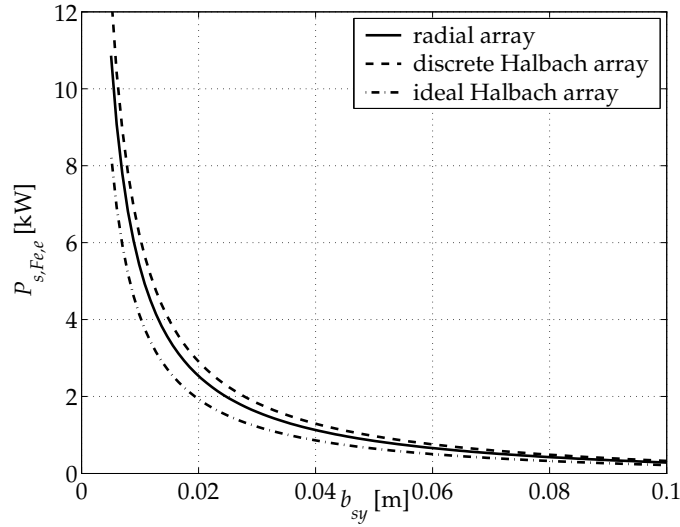
Figure 7.2: The eddy current loss in the stator yoke of the EμFER machine as a function of b_{sy}.

harmonics of the magnets for the three arrays discussed in this thesis. Table 7.5 also lists the values of ξ_k, $F_k(\xi_k)$, and $3/\xi_k$, showing the validity of the assumption that $F_k(\xi_k) \approx 3/\xi_k$ for high frequencies.

From Table 7.5 it can be seen that the loss of the discrete Halbach array is higher than that of the other two arrays, except at the 7th and 9th space harmonics, where the loss for the radial array is higher. Particularly, the 3rd harmonic is significantly higher and the 5th is present, whereas it is zero in the radial array. This can also be seen from Figure 5.15, where the spectral properties of the fields due to the three arrays are shown.

The total loss listed in Table 7.5 is: 1452 W for the radial array, 1666 W for the discrete Halbach array and 1107 W for the ideal Halbach array. These are for a conductivity of iron of $\sigma = 7 \times 10^6$ S/m and a constant permeability of $2500\mu_0$ H/m.

k	1	3	5	7	9	11	13	Tot.
ξ_k	1.662	2.879	3.717	4.398	4.987	5.514	5.994	-
$F_k(\xi_k)$	0.9881	0.9070	0.7951	0.6926	0.6117	0.5503	0.5036	-
$3/\xi_k$	1.805	1.042	0.8071	0.6821	0.6016	0.5441	0.5005	-
$P_{s,Fe,e,rad,k}$	1247	192.4	0	8.311	3.681	0.6065	0.0380	1452
$P_{s,Fe,e,dh2,k}$	1288	350.8	23.59	0.4151	2.242	0.9447	0.1744	1666
$P_{s,Fe,e,ih,k}$	1107	0	0	0	0	0	0	1107

Table 7.5: The eddy current loss [W] in the stator iron calculated from (7.48) for the first 13 space harmonics. The rotational speed for these calculations was 30 000 rpm.

7.4.3 Total stator iron losses

The previous subsection discussed the calculation of the stator eddy current loss due to the rotating permanent magnets. If expressions for the other two loss components can be found, this is useful. However, finding $P_{Fe,h}$ and especially $P_{Fe,a}$ for rotating non-sinusoidal magnetic fields is a very complicated task.

A simple but effective way of estimating the total stator iron loss is to use the following expression for the loss density [Pol98]:

$$k_{Fe} = c_{Fe}k_{Fe,0} \left(\frac{\omega}{\omega_0} \right)^{\frac{3}{2}} \left(\frac{\widehat{B}}{\widehat{B}_0} \right)^2 \quad \text{[W/kg]} \tag{7.52}$$

where c_{Fe} is a dimensionless constant obtained empirically, $k_{Fe,0}$ is the specific iron loss at ω_0 and $\widehat{B}_0$ is obtained from the material manufacturer, ω and $\widehat{B}$ are the frequency and flux density at which the loss is to be obtained, respectively.

In the EµFER machine, high-frequency laminated steel with a lamination thickness of 0.2 mm is used. The specific iron loss is given as $k_{Fe,0} = 140$ W/kg at $\omega_0 = 2\pi \times 1000$ rad/s and $\widehat{B}_0 = 1.5$ T. When this is substituted into (7.52) and

worked out for the total stator mass, the total iron loss is as that given in Table 7.6, where the correction constant was set equal to $c_{Fe} = 2$.

The total loss is obtained by adding the losses at the different harmonic components. For the three arrays the total loss is: radial: 2970 W; discrete Halbach: 3292 W; and ideal Halbach: 2391 W.

k	1	3	5	7	9	11	13	Tot.
$P_{s,Fe,tot,rad,k}$	2694	261.4	0	9.681	4.282	0.7092	0.0447	2970
$P_{s,Fe,tot,dh2,k}$	2783	476.6	28.33	0.4835	2.608	1.105	0.2050	3292
$P_{s,Fe,tot,ih,k}$	2391	0	0	0	0	0	0	2391

Table 7.6: The total loss [W] in the stator iron calculated from (7.52) for the first 13 space harmonics. The rotational speed for these calculations was 30 000 rpm.

7.5 The locked-rotor resistance revisited

In Chapter 6, the locked-rotor resistance was calculated as a function of frequency from the Poynting vector in the air gap. Figure 6.8(a) showed the results of the analytically calculated and the measured per-phase resistance. It was clear from Figure 6.8(a) that at high frequencies, the reflected rotor resistance was not the only effect playing a role in the frequency-dependent resistance of the stator. It was also mentioned that the difference at high frequencies is due to the stator iron losses.

Expression (7.52) of the previous section now gives us the opportunity to also include the stator losses in the frequency-dependent stator resistance. One assumption made for this purpose is that the resistive effect due the stator losses $R_{s,statorFe}$ may be linearly added to the resistive effect of the shielding cylinder on the rotor $R_{s,sc}$ and the DC resistance R_{dc}.

The first step is the translation of (7.52) into a resistance $R_{s,statorFe}$, which follows a similar procedure as that for $R_{s,sc}$ in Chapter 6. The same loss data are used from the stator iron's data sheets as were used in the previous section. Figure 7.3 shows the result of this calculation. The experimentally obtained resistance is shown as stars, and three other curves are shown: $R_{s,sc} + R_{dc}$, $R_{s,statorFe,tot}$ and $R_{s,statorFe,tot} + R_{s,sc} + R_{dc}$.

It can be seen that the last curve fits the measured data quite well, even at the higher frequencies where the reflected rotor resistance (including the skin effect in the shielding cylinder) $R_{s,sc}$ of Chapter 6 was insufficient. The largest difference between the calculated and measured resistance is in the bandwidth 3–20 kHz. In this bandwidth, the measured result appears to be a function of frequency squared.

A resistance $R_{s,statorFe,e}$, due to the eddy current loss of (7.48) (and therefore a function of frequency squared for lower frequencies), may be introduced to better model the per-phase frequency-dependent resistance of the machine. However, the critical frequency, where the eddy current loss changes from being proportional to f^2
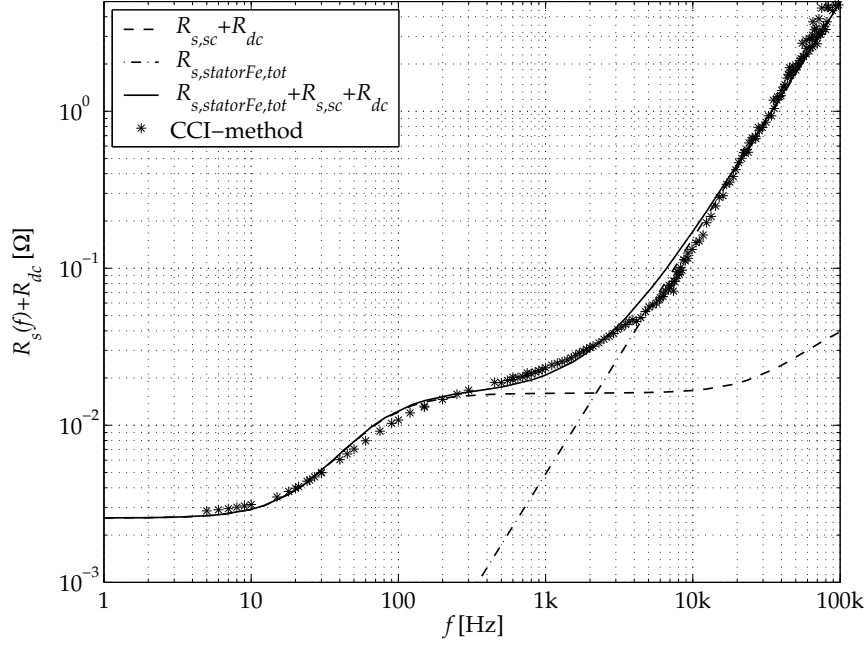
Figure 7.3: Comparison of results of the analytically calculated and the measured per-phase resistance. The calculated result includes the stator losses.

to $f^{3/2}$, is at 4 kHz for the used 0.2 mm plates.[7] This is therefore not a better method and the total loss dependency of $f^{3/2}$ is used for the whole bandwidth. If a smaller plate thickness is substituted into (7.48), the critical frequency moves to the right. For example, for $2b = 0.1$ mm, the critical frequency is 20 kHz. In this case it makes sense to model the "centre" bandwidth of the resistance with the eddy current loss model of (7.48), and at the higher frequencies, to model it with the total loss model of (7.52).

7.6 Induced loss in the stator winding

This section takes a look at the eddy current loss induced in the stator Litz wire winding due to the rotating field of the permanent magnets. The winding distribution was introduced in Figure 3.8 as a double-layer winding that is short pitched by one slot. There is one conductor per slot per layer and each conductor consists of two Litz-wire cables of 28 mm^2 each, thus the copper area per conductor is 56 mm^2. Each cable is constructed of 3564 strands with a diameter of 0.1 mm, configured in a $6 \times 6 \times 3 \times 33$ configuration.

---

[7] $R_{s,statorFe,e}$ is not plotted in Figure 7.3.

When calculating the eddy current loss induced in such a Litz winding, one cannot use standard techniques for pulsating fields since the field that the winding is subject to is rotating. Furthermore, it is possible to account for skin and proximity effects by looking at the field due to the current in every strand itself as well as at the fields of the adjacent strands. These complete but complicated analyses have been reported by, among others, [Fer92] and [Tou01].

For the stator winding of the EμFER machine, a simpler analysis would suffice for two reasons:

1. The eddy current loss in the winding is approximately an order of magnitude lower than that of the stator iron. Increasing the accuracy of the analysis by, say, 20% would not result in a much more accurate estimation of the no-load loss of the flywheel machine; and

2. the strand diameter chosen is very small, which reduces the eddy current loss and strengthens the argument of reason 1.

Neglecting the field of the current in the strand itself, one may obtain the eddy current density in a strand $J_{se,z}$ directly by Faraday's Law (4.7b) and Ohm's Law (4.8a). When integrating the square of $J_{se,z}$ over the surface of the strand, dividing by the conductivity σ, and multiplying by the total copper volume, one obtains the expression [Car67]:

$$P_{s,Cu,e} = \frac{1}{8}\,\omega^2 r_{strand}^2\, \sigma \left(\widehat{B}_r^2 + \widehat{B}_\phi^2 \right) A_{Cu} l_s, \tag{7.53}$$

where $\widehat{B}_r$ and $\widehat{B}_\phi$ are the peak values of the radial and tangential magnetic flux densities into the strand, respectively, and A_{Cu} is the total copper area of the winding. Equation (7.53) was originally derived in [Car67] and used in [Lov98], [Spo92] and [Ark92] for air gap windings.

For the dimensions of the EμFER machine, Table 7.7 lists the eddy current loss in the stator winding at 30 000 rpm. This is done as a function of the first 13 space harmonics of the magnets for the three arrays discussed in this thesis.

The total loss of Table 7.7 is: 115.1 W for the radial array, 136.8 W for the discrete Halbach array and 80.4 W for the ideal Halbach array. The above calculations were done for a conductivity of copper of $\sigma = 5 \times 10^8$ S/m.

The difference between the fundamental of the radial array and that of the ideal Halbach array is smaller in the induced iron loss of Table 7.5 than in the induced copper loss of Table 7.7. This is because the ratio of the tangential to radial flux density in the winding region is higher for the radial array than for the ideal Halbach array. Both the radial and tangential components play a role in the stator winding eddy current loss calculation of (7.53), while in the iron eddy current loss of (D.18), only the radial component of the flux density is considered. This is because flux enters iron radially.

k	1	3	5	7	9	11	13	Tot.
$P_{s,Cu,e,rad,k}$	90.53	18.78	0	2.574	2.296	0.7790	0.1012	115.1
$P_{s,Cu,e,dh2,k}$	95.72	34.28	3.539	0.1722	1.434	1.192	0.4418	136.8
$P_{s,Cu,e,ih,k}$	80.36	0	0	0	0	0	0	80.4

Table 7.7: The eddy current loss in the stator winding [W] of the EμFER machine for the first 13 space harmonics. The rotational speed for these calculations was 30 000 rpm.

7.7 Summary and conclusions

This chapter focussed on the combined field of the machine: $\mathbf{A}_{total} = \mathbf{A}_{magnets} + \mathbf{A}_{stator\ currents}$.

Section 7.2 showed the details of combining the two fields into one, whereafter Section 7.3 started the discussion of quantities derived from this field by looking at electromagnetic torque. Both the Poynting vector and Lorentz force methods were used to obtain the torque.

Section 7.4 looked at calculating the induced loss in the stator iron, whereafter Section 7.5 made use of this by adding the resistive effect of the stator iron losses to the frequency-dependent stator resistance. The discussion on induced losses continued in Section 7.6, this time in the stator winding.

Some of the important conclusions reached in this chapter are:

- The Poynting vector can be used to find the torque and the eddy current loss induced in the shielding cylinder by calculating the air gap power. This method delivers similar constant torque results to the Lorentz force method.

- The air gap power calculated by the Poynting vector method is different in rotor and stator coordinates:

    - In rotor coordinates, it only contains dissipation and no mechanical terms, and no interaction between the stator and rotor fields is observable. This is because the surface over which the Poynting vector is integrated rotates with the rotor.

    - In stator coordinates, the air gap power is made up of both a dissipation and a mechanical power part. The interaction terms (where the rotor and stator fields interact) result in only constant mechanical power for equal space and time harmonics. The stator field term contains both mechanical and dissipation terms and these may be separated by means of the rotor slip.

    - The dissipation part of the stator-field power is equal to the air gap power calculated in rotor coordinates. This is the induced loss in the shielding cylinder.

- The Lorentz force method results not only in constant torque terms, but also in the ripple torque. It provides no information on dissipated power, however, since by definition it only calculates mechanical power.

- Although stator losses are a combined field effect, the role played by the field due to the stator currents is so small that it may be neglected.

- A simple expression which states that iron loss is proportional to frequency to the power of 3/2 can be used to find the total iron losses. It can also be used to find the iron-loss part of the frequency-dependent stator resistance.

- To calculate the induced eddy current loss in copper, one has to take both the radial and tangential components of the magnetic field into consideration. In iron, due to its high permeability, the magnetic flux enters radially and only the radial component is required.

- The induced eddy current loss in the stator winding is approximately 20 times smaller than the total losses in the stator iron.

Optimization

8.1 Introduction

In Chapter 3, an external-rotor permanent-magnet synchronous machine with a slot-less stator was introduced for use in a flywheel energy storage system. An analytical model was developed for the design and analysis of such a machine in Chapters 4–7. Chapter 4 presented an overview of the method, while Chapters 5 and 6 discussed the fields due to the permanent magnets and stator currents, respectively. The latter included the effect of the eddy currents in the shielding cylinder on the rotor on the stator current field. Chapter 7 combined these two fields into one to study the magnetic field in the loaded machine.

In the last three chapters, useful quantities were derived from the fields. They were:

- Permanent magnet field (Chapter 5):

    – No-load voltage;

- Stator current field (Chapter 6):

    – Main-field inductance (including the locked-rotor machine inductance);

    – Rotor loss (induced loss in the shielding cylinder);

- Combined field (Chapter 7):

    – Electromagnetic torque;

    – Stator losses (induced eddy current loss in the stator winding, and induced losses in the stator iron);

    – The locked-rotor machine resistance.

These fields and derived quantities completely describe the machine.

Two of the advantages of an analytical approach mentioned in Chapter 4 were:

- lower computation time; and

- the analytical approach allows one greater insight into the problem.

The latter was motivated by R.L. Stoll in [Sto74], where he mentioned that relationships between analysis inputs (for instance the machine geometry) and analysis outputs (e.g. torque and losses) may be established quicker with the analytical method than with the finite element method.

Although Stoll wrote this in 1974, at a time when computers were very slow and bulky compared with what is available today, his argument remains valid. Even with the very fast desktop PCs of today, it still takes hours and for some complicated geometries even several days to compute a field solution with derived quantities. To do optimization with this method, the geometry (for example) has to be iteratively changed and a recalculation has to be done for every new geometry. This takes the total computation time from hours to days or from days to weeks.

In contrast, the computation time for field solutions with the analytical method is in the order of minutes for geometries for which the finite element method requires hours. Even if a complete field solution is done iteratively for varying geometries like that described above for the finite element method, one still typically waits less than an hour for the total computation to run. Furthermore, the real power of the analytical method lies in the fact that one does not have to do a complete field solution for the parametric changes in geometry (or any other input variables), i.e., the output quantities (torque and losses, for example) can be written *directly* in terms of the input variables. This means to that the same optimization routine that required between days and weeks with the finite element method now only takes seconds to minutes to compute.

In this chapter, the power of the analytical model of Chapters 4—7 is exploited due to the above two facts by performing several different optimizations on the machine. Section 8.2 starts the discussion by looking at possible optimization criteria and independent variables. Three criteria are chosen: electromagnetic torque, total stator losses and rotor loss in the shielding cylinder. The rest of the chapter focusses on these three criteria. Section 8.3 discusses the influence of the permanent-magnet array on these three quantities, whereafter Section 8.4 takes a look at the effect of the winding distribution on them. Section 8.5 discusses machine geometry optimization, by which is meant the variation of the different radii in the machine and the influence thereof. Section 8.6 makes use of the results of Section 8.5 to find the optimum machine geometry for a fixed rotor outer diameter. The machine does not operate in isolation, but is connected to a power electronics converter. The influence of the choice of the converter on the induced rotor loss will be the brief focus of attention in Section 8.7. Generalizing the analytical machine model will be discussed in Section 8.8, whereafter the chapter will be summarized and concluded in Section 8.9.

8.2 Optimization criteria and input variables

8.2.1 Possible optimization criteria

Typically in optimization problems, some criteria are identified that need to be maximized or minimized, together with the input variables that these criteria depend upon. In the electrical machine under consideration in this thesis, several optimization criteria are possible:

1. high torque;

2. very low rotor losses;

3. low induced stator losses (with neglect of the stator current field this is the no-load losses);

4. low stator conduction losses (i.e. losses due to the stator currents at load);

5. high total cycle efficiency (energy in and out);

6. compact (i.e. high power or torque density);

7. low manufacturing cost;

8. low material cost;

9. high reliability;

10. low maintenance;

11. safe for use in a public vehicle;

12. robust, etc.

8.2.2 Input variable possibilities

As above, several input variables may be identified:

1. number of pole pairs p;

2. permanent-magnet array;

3. magnet pole arc;

4. winding distribution;

5. machine geometry, i.e. radii, ratios of radii (thicknesses), axial length and air gap length;

6. materials;

7. converter choice, etc.

8.2.3   The chosen optimization criteria and input variables

It is a very large task to do all the optimizations of the criteria of Section 8.2.1 for all the inputs of Section 8.2.2. For some of the criteria of Section 8.2.1, some numerical value must first be defined, for example for safety. It is beyond the scope of this thesis to find these or to optimize for all the optimization criteria in the list. Only the most important ones are selected, and these are chosen as: #1, 2, and 3 for all the input variables of Section 8.2.2.

8.3   Magnet array

8.3.1   Introduction

Several different permanent-magnet arrays can be used in a permanent-magnet synchronous machine, as mentioned earlier in this thesis. Chapter 5 discussed three examples of magnet arrays: the conventional radial array, the discrete Halbach array with two segments per pole, and the ideal sinusoidal Halbach array. This section starts with a discussion of types other than these three. Thereafter, the variation of the magnet pole arcs of the radial and discrete Halbach arrays will be discussed in conjunction with the variation of the number of pole pairs. Finally, the effects upon the losses and torque by this pole arc variation will be examined. Only the variation in the number of pole pairs and the polar arcs of the magnets will be discussed here. The magnet thickness is left for Section 8.5.

8.3.2   The number of segments per pole

In Chapter 5, [Mar92], [Ata97] and [Ofo95] were cited as having discussed different magnet arrays analytically. Of these, [Ata97] examined discrete Halbach arrays with three and four segments per pole, while [Mar92] and [Ofo95] treated arrays with two segments per pole.

Figure 8.1 shows some examples of different permanent-magnet arrays, where the stator has been removed for clarity. In Figure 8.1(a), a standard radial array is shown with a customary 80% pole arc[1]. For a four-pole machine, this translates to 72°. The radial array may also be called the discrete Halbach array with 1 segment per pole.

Figures 8.1(b), (c) and (d) show discrete Halbach arrays with 2, 3 and 4 segments per pole, respectively. In these figures, the polar magnet spans are equal for the magnet segments. For example, for the discrete Halbach array with 2 segments per pole, an equal magnet span translates into a 50% span per magnet. For the four-pole machine shown as an example, the magnet polar arc then becomes 45°. The other two arrays have correspondingly smaller polar magnet spans since they have more segments per pole.

---

[1]A 80% pole arc means that 80% of the circumference is filled with magnet material
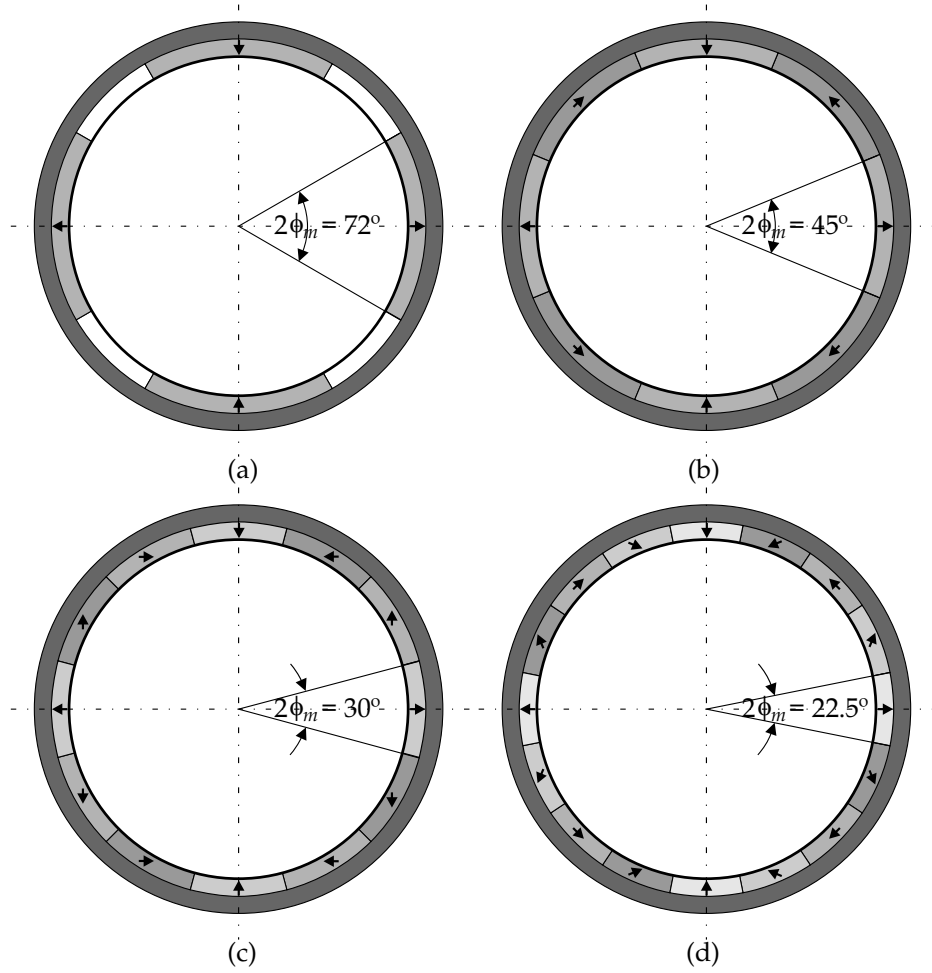
Figure 8.1: Examples of different permanent-magnet arrays for a four-pole external rotor machine: (a) the standard 80% pole arc radial array (or 1 segment per pole discrete Halbach array); (b), (c) and (d): discrete Halbach arrays with: (b) two segments per pole; (c) three segments per pole; and (d) four segments per pole.

In this thesis, the only arrays solved analytically were those of Figures 8.1(a) and (b). Due to lack of time, more segments per pole could not be investigated. However, the ideal Halbach array was also included in the analysis in the thesis. This array, also described in [Ata97], is formed by continuing the process of Figure 8.1. The number of segments per pole is increased to infinity while each segment has zero magnet span. This results in a sinusoidally magnetized array as described in Chapter 5, and may be regarded as the limit of the process of increasing the number of segments per pole.

Solving for the magnetic field of other array types entails finding expressions for the remanent magnetization as in (5.17):

$$\mathbf{B}_{rem} = B_{rem,r}\hat{\mathbf{i}}_r + B_{rem,\phi}\hat{\mathbf{i}}_\phi. \tag{8.1}$$

The remanence should first be written down as in (5.10) for the radial array, and then converted into a Fourier-series representation as in (5.12). In the discrete Halbach array, the Fourier-series representation of the radially magnetized magnets was also given by (5.12), while that of the tangentially magnetized magnets was given by (5.19). In some of the magnet segments in Figure 8.1, both a radial and a tangential component exist simultaneously, requiring an expression from (8.1) with both a radial and a tangential component for those segments.

Another important remark about the discrete Halbach array with 2 segments per pole is that this array, as solved in Chapter 5, did not have the 50/50 ratio as shown in Figure 8.1(b). It was made to have a 80/20 magnet-span ratio between the radially and tangentially magnetized magnets instead. The reason for this is that it corresponds to the radial array discussed in Chapter 5, with the air between the radially magnetized magnets filled up with tangentially magnetized magnets. In the next two subsections, variations in pole arc and the corresponding ratios between radially and tangentially magnetized magnets will be studied, first for the radial array and then for the discrete Halbach array.

8.3.3 The influence of pole arc variation and the number of pole pairs on torque and loses

Electromagnetic torque

The radial and discrete Halbach arrays may be compared with respect to their torque production when varying the polar magnet span. This has been done in Figure 8.2 for the fundamental space and time harmonic component, which also shows the torque of the ideal Halbach array for comparison. (The angle ϕ_m is not defined for the ideal Halbach array.)

Figure 8.2 shows the variation in electromagnetic torque for varying pole arc and four different numbers of pole pairs: Figure 8.2(a): $p = 1$, (b): $p = 2$, (c): $p = 3$ and (d): $p = 4$.

From Figure 8.2, the following observations may be made:

- The difference between the torque produced by the radial and discrete Halbach arrays gets smaller with increasing pole arc. At a polar arc of 100%, these two arrays are the same since no tangential magnets are left.

- The difference between the torque produced by the radial and discrete Halbach arrays gets larger as the pole number gets higher.

- The polar arc where the radial and discrete Halbach arrays produce more torque than the ideal Halbach array gets larger for more poles. This effect is slight for the discrete Halbach array but strong for the radial array.
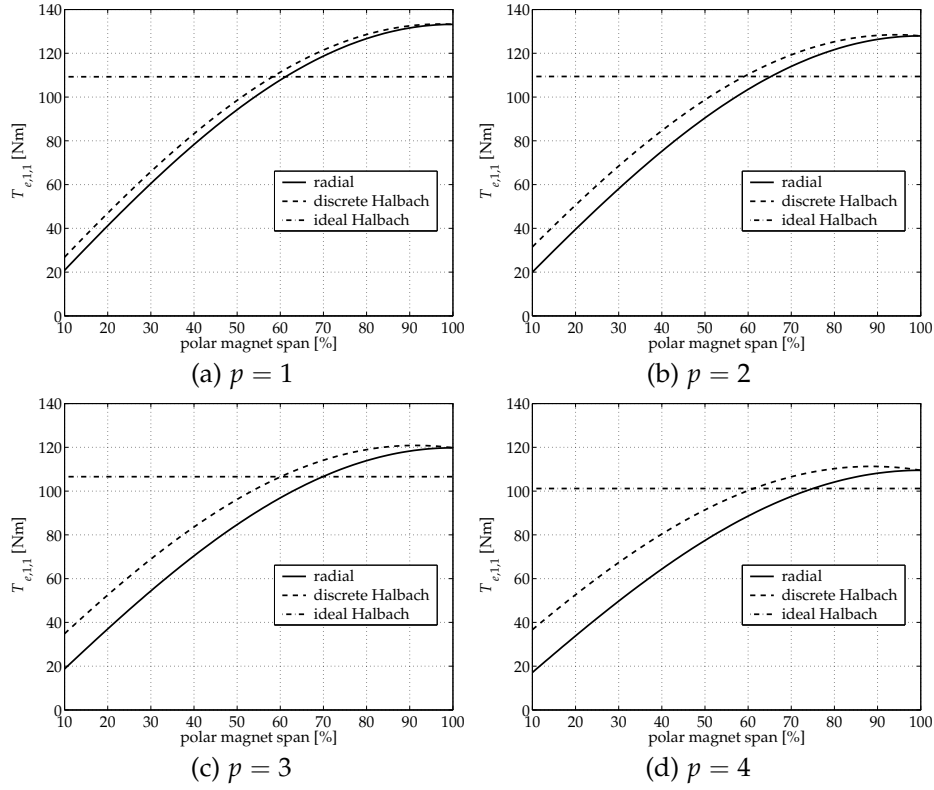
Figure 8.2: Fundamental space and time harmonic component of the torque as a function of the the polar magnet span and the number of pole pairs.

- The torque drops for all three arrays as more poles are used. This is due to the fact that for more poles but the same geometry (machine radii and axial length), less flux crosses the air gap to interact with the winding.

- The difference in torque between the two and four pole arrays is small.

Rotor loss

The second and third optimization criteria treated in this chapter are #2 and 3 of Section 8.2.1, i.e. very low rotor loss and low induced stator losses.

The shielding cylinder loss is not influenced by pole arc variation; it is a function of the number of pole pairs. For the EμFER geometry and for the second current waveform of Figure 6.5, the induced rotor loss is equal to: $p = 1$: 143.7 W; $p = 2$: 90.13 W; $p = 3$: 72.9 W; $p = 4$: 58.8 W.

Induced stator iron losses

Figure 8.3 shows the total losses induced in the stator iron calculated by (7.52) as a function of the polar magnet span and the number of pole pairs: (a) $p = 1$; (b) $p = 2$; (c) $p = 3$; (d) $p = 4$. The calculation was done for the first 13 space harmonics.

From Figure 8.3, the following observations may be made:

- The difference between the losses induced by the radial and discrete Halbach arrays gets larger with increasing pole arc.

- The difference between the losses induced by the radial and discrete Halbach arrays gets larger as the pole number gets higher. This is clearly seen at the lowest pole arc, where the difference starts to become visible. For $p = 4$, it is almost over the entire range of magnet span, depicted in Figure 8.3.

- The polar arc at which the radial and discrete Halbach arrays induce higher losses than the ideal Halbach array gets larger at higher pole pair numbers.

- The losses decrease for all three arrays as more poles are used.

Induced stator winding loss

Since the induced eddy current loss in the stator copper is approximately an order of magnitude lower than the induced iron losses,[2] it is not included in the discussion in this chapter. It is valid to neglect the induced stator winding loss in an optimization routine since the stator can be cooled much more efficiently than the rotor.

8.3.4   A magnet span larger than 80%

As already mentioned before, a polar magnet span of 80% is often used for the radial array in industry today. The reason for not using a (much) larger span is evident when field plots are examined. Figure 8.4 shows six field plots: three for the radial array and three for the discrete Halbach array with 2 segments per pole. For both these arrays, three different pole arcs are plotted: 50%, 80% and 100%.

From Figures 8.4(a) and (b) it can be seen that the flux from one magnet to another in the radial array is increased as they come closer to one another. In the extreme case of a 100% pole arc of Figure 8.4(c), the leakage from magnet to magnet is seen to be very substantial.

In Figure 8.4(d), the 50/50 Halbach array is clearly seen to reduce the flux density in the rotor back iron. This is also seen in the 80/20 ratio of Figure 8.4(e), but to a lesser extent. The leakage flux is not substantially reduced when compared with the radial array of Figures 8.4(a) and (b) however.

For the 100% pole arc case of Figures 8.4(c) and (f), the two arrays are identical since there is no tangentially magnetized material.

---

[2]It was designed to be so by choosing the Litz wire strand diameter very small.
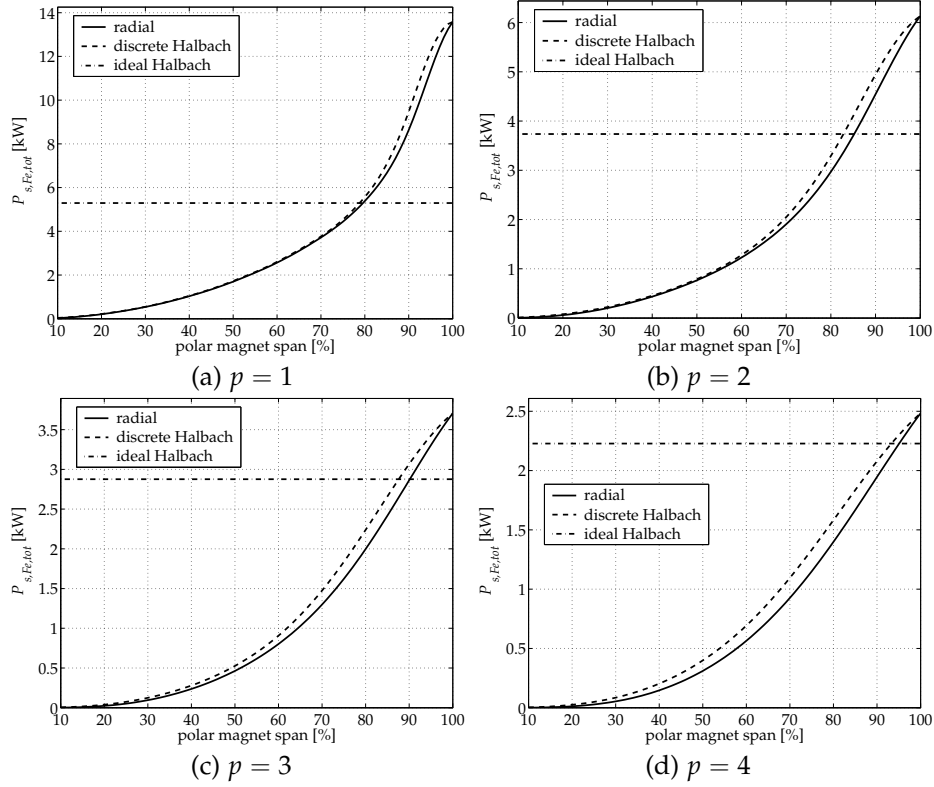
Figure 8.3: Total stator iron loss for the first 13 space harmonics as a function of the polar magnet span and the number of pole pairs.

8.3.5 Magnet skewing

It is customary to skew the magnets with respect to the stator to reduce or eliminate the cogging torque. Since the machine discussed in this thesis has no slots, the cogging torque is zero anyway, negating the need for magnet skewing.

8.4 Winding distribution

8.4.1 Introduction: Four different winding distributions

In Chapter 3, the EµFER machine's 1-2-2-1 winding distribution was introduced. This section will investigate four other winding distributions, shown in Figure 8.5, and their effects upon important quantities.

The winding distributions of Figure 8.5 are: (a) the 1-2-2-1 distribution of Chapter 3, (b) a 1-1-2-1-1, (c) a 2-2-2 and (d) a 3-3 distribution. For the following discussion, the winding factors defined in Appendix A are used. The winding parameters

(a)   (b)   (c)

(d)   (e)   (f)
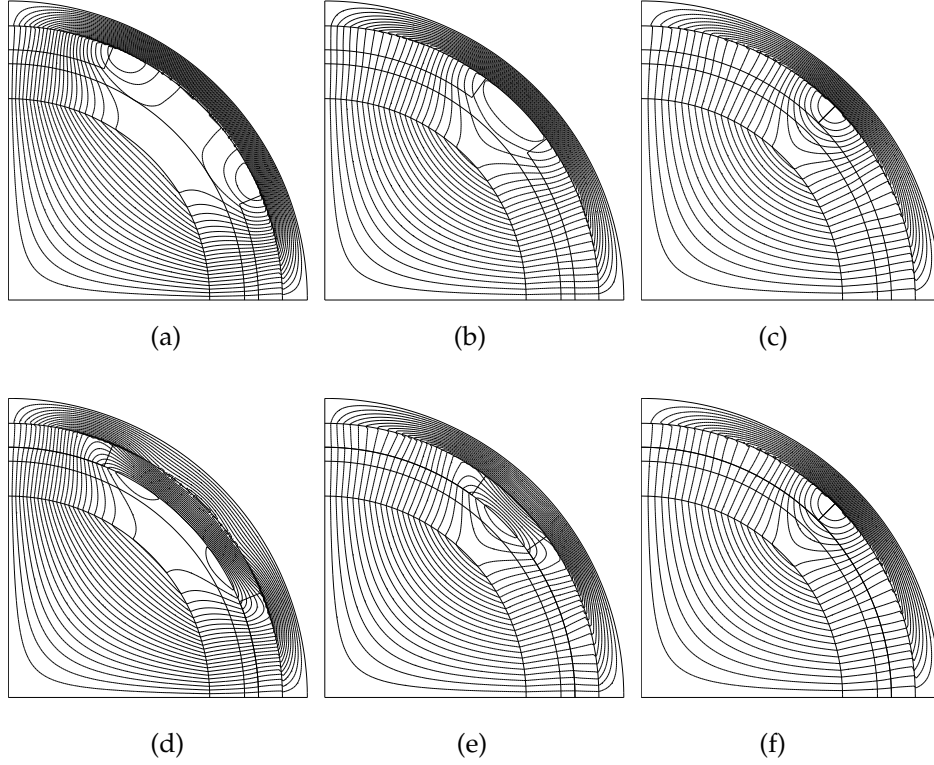
Figure 8.4: Magnetic field lines for different polar magnet spans: radial array: (a) 50%; (b) 80%; (c) 100%; discrete Halbach array with 2 segments per pole: (d) 50%; (e) 80%; (f) 100%.

of the first three are the same except for the pitch angle. In all three, $m = 3$, $p = 2$, $q = 3$, $N = 12$, they have 1 conductor/slot/layer and all are two-layer windings. These three windings all have $s = 2mpq = 36$ slots. The 3-3 winding distribution differs in the number of slots per pole per phase, q, and is a three-layer winding. It has $s = 24$ slots. In all four winding distributions, the slot-opening angle is $\varphi_{so} = 0.8(2\pi/s)$. A summary of these four distributions, of which phase a is shown in Figure 8.5, is as follows:

- 1-2-2-1 distribution: $\varphi_{pitch} = \frac{2\pi}{s} = \frac{\pi}{18}$ rad;

- 1-1-2-1-1 distribution: $\varphi_{pitch} = \frac{4\pi}{s} = \frac{\pi}{9}$ rad;

- 2-2-2 distribution: $\varphi_{pitch} = 0$ rad; and

- 3-3 distribution: $q = 2$ and $\varphi_{pitch} = 0$ rad.
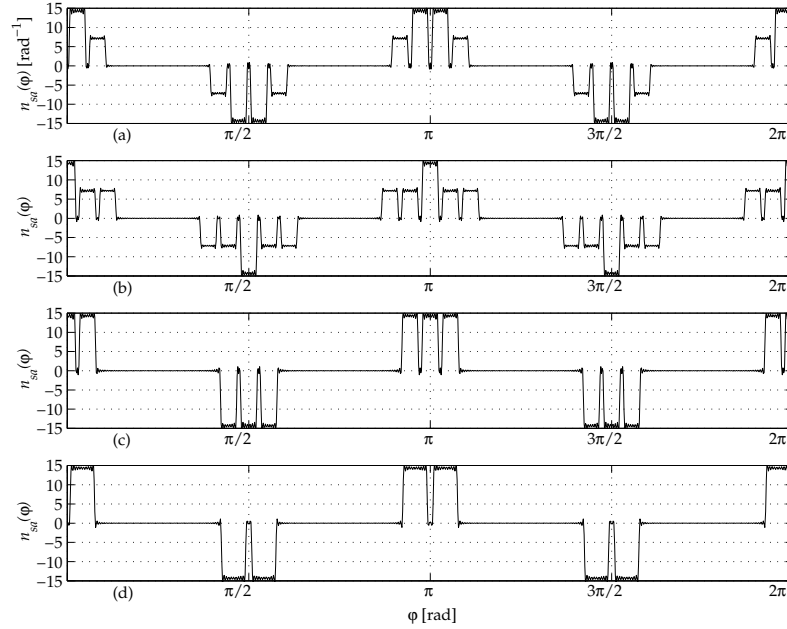
Figure 8.5: Phase *a* of four different winding distributions: (a) 1-2-2-1; (b) 1-1-2-1-1; (c) 2-2-2; and (d) 3-3.

8.4.2 Electromagnetic torque

The fundamental space and time harmonic of the electromagnetic torque for the four different winding distributions of Figure 8.5 and the radial and discrete Halbach arrays is:

- 1-2-2-1: Radial: 135.7 Nm; Discrete Halbach: 139.71 Nm

- 1-1-2-1-1: Radial: 129.48 Nm; Discrete Halbach: 133.3 Nm

- 2-2-2: Radial: 137.8 Nm; Discrete Halbach: 141.87 Nm

- 3-3: Radial: 138.11 Nm; Discrete Halbach: 142.19 Nm

These results were calculated for 80% polar magnet arcs. The torque results above shows that the winding distribution has an influence on the torque, but it is small.

8.4.3 Induced loss in the shielding cylinder

Concerning losses, the only loss component of interest with variation in the winding distribution is the induced loss in the shielding cylinder. The stator iron losses are not influenced by the use of a different winding distribution since the stator current

$|k| \setminus |n|$	1	5	7	1	5	7
	1-2-2-1			1-1-2-1-1		
1	0	54.94	20.23	0	50.02	18.42
5	4.319	0	0.0622	0.3152	0	0.0045
7	0.2599	0.0103	0	1.304	0.0515	0
	2-2-2			3-3		
1	0	56.65	20.86	0	56.91	20.95
5	10.45	0	0.1505	11.94	0	0.1718
7	2.222	0.0878	0	3.027	0.1196	0

Table 8.1: The induced loss in the shielding cylinder [W] for the four different winding distributions of Figure 8.5 and the current waveform of the CSI with $\alpha = 42°$ of Figure 6.5. The totals are: 1-2-2-1: 79.8 W, 1-1-2-1-1: 70.1 W, 2-2-2: 90.4 W, and 3-3: 93.1 W.

field is neglected in its calculation. The stator winding loss is also neglected in the optimization routines since it is very small compared to the stator iron losses.

Table 8.1 compares the induced loss in the shielding cylinder in the case of the four different winding distributions of Figure 8.5. These calculations were done for the current waveform of the CSI with $\alpha = 42°$ of Figure 6.5. The induced loss is a function of the square of the winding distribution, $\hat{n}_{s,k}^2$, as can be seen from equation (6.64). This explains the small difference in the induced loss of the 1-2-2-1 and the 3-3 distributions.

8.4.4 Winding distribution: Comparison and conclusion

It is clear from the torque calculations of Section 8.4.2 and Table 8.1 that the winding distribution only plays a minor role in both the torque production and the induced rotor loss. The following remarks may be made by investigating these tables:

- The 2-2-2 winding distribution is very similar to the 3-3 distribution. This could already be seen in Figure 8.5.

- For the torque, the differences in the higher-order harmonics are negligible. The large mass moment of inertia of the flywheel further strengthens this fact.

- Comparing the fundamental torque components listed in Section 8.4.2, one sees that the 3-3 distribution produces the highest torque. However, the 1-2-2-1 distribution used in the EμFER machine produces only 1.8% less torque.

- The largest shielding cylinder loss component is that for the fundamental space and the fifth time harmonic.

- The lowest induced loss is for the 1-1-2-1-1 winding distribution; the 1-2-2-1 distribution of the EμFER machine results in 8.9% higher loss for the fundamental space and fifth time harmonic component. However, the ratio of effec-

tive output power to the induced loss of the 1-2-2-1 distribution is 9.4% higher than that of the 3-3 distribution.

In conclusion, one can say that the winding distribution influences the torque production hardly at all and the induced rotor loss only a little.

8.5 Machine geometry

8.5.1 Introduction

This section looks at the ratios between the dimensions of different parts of the machine and the influence thereof on the electromagnetic torque production and losses.

8.5.2 Machine radii variation

Figure 8.6 shows the radii that are varied in a sweeping fashion while the rest is kept constant. The constant radii are the stator outer radius r_{so} and the magnet outer radius r_{mo}. The three radii in between, r_w, r_{ci} and $r_{co} = r_{mi}$, are varied with a constant ratio to each other. In other words, the magnet inner radius r_{mi} is varied with respect to r_{so} and r_{mo}, and while doing this, the distance between r_{mi}, r_{ci} and r_w remains constant. Therefore, a constant mechanical air gap $r_{ci} - r_w$ is assumed, and also a constant shielding cylinder thickness $r_{co} - r_{ci}$.

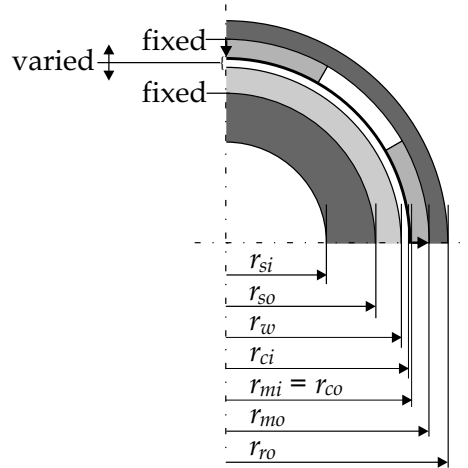By this variation, a ratio between the magnet thickness and the total distance

Figure 8.6: Definition of the radii that are varied and those that stay constant in a study of electromagnetic torque and losses as a function of the machine geometry.

between the stator and rotor surfaces can be defined:

$$R_m \equiv \frac{r_{mo} - r_{mi}}{r_{mo} - r_{so}}. \tag{8.2}$$

8.5.3   Electromagnetic torque

By sweeping the ratio R_m for a constant current density and calculating the fundamental space and time harmonic component of the electromagnetic torque, interesting observations may be made. Graphs that relate R_m to the torque appear in Figures 8.7 and 8.8. These graphs were drawn for four arrays: the radial array with a magnet span of 80%, a discrete Halbach array with 50% magnet span (i.e. 50/50 ratio between radial and tangential magnets), the same array with a 80/20 ratio, and the ideal Halbach array.

   The results of Figures 8.7 and 8.8 are shown for four different values for the stator outer radius r_{so}: $r_{so} = 0.3\, r_{mo}$, $r_{so} = 0.5\, r_{mo}$, $r_{so} = 0.735\, r_{mo}$ and $r_{so} = 0.9\, r_{mo}$. The ratio of r_{so} to r_{mo} indicates how large the active air gap length is, i.e. the length between the stator and rotor surfaces. This is the space for the winding and the permanent magnets.

   The EμFER machine that was extensively discussed in this thesis has a distance between rotor and stator surfaces characterized by the ratio $r_{so}/r_{mo} = 0.735$, i.e. that of Figure 8.7(c) and (g) and Figure 8.8(c) and (g). The ratio between the magnet thickness and this active distance is $R_m = 0.329$ in the EμFER machine, therefore the magnets occupy approximately a third of the thickness of the active air gap length, and the winding approximately two thirds. The value of R_m for the EμFER machine is indicated by a vertical line.

   Several observations may be made from Figures 8.7 and 8.8. These include:

- For $p = 1$ and $p = 2$, the 80/20 discrete Halbach array produces the highest torque for almost all R_m and r_{so}/r_{mo}. The exception is for small r_{so}/r_{mo} (large air gap) and large R_m (thick magnets), where the ideal Halbach array produces higher torque.

- For a high number of pole pairs, large air gap and thick magnets, the ideal Halbach array produces the highest torque.

- The differences between the radial, 80/20 discrete Halbach and ideal Halbach arrays decrease with decreasing air gap for all p.

- The 50/50 discrete Halbach array always produces less torque than the other three arrays, except for high p, a large air gap and thick magnets.

- From Figures 8.7(a) and (e) and 8.8(a) and (e) it can be seen that for higher pole pair numbers and large air gaps, the maximum torque point is reached for thinner magnets in relation to the total air gap length (low R_m between 0.2 and 0.3) than for lower pole pair numbers. As the air gap length is decreased, as in Figures 8.8(b) and (f), this maximum is reached for
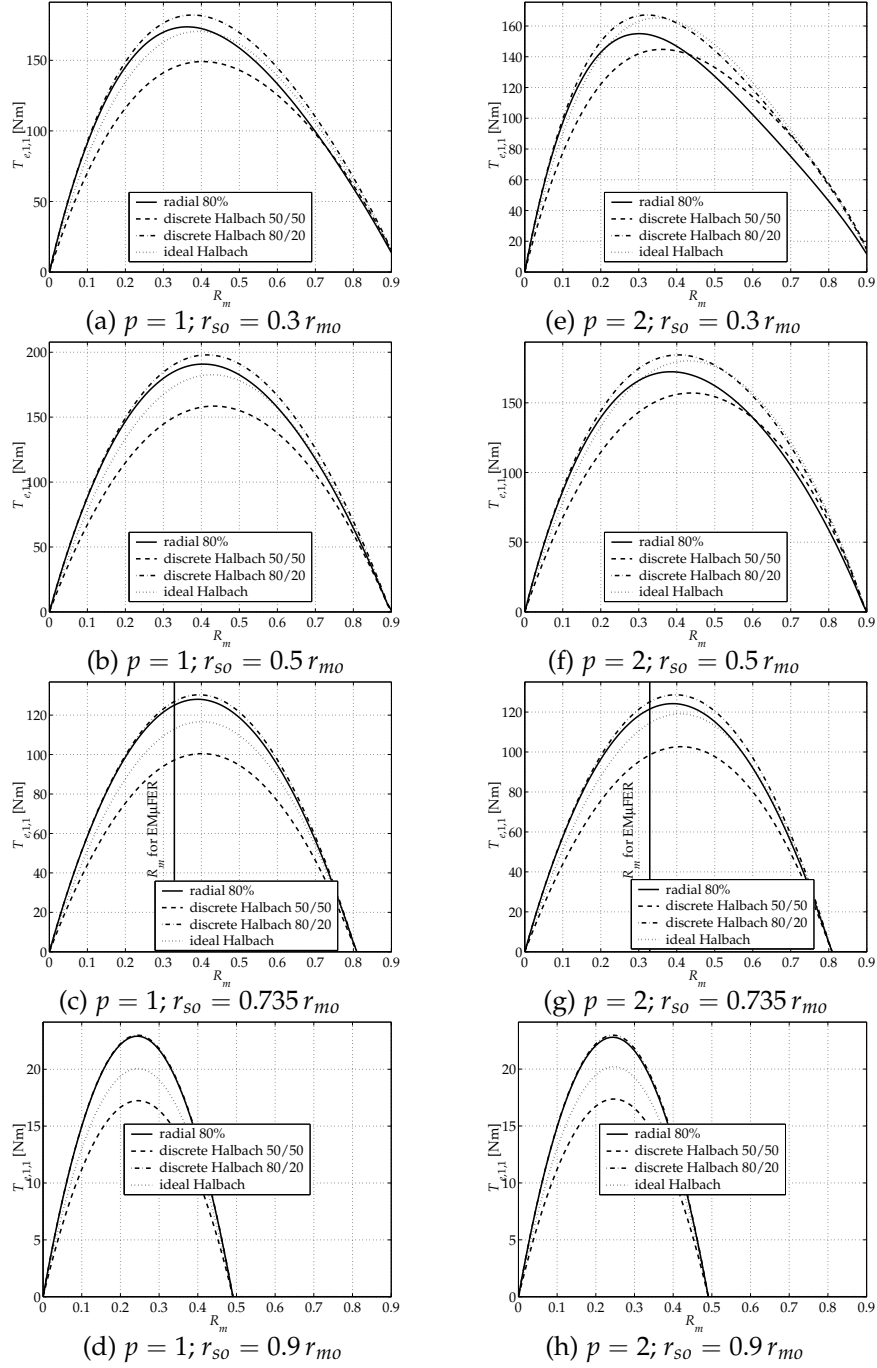
Figure 8.7: Relationship between the torque and R_m for $p = 1$ and $p = 2$.

(a) $p = 3$; $r_{so} = 0.3\, r_{mo}$

(e) $p = 4$; $r_{so} = 0.3\, r_{mo}$

(b) $p = 3$; $r_{so} = 0.5\, r_{mo}$

(f) $p = 4$; $r_{so} = 0.5\, r_{mo}$

(c) $p = 3$; $r_{so} = 0.735\, r_{mo}$

(g) $p = 4$; $r_{so} = 0.735\, r_{mo}$

(d) $p = 3$; $r_{so} = 0.9\, r_{mo}$

(h) $p = 4$; $r_{so} = 0.9\, r_{mo}$
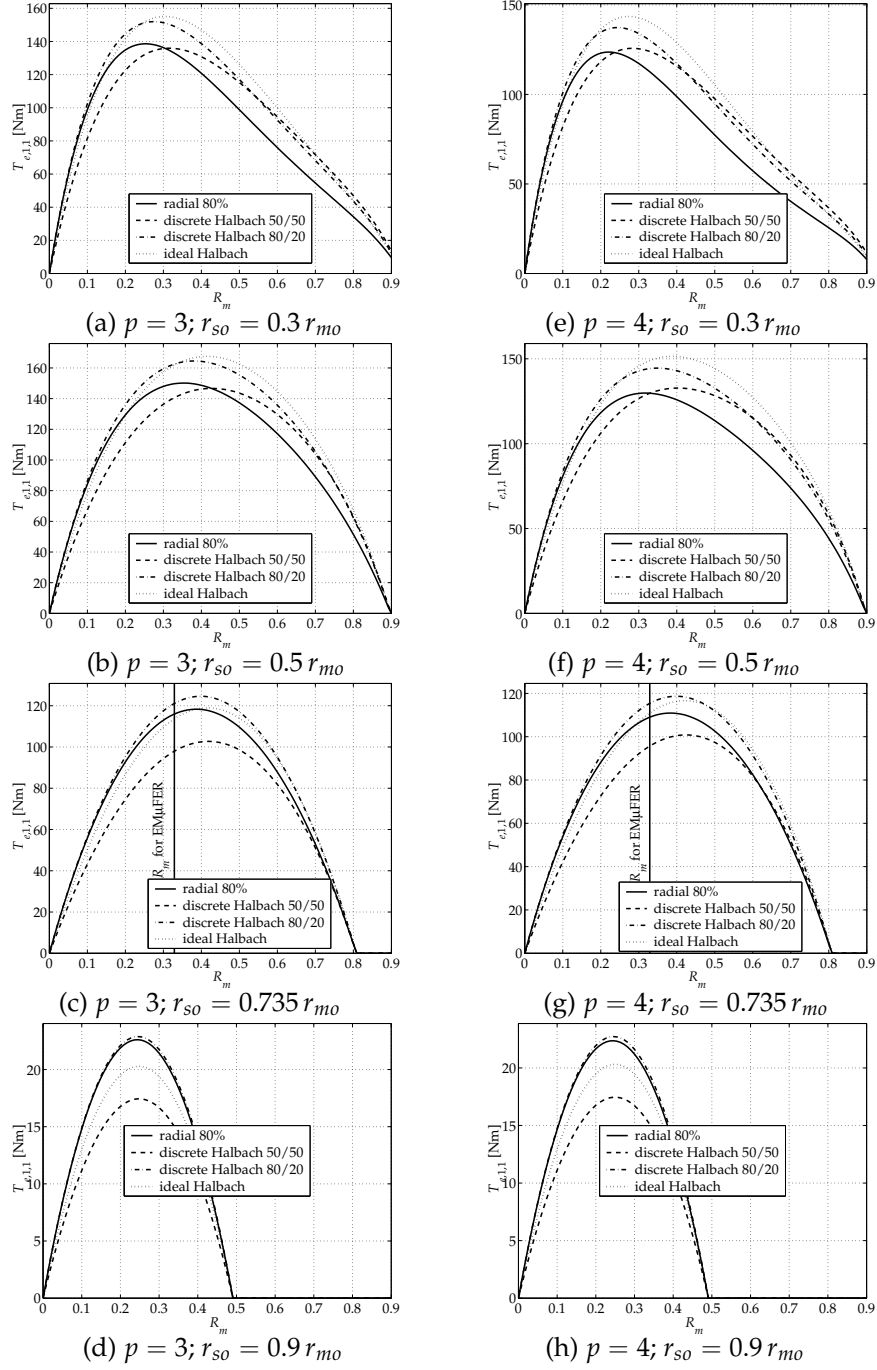
Figure 8.8: Relationship between the torque and R_m for $p = 3$ and $p = 4$.

thicker magnets (R_m between 0.4 and 0.5). For very small air gaps, as in Figures 8.8(d) and (h), the maximum point shifts back towards an R_m between 0.2 and 0.3. This effect is also present for small p, but it is less pronounced.

- The radial array produces less torque in relation to the Halbach arrays when the air gap length, pole pair number and magnet thickness are increased.

- The highest torque of Figures 8.7 and 8.8 is found in Figures 8.7(b). Here, R_m is just over 0.4, the machine has one pole pair and the array is the 80/20 discrete Halbach array with two segments per pole. The torque is just under 200 Nm.

8.5.4 Losses

Only the stator iron losses due to the rotating permanent magnets and the rotor loss induced in the shielding cylinder by the stator currents are investigated in this subsection. The reason for neglecting the induced loss in the stator winding was discussed earlier in this chapter.

The stator iron losses due to the rotating permanent magnets

Figures 8.9 and 8.10 show the induced losses (consisting of a hysteresis and an eddy current loss component, i.e. the total losses discussed in Chapter 7) as a function of R_m for constant current density. The same air gap lengths as used in Figures 8.7 and 8.8 are used in Figures 8.9 and 8.10.

The observations that can be made from Figures 8.9 and 8.10 include:

- For $p = 1$ and small air gaps (see Figure 8.9(d)), the 50/50 discrete Halbach array induces similar total stator losses as the ideal Halbach array. As p increases, this array induces less losses than the ideal Halbach array.

- For all p and air gap lengths, the radial and 80/20 discrete Halbach arrays induce approximately the same losses. The difference increases as the number of pole pairs and R_m is increased. In this case, higher losses are induced by the 80/20 discrete Halbach array.

- For low p and large air gaps, the increase in losses is a weaker function of R_m for the radial array than for the other three arrays.

The induced loss in the shielding cylinder by the stator currents

As indicated in Section 8.3, the eddy current loss induced in the shielding cylinder is a function of the number of pole pairs; not the permanent-magnet array. Figure 8.11 shows the induced loss in the shielding cylinder for the CSI-waveform of Figure 6.5 with $\alpha = 42°$ for constant current density. The results are shown for varying R_m for four different total air gap lengths: (a) $r_{so} = 0.3\, r_{mo}$; (b) $r_{so} = 0.5\, r_{mo}$; (c) $r_{so} = 0.735\, r_{mo}$; and (d) $r_{so} = 0.9\, r_{mo}$.

(a) $p = 1$; $r_{so} = 0.3\,r_{mo}$

(e) $p = 2$; $r_{so} = 0.3\,r_{mo}$

(b) $p = 1$; $r_{so} = 0.5\,r_{mo}$

(f) $p = 2$; $r_{so} = 0.5\,r_{mo}$

(c) $p = 1$; $r_{so} = 0.735\,r_{mo}$

(g) $p = 2$; $r_{so} = 0.735\,r_{mo}$

(d) $p = 1$; $r_{so} = 0.9\,r_{mo}$

(h) $p = 2$; $r_{so} = 0.9\,r_{mo}$
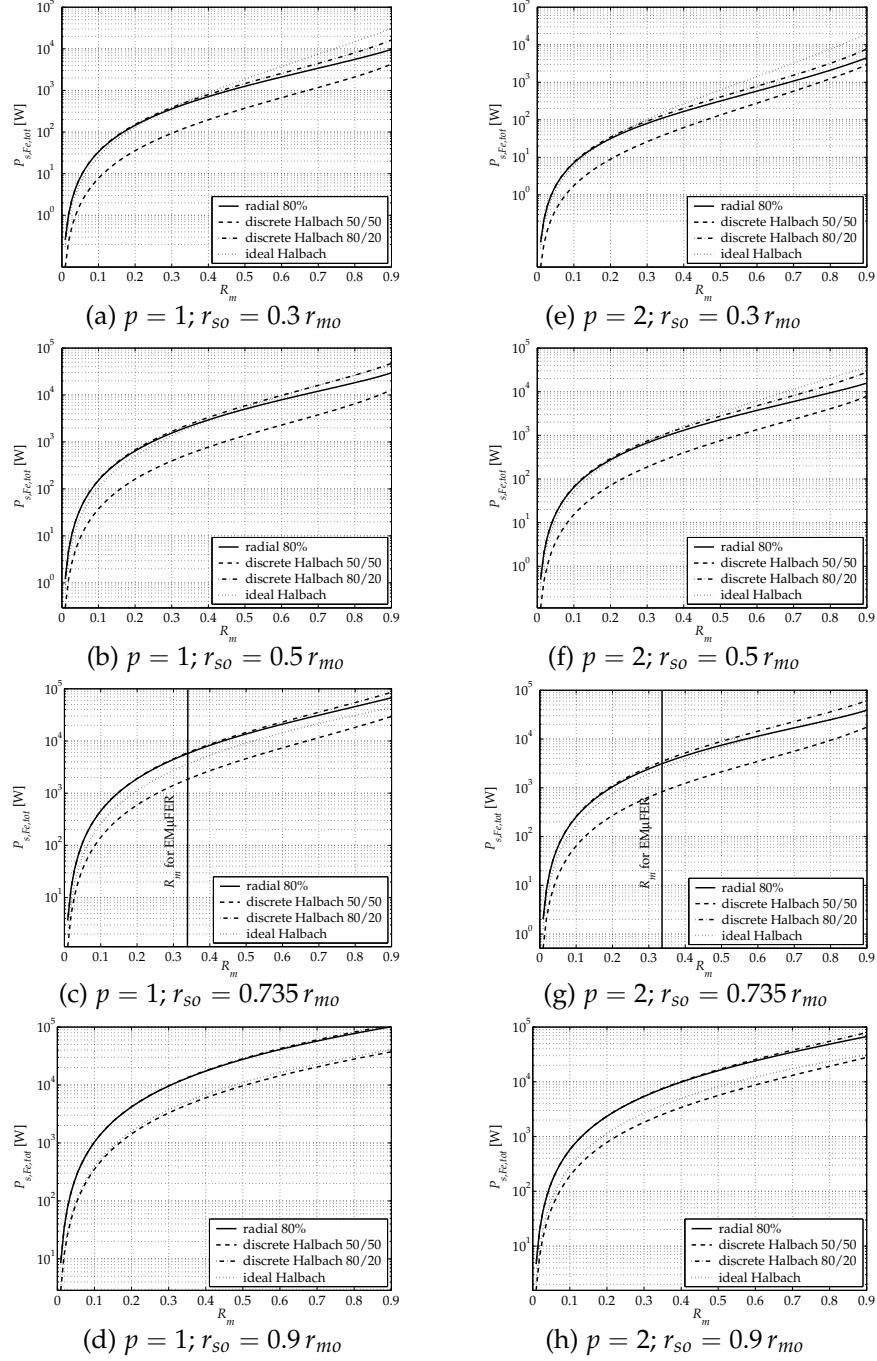
Figure 8.9: Relationship between the total stator loss and R_m for $p = 1$ and $p = 2$.
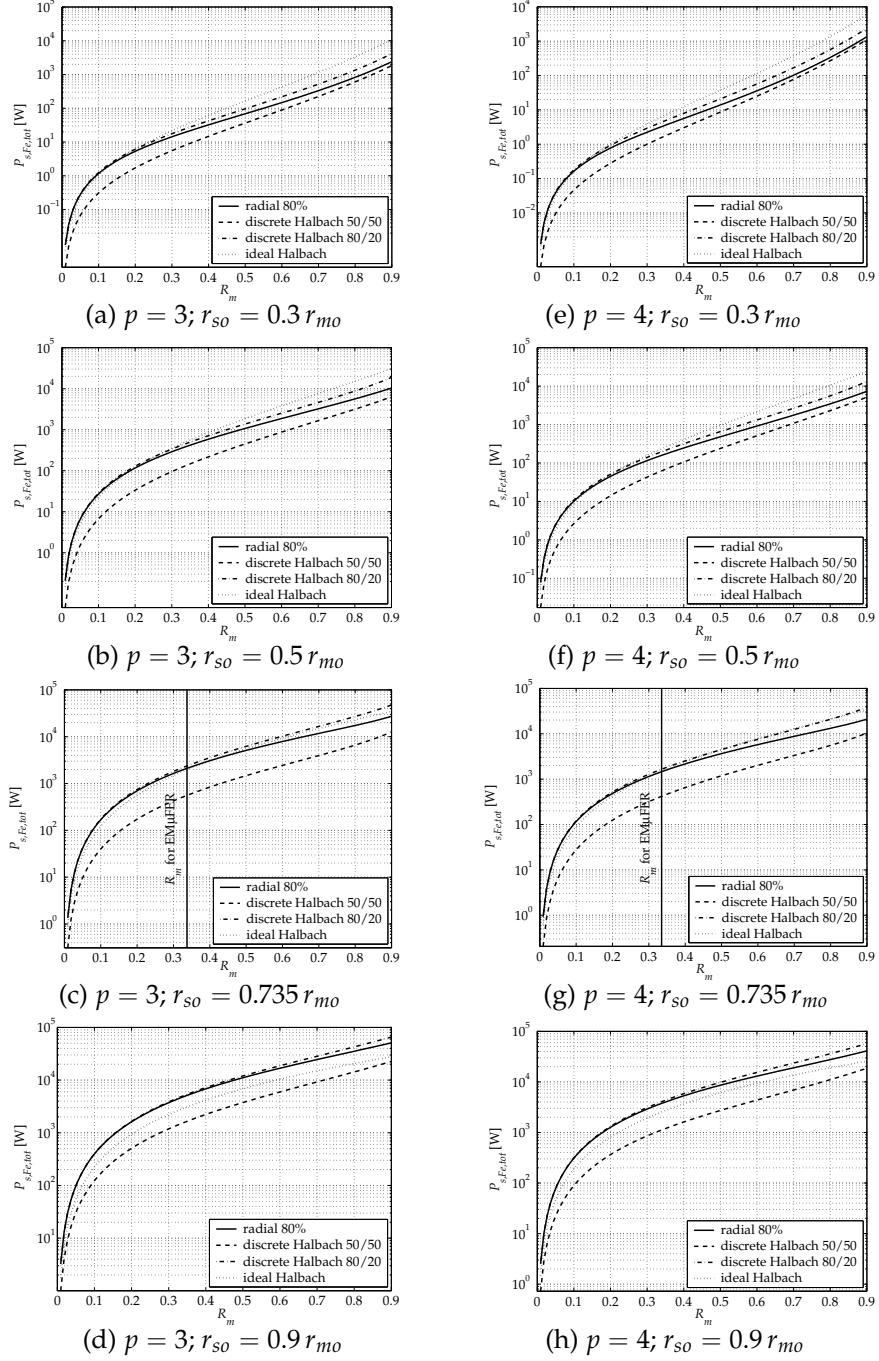
Figure 8.10: Relationship between the total stator loss and R_m for $p = 3$ and $p = 4$.
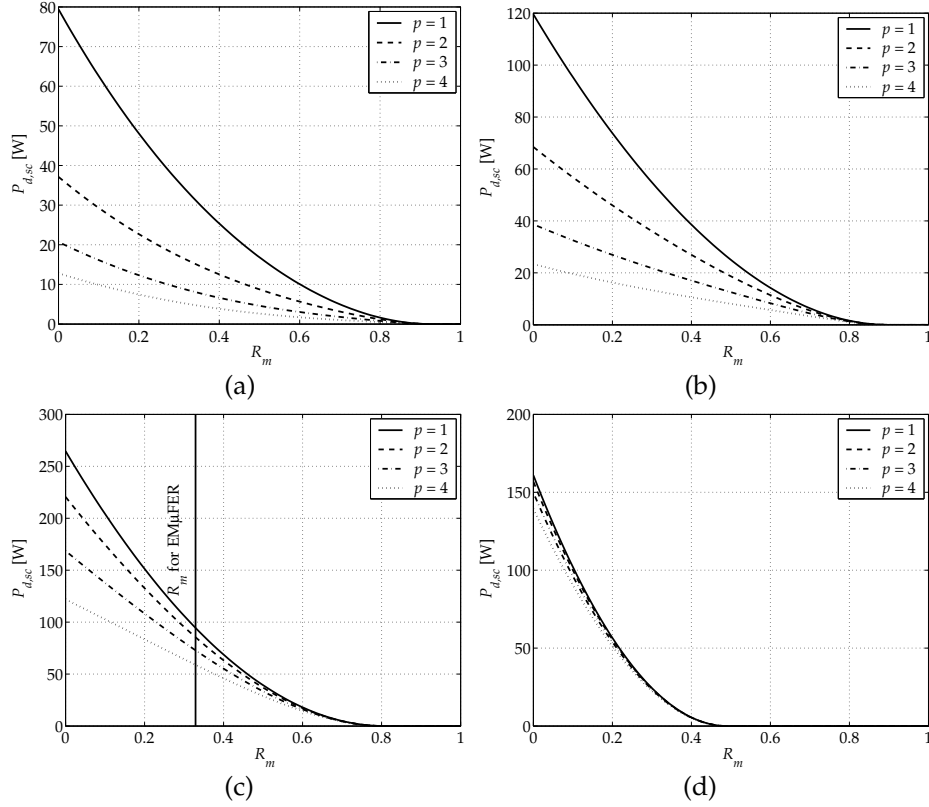
Figure 8.11: Induced loss in the shielding cylinder for the CSI-waveform of Figure 6.5 with $\alpha = 42°$ for constant J_s as a function of R_m: (a) $r_{so} = 0.3\,r_{mo}$; (b) $r_{so} = 0.5\,r_{mo}$; (c) $r_{so} = 0.735\,r_{mo}$; (d) $r_{so} = 0.9\,r_{mo}$.

One can see from Figure 8.11 that:

- The induced loss is lower for larger pole pair numbers.

- The induced loss drops to zero at large R_m since at a certain point, there is no more winding area and consequently zero stator current is reached. The exact value of R_m at which this occurs, is different for different air gap lengths since the mechanical air gap and the shielding cylinder thickness was kept constant.

- The difference in induced loss between the different pole pair numbers decreases with the air gap length.

The induced loss in the shielding cylinder for varying cylinder thicknesses

Figure 8.12 shows the induced loss in the shielding cylinder for varying cylinder thicknesses. One may see from Figure 8.12(c) that for the EμFER air gap of
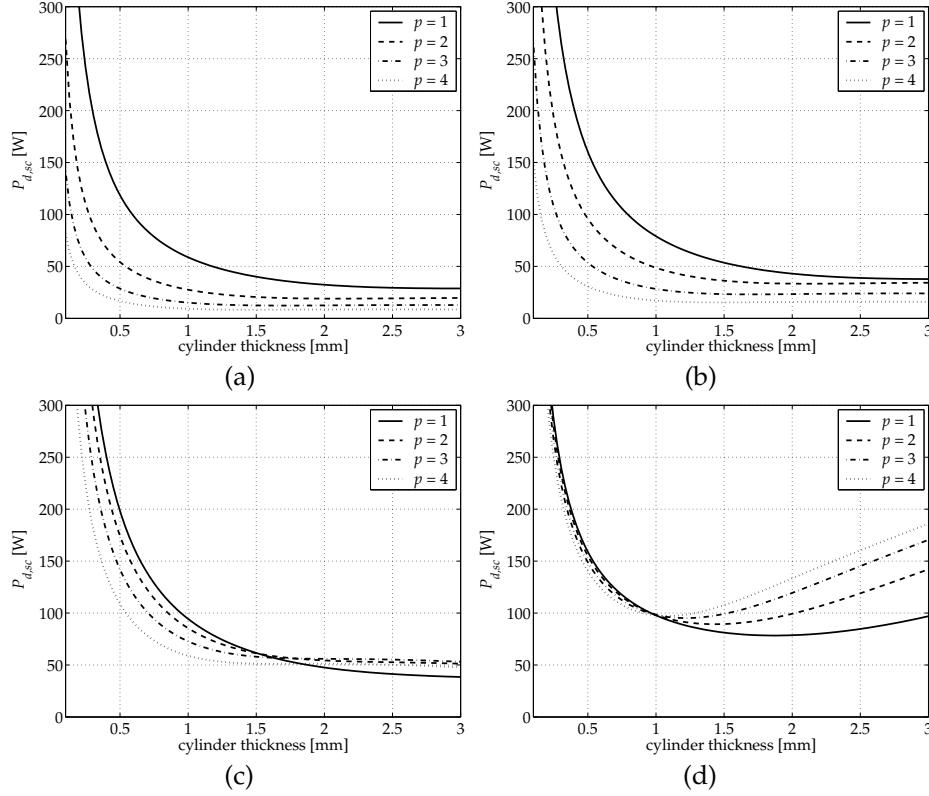
Figure 8.12: Induced loss in the shielding cylinder for the CSI-waveform of Figure 6.5 with $\alpha = 42°$ for constant J_s as a function of the cylinder thickness: (a) $r_{so} = 0.3\, r_{mo}$; (b) $r_{so} = 0.5\, r_{mo}$; (c) $r_{so} = 0.735\, r_{mo}$; (d) $r_{so} = 0.9\, r_{mo}$.

$r_{so} = 0.735\, r_{mo}$ and $p = 2$, the induced eddy current loss in the shielding cylinder was not substantially reduced if the cylinder was thicker than 1 mm.

8.5.5 Conclusion

A clear maximum torque is reached in Figures 8.7 and 8.8 for defined values of R_m. It is therefore possible to optimize the geometry by using the torque as criterion.

However, no clear minima for the total stator losses of Figures 8.9 and 8.10 exist (except for $R_m = 0$, but then the torque is also zero). There is instead a steady increase in stator losses with R_m. Minimizing the total stator losses as a function of R_m is therefore not possible, although one can use the torque optimization of Figures 8.7 and 8.8 in conjunction with the losses of Figures 8.9 and 8.10 to come to a trade-off solution. The stator inner radius r_{si} may of course be selected to minimize the total stator losses, as shown in Figure 7.2 in Chapter 7.

For the induced eddy current loss in the shielding cylinder, from Figure 8.12

values of cylinder thickness exist where the induced loss in the shielding cylinder is a minimum. This may thus also be used as an optimization criterion.

8.6   The optimum machine geometry for constant J_s

8.6.1   Optimization algorithm

To find the optimum machine geometry, the radii that were kept constant in the previous section, r_{so} and r_{mo}, are allowed to vary now. The only radius that is still fixed is r_{ro}, for mechanical reasons.

It is decided that the torque is the most important criterion. The geometry optimization strategy for the torque, total stator losses and induced eddy current loss on the rotor is therefore chosen as having the following steps:

1. $T_{e,1,1}$ is maximized as a variable of all radii except r_{si} (which has no effect on the torque), r_{ro} (which is fixed due to the maximum strength and dimensions of the carbon fibre flywheel), and r_{mo} (which is maximized in step 2). Radii r_w, r_{ci} and r_{co} are kept in constant ratio to each other during this step. (This ratio is revised in step 4.)

2. The flux density in the rotor iron is set to be 2.0 T maximum. Radius r_{mo} is thus adjusted to be the correct distance from r_{ro} to result in this flux density. After the adjustment, step 1 is again performed. This is iterated until the optimum torque is reached for a rotor iron flux density below 2.0 T.

3. The total stator loss is minimized by choosing a r_{si} to result in the maximum allowable value (r_{so} has been obtained in steps 1 and 2).

4. The induced rotor loss is the last step. We have seen in Figure 8.11 that minimum shielding cylinder loss requires large R_m. (Large R_m corresponds to a low winding height h_w and a lower required current for the same torque, since the magnets are thicker. Lower currents induce lower losses in the shielding cylinder.) For optimum torque, however, large R_m is not preferred. Therefore, like for the stator losses, for the rotor loss a maximum allowable value is chosen. The shielding cylinder thickness is adjusted until the loss is below this value (see Figure 8.12). If it cannot be reached, steps 1, 2 and 3 are again performed, requiring this time an increase in R_m, i.e. the torque is reduced.

In optimization, one soon runs into convergence issues and other numerical problems. This was certainly also the case here. Step 1 of the algorithm listed above was implemented by the function `fminsearch` that is available in MATLAB® for unconstrained nonlinear minimization of scalar functions of more than one variable. This function implements the Simplex method, which is a direct search method. The constraints, for example the requirement that all radii be positive and in the order: $r_{so} < r_w < r_{ci} < r_{co} < r_{mo} < r_{ro}$, have been implemented separately from

`fminsearch`. Steps 2, 3 and 4 have been implemented without special tools like this MATLAB® function. If a jump back to Step 1 is required, new constraints should be implemented in that step.

8.6.2 Optimization result

Only the results for the same permanent-magnet array and number of pole pairs as those for the EµFER machine are discussed here: a radial array and $p = 2$. Before the result of the optimization process is started, it is noted that $T_{e,1,1} = 121.68$ Nm and $\widehat{B}_{ry} = 2.03$ T for the EµFER machine, where $\widehat{B}_{ry}$ is the peak value of the rotor yoke flux density. The induced eddy current loss on the rotor of the EµFER machine is 91.83 W (up to the 19th space and time harmonic) for the CSI waveform of Figure 6.5 with $\alpha = 42°$.

Step 1. The optimization process is started with `fminsearch` as described in Section 8.6.1 with the EµFER machine's geometry as initial values. The resulting geometry, fundamental torque and peak flux density in the rotor iron is:

- $r_{so} = 69.921$ mm; $r_w = 104.35$ mm; $r_{ci} = 110.35$ mm; $r_{co} = 111.35$ mm; $r_{mo} = 137.5$ mm; $r_{ro} = 150$ mm; $T_{e,1,1} = 172.33$ Nm; $\widehat{B}_{ry} = 2.5375$ T; $r_{so}/r_{mo} = 0.50852$; $R_m = 0.387$.

It is seen that the peak flux density in the rotor iron is slightly too high. Step 2 is therefore performed to reduce it to below 2.0 T:

Step 2. The rotor yoke thickness is increased from 12.5 mm to $(150 - 137.5) \times 2.5732/2.0 = 16.083$ mm, i.e. the radius r_{mo} is adjusted to 133.92 mm. Now, Step 1 is done again. The result is:

- $r_{so} = 68.036$ mm; $r_w = 101.66$ mm; $r_{ci} = 107.66$ mm; $r_{co} = 108.66$ mm; $r_{mo} = 134.14$ mm; $r_{ro} = 150$ mm; $T_{e,1,1} = 158.85$ Nm; $\widehat{B}_{ry} = 1.9477$ T; $r_{so}/r_{mo} = 0.5072$; $R_m = 0.38539$.

Step 3. Radius r_{si} is found by choosing a maximum accepted value for the stator losses. If this value is chosen as 4 kW, the stator yoke thickness is $b_{sy} = 45$ mm and $r_{si} = 23.036$ mm. The resulting total stator losses are: $P_{s,Fe,t} = 3724.7$ W.

Step 4. The optimum machine with a shielding cylinder thickness of 1.0 mm experiences 156.35 W rotor loss for the CSI waveform of Figure 6.5 with $\alpha = 42°$ (scaled so that the current density is constant). For 0.5 mm, this is 295.95 W and for 2.0 mm: 116.09 W. The shielding cylinder thickness is therefore made 2 mm. (A thicker cylinder is not possible since the mechanical air gap minimum is around 5 mm. The new value of the shielding cylinder thickness changes r_{ci} to 106.66 mm while r_{co} and the other radii remain unchanged.

The geometry of the EµFER machine does not differ much from the optimum geometry. The reason for the small difference is that thinner magnets were chosen because of their high cost.

8.7   Converter options for the flywheel drive: Influence on the rotor loss

8.7.1   Introduction

The main converter options for interfacing the EµFER machine with the DC bus in the energy storage system were already mentioned in Chapter 3: the voltage source inverter (VSI) and current source inverter (CSI). There it was briefly shown that a VSI is a better choice than a CSI when maximizing the system power level is the main consideration. This section continues this discussion by looking at the converter-dependent eddy-current loss induced in the shielding cylinder.

In [Den97] and [Den98], Deng analyzed eddy current losses in the permanent magnets and rotor iron in permanent-magnet synchronous machines. In the first paper, she calculated these losses for a CSI converter connected to the machine. The emphasis in that paper was the commutation-caused loss, i.e. the high-frequency part of the effect of the CSI waveform on the induced loss. In [Den98], she did another analysis on eddy current losses in the magnets and rotor iron, this time for PWM waveforms, i.e. for when a VSI is connected to the machine. These papers showed that it basically boils down to the harmonic content of the stator current waveform. In trying to find reductions of the harmonic content, one has to look at the origin of the harmonics in the converter, as Deng has done. This is beyond the scope of this thesis, however. Only the influence of typical CSI and VSI waveforms on the induced eddy current loss in the shielding cylinder will be investigated.

8.7.2   Influence of using a VSI or CSI on the rotor loss

Current waveform of an idealized CSI

In Section 6.8 the induced loss in the shielding cylinder was discussed, using two CSI current waveforms and the ideal bridge rectifier current waveform as examples. In this section, an idealized CSI current waveform will be described containing only the effects of the commutation angle u.[3] An example of the idealized waveform for $\alpha = 30°$, $u = 12°$ and a rotational velocity of 15 000 rpm is shown in Figure 8.13.

The induced loss in the shielding cylinder due to the idealized waveform of Figure 8.13 is shown in Figure 8.14 as a function of the commutation angle u for $\alpha = 0°$. The loss of Figure 8.14 was calculated for 7 space harmonics and 67 time harmonics. It can be seen from Figure 8.14 that the lowest loss occurs at just over $u = 30°$ and remains fairly constant between $30°$ and $60°$. From this graph, the necessity of a series inductor with the machine to limit the di/dt during commutation may be determined, as well as its value. (In practise, however, a series inductor not

---

[3]Mosebach and Canders did a similar investigation of the current waveform as a function of the commutation angle (among others) [Mos98c]. In their paper, the effects of this parameter on the thrust of a linear machine is investigated.
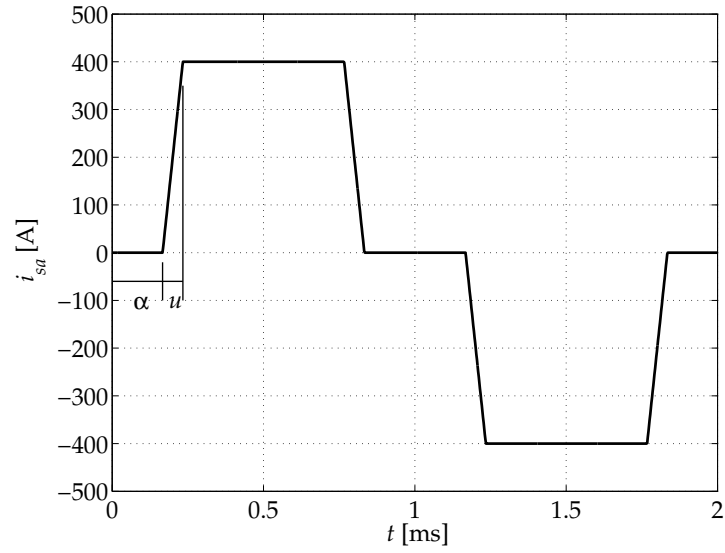
Figure 8.13: An idealized CSI current waveform for $\alpha = 30°$ and a rotational velocity of 15 000 rpm.
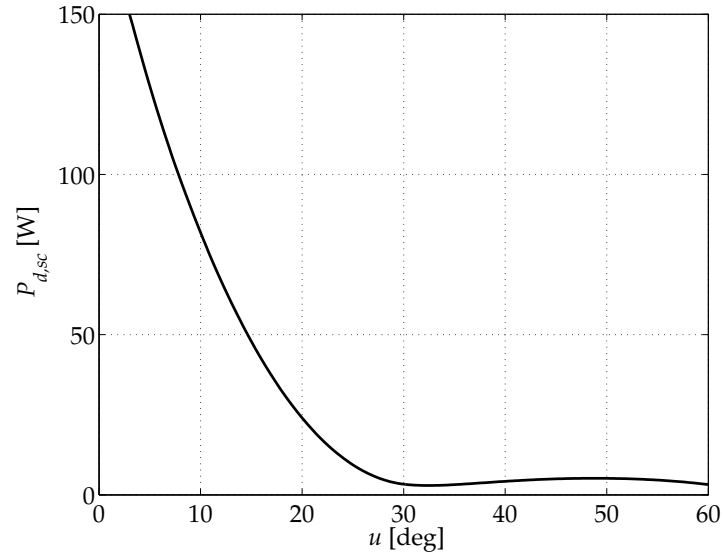
Figure 8.14: The induced loss in the shielding cylinder for the idealized CSI current waveform of Figure 8.13 as a function of the commutation angle u for $\alpha = 0°$.

only limits the di/dt, but also the output power. Therefore, adding an inductor is not a good practical solution.)

Current waveform of an idealized VSI

For PWM converters it is customary to introduce the amplitude modulation ratio:

$$m_a \equiv \frac{\hat{v}_{control}}{\hat{v}_{tri}}, \tag{8.3}$$

where $v_{control}(t)$ is the control signal and $v_{tri}(t)$ is a signal with triangular waveform. For a three-phase inverter, there are three control signals, having the desired waveform shape and frequency, and shifted with respect to each other by $2\pi/3$ and $4\pi/3$: $v_{control,a}(t)$, $v_{control,b}(t)$ and $v_{control,c}(t)$. The signals $v_{control}(t)$ and $v_{tri}(t)$ are compared by means of a comparator, and the on states of the semiconductor switches of the three-phase bridge are controlled by the output of these three comparators.

Another modulation ratio used in PWM converters is the frequency modulation ratio:

$$m_f \equiv \frac{f_{sw}}{f_s}, \tag{8.4}$$

where f_{sw} is the switching frequency of the bridge and f_s the fundamental frequency of the desired voltage waveform, i.e. the stator fundamental frequency and of course also the frequency of $v_{control,a}(t)$, $v_{control,b}(t)$ and $v_{control,c}(t)$.

In Mohan's textbook on Power Electronics [Moh95], three-phase VSI PWM (pulse-width modulation) considerations are listed as:

1. For low values of m_f, to eliminate even harmonics, a synchronized PWM should be used and m_f should be an odd integer. Moreover, m_f should be a multiple of 3 to cancel out the most dominant harmonics in the line-to-line voltage.

2. For large values of m_f, the subharmonics due to asynchronous PWM is small and this PWM scheme may thus be used. However, in machines, even low-amplitude subharmonics can cause large currents at low frequencies (close to zero) and therefore asynchronous PWM should be avoided.

3. During overmodulation ($m_a > 1$), regardless of the value of m_f, the conditions pertinent to a small m_f should be observed.

Since the power level of this machine is quite high, the ratings of the semiconductors require a m_f that is as low as possible to limit the switching loss of the IGBTs. The first consideration above therefore applies, and $m_f = 15$ is chosen for the comparison with the CSI in this section. The time harmonic components of a VSI waveform are centered around integer multiples of the fundamental frequency as sidebands. There are components at $(m_f \pm 2)f_s$, $(m_f \pm 4)f_s$, $(2m_f \pm 1)f_s$, $(2m_f \pm 5)f_s$, $(3m_f \pm 2)f_s$, $(3m_f \pm 4)f_s$, $(4m_f \pm 1)f_s$, $(4m_f \pm 5)f_s$, $(4m_f \pm 7)f_s$, etc.
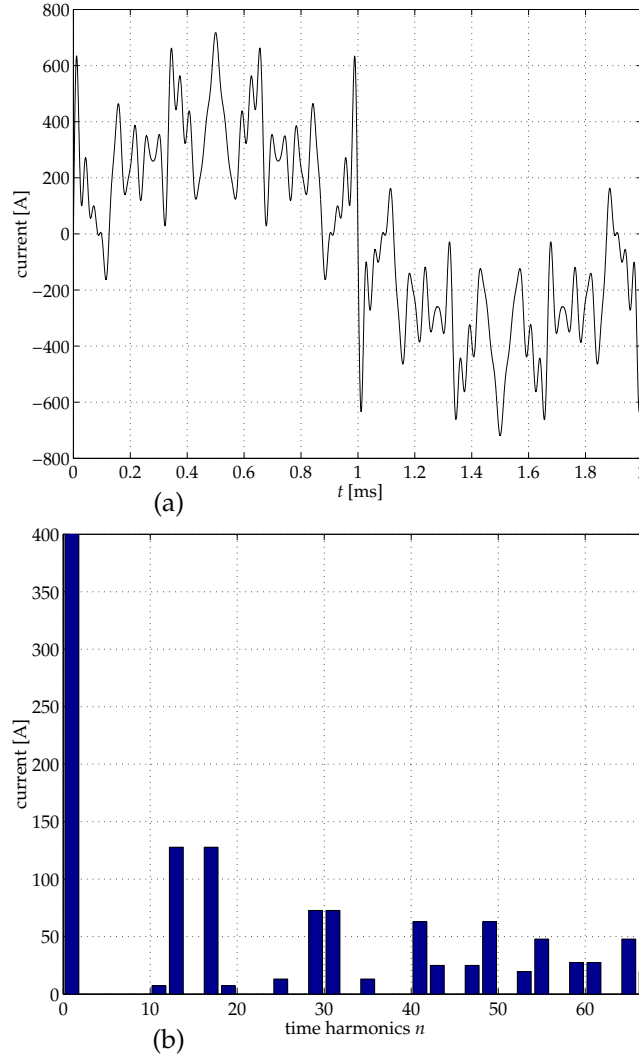
Figure 8.15: A typical PWM VSI current waveform calculated by a table of harmonics [Moh95]: (a) as a function of time; and (b) spectral content.

Figure 8.15 shows a typical three-phase PWM VSI current waveform as calculated by a table of harmonic content in [Moh95]; Table 8.2 lists the harmonic components and the induced loss in the shielding cylinder for this waveform.

The harmonic components and induced shielding cylinder loss of the CSI current waveform of Figure 6.5 (firing angle $\alpha = 42°$) is also listed in Table 8.2. The fundamental harmonic of the two current waveforms of Table 8.2 were made equal.

The loss for the CSI is dominant at low frequencies, since this is where the ma-

jority of its distortion components lie. The loss of the VSI waveform is concentrated around the 15th, 30th, 45th, (etc.) harmonic components in sidebands. The total loss in the shielding cylinder for the CSI is 72 W and that for the VSI is ten times higher: 700 W. The high shielding cylinder loss is a very serious problem since it is mounted on a rotor rotating at very high speeds in vacuum, making it very difficult to cool.

In spite of the fact that more power can be withdrawn from or supplied to the machine with a VSI than with a CSI, this converter is not chosen for the EμFER flywheel system.

The higher shielding cylinder loss is not the only reason for not choosing a VSI for the EμFER system, however. The losses in the converter itself are also much higher than in the case of a CSI. This is due to the high switching losses, since the switches are switched on and off at high voltages and currents. The losses in the converter fall outside the scope of this thesis, as are techniques for lowering these losses; we do remark, however, that these losses are high for a switching frequency of 15 kHz and the required IGBTs are expensive and scarce.

8.8 Generalization of the analytical model

The analytical model developed in this thesis for the EμFER machine is only valid for that geometry: a slotless-stator external-rotor permanent-magnet machine with surface-mounted magnets and a shielding cylinder. With some modifications, this model may be generalized to other geometries. One machine construction that would be of particular interest is that of the EμFER machine, but with a slotted stator.

The permanent-magnet field of Chapter 5 is valid without modification for such a machine. The stator current field of Chapter 6 needs some modification since it was derived for a current density in the air gap, while a surface current density on the stator surface is customarily used for slotted machines. One way to solve the problem is to use the same model, but for a very thin winding height h_w. This has not been investigated, however, and further research into this is recommended.

8.9 Summary and conclusions

This chapter discussed some aspects of optimization of slotless permanent magnet flywheel machines by utilizing the analytical model that has been derived in Chapters 4–7.

Section 8.2 started the discussion by looking at possible optimization criteria and independent variables.

The three criteria chosen were the electromagnetic torque, total stator losses and rotor loss in the shielding cylinder.

Sections 8.3 and 8.4 looked at the influence of the permanent-magnet array and the winding distribution on these three quantities. Section 8.5 discussed machine geometry optimization, while Section 8.6 made use of these results to find the opti-

CSI: current harmonic content [A]							
$\|n\|$	1	5	7	11	13	17	19	23
	401.06	75.83	46.01	16.60	26.02	9.19	5.99	1.83
$\|n\|$	25	29	31	35	37	41	43	47
	2.298	1.997	2.349	2.506	2.472	1.649	1.438	0.907
$\|n\|$	49	53	55	59	61	65	67	
	0.4876	0.6544	0.7958	0.8786	1.124	0.6979	0.5938	

CSI: loss in the shielding cylinder [W]							
$\|n\|$	1	5	7	11	13	17	19	23
	0	45.43	16.72	2.357	5.805	0.8118	0.3448	0.0362
$\|n\|$	25	29	31	35	37	41	43	47
	0.0572	0.0486	0.0673	0.0851	0.0829	0.0405	0.0308	0.0133
$\|n\|$	49	53	55	59	61	65	67	
	0.0038	0.0074	0.0109	0.0143	0.0233	0.0095	0.0069	

VSI: current harmonic content [A]							
$\|n\|$	1	5	7	11	13	17	19	23
	401.06	0	0	7.21	127.8	127.8	7.21	0
$\|n\|$	25	29	31	35	37	41	43	47
	13.11	72.74	72.74	13.11	0	62.91	24.9	24.9
$\|n\|$	49	53	55	59	61	65	67	
	62.91	19.66	47.84	27.52	27.52	47.84	19.66	

VSI: loss in the shielding cylinder [W]							
$\|n\|$	1	5	7	11	13	17	19	23
	0	0	0	0.446	140.0	156.6	0.4984	0
$\|n\|$	25	29	31	35	37	41	43	47
	1.861	64.47	64.47	2.329	0	58.96	9.238	10.03
$\|n\|$	49	53	55	59	61	65	67	
	63.99	6.71	39.7	13.99	13.99	44.61	7.53	

Table 8.2: A comparison of the induced eddy current loss in the shielding cylinder due to typical CSI (Figure 6.5) and VSI (Figure 8.15) waveforms for the same fundamental harmonic.

mum machine geometry for a fixed rotor outer diameter. The influence of the choice of converter on the induced rotor loss was briefly discussed in Section 8.7, and some remarks on generalizing the analytical machine model were made in Section 8.8.

A summary of the most important conclusions reached in this chapter is:

- Magnet array optimization:
    - The discrete Halbach array produces more torque for all ϕ_m than the radial array, but the gap between the two becomes smaller at a larger magnet

span, which is expected since at 100%, the two arrays are the same.

- The torque is lower if more pole pairs are used in the same machine geometry and array.
- Torque increases with pole arc for the radial array and discrete Halbach array.
- The total stator losses increase with increasing pole arc.
- The total stator losses decrease with increasing number of pole pairs.
- The induced loss in the stator winding may be neglected since it is approximately 20 times lower than the stator iron losses, and the stator can easily be cooled.
- A larger span than approximately 80% in the radial and discrete Halbach arrays is not useful because of the short-circuit field between adjacent magnets.
- Magnet skewing is not necessary since the stator is slotless.

- Winding optimization:

  - The winding distribution has very little influence on the torque production and little influence on the induced rotor loss.

- Machine geometry optimization:

  - Halbach arrays produce more torque than the radial array for large air gaps and thick magnets.
  - As the number of pole pairs is increased, Halbach arrays produce more torque than the radial array for large air gaps and thinner magnets. The torque is substantially higher for $p = 4$, and higher with a large air gap.
  - For small air gaps, the torque production of the arrays becomes more and more similar, and for very small air gaps, they are the same. One exception is the 50/50 discrete Halbach array, which produces much less torque than the other arrays for small air gaps.
  - For small air gaps and small p, the radial array induces approximately the same stator losses as the ideal Halbach array.
  - For all p and air gap lengths, the radial and 80/20 discrete Halbach arrays induce more or less the same stator losses. The difference increases with the number of pole pairs and the magnet thickness.
  - The induced eddy current loss in the shielding cylinder decreases with an increasing number of pole pairs.
  - This difference gets smaller for a decreasing air gap.
  - An optimization algorithm has been introduced which places the highest emphasis on torque, then considers the induced stator losses and lastly the eddy current loss in the shielding cylinder.

- – With this algorithm, the optimum machine dimensions have been found for a given rotor outer radius (inner radius of the carbon fibre flywheel).

- Converter options for the flywheel drive:

  - – A VSI allows a higher power level to be withdrawn from or supplied to the machine than when a CSI is used (from Chapter 3).

  - – A VSI induces much higher eddy current loss in the shielding cylinder than a CSI.

  - – The choice of converter not only depends on the power level that can be withdrawn from the machine and the induced rotor loss, but also on the conduction and switching losses in the converter itself. This has not been considered in this thesis.

- Analytical model generalization:

  - – The analytical model derived in this thesis is only valid for external-rotor permanent-magnet machines with slotless stators.

  - – The permanent-magnet field model of Chapter 5 is also valid for slotted machines.

  - – The stator current field model of Chapter 6 may be adapted for use in slotted machines by making the winding height h_w very small.

CHAPTER 9

Conclusions and recommendations

As said in Chapter 1, this thesis deals firstly with finding a suitable energy storage technology for use in a hybrid electric city bus.

Chapter 2 investigated four energy storage technologies: electrochemical, electric field, magnetic field, and kinetic (flywheel) energy storage systems.

Chapter 3 looked at drive system topologies, converter choice and machine type for high-power flywheel energy storage systems. From Chapter 3 onward, the scope of the rest of the thesis was limited to the electrical machine, called the EμFER machine.

The analytical model was derived in Chapters 4—7. Chapter 4 presented an outline of the derivation, while Chapters 5 and 6 solved for the fields and derived quantities of the permanent magnets and stator currents, respectively. Chapter 7 treated the combination of these two fields and discussed quantities derived from the combined field.

Optimization was the topic of Chapter 8. The optimization criteria chosen were the electromagnetic torque, stator iron losses and the induced eddy current loss in the shielding cylinder. These were optimized with respect to the permanent-magnet array, winding distribution, machine geometry and converter options. Chapter 8 also listed the optimum machine geometry for a given rotor outside radius.

In this chapter, conclusions are drawn from the work described in this thesis and recommendations are made for further research.

9.1 Conclusions

The conclusions are grouped into four categories. These correspond to the four thesis objectives listed in Chapter 1:

1. *To find the most suitable energy storage technology for use in large hybrid electric vehicles like busses and trams.*

2. *To design the electrical machine for the EμFER flywheel energy storage system.*

3. *To optimize the machine geometry for given flywheel dimensions.*

4. *To derive a comprehensive analytical model of the electrical machine.*

9.1.1 Energy storage technologies for large hybrid electric vehicles

With the increasing use of hybrid electric vehicles, renewable energy sources and distributed generation, among others, the use of energy storage technologies is sure to increase.

Concerning energy storage technologies for large hybrid electric vehicles, we conclude that flywheel energy storage systems are ideally suited for medium-energy, high-power applications (like large hybrid electric vehicles). This is also true on a per-unit volume and per-unit mass basis. Composite flywheels are expected to keep this position as the most feasible technology for medium-energy, high-power applications in the future.

Furthermore, the continuing development of an increase in tensile strength of composite materials also makes composite flywheels an increasingly attractive option for high-energy, high-power applications.

9.1.2 The electrical machine

In Chapter 1, the challenges for the EμFER system were said to include a high desired power level (150 kW) and losses as low as possible, both at load and at no load. The geometry of the flywheel called for a radial flux machine with surface-mounted magnets and solid back-iron. To reduce the no-load loss induced in the stator iron, the stator teeth (as used in EMAFER) were removed to obtain a slotless stator. This in turn necessitated the use of Litz wire for the stator conductors to limit the induced loss in the stator winding. Since the rotor rotates at 30 000 rpm in a low-pressure atmosphere, cooling it is very difficult. This requires that very low loss is induced in the rotor: a shielding cylinder is thus used.

With these facts as design inputs, the EμFER electrical machine was designed. The results obtained and documented in the thesis show that the design goal of 150 kW output power was met. (The fundamental space and time harmonic power is 177 kW). Furthermore, the low-loss requirements were also met as can be seen from the low induced rotor loss in the shielding cylinder at load and the induced loss in

the stator at no load. The induced loss in the shielding cylinder was calculated as 124 W for a typical CSI current waveform. The induced stator iron loss was calculated as 2970 W and the induced copper loss as 115 W. The sum of these losses is approximately 2% of the nominal power.

Conclusions about the electrical machine include:

- The magnet array (i.e. its space harmonic distribution) has a significant influence on the torque and stator losses. For example, a 20% difference between the produced torque of the 50/50 and 80/20 discrete Halbach arrays has been calculated for the machine geometry. The ratio of induced stator iron losses for the three arrays discussed in this thesis were calculated as:
  ideal Halbach : radial : 80/20 discrete Halbach = 1 : 1.24 : 1.38.

- The influence of the winding distribution (i.e. its space harmonics) on the torque and losses is minimal. The fact that the winding is slotless results in a very large air gap. The large air gap in turn results in the low space harmonic content of the winding. The inherently low space harmonic content of the 1-2-2-1 distribution further improves this desirable quality.

- The induced loss in the stator winding can be neglected since it is approximately 20 times lower than the stator iron losses, and the stator winding can be cooled fairly easily with a liquid.

- For the EμFER geometry, complete shielding of the rotor already takes place at frequencies as low as a few hundred Hertz.

Concerning the converter-machine interaction, we conclude that:

- A VSI allows a greater power level to be extracted from or supplied to the machine than a CSI.

- A VSI induces a much larger loss in the shielding cylinder than a CSI due to the higher harmonic content of the current waveform at high frequencies.

- When a CSI is connected to the machine, a commutation angle of above about 30° is desirable since it leads to a drastic reduction in rotor loss due to the reduced spectral content.

- The choice of a suitable converter also depends on the losses in the converter itself, controllability, cost and other factors. This thesis did not investigate these.

9.1.3 Optimization

The optimum machine geometry for a given carbon-fibre inside radius (150 mm) has been found in the thesis. The optimization criteria were high torque, low total stator losses and very low rotor loss in the shielding cylinder. This optimum is:

- $r_{si} = 23.036$ mm; $r_{so} = 68.036$ mm; $r_w = 101.66$ mm; $r_{ci} = 106.66$ mm; $r_{co} = 108.66$ mm; $r_{mo} = 134.14$ mm; $r_{ro} = 150$ mm.

For this geometry, the peak flux density in the rotor yoke is $\widehat{B}_{ry} = 1.9477$ T; the peak fundamental space and time harmonic component of the electromagnetic torque is $T_{e,1,1} = 158.85$ Nm (corresponding to a power of 249.5 kW at 15 000 rpm). The total stator iron loss was 3725 W (it was chosen to be below 4 kW), and the induced loss in the shielding cylinder 116 W for the same CSI current waveform that was used throughout the thesis as an example.

The EµFER machine's geometry is not far off from this optimum machine geometry. Magnet cost is the reason that the two geometries are not the same: thinner magnets were used in the EµFER machine.

9.1.4   The analytical model

In order to design the electrical machine and to find the optimum geometry, some model of the electrical machine was needed to analyze the designed geometry. In this thesis, an analytical model was chosen. The following conclusions were drawn regarding this model:

- The accuracy and correctness of the analytical model derived in this thesis has been verified experimentally.

- Although it is only two dimensional, the model predicts the machine parameters and behavior accurately. One can therefore conclude that three-dimensional effects do play a role, but not a significant one. This is a surprising conclusion since one would expect a lower accuracy because of the machine's "flat" aspect ratio (the rotor diameter is larger than the active axial length) and because its air gap is very large.

- The machine needs only one voltage equation since all space and time harmonic effects and the effect of the shielding cylinder are included in the vector potential.

- The magnetic vector potential contains all electromagnetic information in the machine and all machine quantities can be derived as simple functions of it. This includes the no-load voltage, machine impedance, torque and losses.

- The analytical model described in this thesis is only valid for slotless stator, external-rotor permanent-magnet machines with surface-mounted magnets and a shielding cylinder. The part of the model that describes the field due to the permanent magnets and its derived quantities (Chapter 5) is, however, also valid for slotted stators. The field due to the stator currents may be modified to be valid for slotted stators by making the winding height h_w very thin in the model.

9.1.5 Thesis contributions

The main scientific contributions of this thesis may be summarized as:

- The six-layer solution of the magnetic field due to the stator current density including the reaction field of the eddy currents in the shielding cylinder; this solution was documented in Chapter 6. By itself, the solution of the magnetic field of a current density is not new, neither is the eddy-current reaction field. The combination of both, however, is unique. A unique model leads to unique results. Two contributions follow from these:

  - The derived analytical model provides a tool that can be used to calculate the induced loss in the machine as a function of the chosen converter. Such a tool is also a contribution.

  - Chapter 8 clearly shows the power of the analytical model in finding the optimum machine geometry for arbitrary criteria. (The criteria chosen there were high torque and low losses.)

- Magnet array investigation. Such investigations are not new on their own. However, the explicit investigation of polar arc variation in Halbach arrays was not found in previous literature. (Mecrow *et al.* implicitly did it in [Mec03].)

- The use of the Theorem of Poynting to calculate the torque and losses in machines is not new. What has been done in this thesis, however, forms a contribution, as an explicit comparison of the result of the power calculated from the Theorem of Poynting in stator and rotor coordinates was not found in literature.

9.2 Recommendations for further research

The analytical model

Although already accurate, the analytical model may be improved. This may be done in the following ways:

- The model's performance may be improved by investigating ways to include 3D effects. It remains a question of whether this 3D modelling should be done analytically. These 3D effects may be modelled separately, or space mapping can be used. This method consists in principle of analytical expressions, with checks by the finite element method where necessary, i.e., it is a hybrid method.

- Some work may be done on generalizing the model so that it is also valid for other machine geometries. One improvement that must certainly be made is to recalculate the solution of Chapter 6 for a slotted stator since these are more commonly used. The slotted stator is a 5-layer system and significantly simpler than the one solved in Chapter 6.

- The analytical model is very complex, especially the stator field of Chapter 6. It is worthwhile to investigate ways to simplify the model to make it easier to use. In [Pol98], for example, the stator field is derived without the effect of the reaction field of the eddy currents in the shielding cylinder on it. Instead, the shielding cylinder currents are modelled as a series of equivalent short-circuited windings, one for each space harmonic. Both methods, that of Polinder and the one derived in this thesis, have pros and cons; a comparison of these will certainly be an interesting and worthwhile venture.

The electrical machine

The designed machine meets the requirements of delivering high power at low loss and having low no-load losses. Some suggestions are nevertheless made to explore possible improvement:

- A comparison between radial and axial flux machines was not done in this thesis. For machines with even flatter aspect ratios than the one investigated in this thesis, or severe lack of space, an investigation of axial flux machines will be interesting.

- Investigating the use of other materials than laminated steel as the stator yoke material, like powdered iron, is suggested.

- Since ideal Halbach arrays are very attractive for low losses, ways to manufacture these should be investigated. This is in spite of the fact that they are not suitable for machines with iron (for the geometries discussed in this thesis) in terms of torque production. (When ironless machines are considered, their torque production surpasses that of the other arrays [Ofo95].)

Modelling of permanent-magnet arrays

- It is recommended that more segments per pole are studied analytically in the future, particularly because the discrete Halbach array with 2 segments per pole is a bad approximation to the ideal Halbach array. This investigation is particularly useful if one has machines with very low losses and ironless machines in mind.

- In this thesis, only three arrays were investigated with a fixed rectangular magnet shape. Other magnet shapes like trapezoids may also be investigated. (Such an investigation has already been started in [Can03].)

Converter-machine interaction

- More work could be done on the converter-machine interaction. An analysis of the loss distribution between machine and converter could be made to more

accurately investigate the type of converter to be used with respect to overall system efficiency.

- This investigation could be combined with soft-switching techniques to lower the switching loss in the converter without increasing the induced loss in the shielding cylinder.

- The power possibilities with a VSI are only mentioned and rudimentarily shown in this thesis. An experimental investigation on this topic is recommended.

BIBLIOGRAPHY

[Abu97] S.M. Abu Sharkh, M.R. Harris, and N. Taghizadeh Irenji. "Calculation of rotor eddy-current loss in high-speed PM alternators". In *Conference Record, International Conference on Electrical MAchines and Drives (EMD 1997)*, pages 170–174, 1997.

[Abu99] S.M. Abu Sharkh, N. Taghizadeh Irenji, and M.R. Harris. "Effect of Power Factor on Rotor Loss in High-Speed PM Alternators". In *Conference Record, International Conference on Electrical Machines and Drives (EMD 1999)*, pages 346–350, September 1999.

[Aca96] P.P. Acarnley, B.C. Mecrow, J.S. Burdess, J.N. Fawcett, J.G. Kelly, and P.G. Dickinson. "Design Principles for a Flywheel Energy Store for Road Vehicles". In *IEEE Transactions on Industry Applications*, volume 32, pages 1402–1408, November/December 1996.

[Alb98] G.F. Albrecht, S.B. Sutton, E.V. George, and W.R. Sooyand W.F. Krupke. "Solid state heat capacity disk laser". In *Laser and Particle Beams*, volume 16, pages 605–625, 1998.

[Alg53] P.L. Alger and W.R. Oney. "Energy flow in induction machines". In *General Electric Review*, volume 56, pages 56–60, 1953.

[Alg54] P.L. Alger and W.R. Oney. "Torque energy relations in induction machines". In *Trans. AIEE, Power Apparatus Systems*, volume 73, pages 259–264, April 1954.

[Ant91] C.S. Antonopoulos, S.M. Panas, and E.E. Kriezis. "Transient electromagnetic shielding in a system of two coaxial cylindrical shells". In *IEE Proceedings-A*, volume 138, pages 281–285, September 1991.

[Ark92] A.A. Arkadan, R. Vyas, J.G. Vaidya, and M.J. Sha. "Effect of Toothless Stator Design on Core and Stator Conductors Eddy Current Losses in Permanent Magnet Generators". In *IEEE Transactions on Energy Conversion*, volume 7, March 1992.

[Ata97] K. Atallah, D. Howe, and P.H. Mellor. "Design and Analysis of Multi-Pole Halbach (Self-Shielding) Cylinder Brushless Permanent Magnet Machines". In *Eighth International Conference on Electrical Machines and Drives*, number 444, pages 376–380, London, UK, 1997.

[Ata98] K. Atallah, Z.Q. Zhu, D. Howe, and T.S. Birch. "Armature Reaction Field and Winding Inductances of Slotless Permanent-Magnet Brushless Machines". In *IEEE Transactions on Magnetics*, volume 34, pages 3737–3744, September 1998.

[Bak99] J.N. Baker and A. Collinson. "Electrical Energy Storage at the Turn of the Millenium". In *Power Engineering Journal*, volume 13, pages 107–112, June 1999.

[Bal95] G.J. Ball, G. Corey, and B.L. Norris. "Government, industry, and utility development and evaluation of a modular utility battery energy storage system". In *IEEE Transactions on Energy Conversion*, volume 10, pages 549–554, September 1995.

[Bas97] V. Basiuk, E. Joffrin, T. Aniel, A. Becoulet, G.T. Hoang, X. Litaudon, Th. Hutter, F. Nguyen, B. Saoutic, W.A. Houlberg, and C.E. Kessel. "FWEH induced high bootstrap current on Tore Supra". In *AIP Conference Proceedings*, number 403, pages 239–242, 1997.

[Bha99] R.C. Bhardwaj. "Constant and Pulse Power Capabilities of Lead-Acid Batteries Made with Thin Metal Film (TMF(R)) for Different Applications". In *Journal of Power Sources*, volume 78, pages 130–138, March/April 1999.

[Bis99] F. I. Bispo, J. Aggar, C. Sarrazin, P. Simon, and J. F. Fauvarque. "Possible Improvements in Making Carbon Electrodes for Organic Supercapacitors". In *Journal of Power Sources*, volume 79, pages 238–241, 1999.

[Bit98] J.G. Bitterly. "Flywheel Technology – Past, Present and 21st Century Projections". In *IEEE Aerospace and Electronic Systems Magazine*, volume 13, pages 13–16, 1998.

[Bla73] J. van Bladel. "Relativistic theory of rotating disks". In *Proc. IEEE*, volume 61, pages 260–268, 1973.

[Blo75] H. Blok. *Elektromagnetische velden in de Energietechniek*. Delft University Press, Delft, The Netherlands, 1975.

[Blo99] H. Blok and P.M. van den Berg. *Electromagnetic Waves*. Delft University Press, Delft, The Netherlands, 1999.

[Bol02] M.H.J. Bollen. "Comparing voltage dip survey results". In *Conference Proceedings, IEEE Power Engineering Society Winter Meeting*, volume 2, pages 1130–1134, January 2002.

[Boo88] R.W. Boom, Y.M. Eyssa, M.K. Abdelsalam, and X. Huang. "Superconductive Magnetic Energy Storage (SMES) System Studies for Electrical Utility Usage at Wisconsin". In *Proceedings of the 2nd Annual Conference on Superconductivity and Applications*, pages 417–431, Elsevier, New York, NY, USA, 1988.

[Bou84] N. Boules. "Two Dimensional Field Analysis of Cylindrical Machines with Permanent Magnet Excitation". In *IEEE Transactions on Industrial Applications*, volume IA-20, pages 1267–1277, 1984.

[Can03] W.-R. Canders, H. Mosebach, and Z. Shi. "Analytical and Numerical Investigation of PM Excited Linear Synchronous Machines with Shaped Magnets". In *Conference Record, 4th International Symposium on Linear Drives for Industry Applications*, pages 465–468, Birmingham, UK, September 2003.

[Car67] G.W. Carter. *The Electromagnetic Field in its Engineering Aspects*. Longmans, 2nd edition, 1967.

[Che97] Y. Chen, J. Shen, and Z. Fang. "Topology and Preliminary Design of Slotless Brushless DC Motor". In *Conference Record, Electric Machines and Drives Conference*, pages WB2–7.1–WB2–7.3, 1997.

[Cra84] C.B. Cray. "Air-gap power flow and torque development in electric machines - Can we teach the fundamentals?". In *IEEE Transactions*, volume PAS-103, pages 874–879, April 1984.

[Dah50] S. Dahlgren. "Some remarks on the energy flow in rotating electrical machines". In *Transactions of the Royal Institute of Technology*, number 38, pages 1–15, Stockholm, Sweden, 1950.

[Dar36] G. Darrieus. "Theorem of Poynting in electrical engineering". In *Bull. S. F.E.*, volume 6, pages 893–920, September 1936.

[Dar99] H. Darrelmann. "Comparison of high power short time flywheel storage systems". In *Conference Proceedings, 21st IEEE International Telecommunications Energy Conference - INTELEC'99*, June 1999.

[Den97] F. Deng. "Commutation-Caused Eddy-Current Losses in Permanent-Magnet Brushless DC Motors". In *IEEE Transactions on Magnetics*, volume 33, pages 4310–4318, September 1997.

[Den98]   F. Deng and T. W. Nehl. "Analytical Modeling of Eddy-Current Losses Caused by Pulse-Width Modulation Switching in Permanent-Magnet Brushless Direct-Current Motors". In *IEEE Transactions on Magnetics*, volume 34, pages 3728–3736, September 1998.

[Die99]   T. Diedrich. "Ultracaps, Power for your Innovative Applications". In *Siemens Power Electronics Seminar*, Huizen, The Netherlands, November 26th 1999.

[Dor97]   D.S. Dorr, M.B. Hughes, T.M. Gruzs, R.E. Jurewicz, and J.L. McCaine. "Interpreting Recent Power Quality Surveys to Define the Electrical Environment". In *IEEE Transactions on Industry Applications*, volume 33, pages 1480–1487, November/December 1997.

[Dri93]   M.D. Driga. "Asynchronous Generators for Fast, High-Energy Pulsed Discharge as Power Supplies for Electromagnetic Launchers". In *Digest of Technical Papers, 9th IEEE International Pulsed Power Conference*, volume 1, pages 196–202, New York, USA, 1993.

[Dri97]   M.D. Driga and M. Ozdemir. ""Compulsators" as pulsed power supplies for high-power, high-energy powder spraying". In *Conference Record, 11th IEEE International Pulsed Power Conference*, volume 2, pages 1066–1071, New York, NY, USA, 1999.

[Dug96]   R.C. Dugan, M.F. McGranaghan, and H.W. Beaty. *Electrical Power Systems Quality*, chapter 2. McGraw-Hill, 1996.

[Dur99]   J. L. Durán-Gómez, P. N. Enjeti, and A. von Jouanne. "An Approach to Achieve Ride-Through of an Adjustable Speed Drive with Flyback Converter Modules Powered by Supercapacitors". In *Conference Record, IEEE Industry Applications Society Annual Meeting*, pages 1623–1629, 1999.

[EPR1]   vol. 1-3. http://www.epri.com/, EPRI report # TR-106294. *EPRI*.

[Ehr93]   P. Ehrhart, M. heeg, G. Heidelberg, G. Reiner, and W. Weck. "The Magnet-Motor Energy Supply System for EML together with a new Coil-Accelerator Concept". In *IEEE Transactions on Magnetics*, volume 29, pages 661–666, January 1993.

[Fan60]   R.M. Fano, L.J. Chu, and R.B. Adler. *Electromagnetic Fields, Eenergy, and Forces*. John Wiley & Sons, Inc., New York, USA, 1960.

[Fer92]   J.A. Ferreira. "Analytical computation of AC resistance of round and rectangular litz wire windings". In *IEE Proceedings-B*, volume 139, pages 21–25, January 1992.

[Fla88] R.C. Flanagan. "Flywheel energy storage design for photovoltaic powered systems". In *Conference Record, 8th E.C. International Photovoltaic Solar Energy Conference*, volume 1, pages 34–38, Dordrecht, The Netherlands, 1988.

[Gen85] G. Genta. *Kinetic Energy Storage – Theory and practice of advanced flywheel systems*. Butterworths, London, 1985. ISBN 0-408-01396-6.

[Gie97] J.F. Gieras and M. Wing. *Permanent Magnet Motor Technology: Design and Applications*. Marcel Dekker, Inc., New York, New York, USA, 1997.

[Gut98] J.J. Gutt and A. Grüner. "Definition of power density as a general utilization factor of electrical machines". In *European Transactions on Electrical Power*, volume 8, pages 305–308, July-August 1998.

[Hag29] B. Hague. *Electromagnetic problems in electrical engineering*. Oxford University Press, London, UK, 1929.

[Hal80] K. Halbach. "Design of Permanent Multipole Magnets with Oriented Rare Earth Cobalt Material". In *Nuclear Instruments and Methods*, volume 169, pages 1–10, Berkeley, USA, 1980.

[Hal85] K. Halbach. "Permanent Magnets for Production and Use of High Energy Beams". In *Proceedings of the 8th International Workshop on Rare-earth Permanent Magnets*, pages 123–136, 1985.

[Ham99] K. Hameyer and R. Belmans. *Numerical Modelling and Design of Electrical Machines and Devices*. WIT Press, Southampton, UK, 1999.

[Har66] H. Harrison. "Field theory applied to electrical machines". In *International Journal of Electrical Engineering Education*, volume 193–200, 1966.

[Hau89] H.A. Haus and J.R. Melcher. *Electromagnetic Fields and Energy*. Prentice-Hall, Inc., London, UK, 1989.

[Haw53] E.I. Hawthorne. "Flow of energy in DC machines". In *AIEE Transactions*, volume 72, pages 438–444, September 1953.

[Haw54] E.I. Hawthorne. "Flow of energy in synchronous machines". In *AIEE Transactions*, volume 73, pages 1–9, March 1954.

[Hea94] R.A. Headifen. "Flywheel energy storage for wind turbines". In *Conference Record, 29th Intersociety Energy Conversion Engineering Conference*, volume 3, pages 1374–1379, Washington, DC, USA, 1994.

[Heb02] R. Hebner, J. Beno, and A. Walls. "Flywheel batteries come around again". In *IEEE Spectrum*, pages 46–51, April 2002.

[Hei94]   K.L. Heitner. "Energy storage requirements and optimization of sustaining power source for hybrid vehicles". In *Conference Record, 29th Intersociety Energy Conversion Engineering Conference*, volume 3, pages 1387–1392, Washington, DC, USA, 1994.

[Her98]   D. Hermance and S. Sasaki. "Hybrid electric vehicles take to the streets". In *IEEE Spectrum*, November 1998.

[Hof96]   H. Hofmann and S.R. Sanders. "Synchronous Reluctance Motor/Alternator for Flywheel Energy Storage Systems". In *IEEE Power Electronics in Transportation*, pages 199–206, New York, USA, 1996.

[Hor97]   D.W. Scherbarth, D.T. Hackworth, T.D. Hordubay, and O.R. Christianson. "Design and Construction of the 4 Tesla Background Coil for the Navy SMES Cables Test Apparatus". In *IEEE Transactions on Apllied Superconductivity*, volume 7, pages 840–843, June 1997.

[Hor99]   T.D. Hordubay, O.R. Christianson, D.T. Hackworth, and D.W. Scherbarth. "Winding of the Navy SMES Background Coil". In *IEEE Transactions on Apllied Superconductivity*, volume 9, pages 205–208, June 1999.

[Hug77]   A. Hughes and T.J.E. Miller. "Analysis of Fields and Inductances in Air-Cored and Iron-Cored Synchronous Machines". In *Proceedings of the IEE*, volume 124, pages 121–126, 1977.

[Hun95]   G.L. Hunt, R.A. Sutula, and K.L. Heitner. "Energy storage requirements and testing for hybrid electric vehicles". In *Conference Record, 30th Intersociety Energy Conversion Engineering Conference*, volume 2, pages 97–102, New York, NY, USA, 1995.

[Jef90]   A. Jeffrey. *Linear Algebra and Ordinary Differential Equations*. Blackwell Scientific Publications, Inc., Cambridge, Massachusetts, USA, 1990.

[Jon02]   K. Jonasson. *Analysing Hybrid Drive System Topologies*. Licentiate Thesis, Departmennt of Industrial Electrical Engineering and Automation, Lund University, Lund, Sweden, May 2002.

[Jon03]   W.D. Jones. "Hybrids to the Rescue". In *IEEE Spectrum*, January 2003.

[Jou99]   A. von Jouanne, P.N. Enjeti, and B. Banerjee. "Assessment of Ride-Through Alternatives for Adjustable-Speed Drives". In *IEEE Transactions on Industry Applications*, volume 35, pages 908–916, July/August 1999.

[Kar01]   E. Karden and R.W. De Doncker. "The non-linear low-frequency impedance of lead/acid batteries during discharge, charge and float operation". In *Conference Proceedings of the 23rd International Telcommuncations Energy Conference (INTELEC 2001)*, pages 65–72, 2001.

[Kar99] V. Karasik, K. Dixon, C. Weber, B. Batchelder, G. Campbell, and P. Ribeiro. "SMES for Power Utility Applications: A Review of Technical and Cost Considerations". In *IEEE Transactions on Apllied Superconductivity*, volume 9, pages 541–546, June 1999.

[Kim98a] U. Kim and D.K. Lieu. "Magnetic Field Calculation in Permanent Magnet Motors with Rotor Eccentricity: Without Slotting Effect". In *IEEE Transactions on Magnetics*, volume 34, pages 2243–2252, July 1998.

[Kim98b] U. Kim and D.K. Lieu. "Magnetic Field Calculation in Permanent Magnet Motors with Rotor Eccentricity: With Slotting Effect Considered". In *IEEE Transactions on Magnetics*, volume 34, pages 2253–2266, July 1998.

[Kol99] W. J. Kolkert and F. Jamet. "Electric Energy Gun Technology: Status of the French-German-Netherlands Programme". In *IEEE Transactions on Magnetics*, volume 35, pages 25–30, January 1999.

[Kot93] D. Kottick, M. Blau, and D. Edelstein. "Battery energy storage for frequency regulation in an island power system". In *IEEE Transactions on Energy Conversion*, volume 8, pages 455–459, September 1993.

[Kru]   www.edtn.com/eexpert/akruger/akruger006.html. *Passive/Active Components and Analog Circuits.*

[Kum91] B. Kumar, T.E. Gist, R.T. Fingers, and R.A. Flake. "Small Magnetic Energy Storage Systems Using High Temperature Superconductors". In *Proceedings of the 26th Intersociety Energy Conversion Engineering Conference*, pages 538–543, Boston, MA, USA, 1991.

[Kun86] H.J. Künisch, K.G. Kramer, and H. Dominik. "Battery energy storage-another option for load-frequency-control and instantaneous reserve". In *IEEE Transactions on Energy Conversion*, number 3, pages 41–46, September 1986.

[Lam66] J. Lammeraner. *Eddy Currents*. Iliffe Books, London, UK, 1966.

[Lov98] H.C. Lovatt, V.S. Ramsden, and B.C. Mecrow. "Design of an in-wheel motor for a solar-powered electric vehicle". In *IEE Proceedings on Electric Power Applications*, volume 145, pages 402–408, September 1998.

[Mag00] G. Maggetto and J. Van Mierlo. "Electric and Electric Hybrid Vehicle Technology: A Survey". In *IEE Seminar on Electric, Hybrid and Fuel Cell Vehicles*, pages 1/1–1/11, 2000.

[Mar92] M. Marinescu and N. Marinescu. "New Concept for Permanent Magnet Excitation for Electrical Machines. Analytical and Numerical Computation". In *IEEE Transactions on Magnetics*, volume 28, pages 1390–1393, 1992.

[Mar99] Marmara Research Center. "Magneto Dynamic Storage Systems". Progress Report 1 (Draft), Turkish Scientific & Technical Research Council, 1999.

[Mat87] L. W. Matsch and J. D. Morgan. *Electromagnetic and Electromechanical Machines*. John Wiley & Sons, Inc., New York, USA, 3 edition, 1987.

[McL55] N. W. McLachlan. *Bessel functions for engineers*. Oxford University Press, London, 1955.

[Mec03] B.C. Mecrow, A.G. Jack, D.J. Atkinson, S. Green, and G.J. Atkinson. "Design and Testing of a 4 Phase Fault Tolerant Permanent Magnet Machine for an Engine Fuel Pump". In *Conference Proceedings, IEEE International Electric Machines and Drives Conference*, volume 2, pages 1301–1307, June 2003.

[Mil96] N.W. Miller, R.S. Zrebiec, R.W. Delmerico, and G. Hunt. "Design and commissioning of a 5 MVA, 2.5 MWh battery energy storage system". In *Conference Record, IEEE Power Engineering Society Transmission and Distribution Conference*, New York, NY, USA, 1996.

[Mil97] J.F. Miller, C.E. Webster, A.F. Tummillo, and W.H. DeLuca. "Testing and evaluation of batteries for a fuel cell powered hybrid bus". In *Conference Record, 32nd Intersociety Energy Conversion Engineering Conference*, volume 2, pages 894–898, New York, NY, USA, 1997.

[Moh95] N. Mohan, T.M. Undeland, and W.P Robbins. *Power Electronics: Converters, Applications and Design*. John Wiley & Sons, Inc., New York, USA, 2nd edition, 1995.

[Moo99] T. Moore. "Powering Up Superconducting Cable". In *EPRI Journal*, pages 8–15, Spring 1999.

[Mos98a] H. Mosebach. "Einfache analytische Rechenmodelle für permanentmagneterregte Synchronmachinen". In *Electrical Engineering*, volume 81, pages 171–176. Springer-Verlag, 1998.

[Mos98b] H. Mosebach. "Direct Two-Dimensional Analytical Thrust Calculation of Permanent Magnet Excited Linear Synchronous Machines". In *Conference Record, 2nd International Symposium on Linear Drives for Industry Applications*, pages 396–399, Tokyo, Japan, April 1998. IEE, Japan.

[Mos98c] H. Mosebach and W.-R. Canders. "Average Thrust of Permanent Magnet Excited Linear Synchronous Motors for Different Stator Current Waveforms". In *Conference Record, International Conference on Electrical Machines (ICEM '98)*, Istanbul, Turkey, September 1998.

[Nel01] R. Nelson. "The Basic Chemistry of Gas Recombination in Lead-Acid Batteries". In *JOM: The Member Journal of The Minerals, Metals & Materials Society*, volume 35, pages 28–33, 2001.

[Nel96] R.J. Nelson, J.R. Legro, G.T. Gurlaskie, N.H. Woodley, M. Sarkozi, and A. Sundaram. "Voltage sag relief: guidelines to estimate DVR equipment ratings". In *Proceedings of the 58th Annual American Power Conference.*, volume 2, 1996.

[Nel97a] B. Nelson. "TMF Ultra-High Rate Discharge Performance Going Boldly Where No Batteries Have Gone Before". In *Proceedings of the 12th Annual Battery Conference on Applications and Advances*, pages 139–143, Long Beach, CA, USA, 1997.

[Nel97b] R. F. Nelson, R. Rinehart, and S. Varley. "Ultrafast Pulse Discharge and Recharge Capabilities of Thin Metal Film Battery Technology". In *Proceedings of the 11th IEEE International Pulsed Power Conference*, pages 636–641, Baltimore, MD, USA, 1997.

[Ng96] K. Ng, Z.Q. Zhu, and D. Howe. "Open-Circuit Field Distribution in a Brushless Motor with Diametrically Magnetized PM Rotor, Accounting for Slotting and Eddy Current Effects". In *IEEE Transactions on Magnetics*, volume 32, pages 5070–5072, September 1996.

[Ofo95] J. Ofori-Tenkorang and J.H. Lang. "A Comparative Analysis of Torque Production in Halbach and Conventional Surface-Mounted Permanent-Magnet Synchronous Motors". In *Conference Record, 30th IEEE Industry Applications Society Conference*, volume 3, pages 657–663, 1995.

[Oh99] S.J. Oh and M.D. Driga. "Fast discharging inertial energy storage systems for industry applications: electromagnetic considerations". In *Conference Record, 12th IEEE International Pulsed Power Conference*, pages 1283–1286, Monterey, California, USA, 1999.

[Owe99] S. Oweis. "The Li-ion Technology at SAFT for High Energy and High Power Applications". In *Proceedings of the 3rd International AECV Conference*, Maritim Hotel, Königswinter, 21–23 September 1999.

[Pal80a] B.B. Palit. "Unified analysis of electrical machines with the help of Poynting vector and the electromagnetic energy flow in the air-gap space: Part I: General theory". In *Zeitschrift für angewandte Mathematik und Physik*, volume 31, pages 384–399, 1980.

[Pal80b] B.B. Palit. "Unified analysis of electrical machines with the help of Poynting vector and the electromagnetic energy flow in the air-gap space: Part II: Application of general theory". In *Zeitschrift für angewandte Mathematik und Physik*, volume 31, pages 400–412, 1980.

[Pal82] B.B. Palit. "On active and reactive power flow in electrical machines: a unified analysis". volume 19, pages 67–78, January 1982.

[Pel99] W. G. Pell, B. E. Conway, W. A. Adams, and J. de Oliveira. "Electrochemical Eficiency in Multiple Discharge Recharge Cycling of Supercapacitors in Hybrid EV Applications". In *Journal of Power Sources*, volume 80, pages 134–141, 1999.

[Pil95] P. Pillay, R. M. Samudio, M. A. Ahmed, and R. T. Patel. "A Chopper-Controlled SRM Drive for Reduced Acoustic Noise and Improved Ride-Through Capability Using Supercapacitors". In *IEEE Transactions on Industry Applications*, volume 31, pages 1029–1038, September/October 1995.

[Pol71] M. Poloujadoff and R. Perret. "Study of an induction machine by the method of Poynting vector". In *Revue Générale de l'Electricité*, volume 80, pages 667–674, September 1971.

[Pol97] H. Polinder. "Analytic Calculation of the Magnetic Field in PM Machines". In *Conference Record, 32nd IEEE Industry Applications Society Conference*, volume 1, pages 35–41, New Orleans, Louisiana, October 5–9 1997.

[Pol98] H. Polinder. *On the losses in a high-speed permanent magnet generator with rectifier*. PhD thesis, Faculty ITS, Delft University of Technology, June 1998.

[Pow]   www.powercache.com. *Technical Information*.

[Raj94] K. Rajashekara. "History of Electric Vehiles in General Motors". In *IEEE Transactions on Industry Applications*, volume 30, pages 897–904, July/August 1994.

[Ras00] K.F. Rasmussen, J.H. Davies, T.J.E. Miller, M.I. McGilp, and M. Olaru. "Analytical and Numerical Computaion of Air-Gap Magnetic Fields in Brushless Motors with Surface Permanent Magnets". In *IEEE Transactions on Industry Applications*, volume 36, pages 1547–1554, November/December 2000.

[Rei97] G. Reiner, P. Ehrhart, M. Heeg, A.M. Jean-Jacques, and W. Weck. "Magnetodynamic Storage as a Main Storage in a Diesel-Electric Main Battle Tank". In *6th European Symposium on Electromagnetic Launch Technology*, pages 475–482, The Hague, The Netherlands, May 25–28 1997.

[Rei98] G. Reiner and W. Gunselmann. "Flywheel energy storage systems in public transportation systems". In *EESAT'98*, 1998.

[Rei99] G. Reiner. "The MDS: Technology and System Benefits in Vehicle Energy Management". In *3rd International AECV Conference*, Maritim Hotel Königswinter, September 21–23 1999.

[Ric67] R. Richter. *Elektrische Maschinen, erster Band*. Birkhaüser, Basel, 3rd edition, 1967.

[Ros03] P. Ross. "10 Techno-Cool Cars". In *IEEE Spectrum*, February 2003.

[Saf] http://www.saftbatteries.com/index.html. *Saft Batteries*.

[Sah01] F. Şahin. *Design and development of a high-speed axial-flux permanent-magnet machine*. PhD thesis, Eindhoven University of Technology, May 2001.

[San] http://www.sanyo.com/batteries/. *Sanyo Batteries*.

[Sch97] J.B. Schillig, H.J Boenig, J.A. Ferner, M.K. Quissek, F. Bogdan, G.O. Linhofer, M. Eichler, G. Kasper, R.P. Marek, and J.R. Martin. "Design and testing of a 320 MW pulsed power supply". In *Conference Record, 32nd Anual IEEE Industry Applications Conference (IAS '97)*, volume 3, New York, NY, USA, 1997.

[Sch99] R. Schöttler and R. G. Coney. "Commercial Application Experience with SMES". 13(3):149–152, June 1999.

[Shi73] T. Shiozawa. "Phenomenological and electron-theretical study of the electrodynamics of rotating systems". In *Proc. IEEE*, volume 61, pages 1694–1702, 1973.

[Sle19] J. Slepian. "The flow of power in electrical machines". In *The Electric Journal*, volume XVI, pages 303–311, 1919.

[Sle42] J. Slepian. "Energy and energy flow in the electromagnetic field". In *Journal of Applied Physics*, volume 13, pages 512–518, August 1942.

[Sle92] Gordon R. Slemon. *Electric Machines and Drives*. Addison-Wesley, Reading, Massachusetts, 1992.

[Spo92] E. Spooner and B.J. Chalmers. "Torus: A slotless, toroidal stator permanent magnet generator". In *IEE Proceedings-B*, volume 6, pages 497–506, November 1992.

[Sri95] K. Sridhar. "Electromagmetic Models for PM Synchronous Motor Drives". In *Conference Record, Tenth Annual Applied Power Electronics Conference and Exposition (APEC 1995)*, pages 367–377, 1995.

[Sto74] R.L. Stoll. *The Analysis of Eddy Currents*. Oxford University Press, London, UK, 1974.

[Sty00] E. Styvaktakis, M.H.J. Bollen, and I.Y.H. Gu. "Classification of power system events: Voltage dips". In *Conference Proceedings, 9th International Conference on Harmonics and Quality of Power*, volume 2, pages 745–750, October 2000.

[Ter94] A. Ter-Gazarian. *Energy Storage for Power Systems*, volume 6 of *IEE Energy Series*. Peter Peregrinus Ltd., London, United Kingdom, 1994.

[Tha99] R.S. Thallam and S. Eckroad. "Multimode battery energy storage system for custom power applications". In *Conference Record, IEEE Power Engineering Society Winter Meeting*, volume 2, Piscataway, NJ, USA, 1999.

[Tho93] F.J.M. Thoolen. *Development of an Advanced High Speed Flywheel Energy Storage System*. PhD thesis, Eindhoven University of Technology, Eindhoven, The Netherlands, December 1993.

[Tou01] F. Tourkhani. "Accurate Analytical Model of Winding Losses in Round Litz Wire Windings". In *IEEE Transactions on Magnetics*, volume 37, pages 538–543, January 2001.

[Tru93] D.L. Trumper, M.E. Williams, and T.H. Nguyen. "Magnet Arrays for Synchronous Machines". In *Conference Record, 28th IEEE Industry Aplications Society Conference*, volume 1, pages 9–18, 1993.

[Vee97] J.L.F. van der Veen, L.J.J. Offringa, and A.J.A. Vandenput. "Minimizing rotor losses in high-speed high-power permanent magnet synchronous generators with rectifier load". In *IEE Proc.-Electr. Power Appl.*, volume 144, pages 331–337, September 1997.

[Wal90] L.H. Walker. "10 MW GTO converter for battery peaking service". In *IEEE Transactions on Industry Applications*, volume 26, pages 63–72, January/February 1986.

[Wat92] P.A. Watterson, J.G. Zhu, and V.S. Ramsden. "Optimization of Permanent Magnet Motors Using Field Calculations of Increasing Precision". In *IEEE Transactions on Magnetics*, volume 28, pages 1589–1592, March 1992.

[Wei98] R.S. Weissbach, G.G. Karady, and R.G. Farmer. "Model and simulation of a flywheel energy storage system at a utility substation using an induction machine". In *Proceedings of the American Power Conference*, volume 2, pages 906–910, Illinois Institute of Technology, Chicago, IL, USA, April 1998.

[Wei99] R.S. Weissbach, G.G. Karady, and R.G. Farmer. "Dynamic voltage compensation on distribution feeders using flywheel energy storage". In

IEEE Transactions on Power Delivery, volume 14, pages 465–471, April 1999.

[Xia96] Z. Xiaojuan, L. Yingying, F. Hanwei, and Z. Chunhao. "Numerical computation of torques in permanent magnet motors". In *ICEMA*, volume 2, pages 629–632, 1996.

[Zhi00] Y. Zhilichev. "Analysis of Permanent Magnet Machines Using Crossing Macro-Elements". In *IEEE Transactions on Magnetics*, volume 36, pages 3122–3124, September 2000.

[Zhu01a] Z.Q. Zhu, K. Ng, N. Schofield, and D. Howe. "Analytical Prediction of Rotor Eddy Current Loss in Brushless Machines Equipped with Surface-Mounted Permanent Magnets, Part 1: Magnetostatic Field Model". In *Proceedings of the Fifth International Conference on Electrical Machines and Systems (ICEMS 2001)*, volume 2, pages 806–810, September 1997.

[Zhu01b] Z.Q. Zhu, K. Ng, N. Schofield, and D. Howe. "Analytical Prediction of Rotor Eddy Current Loss in Brushless Machines Equipped with Surface-Mounted Permanent Magnets, Part ii: Accounting for Eddy Current Reaction Field". In *Proceedings of the Fifth International Conference on Electrical Machines and Systems (ICEMS 2001)*, volume 2, pages 810–813, September 1997.

[Zhu02] Z.Q. Zhu, D. Howe, E. Bolte, and B. Ackermann. "Improved Analytical Model for Predicting the Magnetic Field Distribution in Brushless Permanent-Magnet Machines". In *IEEE Transactions on Magnetics*, volume 38, pages 229–238, January 2002.

[Zhu93a] Z.Q. Zhu, D. Howe, E. Bolte, and B. Ackermann. "Instantaneous Magnetic Field Distribution in Brushless Permanent Magnet DC Motors, Part I: Open-Circuit Field". In *IEEE Transactions on Magnetics*, volume 29, pages 124–135, January 1993.

[Zhu93b] Z.Q. Zhu and D. Howe. "Instantaneous Magnetic Field Distribution in Brushless Permanent Magnet DC Motors, Part II: Armature-Reaction Field". In *IEEE Transactions on Magnetics*, volume 29, pages 136–142, January 1993.

[Zhu93c] Z.Q. Zhu and D. Howe. "Instantaneous Magnetic Field Distribution in Brushless Permanent Magnet DC Motors, Part III: Effects of Stator Slotting". In *IEEE Transactions on Magnetics*, volume 29, pages 143–151, January 1993.

[Zhu93d] Z.Q. Zhu and D. Howe. "Instantaneous Magnetic Field Distribution in Brushless Permanent Magnet DC Motors, Part IV: Magnetic Field on

Load". In *IEEE Transactions on Magnetics*, volume 29, pages 152–158, January 1993.

[Zhu94] Z.Q. Zhu, D. Howe, E. Bolte, and B. Ackermann. "Prediction of Open-Circuit Airgap Field Distribution in Brushless Machines Having an Inset Permanent Magnet Rotor Topology". In *IEEE Transactions on Magnetics*, volume 30, pages 98–107, January 1994.

[Zyl98] A. van Zyl and R. Spée. "Short Term Energy Storage for ASD Ride-Through". In *Conference Record, IEEE Industry Applications Society Annual Meeting*, pages 1162–1167, 1998.

Winding factors

A.1 Introduction

Winding factors have become the method of choice to represent windings mathematically as is evident from literature. Several ways of introducing the winding factors have been introduced over the years. In [Sle92] it is the ratio of the mmf of a physical winding distribution to that of a concentrated one. In [Ric67] the ratio is between the flux linked of these two types of windings, and some other authors introduce the ratio as the one between the surface current densities of the two winding types. In [Pol98], the winding factor is directly the ratio of the equivalent number of turns of a space harmonic of a physical winding to that of a concentrated winding. In whatever way the winding factors are introduced, they have the same meaning since the physical quantity from which they are derived (i.e. the mmf [Sle92], the flux linkage [Ric67], or the surface current density of the stator), disappears in the derivation and only the equivalent number of turns is left. It is for this reason that the winding factors are simply a tool to simplify the Fourier-series representation of a physical winding distribution.

Due to this fact, winding factors may also be used in air gap windings. They have been used in multilayer air gap windings by several researchers: [Ata98], [Sri95] and [Che97], of which [Ata98] and [Sri95] include experimental validation.

A.2 The different winding factors

There are four different winding factors commonly used today. They are the:

- Distribution factor $k_{w,dist,k}$: this factor modifies the Fourier coefficient of the winding distribution for the case where the winding is distributed over several

slots instead of concentrated in an infinitesimal slot. It is given by:

$$k_{w,dist,k} = \frac{\sin\left(\frac{k\pi}{2m}\right)}{q\sin\left(\frac{k\pi}{2mq}\right)}, \tag{A.1}$$

- Pitch factor $k_{w,pitch,k}$: this factor accounts for the short pitching of the winding, i.e. where the return conductors are located at less than a pole pitch from the go conductors. This factor is written as:

$$k_{w,pitch,k} = \cos\left(\tfrac{1}{2}kp\varphi_{pitch}\right), \tag{A.2}$$

if the stator winding is short pitched from π/p to $\pi/p - \varphi_{pitch}$ radians.

- Slot factor $k_{w,slot,k}$: this factor further modifies the Fourier coefficient because of the slotting of the winding (the physical slot width). The slot factor is expressed as:

$$k_{w,slot,k} = \frac{\sin\left(\tfrac{1}{2}kp\varphi_{so}\right)}{\tfrac{1}{2}kp\varphi_{so}}, \tag{A.3}$$

where φ_{so} is the slot-opening angle.

- Skew factor: $k_{w,skew,k}$: when the stator is skewed with respect to the rotor, usually to reduce or eliminate cogging torque, this factor takes that into account. The skew factor is identical in expression to the slot factor:

$$k_{w,skew,k} = \frac{\sin\left(\tfrac{1}{2}kp\varphi_{skew}\right)}{\tfrac{1}{2}kp\varphi_{skew}}, \tag{A.4}$$

where φ_{skew} is the skew angle.

The winding factor is the product of the four different winding factors (A.1)–(A.4) above:

$$k_{w,k} = k_{w,dist,k}\, k_{w,pitch,k}\, k_{w,slot,k}\, k_{w,skew,k}. \tag{A.5}$$

A.3 Fourier analysis of a winding distribution

A.3.1 Introduction

To show that the winding factor approach is a simple way of avoiding a direct Fourier analysis of the distribution of the winding, this section will develop a Fourier-series expression for the EμFER machine's winding distribution by both approaches.

A.3.2   The EµFER machine's winding distribution

The 1-2-2-1 winding of the EµFER machine is shown in Figure 3.8. In this section the winding distribution is shifted 4.5 slots to the right in order to show that also a sine distribution is easily handled with winding factors. In the thesis, a cosine distribution is used so that the triplen- and non-triplen space harmonics can easily be separated as in (3.16a).

   The EµFER machine's winding distribution, shifted by 4.5 slots to the right, is shown in Figure A.1. In Figure A.1(a), the number of conductors in each of the 36 slots is shown, while Figure A.1(b) shows the number of conductors per radian in the slots, i.e. Figure A.1(a) divided by φ_{so}.

A.3.3   Fourier analysis by means of the winding factors

The winding factor $k_{w,k}$ in (A.5) above, when multiplied with $4/\pi$, relates the real (physical) number of turns of a winding N to the equivalent (mathematical) number of turns of the k-th space harmonic $N_{s,k}$. This is derived in [Sle92] and is written as:

$$N_{s,k} = \tfrac{4}{\pi} k_{w,k} N \; \times \; \begin{cases} \sin\left(\tfrac{1}{2} k\pi\right) & \text{for a sine series,} \\ 1 & \text{for a cosine series.} \end{cases} \tag{A.6}$$

   From (A.6), one sees that usually either a sine series or a cosine series is used. The origin of the winding distribution is thus chosen to make the Fourier series either one or the other. Choosing the origin such that both terms are required unnecessarily complicates the analysis. In this appendix, an example is done with a sine-series representation of the EµFER machine's winding distribution, while in the rest of the thesis, the cosine representation is used. These are completely equivalent, since only a physical rotation of $\pi/2p$ is required to obtain the one from the other.

   The Fourier coefficient $\hat{n}_{s,k}$ is half the number of turns of the k-th space harmonic $N_{s,k}$ of (A.6), or:

$$\hat{n}_{s,k} = \tfrac{1}{2} N_{s,k}. \tag{A.7}$$

Making use of this Fourier coefficient, the Fourier-series representation of the winding distribution n_{sa} is written as either:

$$n_{sa}(\varphi) = \sum_{k=1,3,5,\cdots}^{\infty} \hat{n}_{s,k} \sin(kp\varphi), \tag{A.8}$$

for a sine series, or:

$$n_{sa}(\varphi) = \sum_{k=1,3,5,\cdots}^{\infty} \hat{n}_{s,k} \cos(kp\varphi), \tag{A.9}$$

for a cosine series.

   For the EµFER machine's winding distribution, the following parameters were listed in Chapter 3:
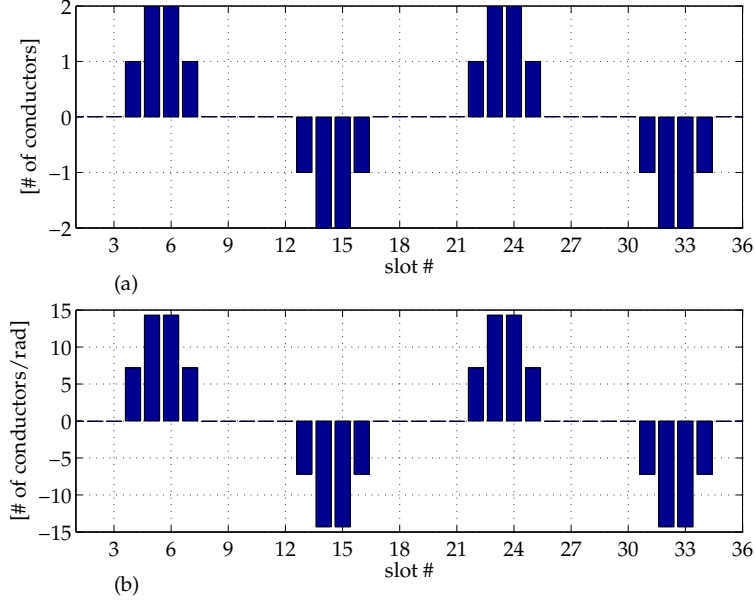
Figure A.1: The 1-2-2-1 winding of the EμFER machine shifted 4.5 slots to the right; (a) number of conductors; (b) number of conductors per radian.

- number of phases: $m = 3$;

- number of pole pairs: $p = 2$;

- number of slots per pole per phase: $q = 3$;

- number of slots: $s = 2mpq = 36$;

- slot-opening angle: $\varphi_{so} = 0.8(\pi/18)$;

- pitch angle: $\varphi_{pitch} = \pi/18$; and

- 1 conductor per slot per layer

These are substituted into (A.1), (A.2), (A.3), (A.5), (A.6), (A.7), and (A.8) to obtain a Fourier series representation of the winding distribution. Note that for the EμFER machine, there is no skew factor.

A.3.4   Direct Fourier analysis

In [Jef90], a formal derivation of a trigonometric Fourier series is done, as in many other mathematical texts. This results in the representation of a periodic function f on an interval $[a, b]$ as:

$$f(\varphi) = \frac{1}{2}a_0 + \sum_{k=1}^{\infty} \left[a_k \cos\left(\frac{2k\pi\varphi}{b-a}\right) + b_k \sin\left(\frac{2k\pi\varphi}{b-a}\right) \right]; \quad a \le \varphi \le b, \qquad (A.10)$$

where

$$a_k = \frac{2}{b-a} \int_a^b f(\varphi) \cos\left(\frac{2k\pi\varphi}{b-a}\right) d\varphi; \quad k = 0, 1, 2, \cdots \qquad (A.11)$$

and

$$b_k = \frac{2}{b-a} \int_a^b f(\varphi) \sin\left(\frac{2k\pi\varphi}{b-a}\right) d\varphi; \quad k = 1, 2, 3, \cdots \qquad (A.12)$$

Recognizing by inspection that $a_k = 0$ for all k when a sine series is used as in (A.8) and Figure A.1, and choosing the periodic interval as $[a, b] = [0, \pi]$, the formula for b_k becomes from (A.12):

$$b_k = \frac{2}{\pi} \int_0^\pi f(\varphi) \sin(2k\varphi) \, d\varphi. \qquad (A.13)$$

From Figure A.1(b), equation (A.13) becomes:

$$
\begin{aligned}
b_k = \frac{2}{\pi\varphi_{so}} \Bigg[& \int_{\frac{3\pi}{18}-\frac{\varphi_{so}}{2}}^{\frac{3\pi}{18}+\frac{\varphi_{so}}{2}} \sin(2k\varphi)\, d\varphi + \int_{\frac{4\pi}{18}-\frac{\varphi_{so}}{2}}^{\frac{4\pi}{18}+\frac{\varphi_{so}}{2}} 2\sin(2k\varphi)\, d\varphi + \int_{\frac{5\pi}{18}-\frac{\varphi_{so}}{2}}^{\frac{5\pi}{18}+\frac{\varphi_{so}}{2}} 2\sin(2k\varphi)\, d\varphi \\
& + \int_{\frac{6\pi}{18}-\frac{\varphi_{so}}{2}}^{\frac{6\pi}{18}+\frac{\varphi_{so}}{2}} \sin(2k\varphi)\, d\varphi - \int_{\frac{12\pi}{18}-\frac{\varphi_{so}}{2}}^{\frac{12\pi}{18}+\frac{\varphi_{so}}{2}} \sin(2k\varphi)\, d\varphi - \int_{\frac{13\pi}{18}-\frac{\varphi_{so}}{2}}^{\frac{13\pi}{18}+\frac{\varphi_{so}}{2}} 2\sin(2k\varphi)\, d\varphi \\
& - \int_{\frac{14\pi}{18}-\frac{\varphi_{so}}{2}}^{\frac{14\pi}{18}+\frac{\varphi_{so}}{2}} 2\sin(2k\varphi)\, d\varphi - \int_{\frac{15\pi}{18}-\frac{\varphi_{so}}{2}}^{\frac{15\pi}{18}+\frac{\varphi_{so}}{2}} \sin(2k\varphi)\, d\varphi \Bigg]. \quad (A.14)
\end{aligned}
$$

The distance from the centre of one slot to the next is recognized to be $2\pi/s = \pi/18$. Equation (A.14) is worked out as:

$$
\begin{aligned}
b_k = \frac{2}{\pi} \frac{\sin(k\varphi_{so})}{k\varphi_{so}} \Bigg[& \sin\left(\frac{3}{9}k\pi\right) + 2\sin\left(\frac{4}{9}k\pi\right) + 2\sin\left(\frac{5}{9}k\pi\right) + \sin\left(\frac{6}{9}k\pi\right) \\
& - \sin\left(\frac{12}{9}k\pi\right) - 2\sin\left(\frac{13}{9}k\pi\right) - 2\sin\left(\frac{14}{9}k\pi\right) - \sin\left(\frac{15}{9}k\pi\right) \Bigg]. \quad (A.15)
\end{aligned}
$$

The slot factor (A.3) is clearly seen in (A.15), while the distribution and pitch factors are contained in the 8 terms in brackets.

The winding distribution for phase a is therefore written from (A.10) as:

$$n_{sa,d}(\varphi) = \sum_{k=1}^\infty b_k \sin(2k\varphi), \qquad (A.16)$$

where the Fourier coefficient b_k is given by (A.15) and the subscript d indicates that the expression comes from a direct Fourier analysis. Since the terms in (A.16) are zero for $k = 2, 4, 6, \cdots$, only uneven k may be used:

$$n_{sa,d}(\varphi) = \sum_{k=1,3,5,\cdots}^{\infty} b_k \sin(2k\varphi). \tag{A.17}$$

A.4   Results and comparison

The two approaches to obtain the winding distribution, i.e. the winding factor approach and the direct Fourier analysis approach, resulted in equations (A.8) and (A.17). These functions are plotted in Figure A.2. The function $n_{sa,d}(\varphi)$ of the Fourier series approach was multiplied by 0.95 so that the graphs can easily compared. Both functions were calculated up to a maximum of $k = 301$ space harmonics. Figure A.2 proves that both approaches led to the same result for the winding distribution.

Both functions $n_{sa}(\varphi)$ and $n_{sa,d}(\varphi)$ can be converted into a cosine series by substituting $\varphi + \frac{\pi}{2p}$ for φ, since $\cos(kp\varphi) = \sin\left[kp\left(\varphi + \frac{\pi}{2p}\right)\right]$. One thus sees that to change a sine into a cosine representation is simple with both methods.

When the number of poles (or any other parameter for that matter) changes, however, the winding factor approach immediately produces the correct Fourier se-
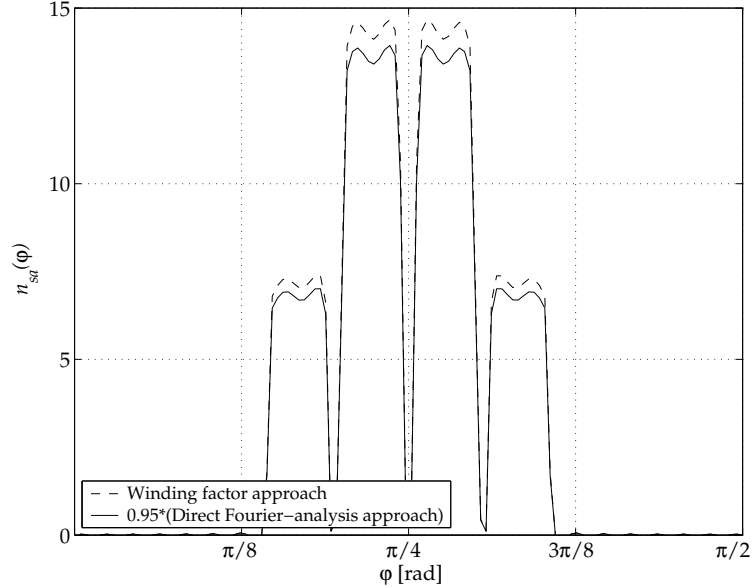

Figure A.2: The winding distribution $n_{sa}(\varphi)$ and $n_{sa,d}(\varphi)$ as calculated by (A.8) and (A.17). The function $n_{sa,d}(\varphi)$ from the direct Fourier analysis approach was multiplied by 0.95 so that both can easily be compared.

ries by changing the appropriate winding factors, while the direct Fourier-analysis approach requires a completely new calculation.

A.5 The current density

Figure A.3(a) shows the winding distribution of all three phases as used in the rest of the thesis, i.e. a cosine distribution calculated by (A.9) for phase *a*.

From the three-phase winding distribution of Figure A.3(a), the total current density can be obtained. It is given by (6.1) as the winding distribution times the stator current, divided by the winding height and winding centre radius. In space and time harmonic form with both the winding distribution and the current written as cosine functions, this results in the following expression for phase *a*:

$$J_{sa,k,n}(\varphi, t) = \frac{\hat{n}_{s,k}\hat{i}_{s,n}}{h_w r_{wc}} \cos(kp\varphi) \cos(n\omega_s t). \tag{A.18}$$

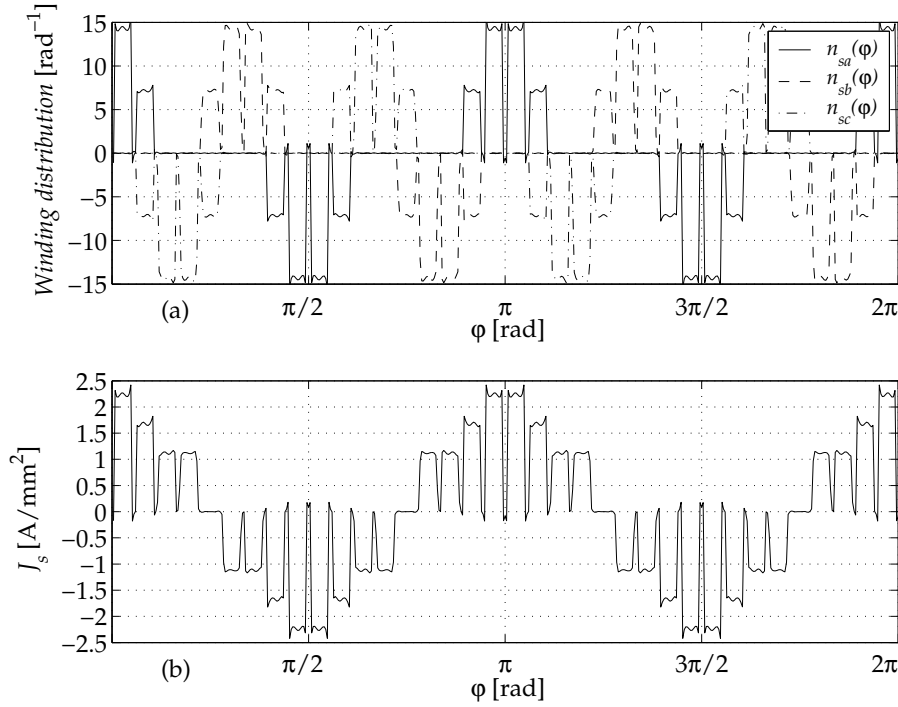The current density of phase *a* is the sum of (A.18) over space and time harmonics *k*

Figure A.3: (a) The stator winding distribution $n_{sa}(\varphi)$ as calculated by (A.9), and $n_{sb}(\varphi)$ and $n_{sc}(\varphi)$. (b) "Snapshot" of the current density $J_s(\varphi, t)$ at *t* such that $i_{sa} = 300$ A, $i_{sb} = i_{sc} = -150$ A.

and *n*:

$$J_{sa}(\varphi, t) = \sum_{k=1,3,5,\cdots}^{\infty} \sum_{n=1,3,5,\cdots}^{\infty} J_{sa,k,n}(\varphi, t). \tag{A.19}$$

For phases *b* and *c*, similar expressions are used with the appropriate phase shifts. The total current density is given by

$$J_s(\varphi, t) = J_{sa}(\varphi, t) + J_{sb}(\varphi, t) + J_{sc}(\varphi, t). \tag{A.20}$$

The total current density is shown in Figure A.3(b) at *t* such that $i_{sa} = 300$ A, $i_{sb} = i_{sc} = -150$ A.

This situation is a balanced three-phase condition. For such balanced three-phase stator currents, the triplen harmonics are zero, as shown in Chapter 6. The *k*-th space and *n*-th time harmonic of the total current density is thus in travelling-wave form:

$$J_{s,k,n}(\varphi, t) = \frac{3}{2} J_{sa,k,n}(\varphi, t) = \frac{3}{2} \frac{\hat{n}_{s,k}\hat{i}_{s,n}}{h_w r_{wc}} \cos(kp\varphi - n\omega_s t); \quad k, n = 1, 5, 7, 11, \cdots \tag{A.21}$$

Maxwell's equations and the Theorem of Poynting

B.1 Introduction

This appendix documents the electromagnetic background of the thesis. Firstly, the equations of Maxwell are listed in Section B.1 and then simplified to the magneto-quasistatic approximation for stationary media in the time domain in Section B.2.

Section B.3 simplifies the Maxwell equations for the magnetoquasistatic approximation, which is the approximation used throughout this thesis.

The Theorem of Poynting is the topic of Section B.4. It is listed in local and integral forms in the time domain for stationary matter.

In Section B.5, things start moving. This section uses results from the theory of special relativity to arrive at Maxwell's equations for matter moving with constant rotational velocity.

Section B.6 combines results of Sections B.4 and B.5 to obtain the Theorem of Poynting for moving matter; once again for constant rotational velocity. It is shown that the Poynting vector in rotor coordinates (*R*-system) only calculates dissipated power while in stator coordinates (*L*-system), both mechanical and dissipated components are present.

Section B.7 applies the results obtained to the electrical machine discussed in this thesis.

B.2 Maxwell's equations in stationary matter

The equations of Maxwell in stationary matter are:

$$-\nabla \times \mathbf{H} + \epsilon_0 \frac{\partial \mathbf{E}}{\partial t} = -\mathbf{J}_{mat}, \tag{B.1a}$$

and

$$\nabla \times \mathbf{E} + \mu_0 \frac{\partial \mathbf{H}}{\partial t} = -\mathbf{K}_{mat}, \tag{B.1b}$$

where the current and surface current densities in the matter are given by:

$$\mathbf{J}_{mat} = \mathbf{J}_{ind} + \mathbf{J}_{ext}, \tag{B.2a}$$

and

$$\mathbf{K}_{mat} = \mathbf{K}_{ind} + \mathbf{K}_{ext}. \tag{B.2b}$$

Furthermore, the induced current and surface current densities are:

$$\mathbf{J}_{ind} = \mathbf{J} + \frac{\partial \mathbf{P}}{\partial t}, \tag{B.3a}$$

where $\mathbf{P}$ is the polarization and

$$\mathbf{K}_{ind} = \mu_0 \frac{\partial \mathbf{M}}{\partial t}, \tag{B.3b}$$

where $\mathbf{M}$ is the magnetization of the matter.

With the flux densities:

$$\mathbf{D} = \epsilon_0 \mathbf{E} + \mathbf{P}, \tag{B.4a}$$

and

$$\mathbf{B} = \mu_0(\mathbf{H} + \mathbf{M}), \tag{B.4b}$$

equations (B.1a) and (B.1b) result in Maxwell's equations in matter:

$$-\nabla \times \mathbf{H} + \mathbf{J} + \frac{\partial \mathbf{D}}{\partial t} = -\mathbf{J}_{ext}, \tag{B.5a}$$

and

$$\nabla \times \mathbf{E} + \frac{\partial \mathbf{B}}{\partial t} = -\mathbf{K}_{ext}. \tag{B.5b}$$

These are supplemented by the constitutive relations for an instantaneous medium:

$$\mathbf{J}(\mathbf{x}, t) = \sigma(\mathbf{x})\mathbf{E}(\mathbf{x}, t), \tag{B.6a}$$

$$\mathbf{D}(\mathbf{x}, t) = \epsilon(\mathbf{x})\mathbf{E}(\mathbf{x}, t), \tag{B.6b}$$

and

$$\mathbf{B}(\mathbf{x}, t) = \mu(\mathbf{x})\mathbf{H}(\mathbf{x}, t). \tag{B.6c}$$

Also, by taking the divergence of (B.5a) and (B.5b) we have the compatibility equations:

$$\nabla \cdot \mathbf{J} + \frac{\partial}{\partial t}(\nabla \cdot \mathbf{D}) = -\nabla \cdot \mathbf{J}_{ext}, \tag{B.7a}$$

and

$$\frac{\partial}{\partial t}(\nabla \cdot \mathbf{B}) = -\nabla \cdot \mathbf{K}_{ext}. \tag{B.7b}$$

Combination of (B.5) and (B.6) results in the electromagnetic field equation:

$$-\nabla \times \mathbf{H} + \sigma \mathbf{E} + \epsilon \frac{\partial \mathbf{E}}{\partial t} = -\mathbf{J}_{ext}, \tag{B.8a}$$

and

$$\nabla \times \mathbf{E} + \mu \frac{\partial \mathbf{H}}{\partial t} = -\mathbf{K}_{ext}. \tag{B.8b}$$

B.3   The magnetoquasistatic approximation

The magnetoquasistatic approximation (MQS), used throughout this thesis, is obtained from (B.5) by setting $\frac{\partial \mathbf{D}}{\partial t}$ and $\mathbf{K}_{ext}$ to zero. The field equation for the MQS approximation is:

$$-\nabla \times \mathbf{H} + \mathbf{J} = -\mathbf{J}_{ext}, \tag{B.9a}$$

$$\nabla \times \mathbf{E} + \frac{\partial \mathbf{B}}{\partial t} = \mathbf{0}, \tag{B.9b}$$

$$\nabla \cdot \mathbf{J}_{ext} = 0, \tag{B.9c}$$

and

$$\nabla \cdot \mathbf{B} = 0, \tag{B.9d}$$

The static part is given by (B.9a) and the dynamic part by (B.9b).

The constitutive relations for a linear isotropic medium are:

$$\mathbf{J} = \sigma \mathbf{E}, \tag{B.10a}$$

and

$$\mathbf{B} = \mu_0 \mathbf{H} + \mu_0 \mathbf{M}. \tag{B.10b}$$

The magnetization $\mathbf{M}$ consists of two parts: a temporary part and a permanent part, or:

$$\mathbf{M} = \mathbf{M}_t + \mathbf{M}_p. \tag{B.11}$$

This fact transforms (B.10b) into:

$$\begin{aligned}\mathbf{B} &= \mu_0 \mathbf{H} + \mu_0 \mathbf{M}_t + \mu_0 \mathbf{M}_p \\ &= \mu \mathbf{H} + \mu_0 \mathbf{M}_p \\ &= \mu \mathbf{H} + \mathbf{B}_{rem},\end{aligned} \tag{B.12}$$

where the remanent flux density of the magnets has been introduced as:

$$\mathbf{B}_{rem} \equiv \mu_0 \mathbf{M}_p. \tag{B.13}$$

Furthermore, by taking the divergence of (B.9a) and by use of (B.9c), we have:

$$\nabla \cdot \mathbf{J} = 0. \tag{B.14}$$

B.4 The Theorem of Poynting

B.4.1 Local form in the time domain

In local form, the Theorem of Poynting in the time domain is written[1] as [Blo99]:

$$\nabla \cdot \mathbf{S} + \mathbf{H} \cdot \partial_t \mathbf{B} + \mathbf{J} \cdot \mathbf{E} = -\mathbf{E} \cdot \mathbf{J}_{ext}, \tag{B.15}$$

where $\mathbf{S}$ is the Poynting vector:

$$\mathbf{S} \equiv \mathbf{H} \times \mathbf{H}. \tag{B.16}$$

By use of the constitutive relations (B.10a) and (B.12), this becomes:

$$\nabla \cdot \mathbf{S} + \partial_t \left(\tfrac{1}{2} \mu \mathbf{H} \cdot \mathbf{H} \right) + \mathbf{H} \cdot \partial_t \mathbf{B}_{rem} + \sigma \mathbf{E} \cdot \mathbf{E} = -\mathbf{E} \cdot \mathbf{J}_{ext}, \tag{B.17}$$

which can be rewritten as:

$$p_{source} + \partial_t w_m + p_{mech} + p_{diss} = p_{ext}, \tag{B.18}$$

by introducing the source power density p_{source} [W/m^3], the energy density in the magnetic field w_m [J/m^3], the mechanical power density p_{mech} [W/m^3], the dissipated power density p_{diss} [W/m^3] and the external power density p_{ext} [W/m^3].

B.4.2 Integral form in the time domain

The integral form in the time domain can be written from (B.17) as:

$$\oint_S \mathbf{S} \cdot d\mathbf{a} + \partial_t \int_V \left(\tfrac{1}{2} \mu \mathbf{H} \cdot \mathbf{H} \right) dv + \int_V \mathbf{H} \cdot \partial_t \mathbf{B}_{rem}\, dv + \int_V \sigma \mathbf{E} \cdot \mathbf{E}\, dv = -\int_V \mathbf{E} \cdot \mathbf{J}_{ext}\, dv, \tag{B.19}$$

where the closed surface S encloses volume V, i.e. $S = \partial V$. Equation (B.19) can be rewritten as:

$$P_{source} + \partial_t W_m + P_{mech} + P_{diss} = -P_{ext} \tag{B.20}$$

The power P_{ext} is the power that passes through the surface S.

B.5 Maxwell's equations in moving matter

B.5.1 Constant rotational velocity

When a body is moving at a constant velocity, results from the theory of special relativity can be used [Blo75]. Strictly speaking, rotating bodies with constant rotational velocities do not have a constant velocity because of the direction change. When the corresponding circumferential speeds are low compared to the speed of light,

---

[1] The notation ∂_t is shorthand for $\frac{\partial}{\partial t}$.

however, one may use the results of the theory of special relativity without getting too large an error. In the case of the machine discussed in this thesis, the ratio of the circumferential speed at the magnet radius to the speed of light in vacuum is $v_c / c_0 \approx 1 \times 10^{-6}$; $c_0 = (\epsilon_0 \mu_0)^{-1/2}$, giving confidence in the validity of the method.

Van Bladel [Bla73] and Shiozawa [Shi73] addressed the issue of electromagnetic field equations for rotating media. Following the discussion in [Shi73], consider the two reference frames of Figure B.1. Reference frame R rotates with constant angular speed ω_m around the Z-axis while reference frame L is in rest; its Z-axis is parallel to that of reference frame R. The coordinates of the R-frame is indicated with primes: (x', y', z', t'), and that of the L-frame without it: (x, y, z, t); t is the time "coordinate". The R-frame is the "rest" frame with respect to the rotating matter; it thus rotates with it. The L stands for "laboratory".

For circumferential speeds that are low with respect to the speed of light in vacuum, the Galilei transformations may be used:

$$
\begin{aligned}
x' &= x \cos \omega_m t + y \sin \omega_m t \\
y' &= -x \sin \omega_m t + y \cos \omega_m t \\
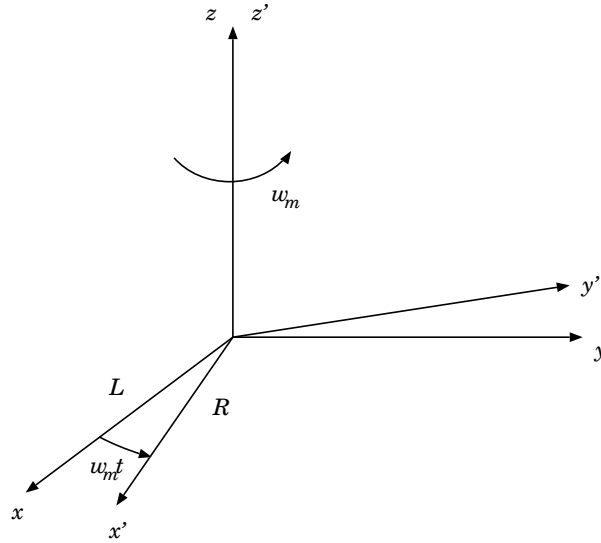z' &= z \\
t' &= t
\end{aligned}
\tag{B.21}
$$

Figure B.1: Rotational reference frames; the R-system is in rest w.r.t. the moving matter and the L-system observes the matter as rotating at constant rotational velocity around the Z-axis. The R-system corresponds to the rotor and the L-system to the stator.

B.5.2 The field equations

The first postulate of special relativity is that the field equations has the same form in both reference frames. The MQS field equation in the *R*-system is:

$$-\nabla' \times \mathbf{H}' + \mathbf{J}' = -\mathbf{J}'_{ext}, \tag{B.22a}$$

$$\nabla' \times \mathbf{E}' + \frac{\partial \mathbf{B}'}{\partial t'} = \mathbf{0}', \tag{B.22b}$$

$$\nabla' \cdot \mathbf{D}' = \rho', \tag{B.22c}$$

$$\nabla' \cdot \mathbf{B}' = 0'. \tag{B.22d}$$

where ρ' is the charge density. In the *L*-system it is:

$$-\nabla \times \mathbf{H} + \mathbf{J} = -\mathbf{J}_{ext}, \tag{B.23a}$$

$$\nabla \times \mathbf{E} + \frac{\partial \mathbf{B}}{\partial t} = \mathbf{0}, \tag{B.23b}$$

$$\nabla \cdot \mathbf{D} = \rho, \tag{B.23c}$$

$$\nabla \cdot \mathbf{B} = 0. \tag{B.23d}$$

B.5.3 Transformation equations

For the Galilei transformations (B.21), the transformation equations for the field quantities are:

$$\mathbf{E}' = \mathbf{E} + \mathbf{v}_c \times \mathbf{B}; \quad \mathbf{B}' = \mathbf{B} - \left(\frac{1}{c_0}\right) \mathbf{v}_c \times \mathbf{E}; \tag{B.24a}$$

$$\mathbf{H}' = \mathbf{H} - \mathbf{v}_c \times \mathbf{D}; \quad \mathbf{D}' = \mathbf{D} + \left(\frac{1}{c_0}\right) \mathbf{v}_c \times \mathbf{H}; \tag{B.24b}$$

$$\mathbf{J}' = \mathbf{J} - \rho \mathbf{v}_c; \quad \rho' = \rho - \left(\frac{1}{c_0}\right) \mathbf{v}_c \cdot \mathbf{J}. \tag{B.24c}$$

B.5.4 The constitutive relations

As already mentioned, the field equations stay the same in both systems. The effect of the movement is seen in the constitutive relations, however.

In the *R*-system

The constitutive relations must be written in the *R*-system since for linear isotropic media, the material properties must be measured in the system that is in rest w.r.t. the matter [Blo75]. The constitutive relations in the *R*-system are:

$$\mathbf{D}' = \epsilon \mathbf{E}'; \quad \mathbf{B}' = \mu \mathbf{H}' + \mathbf{B}_{rem}; \quad \mathbf{J}' = \sigma \mathbf{E}'. \tag{B.25}$$

In the L-system

To obtain the constitutive relations in the L-system, equation (B.24) is substituted into (B.25), the constitutive relations in the R-system. One then obtains after manipulation and making use of the fact that $c_0 = (\epsilon_0 \mu_0)^{-1/2}$:

$$\mathbf{D} = \epsilon \mathbf{E} + (\epsilon \mu - \epsilon_0 \mu_0) \mathbf{v}_c \times \mathbf{H}; \tag{B.26a}$$

$$\mathbf{B} = \mu \mathbf{H} - (\epsilon \mu - \epsilon_0 \mu_0) \mathbf{v}_c \times \mathbf{E} + \mathbf{B}_{rem}; \tag{B.26b}$$

$$\mathbf{J} = \sigma \mathbf{E} + \sigma \mu \mathbf{v}_c \times \mathbf{H}. \tag{B.26c}$$

B.6 The Theorem of Poynting for moving matter

B.6.1 Local form in the time domain: R-system

Equation (B.17) for stationary media can be written exactly as it is in the R-system since this system is in rest w.r.t. the matter:

$$\nabla \cdot \mathbf{S}' + \mathbf{H}' \cdot \partial_t' \mathbf{B}' + \mathbf{J}' \cdot \mathbf{E}' = -\mathbf{E}' \cdot \mathbf{J}'_{ext}. \tag{B.27}$$

The external current density is zero in our case. By use of the constitutive relations (B.25), this becomes:

$$-\nabla \cdot \mathbf{S}' = \partial_t' \left(\tfrac{1}{2} \mu \mathbf{H}' \cdot \mathbf{H}' \right) + \mathbf{H}' \cdot \partial_t' \mathbf{B}_{rem} + \sigma \mathbf{E}' \cdot \mathbf{E}', \tag{B.28}$$

which can be rewritten as:

$$p'_{source} = \partial_t' w'_m + p'_{mech} + p'_{diss}. \tag{B.29}$$

The power density p'_{mech} is the power density delivered to the permanent magnets. In the R-system this term is zero since the remanence does not change with time in this system; i.e.:

$$p'_{source} = \partial_t' w'_m + p'_{diss}. \tag{B.30}$$

In time-averaged form, this is:

$$\langle p'_{source} \rangle = \langle p'_{diss} \rangle. \tag{B.31}$$

B.6.2 Local form in the time domain: L-system

Following the first postulate of the theory of special relativity, the Theorem of Poynting has the same form in the L-system as in the R-system. Thus:

$$\nabla \cdot \mathbf{S} + \mathbf{H} \cdot \partial_t \mathbf{B} + \mathbf{J} \cdot \mathbf{E} = -\mathbf{E} \cdot \mathbf{J}_{ext}. \tag{B.32}$$

By use of the constitutive relations (B.26), this becomes:

$$\nabla \cdot \mathbf{S} + \partial_t \left(\tfrac{1}{2} \mu \mathbf{H} \cdot \mathbf{H} \right) - \mathbf{H} \cdot \partial_t \left[(\epsilon \mu - \epsilon_0 \mu_0) \mathbf{v}_c \times \mathbf{E} \right] + \mathbf{H} \cdot \partial_t \mathbf{B}_{rem}$$
$$+ \sigma \mathbf{E} \cdot \mathbf{E} + (\sigma \mu \mathbf{v}_c \times \mathbf{H}) \cdot \mathbf{E} = -\mathbf{E} \cdot \mathbf{J}_{ext}. \quad \text{(B.33)}$$

In the analytical model of this thesis, all non-iron regions are assumed to have a permittivity and permeability that is equal to that of free space. This makes the third term equal to zero. Once again, as in the *R*-system, the external current density is zero. Equation (B.33) now becomes:

$$-\nabla \cdot \mathbf{S} = \partial_t \left(\tfrac{1}{2} \mu \mathbf{H} \cdot \mathbf{H} \right) + \mathbf{H} \cdot \partial_t \mathbf{B}_{rem} + \sigma \mathbf{E} \cdot \mathbf{E} + (\sigma \mu \mathbf{v}_c \times \mathbf{H}) \cdot \mathbf{E}. \quad \text{(B.34)}$$

B.6.3   Interpretation

The interpretation of Poynting's Theorem in the *L*-system, equation (B.34), is more complicated than in the *R*-system of equation (B.28).

Firstly, $\partial_t \mathbf{B}_{rem}$ is nonzero in the *L*-system, suggesting that power is delivered to the rotating magnets. The other two time-averaged power components represent power delivered to the shielding cylinder. In total, three different time-averaged power components are therefore present, as suggested by (B.34):

1. Mechanical power delivered to the rotating permanent magnets;

2. Dissipation power delivered to the shielding cylinder; and

3. Mechanical power delivered to the shielding cylinder.

In Chapter 6 it was shown that the shielding cylinder only allows the magnetic field to penetrate through it for equal space and time harmonics. The power components corresponding to equal space and time harmonics thus form power component #1: the mechanical power delivered to the rotating permanent magnets.

For nonequal space and time harmonics, a combination of components #2 and #3 listed above is present. To distinguish between these, the rotor slip is needed. This is introduced in Chapter 7, where these power components are also calculated. For the purposes of this section, we conclude with writing equation (B.34) as:

$$p_{source} = \partial_t w_m + p_{mech} + p_{sc,diss} + p_{sc,mech}, \quad \text{(B.35)}$$

which is in time-averaged form:

$$\langle p_{source} \rangle = \langle p_{mech} \rangle + \langle p_{sc,diss} \rangle + \langle p_{sc,mech} \rangle. \quad \text{(B.36)}$$

B.6.4   Frequency-domain forms

Definition of the complex Poynting vector

The field equations in the frequency domain may be obtained from the time-domain form of the field equations by subjecting them to a Laplace transform on the interval

$\{t \in \mathbb{R}, t > 0\}$. The steady-state analysis for time-harmonic sources (which is used throughout this thesis) may be considered as a limiting case of Laplace-transform analysis, where $s \to j\omega$.

In the frequency domain we then have complex vectors, indicated by a bar above the symbol; for example, for the electric field vector: $\bar{\mathbf{E}}$. A hat above the symbol is needed since it is the peak value of the time-harmonic form: $\hat{\bar{\mathbf{E}}}$. To transform back to the time domain, we write:

$$\mathbf{E}(r, \phi, t) \equiv \mathrm{Re}\left\{ \hat{\bar{\mathbf{E}}}(r, \phi, j\omega)e^{j\omega t} \right\}. \tag{B.37}$$

Furthermore, it should be noted that the real-valued vector $\mathbf{E}$ can be written in terms of $\hat{\bar{\mathbf{E}}}$ and its complex conjugate $\hat{\bar{\mathbf{E}}}^*$ as:

$$\mathbf{E} = \mathrm{Re}\left\{ \hat{\bar{\mathbf{E}}}e^{j\omega t} \right\} = \tfrac{1}{2}\left(\hat{\bar{\mathbf{E}}}e^{j\omega t} + \hat{\bar{\mathbf{E}}}^*e^{-j\omega t} \right). \tag{B.38}$$

Making use of this fact, the cross product of $\mathbf{E}$ and $\mathbf{H}$ may now be taken:

$$\begin{aligned}
\mathbf{S} = \mathbf{E} \times \mathbf{H} &= \tfrac{1}{2}\left(\hat{\bar{\mathbf{E}}}e^{j\omega t} + \hat{\bar{\mathbf{E}}}^*e^{-j\omega t} \right) \times \tfrac{1}{2}\left(\hat{\bar{\mathbf{H}}}e^{j\omega t} + \hat{\bar{\mathbf{H}}}^*e^{-j\omega t} \right) \\
&= \tfrac{1}{4}\left(\hat{\bar{\mathbf{E}}} \times \hat{\bar{\mathbf{H}}}^* + \hat{\bar{\mathbf{E}}}^* \times \hat{\bar{\mathbf{H}}} \right) + \tfrac{1}{4}\left(\hat{\bar{\mathbf{E}}} \times \hat{\bar{\mathbf{H}}}e^{j2\omega t} + \hat{\bar{\mathbf{E}}}^* \times \hat{\bar{\mathbf{H}}}^*e^{-j2\omega t} \right) \\
&= \tfrac{1}{2}\mathrm{Re}\left\{ \hat{\bar{\mathbf{E}}} \times \hat{\bar{\mathbf{H}}}^* \right\} + \tfrac{1}{2}\mathrm{Re}\left\{ \hat{\bar{\mathbf{E}}} \times \hat{\bar{\mathbf{H}}}e^{j2\omega t} \right\}.
\end{aligned} \tag{B.39}$$

The first term of (B.39) is time independent and represents the average value of Poynting's vector over a cycle. The second term is a sinusoidal vector with frequency 2ω, and its components cancel out if $\mathbf{E} \times \mathbf{H}$ is a vector of constant length rotating with velocity ω [Fan60].

Following the reasoning above, the complex Poynting vector is defined as:

$$\hat{\bar{\mathbf{S}}} \equiv \tfrac{1}{2}\left(\hat{\bar{\mathbf{E}}} \times \hat{\bar{\mathbf{H}}}^* \right) \quad [\mathrm{W/m^2}]. \tag{B.40}$$

Local form in the frequency domain: *R*-system

The local form of Poynting's Theorem in the frequency domain in the *R*-system is:

$$-\nabla \cdot \left(\hat{\bar{\mathbf{E}}}' \times \hat{\bar{\mathbf{H}}}'^* \right) = j\omega\mu\hat{\bar{\mathbf{H}}}' \cdot \hat{\bar{\mathbf{H}}}'^* + \sigma\hat{\bar{\mathbf{E}}}' \cdot \hat{\bar{\mathbf{E}}}'^*. \tag{B.41}$$

From this, the conservation of energy can be written as:

$$-\mathrm{Re}\left\{ \nabla \cdot \hat{\bar{\mathbf{S}}}' \right\} = \tfrac{1}{2}\mathrm{Re}\left\{ \sigma\hat{\bar{\mathbf{E}}}' \cdot \hat{\bar{\mathbf{E}}}'^* \right\}. \tag{B.42}$$

Local form in the frequency domain: *L*-system

In the *L*-system, the local form of Poynting's Theorem in the frequency domain is:

$$-\nabla \cdot \left(\hat{\bar{\mathbf{E}}} \times \hat{\bar{\mathbf{H}}}^* \right) = j\omega\mu\hat{\bar{\mathbf{H}}} \cdot \hat{\bar{\mathbf{H}}}^* + \hat{\bar{\mathbf{H}}} \cdot j\omega\mathbf{B}_{rem} + \sigma\hat{\bar{\mathbf{E}}} \cdot \hat{\bar{\mathbf{E}}}^* + (\sigma\mu\mathbf{v}_c \times \hat{\bar{\mathbf{H}}}) \cdot \hat{\bar{\mathbf{E}}}^*. \tag{B.43}$$

From this, the conservation of energy can be written as:

$$-\mathrm{Re}\left\{\nabla\cdot\hat{\mathbf{S}}\right\} = \tfrac{1}{2}\mathrm{Re}\left\{\hat{\mathbf{H}}\cdot j\omega\mathbf{B}_{rem}\right\} + \tfrac{1}{2}\mathrm{Re}\left\{\sigma\hat{\mathbf{E}}\cdot\hat{\mathbf{E}}^*\right\} + \tfrac{1}{2}\mathrm{Re}\left\{(\sigma\mu\mathbf{v}_c\times\hat{\mathbf{H}})\cdot\hat{\mathbf{E}}^*\right\}.$$
(B.44)

Integral form in the frequency domain: *R*-system

The final step is to integrate (B.41) over an appropriately chosen volume V to obtain the integral form in the frequency domain in the R-system. In fact, the conservation of energy, equation (B.42) may rather be used because of its physical significance. One obtains:

$$-\mathrm{Re}\left\{\oint_S \hat{\mathbf{S}}'\cdot d\mathbf{a}\right\} = \tfrac{1}{2}\mathrm{Re}\left\{\int_V \sigma\hat{\mathbf{E}}'\cdot\hat{\mathbf{E}}'^*\,dv\right\},$$
(B.45)

where S is the bounding surface of V, i.e. $S = \partial V$.

Integral form in the frequency domain: *L*-system

The volume integral of the conservation of energy (B.44) in the L-system is:

$$-\mathrm{Re}\left\{\oint_S \hat{\mathbf{S}}\cdot d\mathbf{a}\right\} = \tfrac{1}{2}\mathrm{Re}\left\{\int_V \hat{\mathbf{H}}\cdot j\omega\mathbf{B}_{rem}\,dv\right\}$$
$$+ \tfrac{1}{2}\mathrm{Re}\left\{\int_V \sigma\hat{\mathbf{E}}'\cdot\hat{\mathbf{E}}^*\,dv\right\} + \tfrac{1}{2}\mathrm{Re}\left\{\int_V (\sigma\mu\mathbf{v}_c\times\hat{\mathbf{H}})\cdot\hat{\mathbf{E}}^*\,dv\right\}.$$
(B.46)

B.7 Application of the theory to the electrical machine

B.7.1 What is calculated in the thesis?

In the thesis, the average air gap power, or average source power $\langle P_{source}\rangle$, is calculated. This is done by finding the complex Poynting vector $\hat{\mathbf{S}}$ and performing a closed surface integral on it; this is documented in Section 4.6. This air gap power is the power that flows from the stator to the rotor. The calculation is done for the case where the rotor rotates and where it is locked.

In other words, in the thesis, the left-hand sides of equations (B.45) and (B.46) are calculated. The purpose of this appendix is to provide clues to the *interpretation* of the already obtained air gap power. The right-hand sides of equations (B.42) and (B.44) are thus never calculated, only interpreted. The interpretation is a combination of what is derived in this appendix as well as clues from the space and time harmonic information obtained from the left-hand sides.

B.7.2 A freely rotating rotor

In the *R*-system, i.e. in rotor coordinates, we have therefore:

$$\langle P'_{source} \rangle = \langle P'_{diss,sc} \rangle, \tag{B.47}$$

meaning that the average air gap power is the power dissipated in the shielding cylinder. This happens only for nonequal space and time harmonics. For equal space and time harmonics, in rotor coordinates, the air gap power is zero.

In the *L*-system, i.e. in stator coordinates, we have therefore:

$$\langle P_{source} \rangle = \langle P_{mech} \rangle + \langle P_{diss,sc} \rangle + \langle P_{mech,sc} \rangle. \tag{B.48}$$

As in (B.47), the power terms in (B.48) are interpreted depending on the combination of space and time harmonics. Average mechanical power is only transferred when they are equal; for the other cases it is zero. For nonequal space and time harmonics, power is transferred to the shielding cylinder instead of to the permanent magnets. To find the part of this power that is dissipated, and which part is mechanical, the rotor slip needs to be introduced; this is done in Chapter 7.

B.7.3 A locked rotor

In Chapter 6, the locked-rotor machine impedance is calculated. This is done directly from the air gap power of (B.47), since the *L*-system is used when the rotor stands still. (At standstill, the *R*- and *L*-systems are the same.)

In terms of the circuit quantities voltage and current, the active and reactive source power can be written as:

$$\langle P_{source} \rangle + j Q_{source} = \tfrac{1}{2} \hat{v} \hat{i}^*, \tag{B.49}$$

where $\hat{v}$ and $\hat{i}$ are the peak values of an equivalent voltage and current.

The complex impedance is defined by Ohm's Law as:

$$\hat{v} = \bar{Z} \hat{i}^*, \tag{B.50}$$

which suggests dividing (B.49) by $|\hat{i}|^2/2$, leading to:

$$\bar{Z} = \frac{\hat{v}\hat{i}^*}{|\hat{i}|^2} = \frac{2}{|\hat{i}|^2} \left[\langle P_{source} \rangle + j Q_{source} \right]. \tag{B.51}$$

The resistance is calculated by substituting (B.47) into the real part of (B.51):

$$R = \operatorname{Re}\left\{ \bar{Z} \right\} = \frac{2 \langle P_{diss,sc} \rangle}{|\hat{i}|^2}. \tag{B.52}$$

APPENDIX C

A brief overview of Bessel functions

The modified Bessel functions are described in detail in many texts on differential equations, like [Jef90]. McLachlan wrote a book [McL55] entirely devoted to the subject of Bessel functions with the emphasis on practical problem solving.

As a very brief overview, there are four basic Bessel functions. They are generally defined for non-integral order γ. For integral order k, the definitions are slightly different. The four Bessel functions are:

- $J_\gamma(x)$: Bessel function of the first kind of non-integral order γ:

$$J_\gamma(x) = x^\gamma \sum_{m=0}^\infty \frac{(-1)^m x^{2m}}{2^{2m+\gamma}\, m!\, \Gamma(m+1+\gamma)}, \tag{C.1}$$

  where Γ is the Gamma function (factorial function), defined as:

$$\Gamma(x) = \int_0^\infty e^{-t} t^{x-1} dt; \quad x > 0. \tag{C.2}$$

  Although $\Gamma(x)$ is defined for positive x it may be extended to negative x. For negative integers, $\Gamma(x)$ is infinity and for negative rational numbers, $\Gamma(x)$ may be determined from the property $x\Gamma(x) = \Gamma(x+1)$.

- $J_k(x)$: Bessel function of the first kind of integral order k:

$$J_k(x) = x^k \sum_{m=0}^\infty \frac{(-1)^m x^{2m}}{2^{2m+k}\, m!\,(m+k)!}; \quad k = 0, 1, 2, \cdots \tag{C.3}$$

- $Y_\gamma(x)$: Bessel function of the second kind of non-integral order γ:

$$Y_\gamma(x) = \frac{J_\gamma(x)\cos(\gamma\pi) - J_{-\gamma}(x)}{\sin(\gamma\pi)} \tag{C.4}$$

- $Y_k(x)$: Bessel function of the second kind of integral order k:

$$Y_k(x) = \lim_{\gamma \to k} Y_\gamma(x) \tag{C.5}$$

- $I_\gamma(x)$: Modified Bessel function of the first kind of non-integral order γ:

$$I_\gamma(x) = j^{-\gamma} J_\gamma(jx), \tag{C.6}$$

obtained by replacing x with jx in $J_\gamma(x)$.

- $I_k(x)$: Modified Bessel function of the first kind of integral order k:

$$I_k(x) = j^{-k} J_k(jx). \tag{C.7}$$

- $K_\gamma(x)$: Modified Bessel function of the second kind of non-integral order γ:

$$K_\gamma(x) = \frac{\pi}{2} \frac{I_{-\gamma}(x) - I_\gamma(x)}{\sin(\gamma\pi)} \tag{C.8}$$

- $K_k(x)$: Modified Bessel function of the first kind of integral order k:

$$K_k(x) = \lim_{\gamma \to k} K_\gamma(x). \tag{C.9}$$

For integral order k, Bessel functions $J_k(x)$ and $Y_k(x)$ may be used as a basis for the solutions of the Bessel differential equation:

$$x^2 y'' + xy' + (x^2 - k^2)y = 0; \quad k \geq 0, \tag{C.10}$$

while $I_k(x)$ and $K_k(x)$ may be used as a basis for the solutions of the modified Bessel differential equation:

$$x^2 y'' + xy' - (x^2 + k^2)y = 0. \tag{C.11}$$

An elementary change of variable in (C.11) results in the more general form:

$$x^2 y'' + xy' - (\tau^2 x^2 + k^2)y = 0, \tag{C.12}$$

which has the general solution:

$$y(x) = c_1 I_k(\tau x) + c_2 K_k(\tau x). \tag{C.13}$$

Equation (6.38) can be considered a generalized modified Bessel differential equation from (C.12). Its solution, equation (6.39), was obtained from (C.13).

As a final remark on the solution of $\bar{R}$, it should be noted that the variable x used above in the definitions of the Bessel functions may be complex. The boundary condition constants are then also complex.

Eddy current loss in the stator iron

In this appendix, the two-dimensional magnetic field used in Chapters 5–7 is further simplified to a one-dimensional field. It can also be seen as a "snapshot" of the rotating situation where the tangential component of the field is zero. This situation is drawn in Figure D.1, where the permanent magnet is situated in the lower vertical position, and the only field component is radially upwards. The assumption of a one-dimensional **H**-field is valid if $2b \ll h$, which is true for the EμFER machine.

The calculation method is described in detail in [Lam66], where the solution of the power loss in the rectangular sheet conductor II in Figure D.1(c) is developed. The power loss in a laminated core may be estimated from the power loss in sheet II by multiplying with the volume of the stator iron.

The problem is described by assuming a time-harmonic magnetic field only in the x-direction that is only dependent on z: $\bar{\mathbf{H}} = \bar{H}_x(z)\hat{\mathbf{i}}_x$ and by writing the ordinary differential equation:

$$\frac{d^2 \bar{H}_x}{dz^2} = k_\tau^2 \bar{H}_x, \tag{D.1}$$

from Maxwell's equations. In equation (D.1), the constant k_τ is similar to (6.69) and defined by:

$$k_\tau \equiv \sqrt{j\omega\sigma\mu}, \tag{D.2}$$

where $\omega = 2\pi f_s$ is the angular frequency of the field, σ is the conductivity and μ the permeability of the material. The solution to (D.1) is assumed as:

$$\bar{H}_x(z) = \bar{H}_1 e^{k_\tau z} + \bar{H}_2 e^{-k_\tau z}. \tag{D.3}$$

The boundary condition:

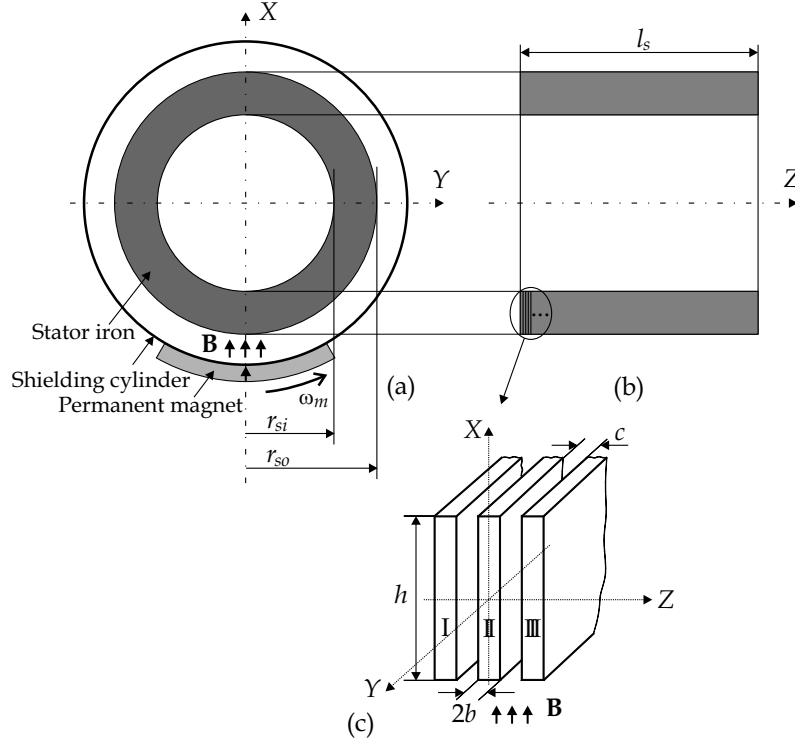$$\bar{H}_x(b) = \bar{H}_x(-b), \tag{D.4}$$

Figure D.1: The stator laminations used for calculating the eddy current loss in the stator iron.

is substituted into (D.5) to result in:

$$\bar{H}_0 = \bar{H}_1 e^{k_\tau b} + \bar{H}_2 e^{-k_\tau b}; \tag{D.5}$$

$$\bar{H}_0 = \bar{H}_1 e^{-k_\tau b} + \bar{H}_2 e^{k_\tau b}, \tag{D.6}$$

where $\bar{H}_0$ is the rms value of the field intensity at the edge of the plate. The solution of the magnetic field intensity is therefore:

$$\bar{H}_x(z) = \bar{H}_0 \frac{\cosh(k_\tau z)}{\cosh(k_\tau b)}. \tag{D.7}$$

The current density is, by applying Ampére's Law to (D.7):

$$\bar{J}_z(z) = \bar{H}_0 k_\tau \frac{\sinh(k_\tau z)}{\cosh(k_\tau b)}. \tag{D.8}$$

By expanding the hyperbolic functions and making use of the skin depth:

$$\delta \equiv \sqrt{\frac{2}{\omega\sigma\mu}}, \tag{D.9}$$

the magnitude of the current density can be written as:

$$|\bar{J}_z(z)| = \frac{\sqrt{2}}{\delta}\bar{H}_0\sqrt{\frac{\cosh(\frac{2z}{\delta}) - \cos(\frac{2z}{\delta})}{\cosh(\frac{2b}{\delta}) + \cos(\frac{2b}{\delta})}} \qquad \text{(D.10)}$$

The rms magnetic field intensity $\bar{H}_0$ can be replaced by the readily available flux density in the stator iron. To do this, a surface integral of $\mu\bar{H}_x$ can be taken to find the total flux Φ, where $\bar{H}_x$ is obtained from (D.7). This total flux is then divided by the area of a lamination to find the mean flux density in the stator iron $\bar{B}_s$:

$$\bar{B}_s = \frac{\mu\delta\bar{H}_0}{b}\sqrt{\frac{\cosh(\frac{2b}{\delta}) - \cos(\frac{2b}{\delta})}{\cosh(\frac{2b}{\delta}) + \cos(\frac{2b}{\delta})}}. \qquad \text{(D.11)}$$

From equation (D.11), H_0 is rewritten in terms of B_s, and substituted into (D.10):

$$|\bar{J}_z(z)| = \frac{\sqrt{2}\bar{B}_s b}{\delta^2\mu}\sqrt{\frac{\cosh(\frac{2z}{\delta}) - \cos(\frac{2z}{\delta})}{\cosh(\frac{2b}{\delta}) - \cos(\frac{2b}{\delta})}}, \qquad \text{(D.12)}$$

which may be integrated to find the loss density due to eddy currents in the stator iron:

$$p_{s,Fe,e,v} = \frac{1}{2b\sigma}\int_{-b}^{b}|\bar{J}_z(z)|^2\,dz = \frac{1}{6}|\bar{B}_s|^2\sigma\omega^2 b^2 F(\xi) \quad [\text{W/m}^3]. \qquad \text{(D.13)}$$

In (D.13), the function:

$$F(\xi) \equiv \frac{3}{\xi}\frac{\sinh\xi - \sin\xi}{\cosh\xi - \cos\xi}, \qquad \text{(D.14)}$$

was introduced. The variable ξ is the ratio of the lamination thickness to the skin depth, or:

$$\xi \equiv \frac{2b}{\delta}. \qquad \text{(D.15)}$$

The k-th space harmonic component of the radial component of the peak magnetic flux density due to the magnets, $\widehat{B}_{r,mag,k}$, is used to find the peak yoke flux: $\widehat{\Phi}_{sy,k} = \widehat{\Phi}_{r,mag,k}/2$, and in turn the rotor yoke flux density $\widehat{B}_{sy,k}$. This flux density is used to find the loss density per space harmonic of the magnets as:

$$p_{s,Fe,e,v,k} = \frac{1}{6}\widehat{B}_{sy,k}^2\sigma\pi^2 f_k^2(2b)^2 F_k(\xi_k), \qquad \text{(D.16)}$$

The total stator loss induced in the stator iron is obtained by multiplying (D.16) with the stator iron volume:

$$V_{s,Fe} = \pi\left(r_{so}^2 - r_{si}^2\right)l_s, \qquad \text{(D.17)}$$

and summing over the space harmonics:

$$P_{s,Fe,e} = \sum_{k=1,3,5,\cdots}^{\infty}\frac{1}{6}V_{s,Fe}\widehat{B}_{sy,k}^2\sigma\pi^2 f_k^2(2b)^2 F_k(\xi_k). \qquad \text{(D.18)}$$

**Modelling and optimization
of a permanent magnet machine
in a flywheel**

PhD thesis
by Stanley Robert Holm

Hybrid electric vehicles

To reduce the emissions of vehicles on our roads in the future, many companies, research institutes and universities are now searching for alternatives for the internal combustion engine.

One obvious solution is to replace it with an electric motor supplied by batteries, resulting in an electric vehicle. Electric vehicles have some problems, though, like the severely limited range and very long recharge times of the batteries. The thesis starts by mentioning the declining sales figures of electric vehicles due to (among others) these reasons. They are opposed to those of hybrid electric vehicles, whose sales figures rose during the same time span.

In a hybrid electric vehicle, the internal combustion engine is not removed, but another traction power source is added. This second power source is an energy storage device of some kind, and provides peak power, while the internal combustion engine provides average power. A hybrid electric vehicle goes a long way in solving the emission problem and the use of the second power source also increases the efficiency of the vehicle; it does so by the load-levelling effect just mentioned, by allowing the internal combustion engine to run in the narrow rpm band where it is most efficient and by re-using energy recovered from braking.

This thesis is concerned with this second power source in the vehicle: the energy storage device and its power delivery capabilities. Specifically, large vehicles like

busses and trams are the focus of attention rather than passenger cars.

Energy storage technologies for large hybrid electric vehicles

At the start of the thesis, it is shown that large hybrid electric vehicles like busses and trams require medium energy and high power. High power is in the order of 100s of kWs, and a corresponding medium energy is the level required to deliver this power for tens of seconds to several minutes.

To find the most suitable energy storage technology to meet these requirements, four technologies were investigated. The result of this investigation is that composite flywheels are the most suitable for applications like these, taking a large number of factors into account.

The EμFER system

A project was started to design and build such a flywheel energy storage system for use in large hybrid electric vehicles like busses and trams. The project was conducted in collaboration with the Centre for Concepts in Mechatronics (CCM) B.V. (Nuenen, the Netherlands). This project follows the successful EMAFER[1] system. The flywheel in the EMAFER system rotates at 15 000 rpm; its energy and continuous power levels are 14.4 MJ and 300 kW, respectively.[2] The follow-up system, called EμFER, was initiated to reduce the overall size and mass, to reduce the no-load losses and to build a system with a flatter profile than that of the EMAFER system. To reduce the required flywheel size and mass, the flywheel of the EμFER system rotates at 30 000 rpm. It stores 7.2 MJ and the desired continuous power output is 150 kW, with the machine losses (both at load and at no load) as low as possible.

The electrical machine

The geometry of the flywheel called for a radial flux machine with surface-mounted magnets and solid back iron. To reduce the no-load loss induced in the stator iron, the stator teeth (as used in EMAFER) were removed to obtain a slotless stator. This in turn necessitated the use of Litz wire for the stator conductors to limit the induced loss in the stator winding. Since the rotor rotates at 30 000 rpm in a low-pressure atmosphere, cooling it is very difficult. This requires that very low loss is induced in the rotor: a shielding cylinder is thus used. With these facts as design inputs, the EμFER electrical machine was designed.

Design methodology: An analytical model

The thesis motivates the use of analytical techniques for the design of a machine of this type and geometry. A comprehensive analytical model was derived that de-

---

[1]EMAFER = **E**lectro-**M**echanical **A**ccumulator **F**or **E**nergy **R**e-**U**se.

[2]Where this system is used, the energy is 7.6 MJ and the power level varies between 133 kW and 200 kW.

scribes the machine completely. This model, based on two-dimensional electromagnetic fields, includes all space and time harmonic effects, as well as high-frequency effects like the skin effect in the shielding cylinder.

This model consists of two parts: the permanent-magnet field (including three permanent-magnet arrays) and the stator current field. The latter includes the effect of the eddy currents in the shielding cylinder. All relevant and interesting machine quantities were derived from these two fields or their combination, in terms of the magnetic vector potential.

Torque and losses were obtained from the combined field by means of the Lorentz force and the Theorem of Poynting.

The analytical model was validated by means of the finite element method (magnetic field) and by means of experimental measurements (the locked-rotor machine impedance and no-load voltage).

Conclusions

The most important conclusions drawn in the thesis are grouped by the thesis objectives:

1. *To find the most suitable energy storage technology for use in large hybrid electric vehicles like busses and trams.*
   The thesis shows that composite flywheels are the most suitable technology for applications like these.

2. *To design the electrical machine for the EµFER flywheel energy storage system.*
   The results obtained and documented in the thesis show that the design goal of 150 kW output power was met. (The fundamental space and time harmonic power is 177 kW.) Furthermore, the low-loss requirements were also met as is evident from the low induced rotor loss in the shielding cylinder at load and the induced loss in the stator at no load. The induced loss in the shielding cylinder was calculated as 124 W for a typical CSI current waveform. The induced stator iron loss was calculated as 2970 W and the induced copper loss as 115 W. The sum of these losses is approximately 2% of the nominal power.

3. *To optimize the machine geometry for given flywheel dimensions.*
   The optimum machine geometry for a given carbon-fibre inside radius (150 mm) has been found in the thesis. The optimization criteria were high torque, low total stator losses and very low rotor loss in the shielding cylinder. This optimum is:

   - $r_{si} = 23.036$ mm; $r_{so} = 68.036$ mm; $r_w = 101.66$ mm; $r_{ci} = 106.66$ mm; $r_{co} = 108.66$ mm; $r_{mo} = 134.14$ mm; $r_{ro} = 150$ mm.

   For this geometry, the peak flux density in the rotor yoke is $\widehat{B}_{ry} = 1.9477$ T; the peak fundamental space and time harmonic component of the electromagnetic torque is $T_{e,1,1} = 158.85$ Nm (corresponding to a power of 249.5 kW at

15 000 rpm). The total stator iron loss was 3725 W (it was chosen to be below 4 kW), and the induced loss in the shielding cylinder 116 W for the same CSI current waveform that was used throughout the thesis as an example.

4. *To derive a comprehensive analytical model of the electrical machine.*
   The analytical model was experimentally validated. The model is two-dimensional; the good agreement with measurements therefore led to the conclusion than 3D effects only play a minor role, in spite of the relatively large effective air gap. The model provides one voltage equation; this is the only voltage equation that is needed to completely describe the machine.

Modelering en optimalisering
van een permanente-magneet machine
in een vliegwiel

proefschrift
door Stanley Robert Holm

Hybride elektrische voertuigen

Voor het reduceren van de emissies van voertuigen op onze wegen zijn veel bedrijven, onderzoeksinstituten en universiteiten tegenwoordig op zoek naar alternatieven voor de interne verbrandingsmotor.

Eén voor de hand liggende oplossing is om die verbrandingsmotor te vervangen door een elektrische machine en batterijen, om zodoende een elektrische voertuig te verkrijgen. Elektrische voertuigen hebben echter problemen, zoals de beperkte actieradius en de lange oplaadtijden van de batterijen. Het proefschrift begint met het noemen van het feit van dalende verkoopcijfers van elektrische voertuigen als gevolg van (onder andere) deze problemen. Deze cijfers vormen een tegenstelling met die van hybride elektrische voertuigen: die zijn gestegen gedurende dezelfde periode.

In een hybride elektrisch voertuig wordt de interne verbrandingsmotor niet verwijderd, maar een ander vermogensbron wordt toegevoegd. Deze tweede bron van vermogen is een energieopslag-eenheid die piek-vermogen levert, terwijl de interne verbrandingsmotor het gemiddelde vermogen levert. Een hybride elektrisch voertuig lost het probleem van emissies gedeeltelijk op en de tweede vermogensbron verhoogt ook het rendement. Dit laatste gebeurt door het "load-levelling" effect door de interne verbrandingsmotor te laten draaien in het optimale toerentalgebied, en door het hergebruik van energie die bij het remmen teruggewonnen wordt.

245

Dit proefsfchrift gaat over deze tweede vermogensbron in het voertuig: de energieopslag-eenheid en zijn vermogensmogelijkheden. Meer specifiek concentreert het zich op grote voertuigen zoals bussen en trams, en niet op personenauto's.

Energieopslag technologieën voor grote hybride elektrische voertuigen

Aan het begin van het proefschrift wordt aangetoond dat grote hybride elektrische voertuigen zoals bussen en trams een gemiddelde hoeveelheid energie en hoog vermogen nodig hebben. Hoog vermogen betekent enkele honderden kW's, en een gemiddelde hoeveelheid energie is de hoeveelheid energie nodig voor het overdragen van dit vermogen gedurende periodes van enkele tientallen van seconden tot enkele minuten.

Om de meest geschikte energieopslag technologie te vinden om aan deze eisen te voldoen, worden vier technologieën onderzocht. Het resultaat van dit onderzoek is dat kunststofvliegwielen het meest geschikt is voor toepassingen als deze.

Het EμFER systeem

Er is een project opgestart om zo'n vliegwielsysteem te ontwikkelen en te bouwen voor gebruik in grote hybride elektrische voertuigen zoals bussen en trams. Dit project is uitgevoerd in samenwerking met het Centre for Concepts in Mechatronics (CCM) B.V. (Nuenen, Nederland). Het project volgt op het succesvolle EMAFER[3] project. Het vliegwiel in het EMAFER systeem draait op 15 000 rpm; de energieopslag is 14.4 MJ en het nominaal vermogen is 300 kW.[4] Het opvolgsysteem, genaamd EμFER, is geïnitieerd om het volume en de massa te verminderen, om de nullastverliezen te reduceren en om een systeem te bouwen met een platter profiel dan dat van het EMAFER systeem. Om de grootte en de massa te verminderen, draait EμFER op 30 000 rpm. De energieopslag is 7.2 MJ en het continu vermogen is 150 kW. De verliezen in nullast en vollast worden geminimaliseerd.

De elektrische machine

De geometrie van het vliegwiel is geschikt voor een radiaal flux machine met magneten op het rotoroppervlak en een rotorjuk van massief ijzer. Om de nullastverliezen te reduceren, zijn de statortanden die aanwezig waren in EMAFER, in EμFER verwijderd. Om het geïnduceerd verlies in de statorwikkeling te beperken zijn geleiders van Litze draad gebruikt. Aangezien de rotor op 30 000 rpm draait in een lage druk atmosfeer, is de koeling ervan erg moeilijk. Dit vereist dat het verlies in de rotor laag wordt gehouden. Daarom wordt een afschermcilinder gebruikt. Met deze ontwerpuitgangspunten is de EμFER elektrische machine ontworpen.

---

[3] EMAFER = **E**lectro-**M**echanical **A**ccumulator **F**or **E**nergy **R**e-**U**se.

[4] Waar dit systeem wordt gebruikt, is de energie 7.6 MJ en het vermogensniveau ligt tussen 133 kW en 200 kW.

Ontwerpmethodologie: Een analytisch model

Het proefschrift motiveert het gebruik van analytische technieken voor het ontwerp van een machine van dit type en geometrie. Een uitgebreid analytisch model dat de machine compleet beschrijft wordt afgeleid. Dit model, gebasseerd op tweedimensionale veldberekeningen, omvat alle effecten van tijdelijke- en ruimtelijke harmonischen, en hoogfrequente effecten zoals stroomverdringing in de afschermcilinder.

In dit model bestaat het magnetisch veld uit twee delen: het veld ten gevolge van de permanente magneten veld (voor drie permanente-magneet configuraties) en het veld ten gevolge van de statorstromen. Het laatsgenoemde veld omvat ook het effect van wervelstromen in de afschermcilinder. Alle relevante en interessante machinegrootheden worden afgeleid van deze twee velden of hun combinatie. Het veld wordt berekend via de magnetische vectorpotentiaal.

Koppel en verliezen worden berekend uit het gecombineerde veld door middel van de Lorentzkracht en de Stelling van Poynting.

Het analytisch model is geverifieerd door middel van de eindige elementen methode (magnetisch veld) en door middel van experimenten (de machine impedantie bij geblokkeerde rotor en de nullastspanning).

Conclusies

De belangrijkste conclusies van het proefschrift zijn gegroepeerd in de doelstellingen:

1. *Het vinden van de meest geschikte energieopslag technologie voor het gebruik in groot hybride elektrische voertuigen zoals bussen en trams.*
   Het proefschrift laat zien dat vliegwielen de meest geschikte technologie zijn voor dit soort toepassingen.

2. *Het ontwerpen van de elektrische machine voor het EµFER vliegwiel energieopslag systeem.*
   Het ontwerpdoel van 150 kW is bereikt. (Het vermogen overgedragen door de grondharmonische (ruimtelijk en tijdelijk) is 177 kW.) Verder zijn de nullastverliezen laag: dit wordt bevestigd door het lage verlies in de afschermcilinder bij vollast en het lage geïnduceerde verlies in de stator bij nullast. Het verlies in de afschermcilinder is berekend als 124 W voor een typische CSI stroomgolfvorm. Het geïnduceerde statorijzerverlies is berekend als 2970 W en het koperverlies als 115 W. Deze verliezen zijn samen ongeveer 2% van het nominaal vermogen.

3. *Het optimaliseren van de machinegeometrie voor gegeven vliegwieldimensies.*
   De optimale machinegeometrie voor een gegeven koolstofvezel binnenstraal (150 mm) is berekend in het proefschrift. De optimaliseringscriteria waren een hoog koppel, lage statorverliezen en een heel laag rotorverlies in de afschermcilinder. Dit optimum is:

- $r_{si} = 23.036$ mm; $r_{so} = 68.036$ mm; $r_w = 101.66$ mm; $r_{ci} = 106.66$ mm; $r_{co} = 108.66$ mm; $r_{mo} = 134.14$ mm; $r_{ro} = 150$ mm.

Voor deze geometrie is de piekwaarde van de fluxdichtheid in het rotorjuk $\widehat{B}_{ry} = 1.9477$ T; de piekwaarde van het elektromagnetische koppel veroorzaakt door de ruimtelijke en tijdelijke grondharmonische component van het veld is $T_{e,1,1} = 158.85$ Nm (wat overeenkomt met een vermogen van 249.5 kW bij 15 000 rpm). Het totale statorverlies is 3725 W (gekozen als onder de 4 kW), en het geïnduceerd verlies in de afschermcilinder voor een typische CSI golfvorm is 116 W.

4. *Het afleiden van een uitgebreid analytisch model van de elektrische machine.*
   Het analytisch model is experimenteel geverifieerd. Het model is tweedimensionaal; de goede overeenkomst van berekeningen en metingen leidt tot de conclusie dat 3D effecten slechts een beperkt rol spelen, ondanks de relatief grote effectieve luchtspleet. Het model resulteert in één spanningsvergelijking; dit is de enige spanningsvergelijking die nodig is om de machine in zijn geheel te beschrijven.

Curriculum Vitae

Stanley Robert Holm was born in Johannesburg, South Africa, in 1973. He received the B.Eng. and M.Eng. degrees in electrical engineering and the B.Sc.(Hons) degree in applied mathematics, all from the Rand Afrikaans University, Johannesburg, South Africa, in 1996, 1998 and 1998 respectively.

From 1998 - 1999 he worked in industry as a power electronics design engineer.

He started working towards the Ph.D. degree in September 1999 at the Delft University of Technology in the Netherlands. This thesis is the result of this research, done in the research group Electrical Power Processing of the Faculty of Electrical Engineering, Mathematics and Informatics.

His current research interests include high-power applications of power electronics, energy storage technologies, permanent magnet machines and various aspects of applied mathematics.